Study of charge density wave materials under current by X-ray diffraction

Ewen Bellec

université PARIS-SACLAY

UNIVERSITÉ PARIS SUD

NNT : 2019SACLS437

Thèse de doctorat

Study of charge density wave materials under current by X-ray diffraction

Thèse de doctorat de l'Université Paris-Saclay
préparée à l'Université Paris-Sud

École doctorale n°564 Physique en Île-de-France (EDPIF)
Spécialité de doctorat : Physique

Thèse présentée et soutenue à Orsay, le 26 Novembre 2019, par

EWEN BELLEC

Composition du Jury :

Véronique Brouet Directrice de recherche, CNRS (LPS)	Président
Jose Emilio Lorenzo Directeur de recherche, CNRS (Institut Néel)	Rapporteur
Sergei Zaitsev-Zotov Directeur de recherche, Russian Academy of Sciences (IRE)	Rapporteur
Serguei Brazovskii Directeur de recherche, Université Paris-Saclay (LPTMS)	Examinateur
Bertrand Toudic Directeur de recherche, CNRS (IPR)	Examinateur
Gerardina Carbone Chercheur, Université de Lund (Max IV)	Examinateur
David Le Bolloc'h Directeur de recherche, CNRS (LPS)	Directeur de thèse
Vincent Jacques Chargé de recherche, CNRS (LPS)	Co-directeur de thèse

Acknowledgment

First of all, I would like to thank my two supervisors David Le Bolloc'h and Vincent Jacques who guided me during my Master 2 internship and then during these 3 years of thesis. Thanks to them, I was able to discover the world of synchrotrons and participate in an experiment at the LCLS free electron laser. They taught me a lot about X-ray diffraction, which on paper seems simple in theory but can sometimes be very difficult in practice. I would always remember spending half an hour with my eyes fixed on a screen displaying the X-ray detector to find the diffraction peak of the charge density wave in NbSe3 and the joy of seeing about ten pixels lighting up indicating that we were approaching the correct diffraction angles. I was also able to learn how to use coherence in diffraction and especially obtained a lot of information on the behaviour of the charge density waves on which they worked for several years. Thank you very much.

I would like to thank the members of my jury for accepting my invitation, for taking the time to read this manuscript and for asking me questions and making very interesting comments during my defence. I would particularly like to thank my two referees Sergei Zaitsev-Zotov and Jose Emilio Lorenzo as well as Gerardina Carbone for sending me comments on my manuscript to allow me to make some corrections.

I also want to thank Isabel Gonzalez-Vallejo who is doing a thesis on charge density waves in rare-earth tritellurides using a time-resolved electron diffraction experiment at the Laboratoire d'optique appliquée. She participated in all the experiments on synchrotrons and LCLS that I used for my thesis. I thank her very much for that and for all the discussions we've had on explaining the measured data.

Many thanks to Pierre Monceau of the Néel Institute in Grenoble and Alexander Sinchenko of the Kotel'nikov Institute of Radioengineering and Electronics of Moscow who participated in the experiments at ESRF, LCLS and MAXIV. Pierre gave us the samples to do all of our experiments and participated in the samples preparation with Alexander in Grenoble. Alexander taught me a lot about the preparation of electrical contacts and especially how to correctly measure the threshold field in a CDW material, which is far from simple in rare earth tritellides elements since they remain metallic in the CDW phase. It was also a great pleasure to see you during my thesis defense.

Thanks to Jonathan Caillaux for giving me the idea to use the Green function and image charge methods to solve the CDW phase equation. Thank you for all these discussions that have always taught me something new and made me want to discover aspects of physics that I didn't know like quantum field theory. Good luck with the rest and for your defense. I also thank Gilles Abramivici for taking a look

at the calculations of the CDW phase in 3D.

I am grateful to Pascale Senzier of the LPS laboratory of Orsay for teaching me how to make proper gold contact evaporation on our $TbTe_3$ samples to measure the threshold current in a 4-points current-voltage measurement configuration.

I thank all the local contacts with whom we have worked: Matthieu Chollet at LCLS; Tobias Schulli, Steven Leake, Tao Zhou and Gilbert Chahine at the ESRF on ID01 beamline; Claire Laulhe and Pierre Fertey at the SOLEIL synchrotron at crystal beamline; Dominique Thiaudiere and Phillipe Joly at SOLEIL on beamline Diffabs; and finally Dina Carbone at the Swedish MAXIV on NanoMax beamline.

Many thanks to all the PhD students and former PhD students of the LUTECE and PULS teams of the LPS: Isabel Gonzalez-Vallejo, Jonathan Caillaux, Min-I Lee, Niloufar Niforoushan, Lama Khalil, Abraham Campos Contreras, Zhang Ziuxiang, Weis Mateusz (Post-doc), Arlensiù Celis.

Thank you to the other members of the LUTECE and PULS teams: Antonio Tejedas Gala, Marino Marsi (whom I thank for giving me the opportunity to get a master's internship at the Elettra synchrotron in Trieste, Italy), Papalazarou Evangelos, Nicolas Moisan, Chen Zhesheng, Olivier Plantevin, Rodrigues Miquitas Douglas, Duden Thomas.

A big thank you to all the members of the Laboratoire de Physique des Solides d'Orsay as well as to all the PhD students with whom we were able to share some good moments (Cookies Club, integration weekends).

And finally I would like to thank all the professors, internship supervisors and friends I was able to have during my undergraduate years at the University of Rennes 1, the Magistère d'Orsay and the Master 2 ICFP. Above all, I thank my family for having encouraged me in my studies and especially my parents for having supported me and helped me to do all these long years of studies in the best conditions.

Contents

Introduction

A charge density wave (CDW) is a low temperature phase predicted theoretically from a 1D model by Herbert Fröhlich in 1954 and independently by Peierls in 1955. At low temperature, the total energy of a 1D atomic chain is lowered by a periodic lattice displacement, called "Peierls distortion". This new periodicity of wavevector $2k_F$ (where k_F is the Fermi wavevector) opens a gap in the electronic energy band, hence this is a metal-to-insulator type of transition. However, real crystals are never strictly 1D. Fortunately, this transition can still occur in 3D metallic materials with a large electronic density at the Fermi energy along with a Fermi surface nesting at the CDW wavevector (this property is described in chapter 1).

In 1976, Monceau et al. observed an anomalous temperature dependence of the conductivity under applied current in the quasi-1D CDW crystal $NbSe_3$ [1]. Several experiments were performed on several other CDW materials ($K_{0.3}MoO_3$, $TbTe_3$,... etc) showing that if one applies a current higher than a threshold I_{th}, an additional collective CDW current is measured. Furthermore, this collective current is periodic (while the applied current is continuous) with a frequency of the order of the MHz. This is the so-called Narrow-Band Noise. This feature can be interpreted as a charge transport by a periodic array of CDW solitons, which were observed in X-ray diffraction on $K_{0.3}MoO_3$ [2].

Despite the fact that the first CDW experimental evidence in TTF-TCNQ [3] was discovered 46 years ago, new observations are made on these materials on a regular basis thanks to the development of modern experimental techniques. During my PhD, we used several large facilities: the ESRF synchrotron, specifically ID01 beamline and the free electron laser LCLS. I participated in other experiments (not shown in this thesis) at synchrotron SOLEIL on beamline Cristal (X-ray diffraction and pump-probe diffraction) and DiffAbs (X-ray diffraction while using a tensile machine to study a CDW under strain) and finally on beamline NanoMAX at synchrotron MAXIV. Using these modern instruments, we were able to measure certain properties of CDW samples which were not accessible 46 years from now such as :

- The "breaking" of the CDW in transverse at high current using the X-ray coherent beam available at LCLS.

- The evidence of CDW surface pinning in the quasi-1D material $NbSe_3$ using the X-ray micro-diffraction tool available at the ESRf synchrotron on beamline ID01.

- The local rotation of the CDW in the quasi-2D material $TbTe_3$ and its spatial inhomogeneity and finally the creation of CDW pinning center from irradiation effect using both X-ray micro-diffraction.

In the first chapter, we present the general CDW theory with a short introduction on the historical development of this topic. We show how the Fermi surface nesting of

a 1D crystal leads to the divergence of the electronic susceptibility at the wavevector $2k_F$. This divergence induces a softening of the phonon at $2k_F$ which "freezes" at the CDW transition temperature T_c, leading to a periodic atom displacement of wavevector $2k_F$. Then, we explain how this transition induces a gap opening in the electronic energy band and show its behavior as function of temperature. Next, we give a non-exhaustive list of recent topics on CDW which includes: CDW in high-T_c supraconductor, time-resolved studies, quantized conductivity in small CDW samples, topology and CDW,...etc. Finally, the two main samples of this manuscript, $NbSe_3$ and $TbTe_3$, are presented.

In the second chapter, we briefly present X-ray diffraction history and X-ray production facilities like synchrotron and free electron laser. Diffraction theory is then detailed and we end this chapter with the calculation of the X-ray diffraction pattern of a CDW.

In chapter 3, we first describe the non-linear current observed above a threshold in several CDW materials like $NbSe_3$, $TbTe_3$ or $K_{0.3}MoO_3$. We present the sliding CDW theory but since it fails to explain the CDW supersatellites measured in $K_{0.3}MoO_3$ [2] we follow the solitonic transport model and present several experimental evidences. Then, we tried to observe the CDW supersatellite in $NbSe_3$ at ID01 beamline of the ESRF using a flight tube under vacuum of 6.5m in order to increase the reciprocal space resolution. The supersatellites were still not visible, thus we calculate a lower limit for the periodicity of the soliton lattice in $NbSe_3$. Finally, we present the preliminary results of coherent X-ray diffraction of the CDW in $NbSe_3$ under current obtained at the free electron laser LCLS in which we observed the "breaking" in transverse of the CDW at the threshold current I_{th}.

Chapter 4 contains the main result of this thesis. Using the micro-diffraction setup of ID01 beamline at the ESRF, we were able to make a spatial map of the CDW deformation in the quasi-1D $NbSe_3$. When current is applied, the CDW displays a transverse deformation. After further data treatment, we were able to calculate the CDW phase ϕ and observe a pinning at the sample surface. Several resistivity experiments from the literature showed a dependence of I_{th} on the sample transverse cross-section which were interpreted as CDW surface pinning. However, this is the first time that we have a space-resolved map of the CDW shear induced by this pinning (by shear we mean the transverse deformation of the CDW induced by a current in the longitudinal CDW direction).

In chapter 5, using the same micro-diffraction setup at ID01 beamline, we measured the CDW evolution under current in the quasi-2D $TbTe_3$. In a first region, we observed a strict rotation of the CDW wavefronts. By "strict", we mean that no compression or expansion of the CDW occurs under current. In calculating the spatial standard deviation of this rotation, we observed that it is not strictly rigid but that it varies greatly depending on the position on the sample. In a second and third regions, we measured the formation of strong pinning centers, probably induced by X-ray irradiation of the sample. Close to these centers, the CDW compress and expand without any rotational components.

Finally in chapter 6, we make a theoretical link between the surface pinning observed in chapter 4 and several threshold I_{th} measurements as function of the sample dimensions (length, height, width) from the literature. First, we calculate the

CDW phase $\phi(\vec{r})$ imposing pinning at the electrical contacts and on the transverse surfaces. The green function and image charge method is described and the detailed calculation of $\phi(x)$ in the 1D case is given. The steps being similar in 3D, we give the full 3D expression of $\phi(\vec{r})$. Using the phase slip process presented in appendix B, we fit several sets of data using our theoretical expression. Next, several ideas on the microscopic origin of the CDW surface pinning are discussed. The last section ends with a necessary examination of the numerical error convergence of an infinite sum used in the fitting procedure.

Chapter 1

Charge density wave transition in solids

1.1 Charge density wave at a glance

The charge density wave (CDW), often referenced as Peierls distortion, was first discussed by Herbert Fröhlich [4] in 1954 in a paper dealing with the case of a one dimensional atomic chain. In this paper, he studied the coupling between electrons and phonons and found an instability toward a periodic lattice distortion which induces a gap opening in the electron spectrum. This low temperature phase of matter is now called a charge density wave. He thought this transition, in the case of an incommensurate CDW, could be related to the superconductivity discovered by Heike Kamerlingh Onnes in 1911. Unfortunately Fröhlich did not take into account pinning of the CDW by crystal impurities and the correct description of superconductivity was later found to be BCS theory [5] (named after its authors Bardeen, Cooper and Schrieffer).

In the meantime, Peierls (after whom the transition is named) published a book in which he describes this instability, still in a 1D system ([6] page 109). He did not think at that time that his theory could be related to real condensed matter systems. In a book published later in 1991, he exposed his early doubts : "This instability came to me as a complete surprise when I was tidying material for my book (Peierls 1955), and it took me a considerable time to convince myself that the argument was sound. It seemed of only academic significance, however, since there are no strictly one-dimensional systems in nature" ([7] page 29).

Indeed, Peierls had good reason to doubt since in 1967, the Mermin–Wagner –Hohenberg theorem [8, 9] showed that no strictly 1D crystal could exist at finite temperature. But, fortunately, this CDW transition can still happen in a real 3D crystal if there is a strong nesting of the Fermi surface (which will be explained later). A first CDW was observed in an organic compound tetrathiafulvalene tetracyanoquinodimethane (TTF-TCNQ) [3] using resistivity measurement. Since the CDW transition is a metal to insulator phase transition, one can observe an increase of the resistivity at the critical temperature. Nowadays several organic and non-organic crystals displaying a CDW are well known as quasi-1D $NbSe_3$ [10], blue bronze $K_{0.3}MoO_3$ [11], KCP [12], etc..., the quasi-2D Rare-earth Tritellurides family

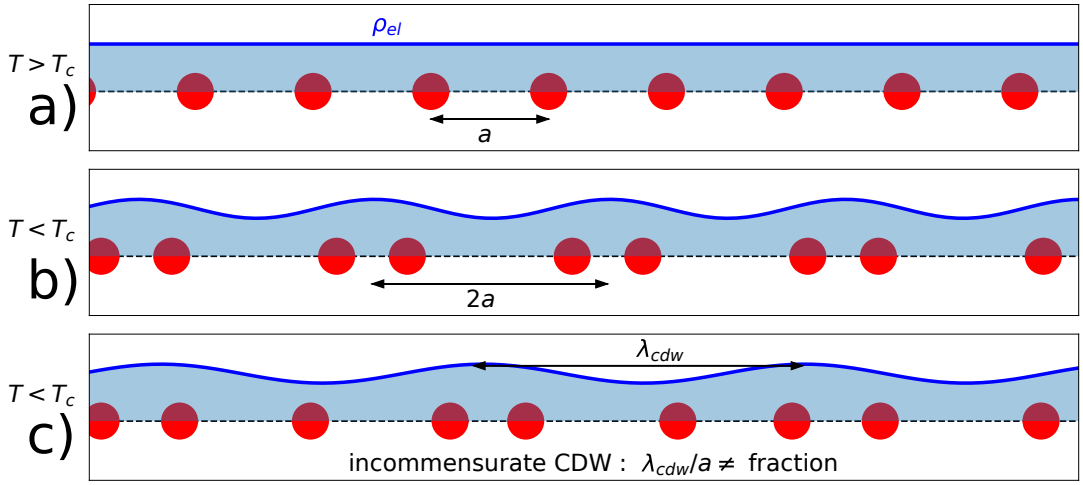

Figure 1.1: Peierls transition in a 1D atomic chain. a) high temperature phase. b) Below a critical temperature T_c, it becomes energetically favorable for the ions (in red) to have a periodic distortion, therefore increasing the lattice parameter. The electronic density ρ_{el} (in blue) follows this displacement. c) In the case of an incommensurate CDW, the system becomes aperiodic and the lattice parameter becomes illdefined.

[13] ($ErTe_3$, $TbTe_3$, $GdTe_3$, etc...) and some purely 3D like Chromium [14, 15]. The CDW is a very common phase of matter observed in a large variety of materials, see [16] for an extensive review.

Before getting into the mathematical formulation, a schematic illustration of the CDW transition is depicted in figure 1.1. Above the transition temperature T_c, the system is a periodic chain of atoms separated by a distance a and the electron density ρ_{el} is a constant. Below T_c, the ions display a periodic displacement, increasing the lattice parameter (here $a \rightarrow 2a$ in b), a dimerization). The negatively charged electrons follow the positive ions and the electronic density becomes periodic. In figure 1.1 b), the lattice parameter at $T < T_c$ is twice the one for $T > T_c$. This is only the case for a half filled electronic band. The CDW wavelength λ_{cdw} will depend directly on this band filling and can even be incommensurate as in figure 1.1 c), meaning that $\frac{\lambda_{cdw}}{a}$ can't be written as a fraction. In this incommensurate case, the CDW system is therefore aperiodic and new phenomena may occur as the CDW non-linear current described in chapter 3.

In the following sections, I will explain how this transition occurs from a simple toy model of a 1D chain of atoms with half filled electronic band (for simplicity of calculations) showing the increase of the electronic susceptibility for $T \gtrsim T_c$, the Kohn anomaly in the phonon spectrum, the opening of a gap in the electronic band and the gap evolution for $T < T_c$ along with some experimental evidences.

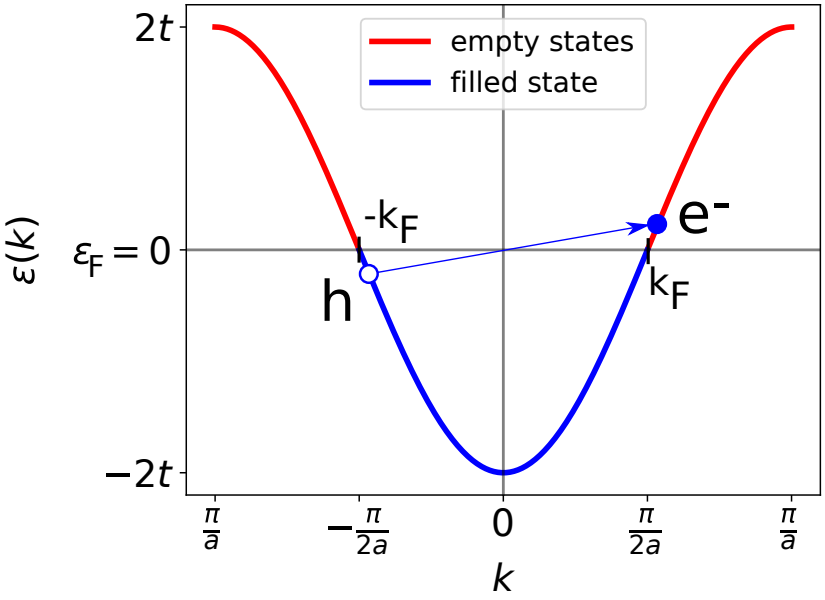

Figure 1.2: Energy band of a metallic 1D atomic chain. It cost very few energy to create an electron (e^-) hole (h) pair near the Fermi level $\epsilon_F = 0$. This property is the main cause of the electronic susceptibility divergence at a wavevector $2k_F = \pi/a$.

1.2 1D crystal electronic band

One of the simplest models for electrons in a 1D crystal with N sites (ions) is the tight-binding Hamiltonian.

$$H = -t \sum_{n=1}^{N} \left(c_{n+1}^{\dagger} c_n + c_n^{\dagger} c_{n+1} \right)$$

where t is electron hopping parameter, $c^{\dagger}$ and c are respectively the creation and annihilation operator for the electrons. Taking periodic boundary conditions (site $N+1 \Leftrightarrow$ site 1) plus using the fourier transformed operators $c_n = \frac{1}{\sqrt{N}} \sum_k c_k e^{ikna}$ and the formula $\sum_{n=1}^{N} e^{ikna} = N\delta_k$, one can show that the diagonalized Hamiltonian is

$$H = \sum_k c_k^{\dagger} c_k \epsilon(k)$$

with $\epsilon(k) = -2t\cos(ka)$. This electronic energy band dispersion is displayed in figure 1.2.

All the states for which $\epsilon(k) < \epsilon_F$ are filled with electrons at 0 K. As said earlier, the half filled case is chosen here for pedagogical purpose. From this picture, one can see that it cost a very small amount of energy to take an electron close to the fermi level $\epsilon(k) \lesssim 0$ and promote it to an excited state at a distance $\sim 2k_F = 2\frac{\pi}{2a}$ in k space where $\epsilon(k) \gtrsim 0$. We know that the amplitude of a periodic electron density of wavevector $2k_F$ is given by the number of electron-hole pairs separated by $2k_F$, $\rho(2k_F) = \frac{1}{\sqrt{N}} \sum_k \langle c_{k+2k_F}^{\dagger} c_k \rangle \Longrightarrow \rho(x) \sim \rho(2k_F)\cos(2k_F x)$. Therefore, in this 1D

crystal, a small amount of additional energy can induces a periodic modulation of the electronic density of wavelength $\frac{2\pi}{2k_F} = 2a$. One say that there is a "nesting" of the Fermi Surface at $2k_F$ meaning, in a more rigorous way, that $\epsilon(k + 2k_F) \approx \epsilon(k) \approx \epsilon_F$ for a large number of k. When the k_y and k_z directions are considered, the 2 Fermi points at $\pm k_F$ becomes 2 planes defined by $(\pm k_F, k_y, kz) \forall\, k_y, k_z$ perfectly nested by the CDW wavevector $(2k_F, 0, 0)$. It is this property that induces a divergence of the electronic susceptibility $\chi(2k_F)$ as shown in the following.

1.3 Divergence of the electronic response to a periodic potential

From linear response theory, the static electronic susceptiblity up to first order is given by the Lindhard formula [17]

$$\boxed{\chi(q) = \frac{2}{L} \sum_k \frac{f_{FD}\left(\epsilon(k+q)\right) - f_{FD}\left(\epsilon(k)\right)}{\epsilon(k+q) - \epsilon(k)}} \tag{1.1}$$

where $f_{FD}(\epsilon) = \frac{1}{\exp\left(\frac{\epsilon}{k_b T}\right)+1}$ is the Fermi-Dirac distribution. $\chi(q)$ measures the reaction of the electrons to an external potential. For example, if an electric field potential $\phi(q)$ of wavelenght $2\pi/q$ is applied to the system (in our case a phonon at $2k_F$), the electronic density will present a periodic modulation given by $\rho(q) = \chi(q)\phi(q)$.

$\chi(q)$ is given to the number of electron-hole (e^--h) pairs separated by a distance q in k space that the potential $\phi(q)$ can create as one can understand from the Lindhard formula from the following arguments. The denominator $\epsilon(k + q) - \epsilon(k)$ stems from the fact that it's easier to create an e^--h pair close in energy as in figure 1.2. The numerator $f_{FD}\left(\epsilon(k + q)\right) - f_{FD}\left(\epsilon(k)\right)$ tells us that one can only create a hole in a filled state and an electron in an empty one. The susceptibility for different temperatures is displayed in figure 1.3.

In the half-filling case, one can use the relation $\epsilon(k + 2k_F) = -2t\cos(ka + \pi) = +2t\cos(ka) = -\epsilon(k)$, and write the susceptibility for the relevant wavevector $2k_F$ as an integral in energy

$$\chi(2k_F) = 2 \int_{-2t}^{2t} n(\epsilon) \frac{f_{FD}(\epsilon) - f_{FD}(-\epsilon)}{2\epsilon}\, d\epsilon$$

In the case of an incommensurate CDW, one can do the same calculation approximating $\epsilon(k)$ by a linearized expression near to the Fermi energy $\epsilon(k) \approx \pm v_f(k \mp k_F)$ where $v_f = \frac{\partial \epsilon}{\partial k}(k_F)$ is the Fermi velocity, see [18] for more details. The most significant contribution to the integral in Eq 1.2 is for $\epsilon \sim \epsilon_F = 0$ hence using the approximation $n(\epsilon) \approx n(\epsilon_F)$ and using the two following relations $f_{FD}(\epsilon) - f_{FD}(-\epsilon) = -\tanh\left(\frac{\epsilon}{2k_b T}\right)$, $\int_0^b \frac{\tanh(x)}{x} \approx \ln\left(\frac{4e^\gamma b}{\pi}\right)$ where $\gamma \approx 0.577$ is the Euler constant one can show that

$$\chi(2k_F) \approx -n(\epsilon_F) \ln\left(\frac{2.27t}{k_b T}\right) \tag{1.2}$$

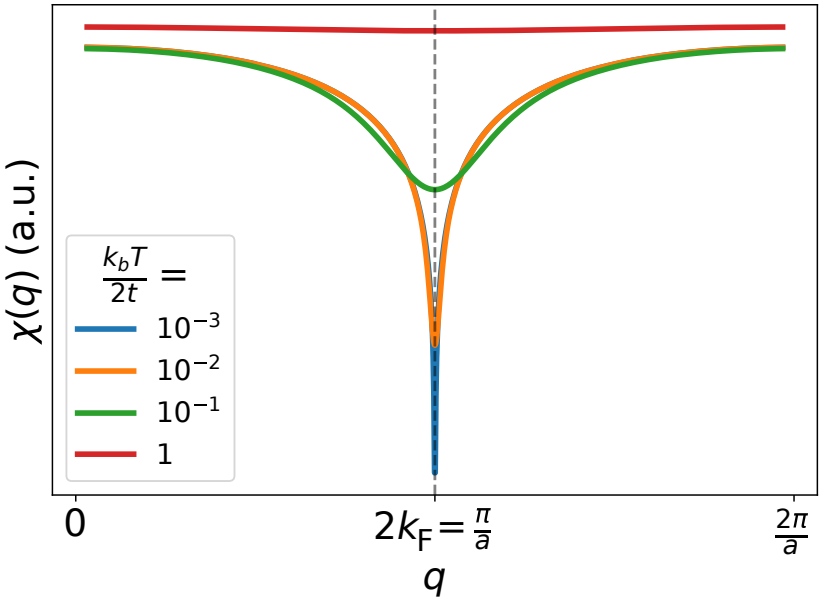

Figure 1.3: Electronic susceptiblity $\chi(q)$ for a 1D crystal calculated using Eq1.1, at several temperature. $\chi(q)$ displays a logarithmic divergence at the CDW wavevector $2k_F$ at low temperature. This property induces the Kohn anomaly as exposed in section below.

Hence the susceptibility displays a logarithmic divergence at low temperature at $q = 2k_F$ (the CDW wavevector) as depicted in figure 1.3. This susceptibility was measured in 1T-TaS_2 and 1T-$TaSe_2$ by Myron and Rath [19] . The large variation of $\chi(q)$ at $q = 2k_F$ induces a phonon softening as demonstrated in the next section. Once again, this divergence comes from the "easiness" to create electron-hole pairs separated by a distance $2k_F$ in reciprocal space near the Fermi energy. Any material exhibiting a strong nesting of the Fermi surface will display this divergence of $\chi(q)$.

1.4 Kohn anomaly and atomic lattice "freezing"

The idea that the electronic susceptibility could change the lattice vibration spectrum (called phonons) was proposed by Kohn in 1959 [20]. This phenomenon is usually described using a simple electron-phonon Hamiltonian introduced first by Frolich in 1952 [21].

$$H = H_{\text{electron}} + H_{\text{phonon}} + H_{\text{electron-phonon interaction}} \tag{1.3}$$

$$= \sum_k \epsilon(k) c_k^\dagger c_k + \sum_q \left(\frac{P_q P_{-q}}{2M} + \frac{M\omega^2(q)}{2} Q_q Q_{-q} \right) + \sum_{k,q} g(q) \sqrt{\frac{2M\omega(q)}{\hbar}} Q_q c_{k+q}^\dagger c_k \tag{1.4}$$

where $c^\dagger$ and c correspond to electron creation and annihilation operators, P_q and Q_q are the Fourier transformed momentum and position operators for the ion at a

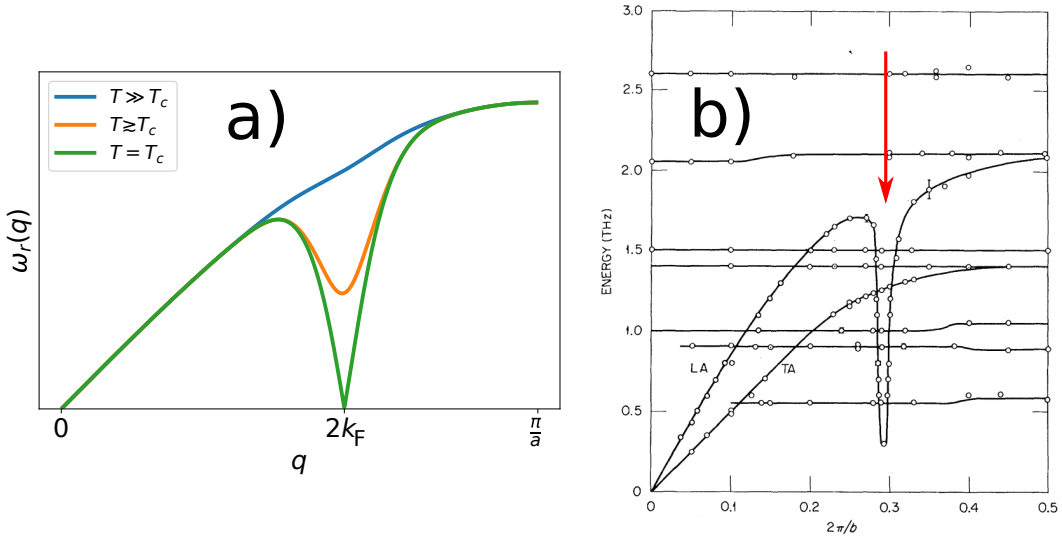

Figure 1.4: a) Schematic phonon softening (Kohn anomaly) in a 1D crystal induced by electron-phonon coupling. b) Phonon spectrum in TTF-TCNQ obtained by inelastic neutron scattering [22]. The Kohn anomaly at the corresponding CDW wavevector is indicated by the red arrow.

wavevector q, $\omega(q)$ is the phonon frequency, M the ionic mass and finally $g(q)$ the momentum dependent electron-phonon coupling constant.

One can use the commutation relation $[Q_{q1}, P_{q2}] = \delta_{q1,q2}$ and adopt the Heisenberg picture from which it follows that $\hbar^2 \frac{d^2 Q_q}{dt^2} = -[[Q_q, H], H]$ to find (after tedious calculations)

$$\frac{d^2 Q_q}{dt^2} = -\omega^2(q) Q_q - g(q)\sqrt{\frac{2\omega(q)}{\hbar M}}\rho_q \tag{1.5}$$

where $\rho_q = \sum_k c^\dagger_{k+q} c_k$ is the electron density at a wavevector q. Furthermore, I assumed $g(-q) = g(q)$ and $\omega(-q) = \omega(q)$. A phonon of wavelength $2\pi/q$ induces a potential $g(q)\sqrt{\frac{2M\omega(q)}{\hbar}}Q_q$ on the electrons. As explained in the previous section, the two are related via the susceptibility, $\rho(q) = \chi(q)g(q)\sqrt{\frac{2M\omega(q)}{\hbar}} < Q_q >$. Therefore, when averaging the operators of Eq1.5, one finds the expression of the renormalized phonon frequency

$$\boxed{\omega_r^2(q,T) = \omega^2(q) + \chi(q,T)\frac{2g(q)^2}{\hbar}\omega(q)} \tag{1.6}$$

where the temperature dependence is explicitly written.

Since $\chi(q)$ is negative (figure 1.3), the renormalized phonon frequency $\omega_r(q,T)$ is smaller than the bare one $\omega(q)$. Moreover, due to the strong divergence of the susceptibility at the CDW wavevector $2k_F$, $\omega_r(2k_F,T)$ can drop to 0 at a finite temperature T_c. Using Eq1.2

$$\omega_r^2(2k_F,T_c) = 0 \Longrightarrow k_b T_c = 2.27t \exp\left(-\frac{\hbar\omega(2k_F)}{2g^2(2k_F)n(\epsilon_F)}\right) \tag{1.7}$$

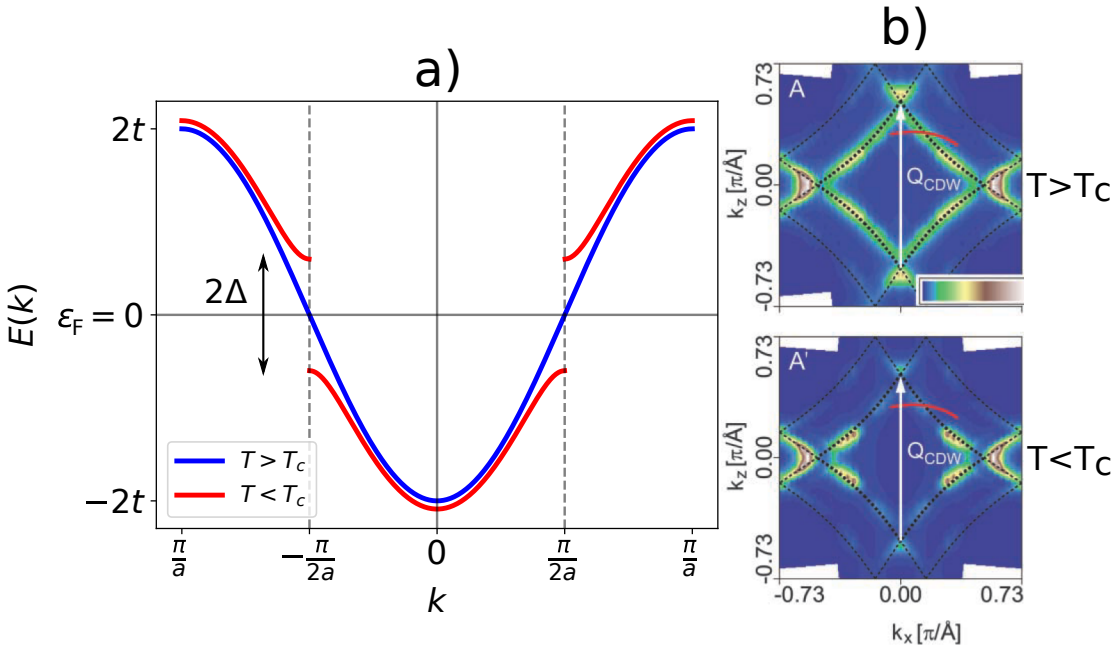

Figure 1.5: a) Energy band above and below the CDW transition temperature T_c. In the CDW state, a gap opens at the Fermi level ϵ_F. b) ARPES measurement of the Fermi surface in $TbTe_3$ above and below T_c[23]. A loss of spectral weight is seen at $T < T_c$ induced by the gap opening on several part of the Fermi surface, specifically the ones concerned by the nesting.

This phonon softening, also called Kohn anomaly, is displayed in figure 1.4 at an arbitrary electronic filling (not half filling) along with an experimental evidence from inelastic neutron scattering [22] in the quasi-1D organic compound TTF-TCNQ.

When $\omega_r(2k_F) = 0$ at $T = T_c$, a static periodic distortion appears in the ionic lattice (lower window of figure 1.1) with a wavelength $2\pi/2k_F$. This periodic lattice distortion is the so-called CDW state.

1.5 Gap in the electronic spectrum

The periodic lattice distortion has a direct influence on the electrons due to the electron-phonon coupling part of the Hamiltonian. For $T \leq T_c$, $\langle Q_{2k_F} \rangle = \langle Q_{-2k_F} \rangle \neq 0$ and one can write an effective Hamiltonian for the electrons (not taking into account the phonon part H_{phonon})

$$H_{eff} = \sum_k \begin{pmatrix} c_k^\dagger & c_{k+2k_F}^\dagger \end{pmatrix} \begin{pmatrix} \epsilon_k & \Delta^* \\ \Delta & -\epsilon_k \end{pmatrix} \begin{pmatrix} c_k \\ c_{k+2k_F} \end{pmatrix} \tag{1.8}$$

where $\Delta = g(2k_F)\sqrt{\frac{2M\omega(2k_F)}{\hbar}}\langle Q_{2k_F} \rangle$ (compare with Eq1.4). The electronic spectrum in the CDW state is given by the eigenvalues of the central matrix of Eq1.8

$$\boxed{E(k) = \pm\sqrt{\epsilon(k)^2 + |\Delta|^2}} \tag{1.9}$$

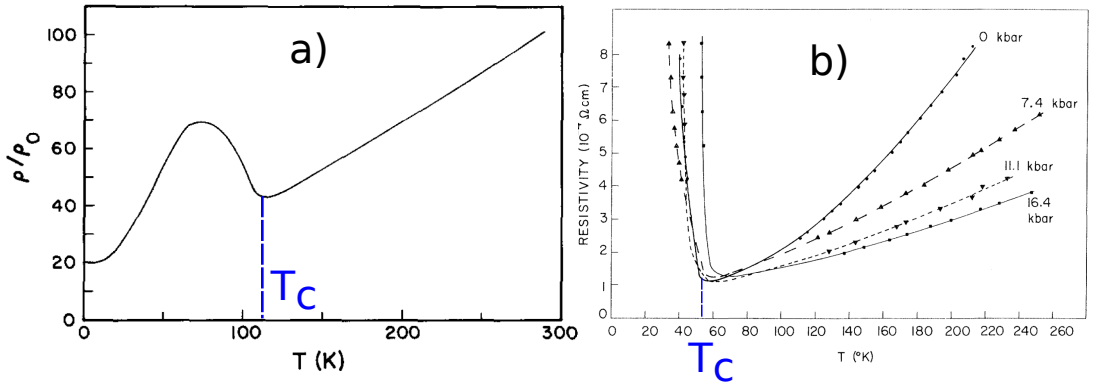

Figure 1.6: Increase of the electrical resistivity at the CDW transition in a) $TIMo_6O_{17}$ ($T_c = 113K$) and b) TTF-TCNQ ($T_c = 54K$ at ambient pressure) from [24, 25].

The electronic band dispersion above and below T_c is depicted in figure 1.5 a). The spectrum is cut in 2 bands with different electron filling at T=0K, an empty conduction band ($E(k) > 0$) and a fully filled valence band ($E(k) < 0$), separated by a gap 2Δ, with no electrons present at the Fermi level anymore. This feature is observed experimentally with ARPES (Angle-resolved photoemission spectroscopy) as in figure 1.5 b) where the Fermi surface of $TbTe_3$ is shown above and below T_c [23]. Several parts of the Fermi surface (specifically the ones concerned by the nesting) display a loss of spectral weight below T_c due to the gap opening. At the transition, the system thus becomes insulator in a 1D band model. However, in real systems, other bands can stay metallic and only a slight increase of resistivity is observed experimentally.

Since the electronic conductivity is directly related to the number of electrons near ϵ_F, it decreases for $T < T_c$ as shown in figure 1.6 a) for $TIMo_6O_{17}$ [24] and for TTF-TCNQ in b) [25].

From figure 1.6 a), the resistivity evolves continuously for $T < T_c$ meaning that the electronic gap 2Δ (see figure 1.5) increases continuously as expected for a second order phase transition. This evolution is described in the next section.

1.6 Gap evolution below T_c

The mean-field description of the CDW is very similar to the BCS theory of superconductivity. This is expected since, assuming the phonons to be a static potential acting on the electrons, a CDW is an electron-hole pair condensation in the same way as BCS describe a condensate of electron-electron pairs. Hence, it's not a surprise that the gap temperature dependence $\Delta(T)$ has the same behavior in both theory.

The renormalized phonon frequency at the CDW wavevector $\omega_r(2k_F)$ is given by Eq1.6 and the electronic susceptibility $\chi(2k_F)$ is calculated from the electronic energy band as in Eq1.1. Since ω_r is a real number, we must enforce $\omega_r(2k_F, T < T_c) = 0 \implies \omega^2(q) + \chi(q, T < T_c)\frac{2g(q)^2}{\hbar}\omega(q) = 0$ where I used Eq1.6. But now, one has to use the new electronic energy dispersion Eq1.9 instead of $\epsilon(k)$ in the susceptibility calculation Eq1.1. Since the relation $E(k + 2k_F) = -E(k)$ is still

valid, one can show, using the same steps as in the calculation of Eq1.2, that the gap equation is

$$2n(\epsilon_F)\int_0^{2t}\frac{\tanh\left(\frac{\sqrt{\epsilon^2+\Delta(T)^2}}{k_bT}\right)}{\sqrt{\epsilon^2+\Delta(T)^2}}d\epsilon=\frac{\hbar\omega(2k_F)}{2g(2k_F)^2} \tag{1.10}$$

The same type of equation is valid in BCS theory (see [26] p515). Figure 1.7 sketches the solution of Eq1.10.

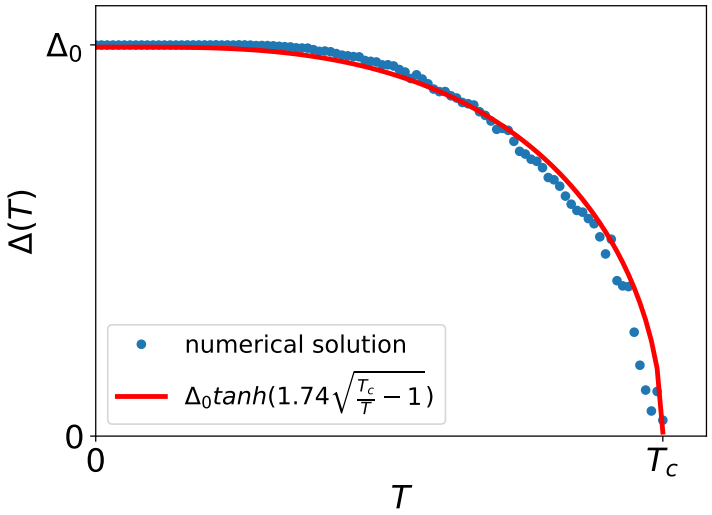

Figure 1.7: Numerical solution of Eq1.10 along with an analytic formula approximation. The full line is the BCS gap temperature dependence.

Diverse experimental probes can be used to measure the CDW transition. Few of them were discussed in this chapter (ARPES, X-ray diffraction, resistivity measurement, neutron scattering) but others should be mentioned such as specific heat measurement [28], STM [29], NMR [30], electronic spin susceptibility [31], etc... For a review of the several CDW materials see Gruner's review [27] and book [18], two collective books written by Gor'kov and Gruner [32] and Schlenker [33], Monceau's review [16] and a last one on size effects in small CDW systems by Zaitsev-Zotov [34].

1.7 Recent topics on CDW

Despite its theoretical prediction 65 years ago, the CDW phase of matter still presents some open topics nowadays both in experimental and theoretical physics. I shall present some of those themes in this section.

The theory of superconductivity in cuprates is still under debate. Recently, nuclear magnetic resonance measurements [38] and resonant X-ray diffraction under magnetic field showed a CDW phase of matter at low temperature for a certain hole doping, indicating a CDW - superconductivity competition in these strongly correlated systems [35, 39]. The charge order was observed above the superconductive

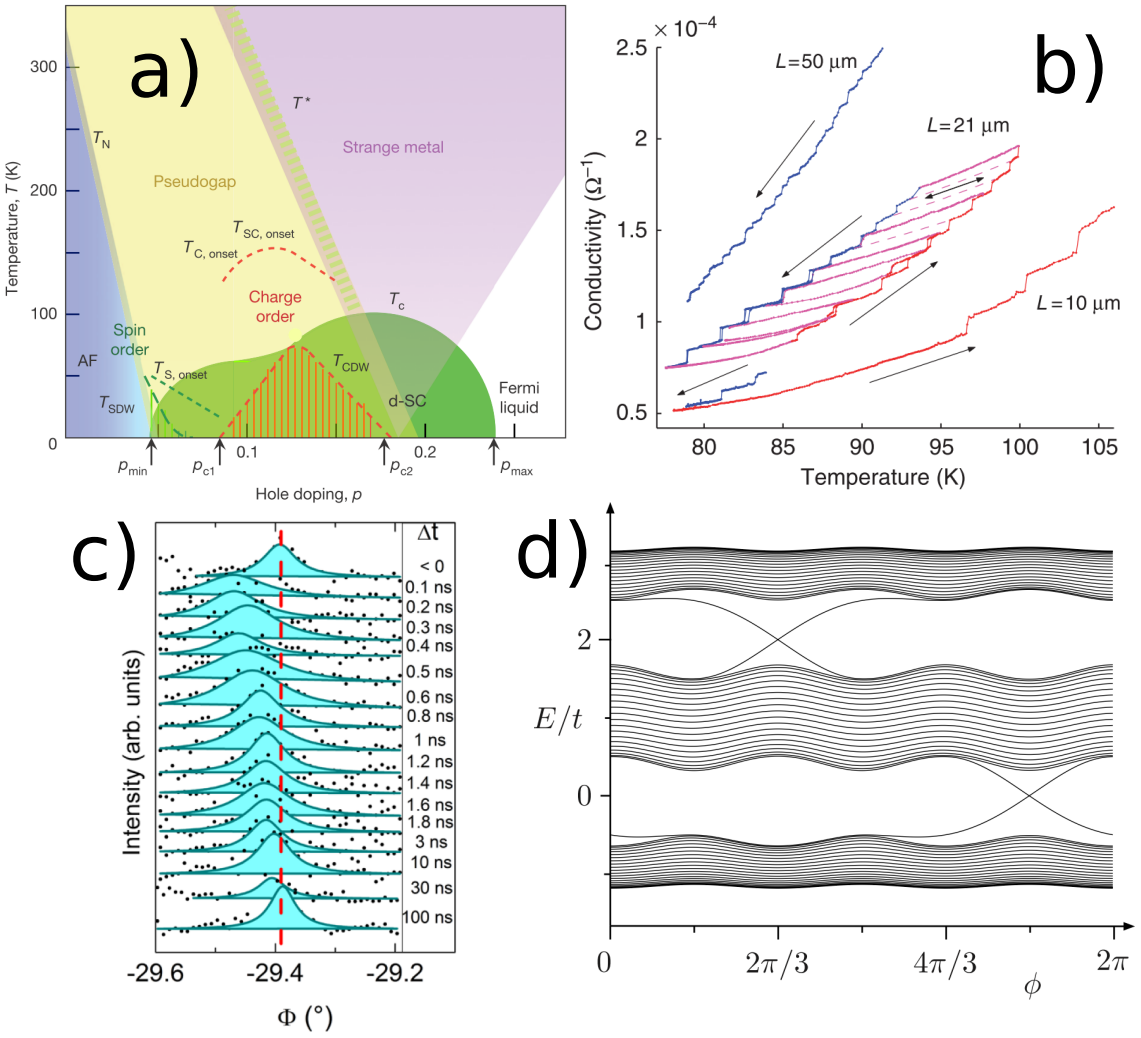

Figure 1.8: a) Cuprate phase diagram showing a CDW order at low temperature for hole doping $p_{c1} < p < p_{c2}$ [35]. b) Quantized conductivity in $K_{0.3}MoO_3$[36]. c) Time resolved CDW relaxation observed in pump probe X-ray diffraction in chromium [15]. d) Topological ingap edge states in a 1D CDW model [37].

dome in the phase diagram of figure 1.8 a). This CDW state can be also visualized in STM [40, 41]. A STM experiment on the superconductor $Bi_2Sr_2CaCu_2O_8$ subjected to a magnetic field demonstrated the presence of a CDW modulation inside the vortex [42]. Several theoretical papers propose an interpretation for the CDW - superconductivity interplay [43, 44, 45].

The question whether the CDW phase is relevant for a theory of superconductivity in high-Tc materials is an unresolved issue at the time of writing.

Macroscopic CDW samples are usually described in a classical way. However Zybtsev et al. showed a quantized conductivity in small $K_{0.3}MoO_3$ specimens having a volume of the order of the μm^3 [36] paving the way for more experiments on CDW quantum properties in small samples, see figure 1.8 b).

Regarding other properties of small CDW samples, Tanda et al. were able to synthesize ring shaped samples of $NbSe_3$ and TaS_3. His team published a large number of papers on the study of these topogical samples and on the observation of the

Aharonov-Bohm effect in these small systems [46, 47, 48, 49, 50, 51]. On the theoretical side, Nakatsugawa et al. proposed that a ring made of an incommensurate CDW material can act as a time crystal [52] which is a new type of order proposed in 2015 by Wilczek (Nobel laureate in 2004) and Shapere [53, 54]

Several experiments have shown interesting results on the CDW transient dynamics. These time-resolved pump-probe experiments consist in sending a 1^{st} optical laser pulse (the pump) on a sample in order to put it in a non-equilibrium state and probing the system with a 2^{nd} pulse (the probe). Schimtt et al. observed the melting of the CDW in $TbTe_3$ in ARPES [23], Laulhe et al. observe the CDW formation in 1T-TaS_2 at nanometer scales using time resolved X-ray diffraction[55], using the same technique Huber et al. studied the dynamics of the standard CDW material $K_{0.3}MoO_3$ [56], Jacques et al. used diffraction on chromium in a laser pump - X-ray probe setup and study the CDW depinning induced by the pump [15] (figure 1.8 c). Using pump probe electron diffraction on $LaTe_3$, Zong et al. observed the appearance of a transient CDW in a direction perpendicular to the one at equilibrium [57], explaining this effect using topological defects [58]. In the commensurate CDW material 1T-TaS_2, Zong et al. were able to create domain wall separating different CDW configurations with a laser pulse [59]. In this same material, a fast electronic resistance switching behavior was measured by Vaskivskyi et al. [60] interpreted as a hidden charge density wave states. Using a laser pulse and an STM setup, Gerasimenko et al. studied a light-induced CDW state in 1T-TaS_2 [61]. Demsar et al. [62] used pump-probe optical reflectivity on $K_{0.3}MoO_3$ to see the CDW amplitude mode which is discussed in append A. The number of scientific publication about time resolved experiment on CDW systems increases regularly over time, the list presented here is not an exhaustive one.

As for a last example, a CDW can display a topological behavior. For example, one can describe the electrons in the CDW phase by a SSH (Su-Schrieffer–Heeger) Hamiltonian well known to display topological edge states. As for examples, Flicker and Wezel studied the topology of an incommensurate CDW [63] and Lizunova et al investigated the quantized charge transport in relation to the topological edge states [37] (figure 1.8 d)).

Before ending this introductory chapter, we need to mention several other theories of CDW transition.

Firstly, in our case, the sample is metallic in the high temperature phase. Another approach, relevant for 1T-$TiSe_2$, describes a CDW transition starting from a semiconducting phase with an indirect band gap [64, 65] where an exciton gas enhances the CDW instability.

Secondly, in this chapter, I assumed the CDW wavevector to be the one for which the susceptibility is higher ($2k_F$). But looking at Eq1.6, the renormalized phonon frequency is also related to the electron-phonon coupling $g(q)$. If for a certain wavevector q_0 we have $g(q_0) \gg g(2k_F)$, $\omega_r(q_0)$ could drop to zero before $\omega_r(2k_F)$, hence the CDW would have a wavelength $2\pi/q_0$ instead of $2\pi/2k_F$. This feature could be significant in 2H-$NbSe_2$ for example [66].

Finally, the mean-field description fails to relate the gap value at $T = 0$ to the transition temperature T_c experimentally. In the weak coupling theory considered in this chapter, one should have the relation $2\Delta(T = 0) = Ck_bT_c$ where $C =$

3.52. However, in most CDW materials, C is higher than expected ($C = 5$ in $K_{0.3}MoO_3$), see [18] p59. Aubry and Quemerais proposed a very different strong coupling description of the CDW transition which could fix this discrepancy ([67] and [33] p295-405). On the other hand Varma and Simons proposed adding higher order terms in the susceptibility calculation [68]. These strong coupling theories are out of the scope of this manuscript.

1.8 CDW systems with different dimensionalities

1.8.1 $NbSe_3$, a quasi-1D system

$NbSe_3$ is a material with a ribbon-like shape made of 3 types of quasi-1D chains along the b axis (see figure 1.9). It's a monoclinic crystal with lattice parameters at room temperature a = 10.006$\mathring{A}$, b = 3.478$\mathring{A}$, c = 15.626$\mathring{A}$, an angle between the a and c axis of $\beta = 109.3°$ and a space group P_{2_1}/m. The typical size of a sample is few millimeters long, a width along c of tens of μm and a thickness of few μm. As an example, the one used in the experiment described in chapter 4 is of 2.25mm×39μm×3μm. Ong and Brill measured a large conductivity anisotropy $\sigma_b/\sigma_c \approx 18$ at 200 K [69] which can be linked to the low dimensionality (quasi-1D) of the microscopic structure i.e. near dispersionless phonon branches propagating perpendicularly to the b axis.

Two CDW transitions occur in this material at low temperature. The first at T_{c1} = 144 K with a CDW distortion along the b axis given by the wavevector q_1 = (0, 0.241b*, 0) and the second one at T_{c2} = 59 K of wavevector q_2= (0.5, 0.260b*,0.5). Those CDWs open 2 gaps and one observed in ARPES [70] is shown in figure 1.10. Those transitions were first observed in a resistivity measurement as a function of temperature by Chaussy et al. [71] displayed in (c). See Monceau review for further details [16].

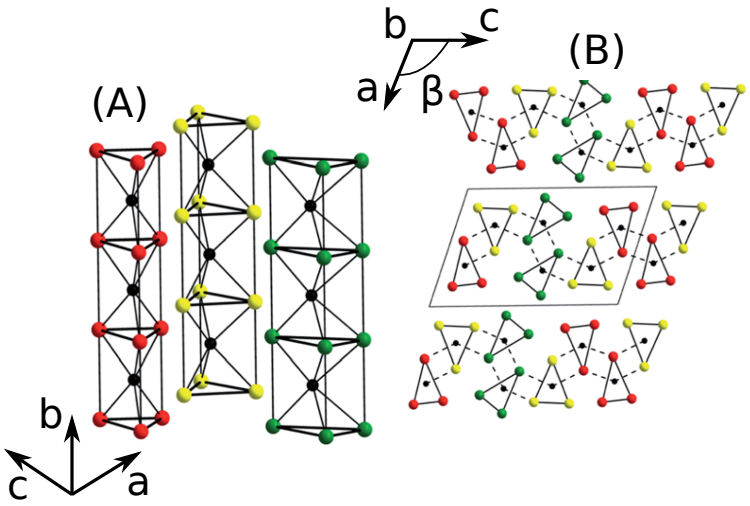

Figure 1.9: (A) $NbSe_3$ crystal structure composed of 3 types of quasi-1D chains along the b axis direction and weakly coupled between each other. (B) view from above showing the chains arrangement in the (a,c) plane. Figure adapted from [72].

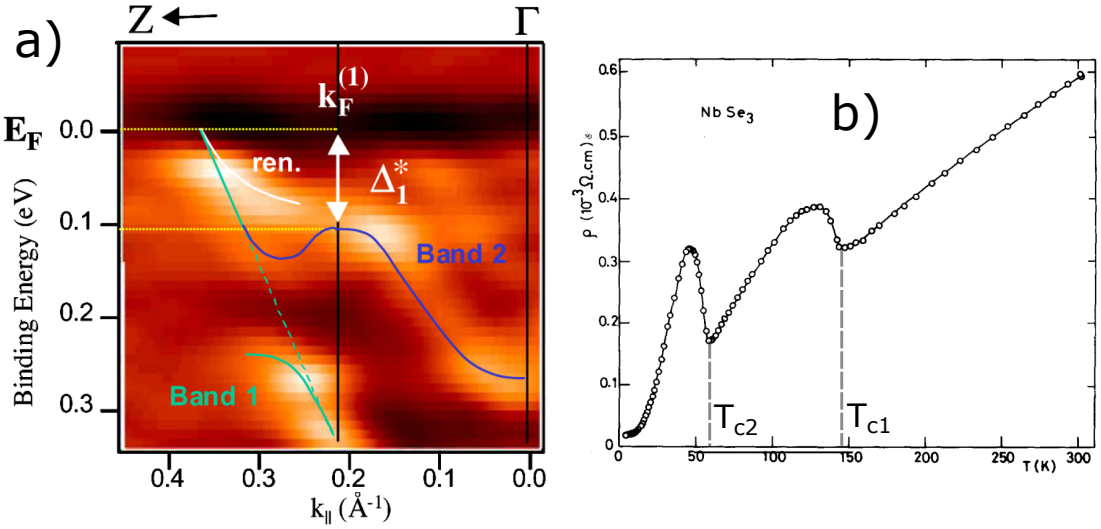

Figure 1.10: a) Gap in the spectral function of $NbSe_3$ measured in ARPES at $T = 15$ K from [70]. b) Resistivity as function of temperature showing the two transitions at T_{c1} and T_{c2} (from [71]).

1.8.2 $TbTe_3$, a quasi-2D system

Contrary to $NbSe_3$, the structure of $TbTe_3$ presents a quasi-2D character (see figure 1.11). This crystal is orthorhombic with space group Cmcm [73, 74] and lattice parameters a=4.3081$\mathring{A}$, b = 25.47$\mathring{A}$, c = 4.3136$\mathring{A}$ at room temperature [13]. Its unit cell is composed of several almost square Tellurium arrays separated by TbTe planes. A single Te plane is displayed in figure 1.11 (b) along with the directions a and c and the p-type orbitals. The electron hopping parameters t_{perp} and t_{para} from which a 2 bands tight-binding model can be used to describe the CDW transition [75, 76, 77] are also shown.

This material is almost isotropic in the (a,c) plane [78] with a macroscopic "wafer-like" structure. But, the slight difference between a and c (inducing a small breaking of the symmetry in the Te planes) could be the reason for the appearance of a CDW transition at T_c = 336K along the c axis. At room temperature, the CDW wavevector is q = $0.2860 \times \frac{2\pi}{c}$.

More generally, $TbTe_3$ belongs to the Rare-Earth Tritellurides family denoted RTe_3 with R = Tm,Er,Ho,etc. All compounds of this family display a CDW along c with a T_c depending on the rare-earth element R (see figure 1.12). However, for the materials with smaller lattice parameters, a second CDW transition occurs at lower temperature, along the a axis, i.e. in the perpendicular direction of the first CDW. From the physical properties point of view, the Rare-Earth element typical size is inversely proportional to its weight. The heavier is the Rare-earth, the smaller is the lattice parameter. Another way to present figure 1.12 is to say that the second CDW occurs in members of the family with the smallest size (heaviest elements).

One could ask which physical parameter is important to explain the evolution of the transition temperature T_c as a function of the rare-earth element (figure 1.12), whether this is due to an increase in the number of electrons or to the change of lattice parameter from chemical pressure. Since the CDW occurs in the Tellurium

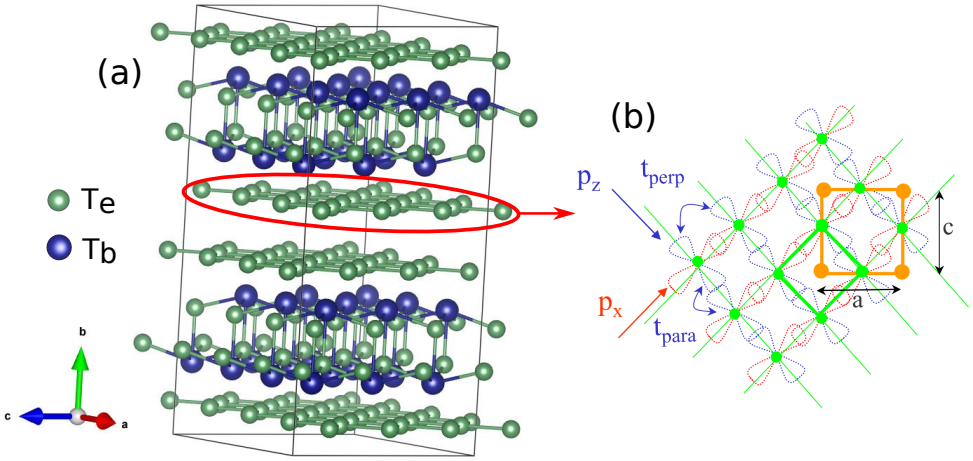

Figure 1.11: (a) 3×1×3 cell of $TbTe_3$ showing the Te rectangular nets separated by planes of TbTe. (b) View from above of one of the Te array showing the p_x and p_y orbitals along with the a and c directions. t_{perp} and t_{para} are the electron hopping parameters (figure (b) from [75])

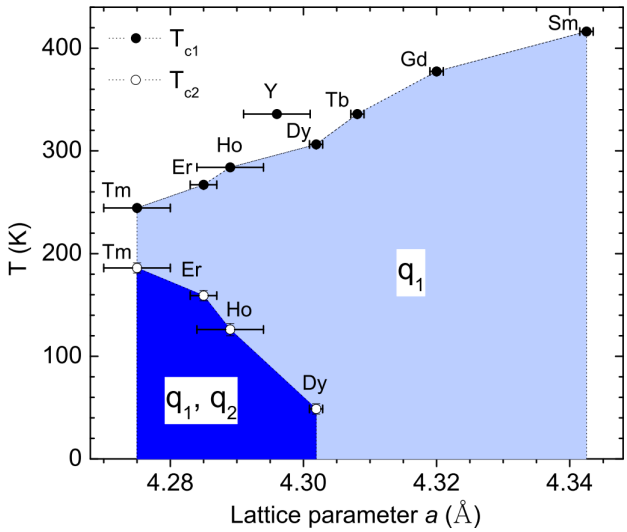

Figure 1.12: CDW transition temperature for several rare-earth elements R of the RTe_3 family. q_1 appear along the c axis while q_2 is along a and only exist for some the heaviest rare-earth elements (from [13]).

plane, and one can use the p_x and p_z Te orbitals to describes the CDW transition [13, 75], changing the number of electrons on the rare-earth element shouldn't change the value of T_c. On the other hand, chemical pressure changes the lattice parameters of the Te plane (figure 1.12) which can induce the variation of T_c.

If this is the case, one should observe the same evolution by putting pressure on the sample. Hamlin et al. measured a decrease of T_c when applying pressure [79], hence T_c decreases when the lattice parameter decreases, which is the same evolution observed in figure 1.12 by changing the Rare-earth element. As a second example, Sacchetti et al. observed a decrease of the single particle excitation energy for a decreasing lattice parameter by applying pressure[80].

See [13] for a detailed study of those compounds from X-ray diffraction experiments.

Chapter 2

X-ray diffraction of a CDW system

2.1 Old and modern X-ray diffraction

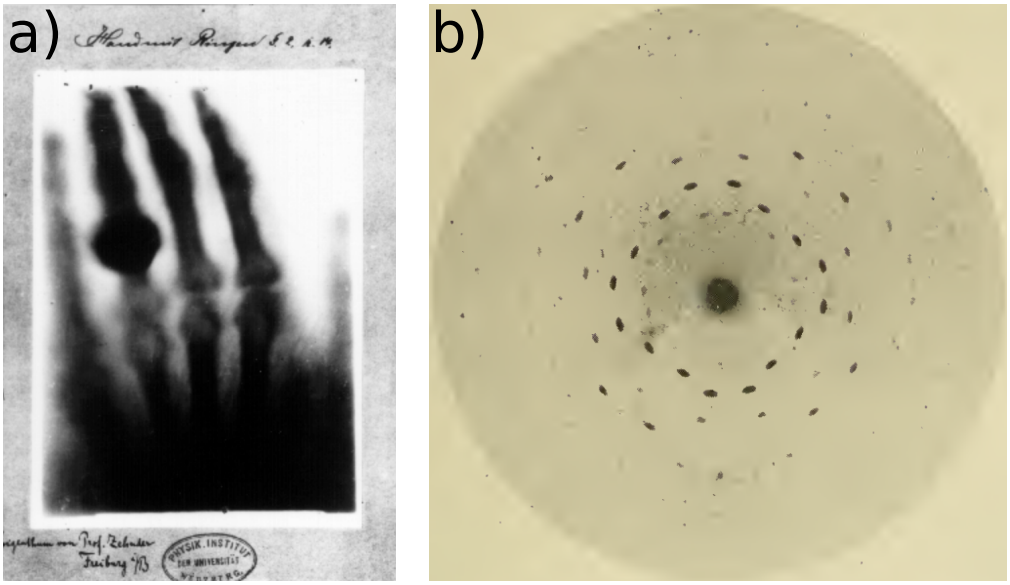

Figure 2.1: a) First medical X-ray picture of Röntgen's wife's hand taken in 1895. b) Diffraction of cubical ZnS crystal by Max von Laue and interpreted by W. L. Bragg from [81] p56-57

X-ray radiations were discovered in 1885 by Wilhelm Röntgen while working on cathode ray tubes. Röntgen labeled this new radiation 'X' as it was unknown until then. He received the 1^{st} Nobel prize in Physics in 1901 for his discovery. It was shown later that those X-rays were electromagnetic-wave (light) of high energy (between 100eV to 100kev). Since the light absorption for those short wavelength radiations is much smaller than for visible light, Röntgen could use them to take a picture of the bones inside his wife's hand (figure 2.1 a)).

Since it was now possible to have access to light radiations with a wavelength of the same order as the distance between atoms in a crystal (few $\mathring{A}$), Max Von Laue performed X-ray scattering first on a copper sulfate and later on a zinc blende crystal shown in figure 2.1 b). As will be explained in the following sections, several peaks

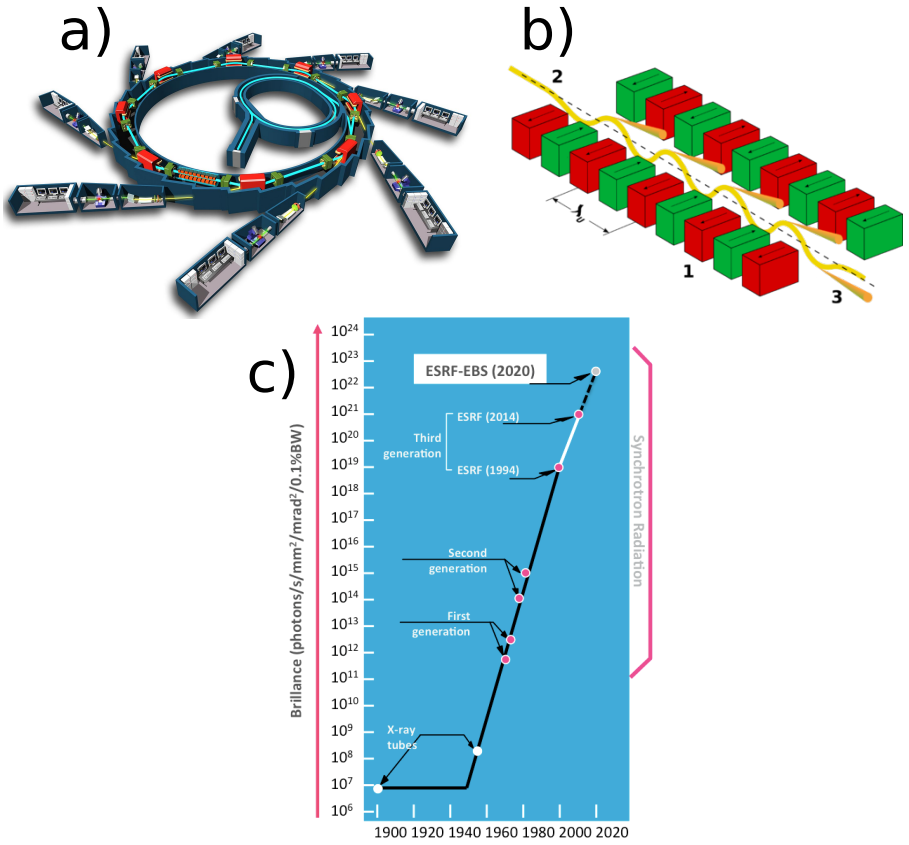

Figure 2.2: a) Schematic of the ESRF synchrotron of Grenoble. b) Schematic of an undulator, a periodic array of magnets used to emit X-ray radiations. c) Evolution of the synchrotron brilliance as function of time.

(called Bragg peaks) are visible from this picture. Later William Henry Bragg and William Lawrence Bragg gave a theoretical interpretation of the diffraction pattern [81].

Nowadays, X-ray diffraction is commonly realized by X-ray tube in a large number of laboratories over the world to perform crystallography. We used a rotating copper cathode at the Laboratoire de Physique des Solides of Orsay for preliminary X-ray diffraction studies on samples used later on in large facilities. X-ray can also be produced in large facilities like synchrotrons, an evolution of the cyclotron invented in 1929-1930. As shown in figure 2.2 a), it is made of 4 different parts. First a bunch of electrons are emitted in a linear accelerator (LINAC) and accelerated. The electrons then enter a booster synchrotron, a ring with a circumference of 300m in the case of the ESRF of Grenoble. They are accelerated up to an energy of 6GeV (ESRF) and finally sent into the storage ring, with a circumference of 844m (ESRF). In this storage ring, the electrons pass through undulators (see figure 2.2 b)) which is a periodic array of magnets in which electrons are decelerated and emit X-ray radiations with a wavelength of the order of 0.1nm, for example ID01 beamline can provide X-ray between 6 and 24keV. Finally, this X-ray beam is used in the several experimental station (beamlines) placed all around the storage ring as shown in figure 2.2 a). In this thesis, we used the ESRF before 2020, hence a third generation synchrotron (see figure 2.2 c)). This synchrotron will have an

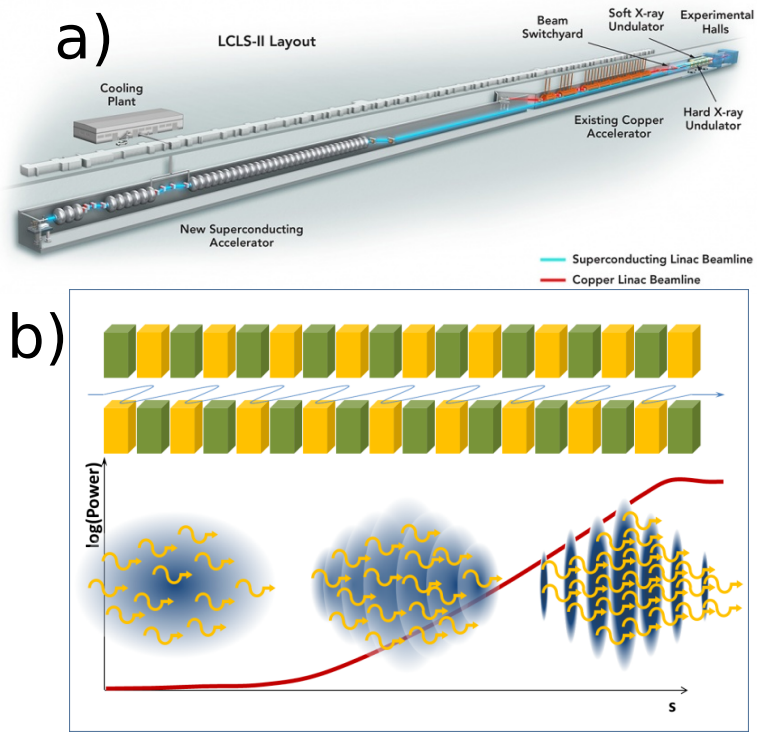

Figure 2.3: a) Schematic of the LCLS free electron laser at Stanford. b) Illustration of the self-amplified spontaneous emission (SASE) effect in which the electrons close to the speed of light moving inside the undulator interact with their own emitted radiation and form bunches of electrons emitting short and coherent X-ray pulses.

upgrade in 2020 and is expected to produce a X-ray source of even higher brilliance. The several synchrotrons over the world provides X-ray that can be used for a large range of experimental techniques including diffraction but also X-ray photo emission spectroscopy, X-ray powder diffraction (XRD), X-ray absorption spectroscopy (XAS), resonant inelastic X-ray scattering (RIXS), X-ray magnetic circular dichroism (XMCD), etc...

Recently, several free-electron lasers (FEL) were constructed around the world, SACLA in Japan, European XFEL in Hamburg and LCLS in Standford (the one we used during this PhD). The principle is slightly different from a synchrotron as seen in figure 2.3 a). Instead of a circular storage ring, a FEL consists in a long tube under vacuum (3.2km for LCLS) in which electrons are accelerated in a linear motion. At the end of the accelerator, an undulator acts on the electrons to generate X-ray in a broad energy range from 280eV to 11.2kev. Furthermore LCLS use the self-amplified spontaneous emission (SASE) effect to further increase the source brilliance. At the undulator, the electrons are decelerated by the magnets array (figure 2.3 b)). But since these electrons travel close to the speed of light, they interact with their own emitted electric field. The electron bunch density becomes periodically modulated and emits short X-ray pulses with a pulse duration of 40 to 300fs and a repetition rate of 120Hz. Furthermore, these electron bunches are coherent X-ray sources and the emitted X-rays naturally have a large transverse coherent length [134].

In the next sections, I will first present X-ray scattering (diffraction) by 2 point

charges for pedagogical purposes before showing diffraction by an atom and a perfect crystal. I will then introduce the Ewald sphere construction and end with the diffraction pattern of a CDW.

2.2 X-ray diffraction by 2 point charges

A charged particle in an electromagnetic field can vibrate and re-emit a radiation in a different direction. Since the X-ray wavelength used in this thesis ($\sim 10^{-10}m$) is much larger than the electron Compton wavelength ($\sim 10^{-12}m$), we can consider elastic Thomson scattering in which the scattered beam has the same wavelength as the incident one as the dominant contribution (see figure 2.4).

Futhermore, since the Thomson cross-section (related to the ratio of scattered to incident number of photons) is proportional to the inverse square mass of the particle $\sigma_T \propto 1/m^2$, the electron cross section is more than a million times larger than the one of the proton. Hence, diffraction from the nuclei is neglected and only diffraction from the electron clouds are considered.

Before turning toward crystal diffraction, let's mention a pedagogical example of scattering by two point charges as displayed in figure 2.4. Since, in the following, we will only consider the scattered beam, we will express the scattered amplitude in units of the Thomson scattering length ([82] p8 and p115) and consider the amplitude of the incident beam to be equal to one.

As in figure 2.4, we will consider an incident X-ray monochromatic beam of wavevector $\vec{k}$ (plane wave). This radiation is then scattered into a plane wave by the 2 point charges 1 and 2 separated by a vector $\vec{r}$. This scattered beam is a plane wave with a direction, different from the incident one, represented by the wavevector $\vec{k'}$. Since Thomson scattering is an elastic process, $|\vec{k}| = |\vec{k'}| = 2\pi/\lambda$, where λ is the X-ray wavelength.

For notational convenience we will define $\vec{Q} \equiv \vec{k'} - \vec{k}$. The scattered amplitude is the sum of scattering from charge 1 (considered at the origin) and charge 2. Since scattering by 2 is delayed by a phase difference $\phi_{int} = \vec{k}.\vec{r}$ compared to 1 and ahead by $\phi_{out} = -\vec{k'}.\vec{r}$, the total phase difference is $\phi = (\vec{k} - \vec{k'}).\vec{r} = -\vec{Q}.\vec{r}$. Therefore, far from the charges, the total scattered amplitude is

$$A(\vec{Q}) = 1 + e^{-i\vec{Q}.\vec{r}} \tag{2.1}$$

A generalization for more than 2 point charges would be $A(\vec{Q}) = \sum_{n=1}^{N_{charge}} e^{-i\vec{Q}.\vec{r}_n}$ where N_{charge} is the number of point charges and $\vec{r}_n$ the position of the n^{th} charge.

Generalizing this discrete sum to a continuous charge density $\rho(\vec{r})$, the scattered amplitude is directly the Fourier transform of $\rho(\vec{r})$. Since the CDW is a periodic charge density with wavevector q_{cdw}, one can expect sharp contribution in the diffraction pattern at $Q = q_{cdw}$ as is described in the last section of this chapter.

$$\boxed{A(\vec{Q}) = \int \rho(\vec{r}) e^{-i\vec{Q}.\vec{r}}\, d^3\vec{r}} \tag{2.2}$$

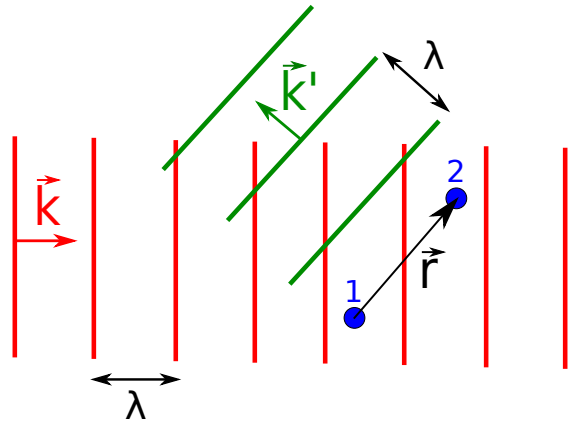

Figure 2.4: X-ray light scattering by 2 point charges (in blue). $\vec{k}$ and $\vec{k}'$ are respectively the wavevectors of the incident (red) and scattered (green) beam. $\lambda = 2\pi/|\vec{k}| = 2\pi/\vec{k}'$ is the X-ray wavelength. Figure adapted from [82]

Since the Fourier transform is best suited to study periodic system and the CDW is a periodic displacement of atoms, we will observe sharp peaks in the diffraction pattern of a CDW material as shown in the last section of this chapter.

2.3 Atomic form factor and crystal diffraction

2.3.1 Atomic form factor

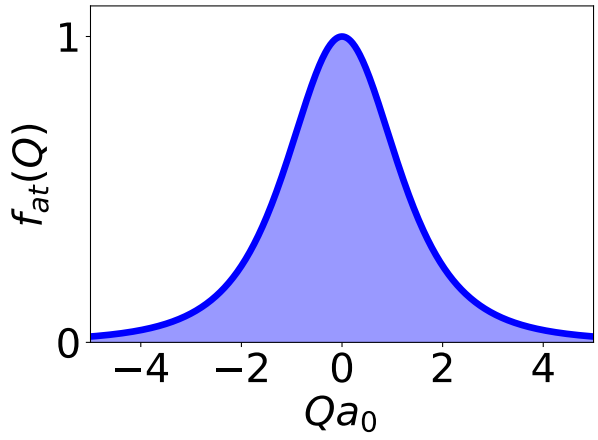

Figure 2.5: Atomic form factor for the hydrogen 1s state. f_{at} decreases on a typical distance $Q \sim \frac{1}{a_0}$ where a_0 is the Bohr radius.

Before going to the perfect crystal diffraction pattern, we will need the atomic form factor describing X-ray scattering by an atom. As an example, we will use the simplest atomic state $1s$ of an hydrogen atom ([83] p813)

$$\psi_{1s}(\vec{r}) = \frac{1}{\sqrt{\pi a_0^3}} e^{-r/a_0}$$

where $a_0 \approx 0.53\,\mathring{A}$ is the Bohr radius and can be classically interpreted as the radius of an atom in the $1s$ quantum state. The electronic density being the square modulus of the wavefunction, the scattered amplitude is

$$\begin{aligned} f_{at}(\vec{Q}) &= \int |\psi_{1s}(\vec{r})|^2 e^{-i\vec{Q}.\vec{r}} d^3\vec{r} \\ &= \frac{1}{[1+(Qa_0/2)^2]^2} \end{aligned} \tag{2.3}$$

where $Q = |\vec{Q}|$. This squared Lorentzian function is displayed in figure 2.5 a) (green curve). It drops on typical distance $Qa_0 \sim 1 \Longrightarrow Q \sim \frac{1}{a_0}$ which can be quantitatively expected from the Heisenberg inequality $\Delta x \Delta Q \geq \frac{1}{2}$. Therefore, for heavier atoms, $f_{at}(\vec{Q})$ will drop faster for high values of Q on a length scale $Q \sim \frac{1}{\text{atomic radius}}$. This form factor constrains the diffraction pattern of a crystal, limiting the Q range of significant signal to low and medium values.

2.3.2 Diffraction of a perfect crystal

As said earlier, the diffraction diagram for any charge distribution is given by Eq2.2. But, for a crystalline sample, several simplifications arise from the properties of a crystal which are :

- A crystal is a periodic arrangement of a finite number of unit cells
- A unit cell is composed of one or several atoms at given positions regarding the center of the cell.

For pedagogical purposes, we consider here a 1D crystal with lattice parameter a. Taking into account the 2 elements mentioned above, the electron density of the crystal is

$$\begin{aligned} \rho(x) &= \sum_{n=1}^{N_{cell}} \rho_{cell}(x - na) \\ &= \sum_{n=1}^{N_{cell}} \sum_{i=1}^{N_{at}} \rho_{at_i}(x - na - x_i) \end{aligned}$$

where N_{cell} is the number of unit cells, N_{at} the number of atoms in a unit cell, $\rho_{at\,i}$ the electronic density of atom i and x_i its position regarding the unit cell center.

Inserting this expression in Eq2.2 and with a change of variable in the integral $u = x - na - x_i$ one finds

$$A(Q) = \underbrace{\sum_{n=1}^{N_{cell}} e^{-iQna}}_{\text{crystal form factor}} \underbrace{\sum_{i=1}^{N_{at}} e^{-iQx_i} \underbrace{\int \rho_{at\,i}(u) e^{-iQu}\, du}_{\text{atomic form factor}}}_{\text{unit cell structure factor}} \equiv S(Q)F(Q) \tag{2.4}$$

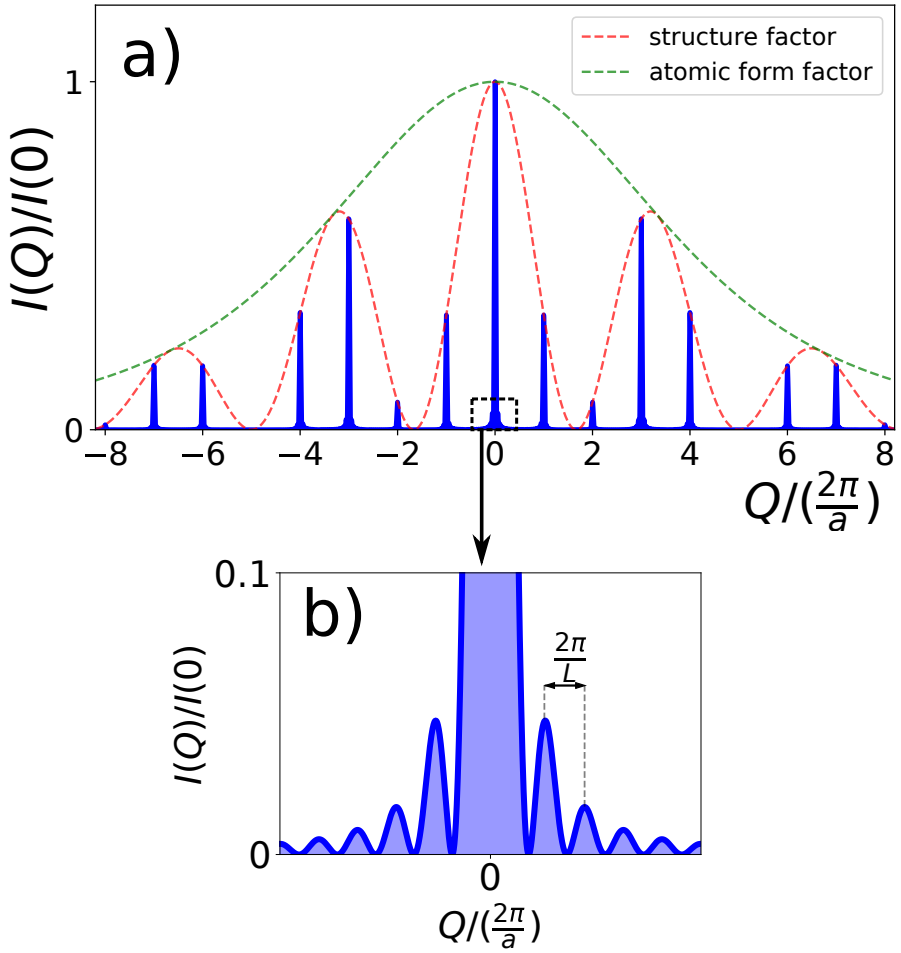

Figure 2.6: a) Diffraction pattern $I(Q) = |A(Q)|^2$ of a 1D crystal with lattice parameter a and a unit cell consisting of 2 identical atoms. The atomic form factor $f_{at}(Q)$ and structure factor $F(Q)$ are shown in green and red respectively. b) Zoom near one of the peaks showing oscillations coming from the crystal form factor $S(Q)$.

Where I defined $S(Q)$ the crystal form factor and $F(Q)$ the structure factor. In 3D, this expression becomes

$$A(\vec{Q}) = \sum_{n_1=1}^{N_{cell1}} \sum_{n_2=1}^{N_{cell2}} \sum_{n_3=1}^{N_{cell3}} e^{-i\vec{Q}.\vec{R}_n} \sum_{i=1}^{N_{at}} e^{-i\vec{Q}.\vec{r}_i} \underbrace{\int \rho_{at\,i}(\vec{r}) e^{-i\vec{Q}.\vec{r}}\, d^3\vec{r}}_{f_{at\,i}(\vec{Q})} \tag{2.5}$$

where $\vec{R}_n = n_1\vec{a}_1 + n_2\vec{a}_2 + n_3\vec{a}_3$ in which $\{\vec{a}_1, \vec{a}_2, \vec{a}_3\}$ are the crystal lattice vectors.

The diffracted intensity $I(Q) = |A(Q)|^2$ for a 1D crystal with a unit cell of 2 identical atoms is shown in figure 2.6. It consist in several Bragg peaks (as in figure 2.1 b)) with an intensity modulated by the structure form factor, itself modulated by the atomic form factor.

By zooming on one of the Bragg peaks as in figure 2.6 b), short-range oscillations are visible, and are coming from the crystal form factor $S(Q)$. Since these have a periodicity $2\pi/L$ where L is the crystal lattice length, those oscillations will only be visible for small sample, up to few micrometers, depending on the experimental

resolution [84]. Again the different length scales for the variations of $I(Q)$ can be quantitatively linked to the different typical sizes of the crystal via Heisenberg inequality, atom radius < unit cell size < crystal length $\Longleftrightarrow$ $f_{at}(Q)$ varies on a typical scale in Q space larger than $F(Q)$ which itself varies on a typical scale larger than $S(Q)$.

2.4 Ewald sphere construction

As we will see in the following, the calculation of the exact location of the Bragg peaks is sometimes not straightforward. For this purpose, let us consider the first term of Eq2.5. Constructive interference takes place between each complex exponential term if $e^{-i\vec{G}.\vec{R_n}} = 1 \Longleftrightarrow \vec{G}.\vec{R_n} = p \times 2\pi \ \forall \ \{n_1, n_2, n_3\}$ where I called $\vec{G}$ the corresponding Bragg wavevector and $p \in \mathbb{Z}$. Constructing a lattice (in so called reciprocal space) of basis vectors $\{\vec{a}_1^*, \vec{a}_2^*, \vec{a}_3^*\}$ satisfying the following relations

$$\vec{a}_i^*.\vec{a}_j = 2\pi\delta_{i,j} \tag{2.6}$$

One can see that a vector $\vec{G}_{hkl}$ defined by

$$\vec{G}_{hkl} = h\vec{a}_1^* + k\vec{a}_2^* + l\vec{a}_3^* \text{ where } h, k, l \in \mathbb{Z} \tag{2.7}$$

will satisfy the required relation $\vec{G}.\vec{R_n} = (hn_1 + kn_2 + ln_3)2\pi = p2\pi$ where $p \in \mathbb{Z}$. Hence the condition for Bragg diffraction, also called Laue condition is

$$\boxed{\vec{Q} = \vec{G}_{hkl}} \text{ (Laue diffraction condition)} \tag{2.8}$$

An useful way to calculate the sample orientation needed to see a Bragg peak is given by the Ewald sphere, as shown in figure 2.7, for a 2D crystal to simplify our explanation.

During a diffraction experiment, the incident X-ray beam is fixed (red vector $\vec{k}$ in figure 2.7). As said earlier, X-ray diffraction is an elastic scattering process, hence the diffracted wavevector (green $\vec{k'}$ of figure 2.7) can only span a circle (a sphere for a 3D system), so called "Ewald sphere", of radius $|\vec{k}| = \frac{2\pi}{\lambda}$ where λ is the X-ray wavelength.

But in order to see a Bragg peaks, one needs to satisfy the Laue condition Eq2.8 $\vec{Q} = \vec{k'} - \vec{k} = \vec{G}$ hence $\vec{G}$ must also be on the Ewald sphere. This is done by turning the sample. Since the reciprocal lattice is related to the real space crystal's one by Eq2.6, rotating the sample will turn the reciprocal lattice as well. One needs to rotate the crystal until a Bragg $\vec{G}$ crosses the Ewald sphere as in figure 2.7.

The Ewald sphere construction is the geometrical equivalent to the wellknown Bragg's law.

2.5 CDW diffraction and formation of satellites

At low temperature, when the CDW phase takes place in the crystal, (some of) the atoms get periodically displaced from their high temperature position. Therefore, one would expect an evolution of the diffraction pattern. Indeed, any new

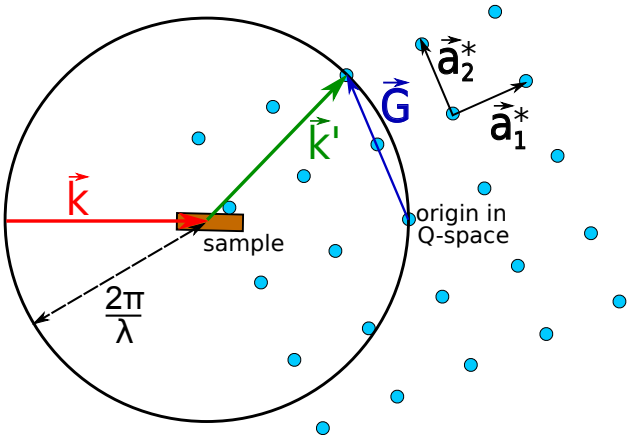

Figure 2.7: Ewald sphere for a 2D crystal. $\vec{k}$ is the fixed incident X-ray beam, $\vec{k}'$ the scattered one, $|\vec{k}| = |\vec{k}'| = 2\pi/\lambda$ where λ is the X-ray wavelength. $\{\vec{a}_1^*, \vec{a}_2^*\}$ is the reciprocal lattice basis and $\vec{G}$ a Bragg wavevector. See the main text for further details.

periodicity in the sample should induce new peaks in reciprocal space. As a simple example, let's take a 1D crystal with only 1 atom per unit cell. Its electronic density in the CDW phase becomes

$$\rho(x) = \sum_{n=1}^{N_{cell}} \rho_{at}[x - na - \Delta_x \cos(q_{cdw} na)]$$

where $\Delta_x = \sqrt{\frac{2\hbar}{NM\omega(2k_F)}} \frac{\Delta}{g(2k_F)}$ is the amplitude of the atomic displacement ([18] p38). I used the notation q_{cdw} for the CDW wavevector since, as will be explained in a following chapter, q_{cdw} can differ from $2k_F$ when applying an external electric field. Calculating the diffracted amplitude, one has

$$A(Q) = \sum_n e^{-iQ[na + \Delta_x \cos(q_{cdw} na)]} f_{at}(Q)$$

Assuming Δ_x to be small enough so that a Taylor expansion is justified, the expression becomes

$$\begin{aligned} \frac{A(Q)}{f_{at}(Q)} &\approx \sum_n e^{-iQna}[1 - iQ\Delta_x \cos(q_{cdw} na)] \\ &= \underbrace{\sum_n e^{-iQna}}_{\text{original Bragg peaks } G_h} - iQ\frac{\Delta_x}{2}\Big(\underbrace{\sum_n e^{-i(Q+q_{cdw})na}}_{\text{peaks at } G_h - q_{cdw}} + \underbrace{\sum_n e^{-i(Q-q_{cdw})na}}_{\text{peaks at } G_h + q_{cdw}}\Big) \end{aligned} \tag{2.9}$$

The formula consists of 3 different sums. The first one is similar to the perfect 1D crystal case, therefore, it is the Bragg peaks $G_h = h\frac{2\pi}{a}$, the 1D version of Eq2.7. Calculating the next terms of the expansion, one would find a modulation of their intensity, but their position stay the same at any order (see Bragg peaks in figure 2.8). The second term satisfies the Laue condition when $Q + q_{cdw} = G_h \Longrightarrow Q = G_h - q_{cdw}$, hence it is a CDW satellite peak at a distance q_{cdw} from each Bragg with

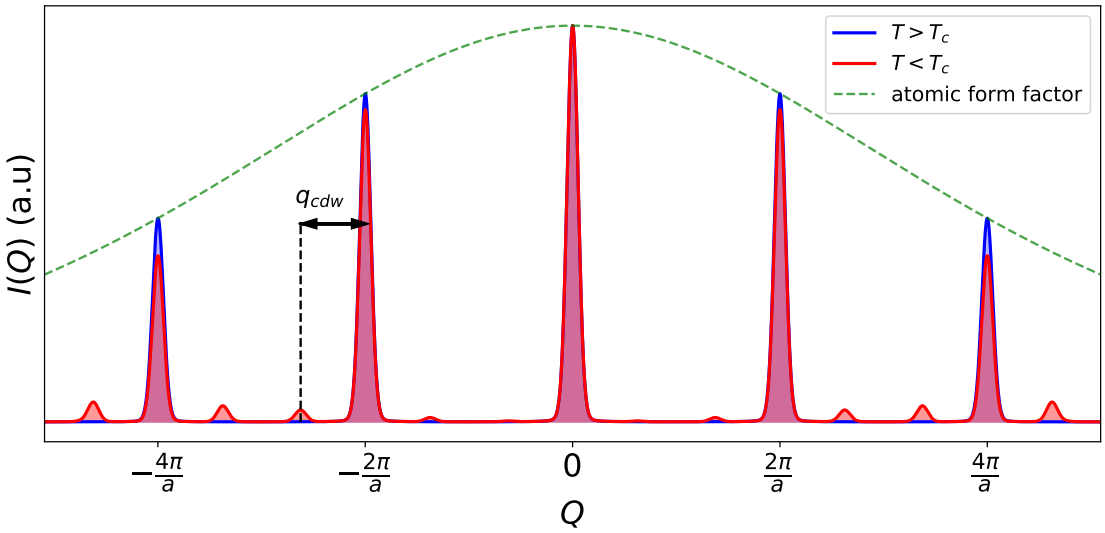

Figure 2.8: Comparison of diffracted pattern from a 1D atomic chain above (blue) and below(red) the CDW transition temperature T_c. Several peak, known as CDW satellites, appear at a distance $\pm q_{cdw}$ from the Bragg.

an intensity $\propto Q^2 \frac{\Delta_x^2}{4}$ (in diffraction, we measure the intensity $I(Q) = |A(Q)|^2$). The last term is the CDW satellite at $Q = G_h + q_{cdw}$ (see figure 2.8).

Since the satellite displays an intensity $\propto Q^2$, one needs to go at high Q values in order to increase the satellite intensity. However, since the atomic form factor decreases for large Q (green dashed line curve of figure 2.8), depending on the system, one needs to find the optimum zone in Q space taking into account those two antagonist effects.

Several points need to be nuanced here. This formula is correct for non-resonant X-ray diffraction which is the type of experiments shown in this manuscript. Resonant X-ray diffraction include other terms as for example the electronic quadrupole transition [85].

With regard to neutron diffraction, the atomic nuclei cross-section are larger than for the electronic cloud. Furthermore, neutrons have a higher penetration depth than X-ray and can be used to probe the bulk of the sample. Finally, since neutrons carry a magnetic momentum, they can interact with the crystal magnetic structure and are used as a probe for magnetic phase transition as ferromagnetism, antiferromagnetism, etc...

Finally, formula 2.9 is correct at zero temperature. In order to take the effect of temperature into account, one has to multiply the expression by the Debye–Waller factor which is, in this 1D model, $\exp(-Q^2\langle u^2\rangle)$ where $\langle u^2\rangle$ is the mean squared atomic displacement induced by thermally excited phonons.

A more general formula can be given for a 3D crystal with more than 1 atom per cell. Given a general 3 dimensional electronic crystal density in the CDW state

$$\rho(\vec{r}) = \sum_{n_1,n_2,n_3} \Bigg[\sum_{i=1}^{N_{at,cdw}} \rho_{at\,i}\left(\vec{r} - \vec{R}_{n_1n_2n_3} - \vec{r}_i - \Delta_{x,i}\vec{u}_i \cos\left(\vec{q}_{cdw}.\vec{R}_{n_1n_2n_3}\right)\right) \sum_{j=1}^{N_{at,not\,cdw}} \rho_{at\,j}\left(\vec{r} - \vec{R}_{n_1n_2n_3} - \vec{r}_j\right)\Bigg]$$

where n_1,n_2 and n_3 run over the number of cells along each dimensions, $\vec{R}_{n_1n_2n_3} = n_1\vec{a}_1 + n_2\vec{a}_2 + n_3\vec{a}_3$ (in which $\{\vec{a}_1, \vec{a}_2, \vec{a}_3\}$ are the crystal lattice vectors), i runs from 1 to $N_{at,cdw}$ corresponding to the numbers of atoms displaced by the CDW formation while j runs from 1 to $N_{at,not\,cdw}$ the number of atoms that are not participating to the CDW. Finally $\Delta_{x,i}$ is the amplitude of the atomic displacement which depends on the atom and $\vec{u}_i$ (where $|\vec{u}_i| \equiv 1$) is the direction of this distortion.

Computing the Diffraction amplitude and making a Taylor expansion in first order on the small parameter $\Delta_{x,i}$, one finds

$$A_{cdw}\left(\vec{Q}\right) = \sum_{n_1,n_2,n_3} e^{-i\vec{Q}.\vec{R}_{n_1n_2n_3}} \sum_{p=1}^{N_{at}} e^{-i\vec{Q}.\vec{r}_p} f_{at\,p}\left(\vec{Q}\right) - i\frac{1}{2}\sum_{i=1}^{N_{at,cdw}} \vec{Q}.\vec{u}_i\Delta_{x,i}e^{-i\vec{Q}.\vec{r}_i} f_{at\,i}\left(\vec{Q}\right) \times \sum_{n_1,n_2,n_3}\left[e^{-i(\vec{Q}-\vec{q}_{cdw}).\vec{R}_{n_1n_2n_3}} + e^{-i(\vec{Q}+\vec{q}_{cdw}).\vec{R}_{n_1n_2n_3}}\right]$$

where $f_{at\,p}\left(\vec{Q}\right)$ is the atomic form factor for atom i as defined in eq2.4. In the first term, p runs over all the atom inside the unit cell, therefore the first term correspond to the Bragg peaks of the crystal lattice without the CDW. In a first order Taylor expansion, their intensity remains the same whether the CDW is present or not. This is not true if one compute the expansion to higher order where the Braggs intensity is slightly reduced by the CDW apparition. The last two terms correspond to CDW satellite peaks at $\pm\vec{q}_{cdw}$ from the Bragg peaks. Their intensity is modulated by $\sum_{i=1}^{N_{at,cdw}} \vec{Q}.\vec{u}_i\Delta_{x,i}e^{-i\vec{Q}.\vec{r}_i} f_{at\,i}\left(\vec{Q}\right)$ which can be seen as a structure factor (compare with eq2.4) where only the atoms displaced by the CDW are taken into account. Therefore, the structure factors for the CDW satellite peaks and the Bragg peaks are different and we can even find a strong CDW peak near a Bragg of weak intensity as shown below.

Figure 2.9 presents a diffraction pattern of $TbTe_3$ collected at the beamline Cristal of SOLEIL synchrotron. This sample has a CDW along the $\vec{c}^*$ direction with a transition temperature $T_c = 336K$. Hence, the satellites are visible even at room temperature. From this figure, we see that the satellites are stronger near weak Bragg peaks and weaker around the strong ones.

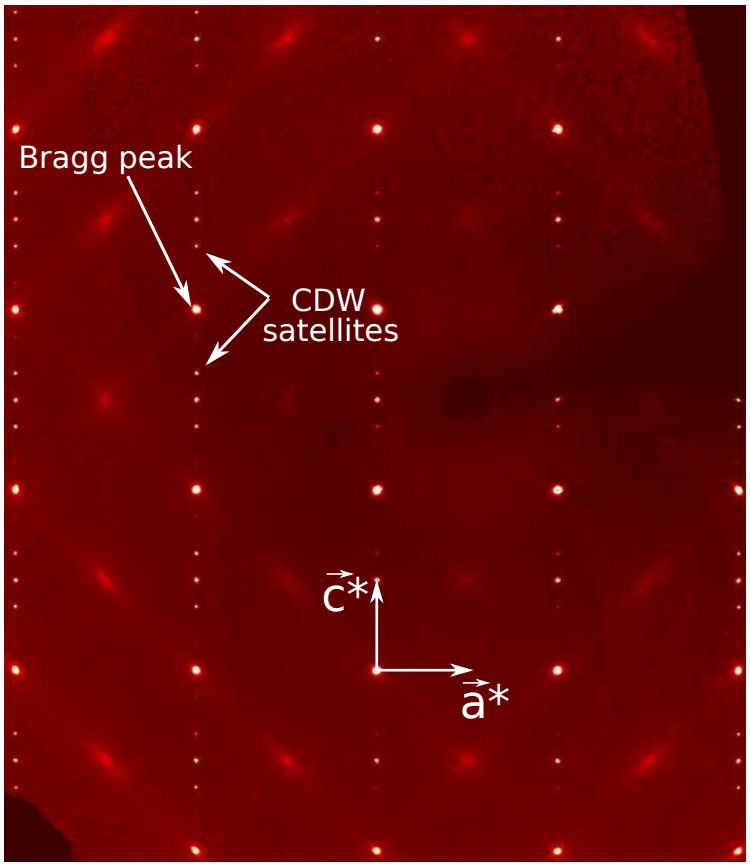

Figure 2.9: Diffraction of $TbTe_3$ at 300K performed on the 4 circles diffractometer of Cristal beamline at synchrotron SOLEIL. The CDW is along $\vec{c}^*$ and the satellite are visible at $\pm q_{cdw}$ around several Bragg peaks.

Chapter 3

CDW non-linear current and solitons

3.1 Strange non-linear behavior under current

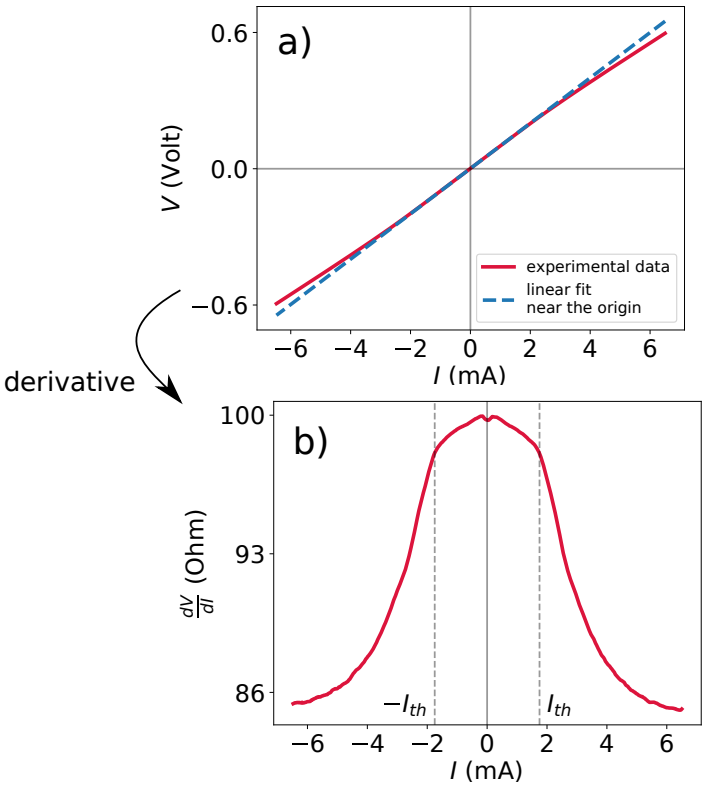

Figure 3.1: a) Current-Voltage measurement in $NbSe_3$ at 120K. The linear fit corresponds to the expected linear Ohm's law behavior. At higher applied electric fields, an additional current appears, hence deviating from Ohm's law. b) derivative of a). Here, the differential resistivity $\frac{dV}{dI}$ drops above a threshold current $I_{th} = 1.8$ mA (A. A. Sinchenko et al., private communication).

In 1976, Monceau et al. observed an anomalous temperature dependence of the

conductivity under applied current in $NbSe_3$ [1]. Since then, a large number of articles were published on this subject (see the book [18] and references therein).

This curious feature is better seen at a fixed temperature in a Current-Voltage (I-V) measurement (see figure 3.1 a)). At low current values, the curve is linear as expected from the simple Ohm's law. But above a certain threshold I_{th} mA, the I-V curve characteristics differs from the Ohm's law and becomes non-linear. This non-linearity is due to the appearance of an additional current related to the existence of the CDW phase. This feature is well observed within the derivative of this curve, displayed in figure 3.1 b). Below I_{th}, the differential resistivity $\frac{dV}{dI}$ is almost constant ($\approx$ 98 Ohms). For $I > I_{th}$, $\frac{dV}{dI}$ drops until it reaches a lower value ($\approx$ 86 Omhs) for large currents. The same non-linear current can be observed in other CDW materials like in blue bronze $K_{0.3}MoO_3$ [86] or Rare earth Tritellurides family $TbTe_3$ [87, 88, 89, 90] (see figure 3.2) or TaS_3 [91].

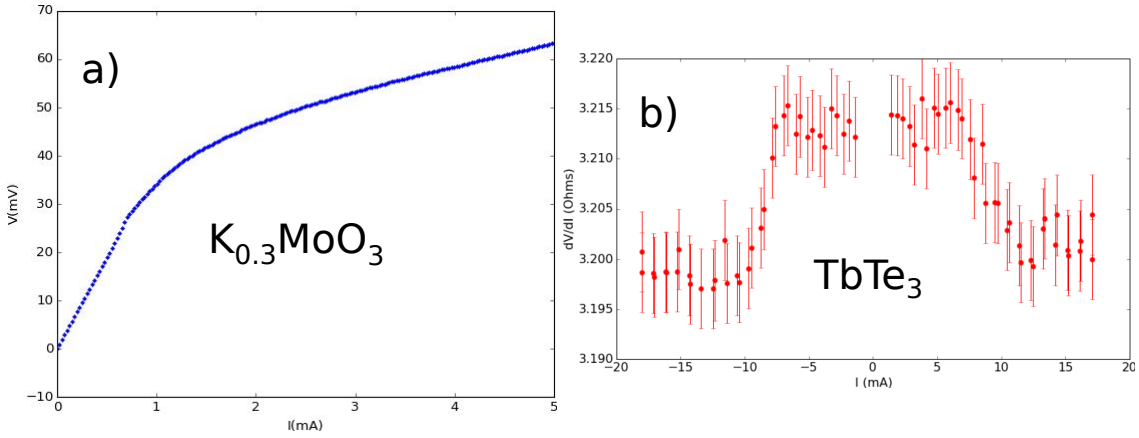

Figure 3.2: a) Current-Voltage measure of $K_{0.3}MoO_3$. The non-linear behavior is clearly visible for $I > 1$ mA. b) Differential resistivity of $TbTe_3$ at room temperature. The drop of $\frac{dV}{dI}$ is small in this material since it's still metallic in the CDW state, the differential resistance shift is 10 to 20 times larger in $K_{0.3}MoO_3$ and in $NbSe_3$.

To explain the observed non-linearity, the destruction of the CDW state, one could invoke heating effect since the high temperature phase is metallic, hence reducing the resistivity. However, the diffracted intensity of the satellite reflection is proportional to the square of the CDW amplitude ($I \propto \Delta^2$) and Fleming and al. [92] have shown that the satellite intensity remains constant in the non-linear regime. Therefore, the amplitude of the CDW is not reduced by the applied current and the additional current is directly due to the CDW itself.

This feature is also visible in NMR (Nuclear Magnetic Resonance), Ségransan et al. measured in $Rb_{0.3}MoO_3$ a narrowing of a transition of the ^{87}Rb nuclei under applied current [93]. They attributed this feature to a collective motion of the CDW.

Even more interesting is the temporal structure of this non linear CDW current. For a current $I < I_{th}$, the measured voltage is continuous, nothing specific is observed in the frequency domain. But above the threshold $I > I_{th}$, a periodic collective current appears. Thorne et al. measured the frequency spectrum of the voltage in $NbSe_3$ [94] and observed a sharp fundamental frequency peak and 23 harmonics (see figure 3.3 a)). The same periodic current was found in $Rb_{0.3}MoO_3$ (see

figure 3.3 b)). Finally, the frequency spectrum of $K_{0.3}MoO_3$ for several currents was measured in STM [95] (see figure 3.3 c)). Above the threshold, a new peak emerges, corresponding to the collective current's frequency. This frequency increases as a function of applied current as should be expected.

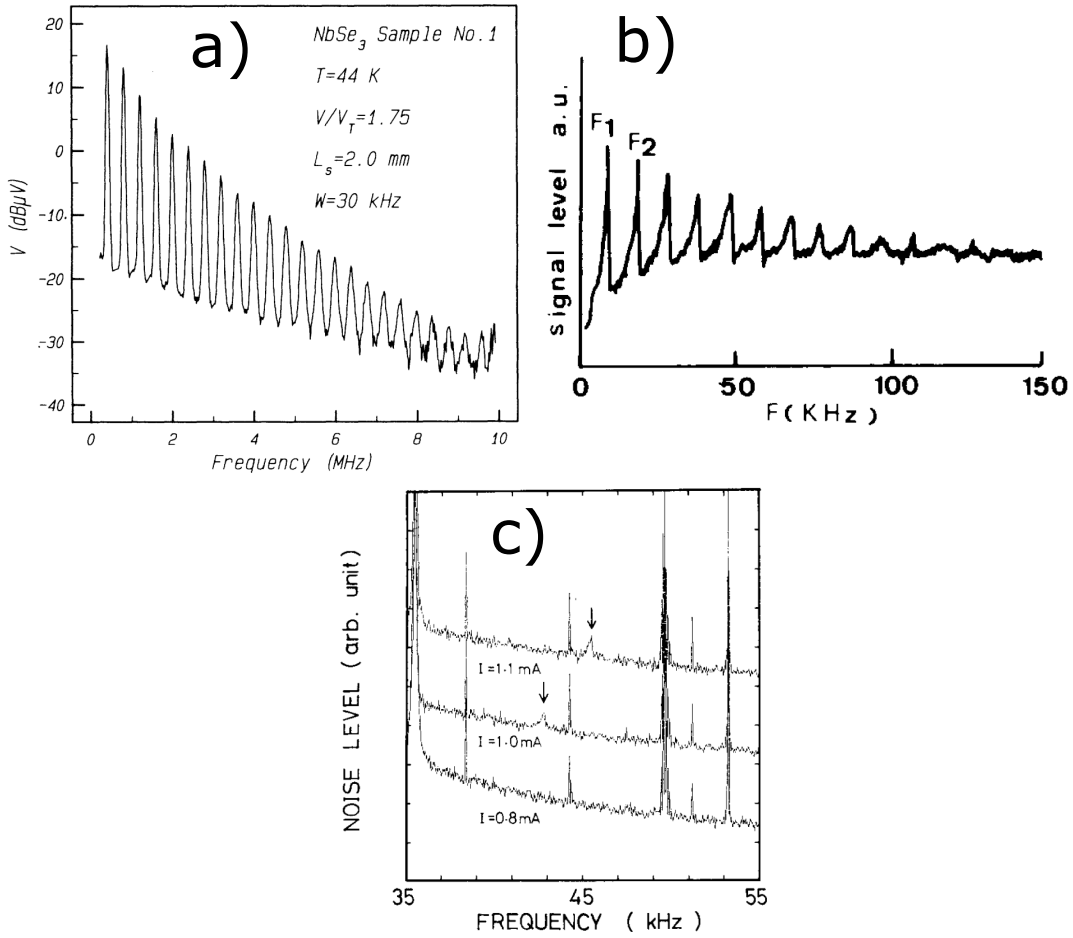

Figure 3.3: a) Frequency spectrum of the additional current above the threshold I_{th} in $NbSe_3$ [94]. A single fundamental peak and 23 harmonics are visible. b) Same measurement as in a) on a $Rb_{0.3}MoO_3$ sample (from [96]) c) Spectrum below (I = 0.8 mA) and above (I = 1.0 and 1.1 mA) I_{th} in $K_{0.3}MoO_3$ observed in STM [95]. A peak (indicated by an arrow) appears for $I > I_{th}$ and moves to larger frequencies as the current increases.

Several theories were proposed in order to explain this additional non-linear current. In next section we will present the simplest one which unfortunately fails to describe all experimental results. we will then present a description of the collective charges motion which appears in CDW in terms of a travelling soliton lattice which is well known from the literature [97, 98, 99, 100, 2]. This interpretation is in agreement with the experimental data.

3.2 Sliding CDW and theory of a solitonic charge transport

3.2.1 Rigid CDW sliding model

One of the first idea to explain those anomalous charge transport properties was based on a rigid and global "sliding" of the charge density wave. A CDW is usually described in 1D by its charge density $\rho = A\cos(2k_F x + \phi)$ where A is the CDW amplitude and ϕ its phase. By "sliding CDW", we mean a phase that linearly increases with time $\phi(t) \propto t$.

As will be described in a later chapter, the total energy of a commensurate CDW ($\lambda_{cdw} \equiv \frac{2\pi}{2k_F} = r \times a$, $r \in \mathbb{Q}$ with a the crystal lattice parameter) depends on the value of ϕ. Therefore, a global translation of the CDW with respect to the host atomic lattice costs a certain amount of energy which scales with the sample length. Thus, this energy is generally very high and the sliding phenomenon is not expected for a commensurate system.

In incommensurate CDW systems, however, the total energy does not depend on the phase ϕ (in a macroscopic sample) since the system is invariant by translation. The location of the CDW with respect to the lattice does not play any role. This means that a rigid translation of the whole CDW does not change the total energy. Therefore, an infinitesimal small force can drive the CDW into motion and one gets a system with zero resistivity.

The experimental reality is however slightly more complex than the previous picture. In particular, the existence of impurities and pinning must be taken into account. Indeed, a real macroscopic crystal contains lattice defects (dislocations, grain boundaries, atomic site vacancies, additional atoms in interstitial sites, etc...). Taking into account their interaction with the CDW, they break the translational invariance of the system's total energy.

One can describe this global sliding using a typical equation of motion dealing with the phase ϕ only ([18] p 184), taken from EqA.6 of Appendix A without the spatial derivative (assuming a rigid CDW) and adding a phenomenological damping term, to avoid finding an infinite CDW velocity. The third periodic term of this equation is due to the interaction energy between the impurities and the periodic CDW modulation ([18] p184)

$$\phi_{tt} + \frac{1}{\tau}\phi_t + \omega_0^2 \sin(\phi) = \eta E \tag{3.1}$$

where I used the notation $\phi_t \equiv \frac{\partial \phi}{\partial t}$. Let us start by neglecting the inertial term ϕ_{tt} which remains a valid assumption for small velocities. The equation reduces to (defining for simplicity $U \equiv \omega_0^2 \tau$ and $F \equiv \eta E \tau$)

$$\phi_t + U\sin(\phi) \approx F \tag{3.2}$$

which can be analytically solved for $F \geq U$, which defines the threshold field above which an additional current appears. The electrical conductivity is given by $\sigma = C\frac{\phi_t}{F}$ where C is a constant. The full expression is given by

$$\sigma = \frac{C(F^2 - U^2)}{F^2 - U^2 \cos\left(t\sqrt{F^2 - U^2}\right) + V\sqrt{F^2 - U^2}\sin\left(t\sqrt{F^2 - U^2}\right)} \tag{3.3}$$

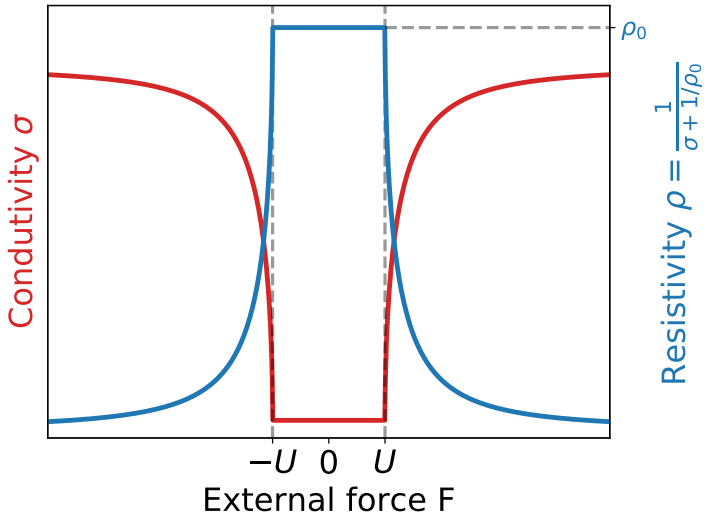

Figure 3.4: Conductivity (red) and associated resistivity (blue) from the averaged of Eq 3.3 as a function of applied force (proportional to electric field). Above a threshold value U, the force is strong enough to induce the sliding of the CDW and to create the additional current. This model reproduces well the experimental data shown in figures 3.1 b) and 3.2 b).

which is a function which oscillates on a period $T = \frac{2\pi}{\sqrt{F^2-U^2}}$. Experimentally, we measure the averaged conductivity $\langle\sigma(t)\rangle = \frac{1}{T}\int_0^T \sigma(t)\,dt$. This function was calculated numerically for several values of F (corresponding to several applied currents) and is shown in figure 3.4 along with the corresponding resistivity $\rho = \frac{1}{\sigma+1/\rho_0}$, ρ_0 being the resistivity below the threshold current I_t.

This non-linear behavior can be understood as follows: for a small applied current $F < U$, the CDW is pinned by crystal impurities, therefore it can't move freely and does not contribute to the current. Above a threshold force $F > U$, or in other words, above a threshold current $I > I_t$, the CDW has enough energy to be depinned from impurities and to move freely over the atomic lattice, to slide. This translation of a periodic modulation of charges creates an additional current in the sample inducing an increasing conductivity and a decreasing resistivity.

Despite its simplicity, this equation is very attractive. This model fits quantitatively to experimental data (blue curve of figure 3.4 compared to 3.1 b) and 3.2 b). In addition, it can explain the periodic collective current measured in figure 3.3. Since the CDW is periodic in space, a global translation of the CDW will bring charges periodically in times at the cathode.

Unfortunately, this theory can't explain all experimental features, especially a coherent diffraction experiment of 2008 of figure 3.9 [101, 2] as we will present in a next section, hence one must discard this simplistic description and move on to the next simplest one, the charge transport by a periodic CDW soliton lattice.

3.2.2 Solitonic transport theory

In the following, we will discard the "rigid" CDW approximation. One way to construct a coherent Ginzburg-Landau functional for the description of low energy CDW dynamics is either by starting from a microscopic Hamiltonian and deriving the free energy [102, 103, 104, 105], or guessing an effective model from experimental results on collective mode excitations [106, 107, 108, 109, 110]. Both way end up with a gap becoming space and time dependent $\Delta(x,t) = [\Delta_0 + \delta(x,t)]e^{i\phi(x,t)}$ which further involves a charge density expression $\rho(x,t) = A(x,t)\cos[2k_F x + \phi(x,t)]$. Since the amplitude mode (varying A or δ) costs more energy than the phason mode (varying ϕ) as shown in Appendix A, we will consider A and δ as constant in the following. As was already mentioned, the rigid CDW sliding theory can't explain all experimental data and we choose to follow the solitonic transport theory. I will explain what is this soliton transport theory and then present several experiments consistent with it and not with the former one.

In the soliton model, the non-linear and periodic current observed above I_{th} is due to a periodic lattice of phase solitons, meaning a regularly spaced $+2\pi$ jumps of ϕ moving at constant speed v as shown in figure 3.5 b). The corresponding phase is given by the expression

$$\phi(x,t) = 4\sum_n \text{atan}\left[\exp\left(\frac{x - nl - vt}{l_s}\right)\right] \tag{3.4}$$

Where l is the distance between solitons, l_s the soliton width and v the soliton velocity. This expression of a train of solitons can be compared with the single soliton expression EqA.8 of Appendix A.

Since each soliton contains 2 electrons (see Appendix C for a numerical demonstration), they carry an electric charge from one electrical contact to the other. In addition, the solitons are very stable since they are topologically protected (see [111] for more detailed) meaning that they can only be destroyed in a limited number of ways: during a soliton-antisoliton collision (where the antisoliton is a soliton with a -2π phase jump), at the sample boundaries or by canceling the CDW amplitude and this costs a lot of energy. As a consequence, the impurities won't destroy the solitons. However, they can change their shape or temporary slow them down. Since we have a periodic array of robust charges moving at the same speed, the measured current will be periodic as well, consistent with the measured spectra of figure3.3.

Let's consider the creation of solitons at the anode from the sine-gordon equation (Eq A.10 of Appendix A). The applied electric field induces a distortion of the CDW phase given in the static regime and assuming $\phi \ll 2\pi$

$$c^2\phi_{xx} - \omega_0^2\phi \approx \eta E \Longrightarrow \phi(x) = \frac{\eta E}{\omega_0^2}\left[\frac{\cosh\left(\frac{x\omega_0}{c}\right)}{\cosh\left(\frac{L\omega_0}{2c}\right)} - 1\right]$$

This function is shown in figure 3.6 along with the CDW charge density $\rho(x) = A\cos[2k_F x + \phi(x)]$. The presence of E induces a dilation (compression) of the CDW near the left (right) contact, hence an elastic stress. Above a threshold field E_{th}, the elastic energy is too high and a soliton is created at the left contact by a vortex ring, partially decreasing the stress. This is the so called phase-slip process (see Appendix

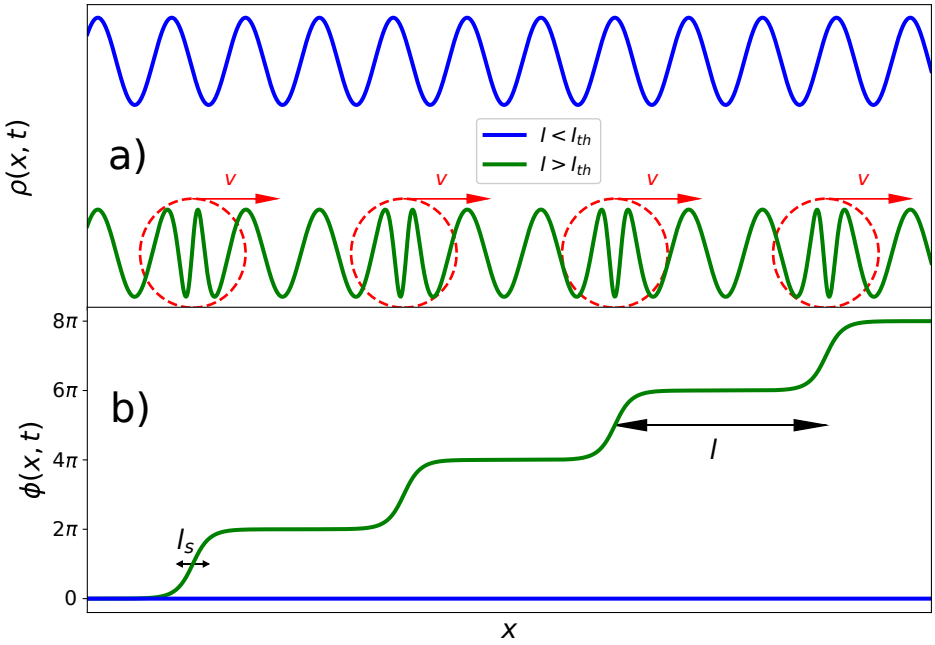

Figure 3.5: a) CDW charge density $\rho = A\cos(2k_F x + \phi)$ below and above the threshold current I_{th}. b) Corresponding phase ϕ profile given by Eq3.4 which is for $I > I_{th}$ a periodic array of 2π jumps of width l_s, separated by a distance l and moving with the same velocity v.

B for a detailed description of this phenomenon). As described by Fogel et al. [112], under the external force ηE and damping, the soliton will accelerate until it reaches a constant speed. As the soliton moves away from the contact region, the stress increases again until another soliton appears leading to a periodic nucleation of solitons.

The phase-slip process has been discussed in details in the literature [113, 114] even on a quantum level considering a tunnel effect of the soliton at the contact, sometimes using the instanton technique to calculate this tunneling probability [115, 97, 116, 117]. John Bardeen also participated in this debate [118, 119, 120, 121, 122].

With regards to experimental observations, Lemay et al. have shown that the CDW current has a spatial dependence [123]. The result is displayed in figure 3.7. The current density j_c is lower near the 2 electrical contacts in $x = \pm 300\mu m$ while being almost constant in the middle of the sample. This is inconsistent with a rigid sliding of the CDW, where j_c should be constant over the whole sample length. This observation is in agreement with the phase slip theory in which solitons or antisolitons are created in the vicinity of the two contacts.

3.2.3 X-ray diffraction of the solitons periodic lattice

One can expect the X-ray diffraction pattern near the CDW satellites of figure 2.8 to change when the periodic solitons lattice appears above the threshold current. A numerical calculation of this diffraction pattern is shown in figure 3.8 for a CDW with a constant null phase $\phi(x) = 0$ (in blue) and with a phase corresponding to

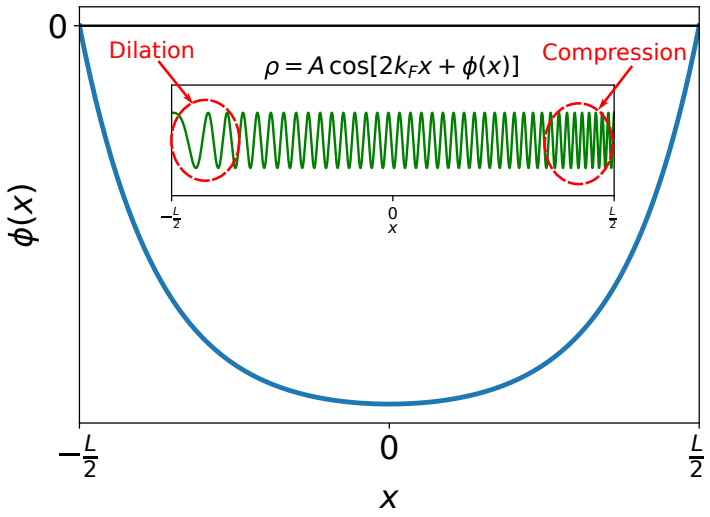

Figure 3.6: $\phi(x)$ under applied electric field, the electrical contacts are in $\pm\frac{L}{2}$. Inset : corresponding charge density. An expansion (compression) is visible near the left (right) contact, inducing a stress of the CDW in these regions.

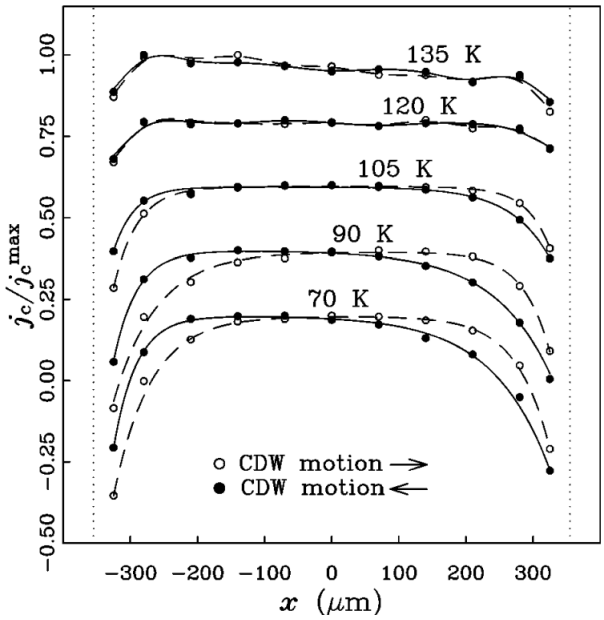

Figure 3.7: CDW current density as function of position for several temperatures in $NbSe_3$, from [123].

the periodic solitons lattice given by Eq 3.4 at a fixed time $t = 0$. Two features are observed and can be understood from a qualitative point of view.

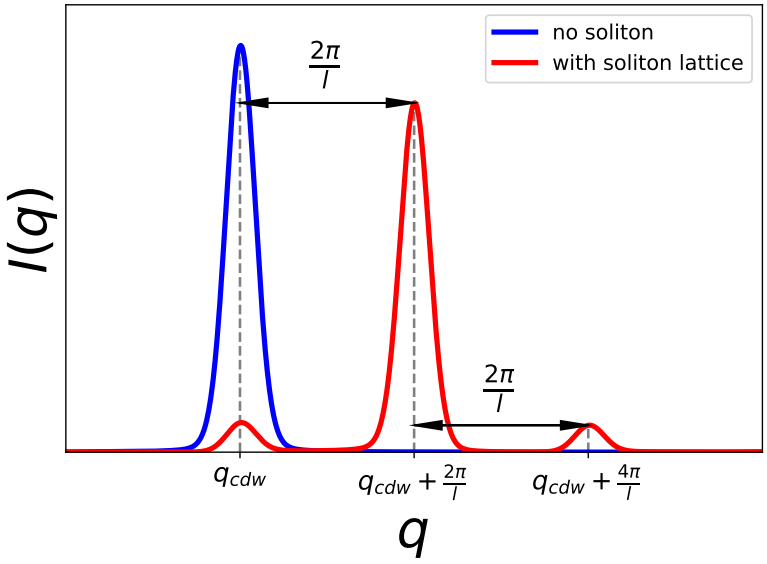

Figure 3.8: Numerical calculation of the X-ray diffraction pattern close to the CDW satellite position. In blue, when no current is applied, the satellite is at position q_{cdw} (more specifically Bragg+q_{cdw} as in figure 2.8). When current is applied above the threshold, a periodic soliton lattice appear given by Eq 3.4, inducing a shift of the CDW satellite and the emergence of two small supersatellites.

First, the CDW satellite shifts by a distance $\frac{2\pi}{l}$ in q space where l is the spacing between each soliton (see figure 3.5). Call the longitudinal (along x) X-ray coherent beam size L. When no solitons are present, from $x = 0$ to $x = L$ the CDW total phase increases by $q_{cdw}L$. Thus, one observe the CDW satellite at q_{cdw}. But when the soliton lattice is present, the beam "sees" $\approx \frac{L}{l}$ solitons. Since the soliton is a 2π phase jump, the CDW total phase increases now by $\approx q_{cdw}L + 2\pi\frac{L}{l}$ in the coherent volume, hence $q_{cdw} \rightarrow q_{cdw} + \frac{2\pi}{l}$ and one observes a shift of the satellite as in the red curve of figure 3.8. This argument is correct as long as $L \gg l$ and the soliton width l_s is large enough otherwise one would observe a variation of the CDW satellite shape. Note that if the soliton jump is different than 2π, as it is the case for CDW discommensurations, the satellite would be at $q_{cdw} + \frac{\text{phase jump}}{l}$

The second feature is the emergence of 2 small peaks on each side of the satellite, which are called "supersatellites". Remember that in diffraction, a new peak in reciprocal space corresponds to a new periodicity is real space. For example, the CDW phase with wavelength λ_{cdw} induces satellites at $\pm\frac{2\pi}{\lambda_{cdw}} = \pm q_{cdw}$ from the Braggs. Therefore, the emergence of a CDW solitons lattice of period l in real space induces new peaks in reciprocal space at $\pm\frac{2\pi}{l}$ from the CDW satellite.

3.2.4 Soliton supersatellites in $K_{0.3}MoO_3$ and comparison with narrow-band noise frequency

In an experiment by Le Bolloc'h et al. the authors used a coherent X-ray beam in order to observe the diffraction pattern of the CDW under current [2, 101, 124]. In this experiment, the X-rays coherence length is larger than the solitons lattice period l. Therefore, they could observe X-ray interference between solitons. The diffraction pattern in $K_{0.3}MoO_3$ is shown in figure 3.9 (a) next to the projection along the CDW direction in (b).

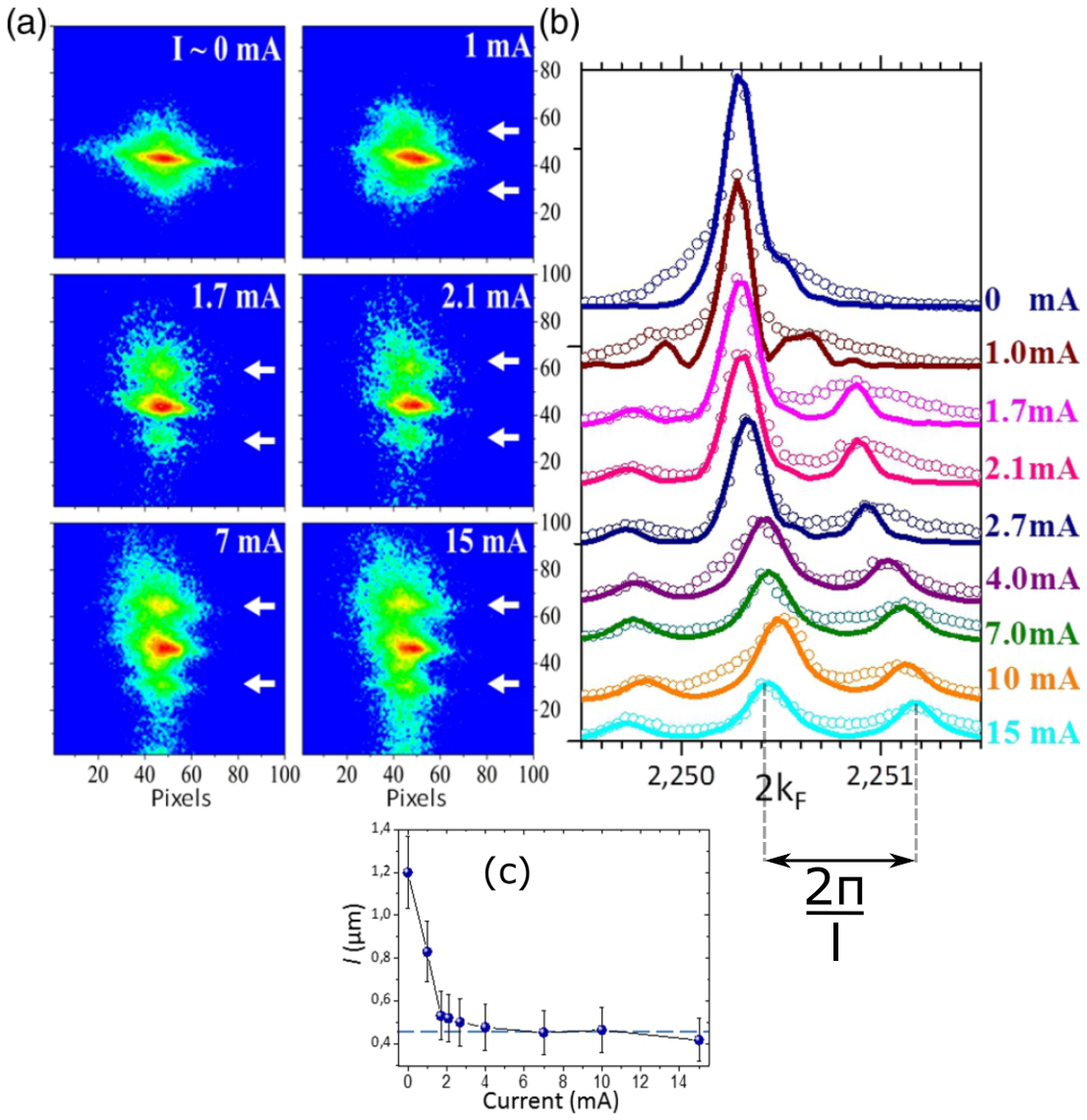

Figure 3.9: a) CDW satellite in $K_{0.3}MoO_3$ for several currents from [2]. White arrows indicate the 2 supersatellites. b) Fit of the projection along the CDW direction using the solitons lattice expression Eq3.4. The distance satellite-supersatellite between the peaks gives directly the soliton separation l which is shown in (c) as a function of the current.

Figure 3.9 (a) shows, for several currents, the CDW satellite at position $Q_s = (5,-1,-3)+\vec{q}_{cdw}$ where we use the symbolic notation (h,k,l) for the Bragg wavevector $\vec{G}_{hkl}$.

As current increases above the threshold $I_{th} = 1.2$ mA, two new peaks appear on both sides of the CDW satellite which corresponds to the emergence of the solitons lattice as said earlier (compare figure 3.9 (b) and figure 3.8). Since the solitons are created periodically and move through the sample at the same speed, at a given time the X-ray beam "sees" a periodic lattice of solitons. Therefore, the authors used expression 3.4 to fit the diffraction patterns as shown in figure 3.9 (b).

As said before, the distance satellite-supersatellite highlighted by the double-headed arrow of figure 3.9 (b) directly gives the periodicity l of the soliton lattice. This periodicity of the order of 1μm, which is huge compared the the CDW wavelength of few Angstroms (around $10\mathring{A}$). The evolution of l as function of current is shown in figure 3.9 (c). As expected, as the current increases, more and more solitons are created, thus their periodicity l decreases.

One can obtain an order of magnitude of the solitons speed using the result of figure 3.9 (c) and the narrow-band noise frequency measured in $K_{0.3}MoO_3$ shown in figure 3.3 b) and c). This gives a soliton velocity $v \sim 10\text{kHz} \times 1\mu\text{m} = 10^{-2}\text{m.s}^{-1}$. Several papers [125, 126, 127] give the dependence of the narrow band noise fundamental frequency ν (1^{st} peak of figure 3.3 b)) as function of either the current I, or the CDW additional current $I_{cdw} = I - V \times R(I = 0)$ where V is the electric potential and $R(I = 0)$ the resistivity at zero current. Unfortunately, one can't obtain the solitons velocity v as function of the current using data of $\nu(I)$ from these articles and l from figure 3.9 (c) since the samples don't have the same dimensions. The relevant parameter (force acting on the soliton) is neither V, I or I_{cdw} but the electric field E. Since we can't calculate obtain $\nu(E)$ from [125, 126, 127], we can't calculate $v(E)$.

However, one can still make a qualitative comparison making use of a hypothesis. Fogel et al. [112] and Nakajima et al. [128] showed that, under an applied force E, if damping is taken into account, the soliton reaches a constant velocity proportional to E. Calling the proportionality constant α, the soliton velocity in the sample is $v(E) \equiv \alpha E$. Since the length of the sample used for the diffraction experiment of figure 3.9 is given, one can have $v(V) = \alpha\frac{V}{L}$. Furthermore, the curve $\frac{dV}{dI}$ is given, hence one has also $V(I)$, thus we have $v(I) = \alpha\frac{V(I)}{L}$. From this and $l(I)$ given in figure 3.9 (c), one finds $\nu(I) = \frac{v(I)}{l(I)}$ and can compare (choosing an arbitrary value of α) the shape of $\nu(I)$ with the ones from the literature [125] in figure 3.10 a1) and b1). One can also obtain $\nu(I_{cdw})$ and the comparison with [126, 127] is shown in figure 3.10 a2), b2) and c2).

The behaviors of the calculated $\nu(I)$ and $\nu(I_{cdw})$ match the one obtained from the narrow-band noise spectrum. Therefore, Fogel's approximation of a soliton velocity linear with the electric field $v(E) = \alpha E$ works in our case. In order to have an experimental value of α one needs a narrow-band noise measurement as a function of the electric potential $\nu(V)$ knowing the sample length and at the same temperature T = 70 K as in [2].

As a last remark, from figure 3.9 (b), one can observe that the CDW satellite shift is less than the $\frac{2\pi}{l}$ that is expected and shown in figure 3.8. This is probably due to the fact that current was already applied to the sample before taking the diffraction picture at 0 mA. It is well-known from the literature that an hysteresis effect occurs in CDW material under current [129, 130, 131]. One can understand

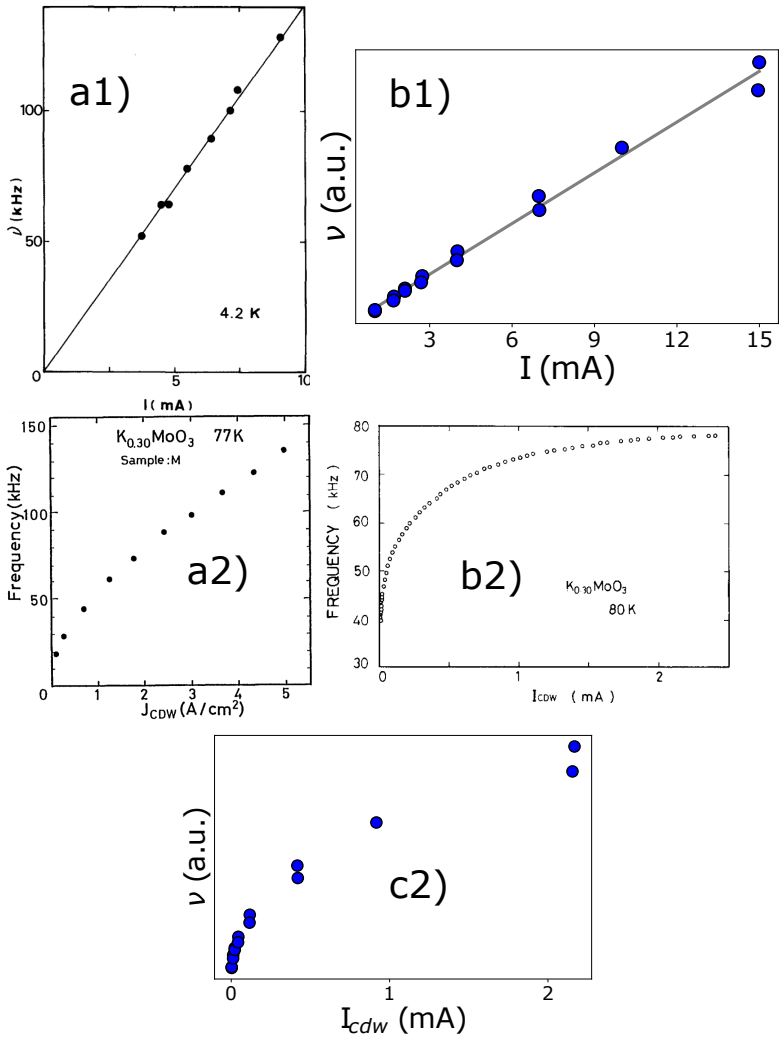

Figure 3.10: Comparison of the measured narrow band noise from [125, 126, 127] in a1),a2) and b2) with the one derivated from the distance between the solitons of [124] at 70K in b1) and c2). a1) and b1) correspond to $\nu(I)$ while a2),b2) and c2) show $\nu(I_{cdw})$.

this effect by the solitons being blocked inside the sample, when current comes back to 0mA, from damping by interaction with impurities, surface pinning,...etc. In this case, the periodicity of the soliton lattice could be lost (since impurities are randomly distributed in the sample), hence the supersatellites disappear. But since the solitons are still present, the CDW satellite is slightly shifted from q_{cdw}. Therefore, when current is applied again the CDW satellite shift is smaller than $\frac{2\pi}{l}$.

3.2.5 CDW satellite shift under current in $NbSe_3$

When the X-ray coherence length is less than the soliton lattice spacing l, one can't observe the two supersatellites of the red curve of figure 3.8. Still, the shift $q_{cdw} \rightarrow q_{cdw} + \frac{2\pi}{l}$ should be observed.

This was the case in a X-ray diffraction experiment performed on $NbSe_3$ [132]. The authors measured the position of the CDW satellite as a function of applied

current close to the electrical contact. The results are shown in figure 3.11. When a small current $I < I_{th}$ is applied to the sample, the satellite doesn't move within the error bar as seen in figure 3.11 a). But when $I > I_{th}$, the satellite clearly shifts in position, as expected from figure 3.8.

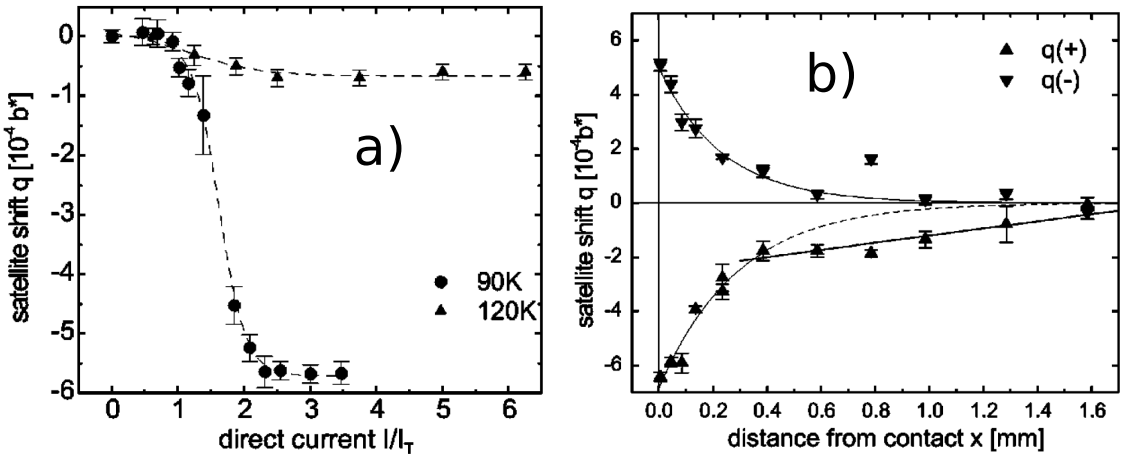

Figure 3.11: a)Shift of the CDW satellite position near the electrical contact as function of applied current in $NbSe_3$.b) Amplitude of the CDW satellite shift as function of the distance from the left electrical contact. Figures from [132].

In this case, the shift is negative, meaning that instead of solitons ($+2\pi$ phase jump), antisolitons (-2π phase jump) are created at the contact. This depends at which contact (left or right) one is measuring or equivalently on the direction of the current. Knowing that the satellite shift is $-\frac{2\pi}{l}$, we observe an increase of this shift, meaning a decrease of the soliton spacing l as in $K_{0.3}MoO_3$ (see figure 3.9 (c)). In figure 3.11 b), one can observe that the shift amplitude is larger close to the electrical contact ($x \approx 0$) while being almost zero in the middle of the sample ($x \approx 1.6$).

From figure 3.11, one can calculate the soliton lattice spacing in $NbSe_3$ **close to the contact** at high current $-\frac{2\pi}{l} \approx -5.6 \times 10^{-4} \times b^* \Rightarrow l \approx 0.6\mu$m (taking $b \approx 3.46\mathring{A}$) similar to the one in the bulk of $K_{0.3}MoO_3$ (see figure 3.9 (c)).

3.3 Attempt to observe the solitons in $NbSe_3$ using high resolution X-ray diffraction

Unlike in $K_{0.3}MoO_3$, the soliton lattice supersatellites have never been observed in $Nbse_3$ by X-ray diffraction, despite particularly good narrow-band noise measurements. Note that the narrow-band noise frequency is 100 times larger in $NbSe_3$ than in $K_{0.3}MoO_3$ (compare figure 3.3 a) and b)). Precise measurements of satellite profiles have, however, shown asymmetrical profiles at the foot of the CDW satellite [132] compatible with the existence of a soliton lattice, without being able to resolve the supersatellites. Our explanation of this lack of measurement by diffraction is the existence of a larger period of the soliton lattice in $NbSe_3$ at the center of the sample.

To be able to see correlations in the micrometer range by X-ray is already not so easy. For the experiment shown in figure 3.9, the authors used a coherent beam, parallel and they used a 22μm pixel size detector, located 1.7m from the sample. The reciprocal space resolution was good enough to observe the supersatellites at wide angles.

In order to have a resolution sufficient enough to see the supersatellites in $NbSe_3$, we went to the beamline ID01 of the ESRF synchrotron of Grenoble to perform X-ray diffraction. This beamline is made of a Huber 3+2 circle diffractometer and a long flight tube with an Andor 2D X-ray detector at the end, see figure 3.12. The tube is under primary vacuum in order to avoid absorption of diffracted X-rays by air. In a diffraction experiment, the larger the sample-detector distance is, the better the resolution on the diffraction pattern. Since we expect the soliton lattice period to be of the order of few micrometers, we need a good resolution in Q space, which (following Bragg's law) is equivalent to a good resolution in diffraction angle. Increasing the sample-detector distance using the setup of figure 3.12, we can obtain this higher angular resolution.

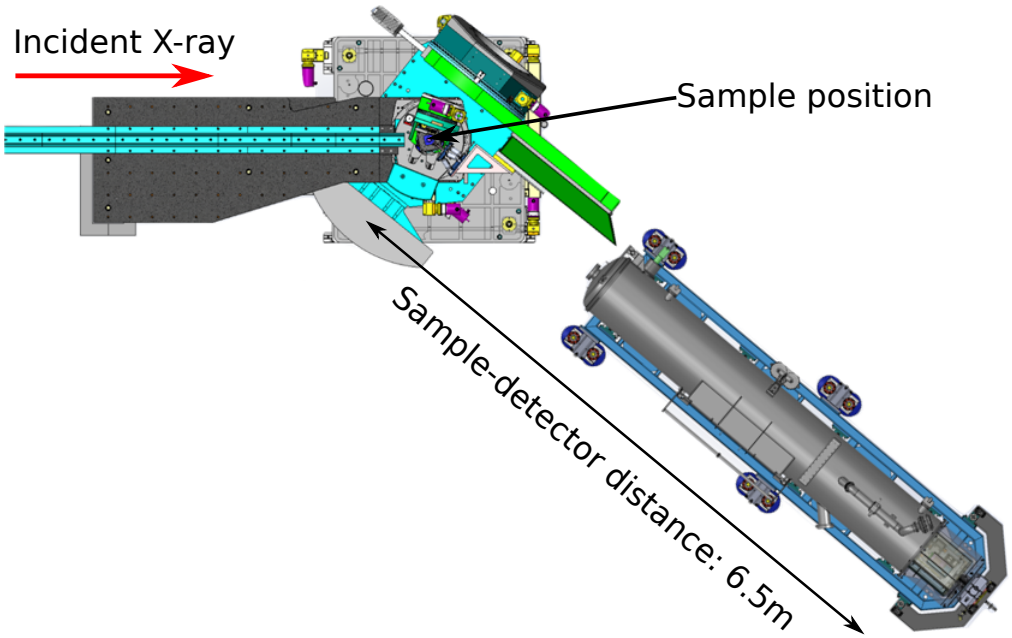

Figure 3.12: Schematics of ID01 beamline of ESRF synchrotron. The Andor X-ray detector is at the end of a flight tube under vacuum, at a distance of 6.5m from the sample.

Four gold contacts were evaporated on the sample prior to experiment by A.A. Sinchenko and Pierre Monceau. The sample was then mounted in a cryostat, connected to an external current source and mounted on the diffractometer. It was then cooled down below the CDW transition until reaching a temperature of 120 K. The threshold current for this temperature was measured to be $I_{th} = 5$ mA. Since using the flight tube constraints the experiment to be performed in the horizontal plane of the lab, we carefully oriented $NbSe_3$ to have the b axis (along which the CDW appears) in this specific plane. We went over to the CDW satellite position

(0,1.243,0) close to the (0,1,0) Bragg. Then, we increased the current and hoped to observe similar supersatellite as the ones of $K_{0.3}MoO_3$ of figure 3.9.

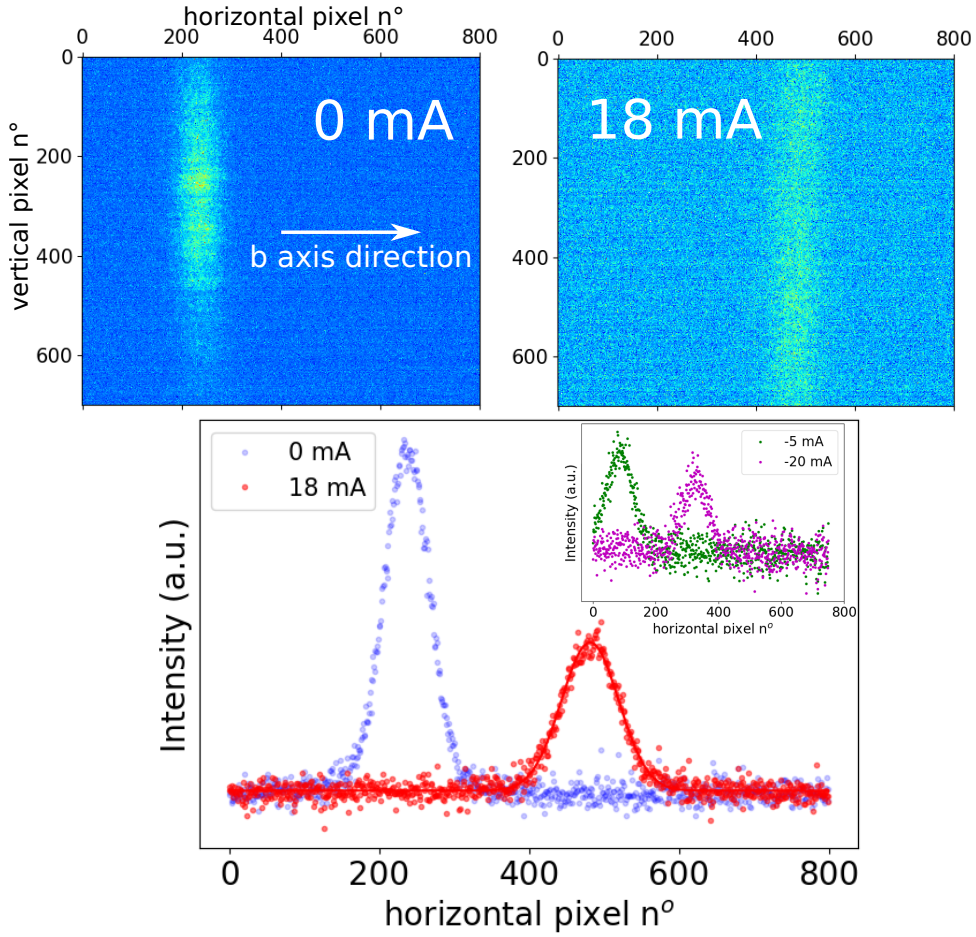

Figure 3.13: CDW satellite in $NbSe_3$ at the maximum of the rocking curve on the 2D detector at 0mA and 18mA and their projections along the CDW direction. The satellite at 18mA $= 3.6 \times I_{th}$ (red dots) is displayed along with its corresponding gaussian fit (red line). No supersatellite are visible. Inset : CDW satellite at -5mA and -20mA showing a shift in the same direction for positive and negative current, thus illustrating that this shift is only induced by Joule effect.

Unfortunately, this was not the case. Even at a high currents in comparison to I_{th}, the supersatellite did not appear. In figure 3.13 we see the CDW satellite on the detector at 0 mA and its projection along b (blue curve) which is the equivalent of figure 3.9 (b). The same projection is shown for a current I =18 mA $= 3.6 \times I_{th}$, but no extra supersatellite is observed. The shift in position regarding the one at 0mA is due to sample heating by the applied current since the same shift was seen for positive and negative current and the satellite peak intensity decreases for large currents. The shift in the same direction at negative currents (-5mA and -20mA) is observed in the inset of figure 3.13.

Still, important information can be extracted from these data. Either the soliton lattice doesn't exist in $NbSe_3$ but if it does exist, we can get a lower bound value l_{min} for the distance between the solitons. We perform a gaussian fit of the projection

at 18 mA. The fit is displayed as a red curve in figure 3.13 and fits very well to the data points. From this fit, we get the FWHM (Full Width at Half Maximum) in number of pixel (converted to a distance knowing the pixel size of $6.7\mu m$) which we call $\sigma \approx 236$ pixels $\times 6.7\mu m$. If the supersatellites are present (which may not be the case), they are at a distance less than $\sigma/2$ of the CDW satellite, meaning that they are hidden inside the satellite.

The CDW satellite position in angle is given by Bragg law $2d\sin(\theta) = \lambda$ with $\lambda = 1.55\mathring{A}$ the X-ray wavelength for an energy of 8keV and $d = \frac{2\pi}{Q_{0,1.243,0}} = \frac{b}{1.243}$ with $b = 3.463\mathring{A}$ the $NbSe_3$ lattice parameter. Using these numerical values, we find the corresponding angle $\theta \approx 16.2°$.

Now say the supersatellite corresponding to a minimum distance l_{min} between solitons hidden at $\pm\sigma/2$ from the CDW satellite. With the help of figure 3.14, we see that a distance $\sigma/2$ corresponds to a change of the angle in Bragg's law $\theta \to \theta + \delta\theta$ with this additional angle given by $2\delta\theta \approx \frac{\sigma}{2D}$ in radians. The Bragg's law is now changed to $2d'\sin(\theta + \delta\theta) = \lambda$ where $d' = \frac{2\pi}{Q_{0,1.243,0}+2\pi/l_{min}}$. Doing a Taylor development in $\delta\theta$ and using from the CDW satellite Bragg law $Q_{0,1.243,0} = 4\pi\sin(\theta)/\lambda$, one finds

$$\begin{aligned}
\frac{4\pi}{Q_{0,1.243,0} + 2\pi/l_{min}}\sin(\theta + \delta\theta) &= \lambda \\
Q_{0,1.243,0} + \frac{2\pi}{l_{min}} &\approx \frac{4\pi}{\lambda}\left[\sin(\theta) + \delta\theta\cos(\theta)\right] \\
l_{min} &= \frac{\lambda}{2\delta\theta\cos(\theta)} \approx 1.33\mu m
\end{aligned}$$

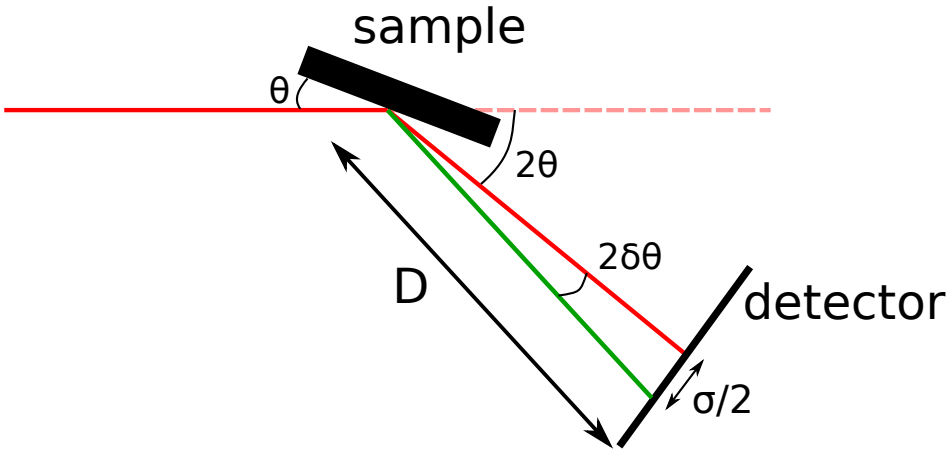

Figure 3.14: Sketch used to calculate the minimal distance between solitons in $NbSe_3$. See text for details.

Therefore, the distance between solitons in $NbSe_3$ **in the middle of the sample** is constrained by

$$\boxed{l_{NbSe_3} > 1.33\mu m} \tag{3.5}$$

3.4 A first experiment on sliding CDW performed on the X-ray Free Electrons Laser (XFEL) LCLS

We have performed diffraction experiment on a sliding CDW from a highly coherent source, an X-ray Free Electron Laser (XFEL) source. We went to the XFEL LCLS at Stanford on XCS beamline to perform coherent and femtosecond diffraction on $NbSe_3$.

3.4.1 Short definition of the X-ray coherence

The X-ray beam emitted by a synchrotron is never strictly a plane wave. It would be the case if the electrons bunch was a point source. In reality, this bunch has a certain size and X-ray radiating from different parts of the bunch can interfere and destroy coherence. One way to retrieve coherence is to go very far from the source. This is more evident from the transverse coherence length expression

$$\xi_T = \frac{\lambda R}{S} \tag{3.6}$$

where λ is the X-ray wavelength, R the distance from the source and S the source transverse size. From this formula, we see that it's easier to have a large coherence length for an optical laser with $\lambda \sim$ some hundreds of nanometers than for an X-ray beam with $\lambda \sim$ few $\mathring{A}$. The usual method to get a coherent X-ray beam is to place the sample far from the source as it is done at ID01 beamline at ESRF synchrotron.

However, equation 3.6 is valid for an incoherent electron bunch source, meaning one electron emits X-ray radiations without phase matching regarding the others. On the contrary, the electron bunch from a free electron laser as LCLS is coherent, hence emitting a X-ray beam with a non-zero ξ_T at the undulator exit [134]. Then, the X-ray beam travels from the undulator to the user station (our sample position) which further increases the transverse coherence length and can be of the order of 0.32mm^2 [134], therefore much larger than the beamsize used in our experiment ($15\times15\mu\text{m}^2$).

Therefore, in the diffraction pattern, we can see interferences from an object with a size of the order of or smaller than the beamsize. In order to check the beam coherence, we used a system of 2 slits closed at 10×10 μm^2 and recorded the direct beam on a CSPAD-2.3M detector, see figure 3.15. In theory we should see the absolute square of the Fourier transform of the slits geometry

$$\begin{aligned} I(q_x, q_y) &= \left| \int_{-L_x/2}^{L_x/2} \int_{-L_y/2}^{L_y/2} e^{i(q_x x + q_y y)}\, dxdy \right|^2 \\ &= \left(\frac{4 \sin\left(q_x \frac{L_x}{2}\right) \sin\left(q_y \frac{L_y}{2}\right)}{q_x q_y} \right)^2 \end{aligned} \tag{3.7}$$

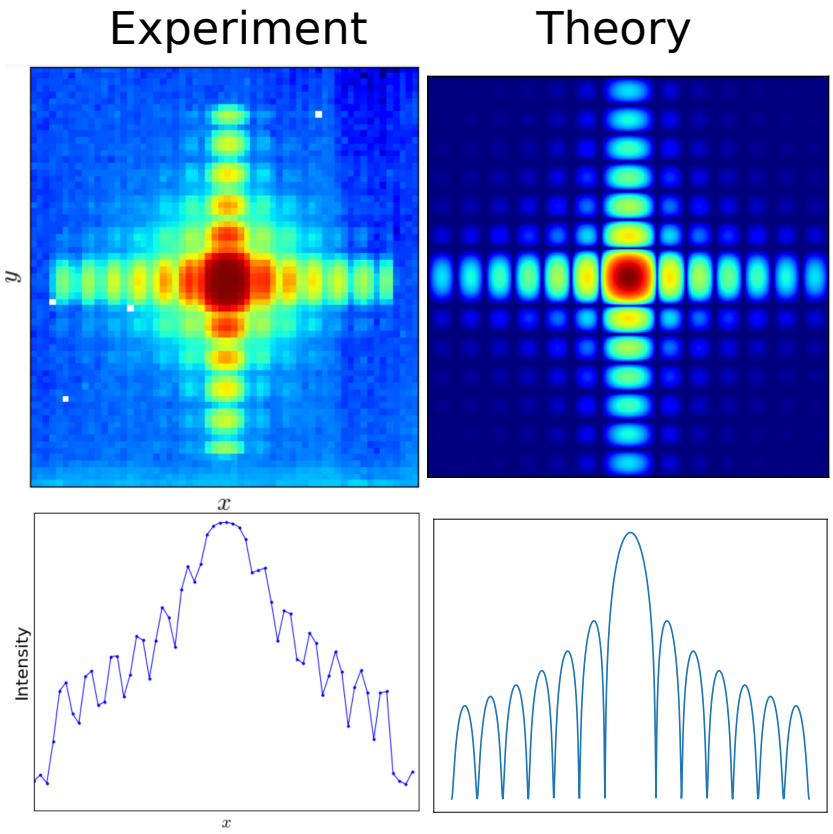

Figure 3.15: Comparison between experiment and theory of a direct X-ray coherent beam diffracted by square slits in a log scale. The fringes linked to the slits opening are clearly visible. The degree of coherence [133] is $V = \frac{I_{max}-I_{min}}{I_{max}+I_{min}} \approx 77\%$ *calculated with the figure on the left in linear scale.*

The comparison between the theory and the experiment matches well (see fig 3.15 in Log scale). The finite visibility of the experiment is probably not due to the finite degree of coherence of the x-ray beam but rather to the beam instability and the finite pixel size.

3.4.2 Breaking of CDW coherence under current

In figure 3.16 a) is depicted the differential resistivity measured in-situ during the diffraction experiment of $NbSe_3$ at a temperature of 120 K. We selected this temperature so the threshold current is large enough to observe the CDW evolution for $I < I_{th}$ and small enough to measure above the threshold while avoiding heating the sample. The threshold current is visible at $I_{th} \approx 0.8$ mA. We looked at the CDW satellite at the maximum of the rocking curve for several currents displayed in b). For each current, one has the 2D matrix Intensity(x,y) where x is the direction on the detector corresponding to the CDW axis, while y corresponds to the transverse direction.

One could deduce from figure 3.16 that the CDW amplitude decreases by Joule effect but this is not the case. The CDW amplitude Δ is related to the square root of the integrated satellite peak intensity ($\Delta^2 \propto \sum_{x,y}$ Intensity(x,y)) as can be

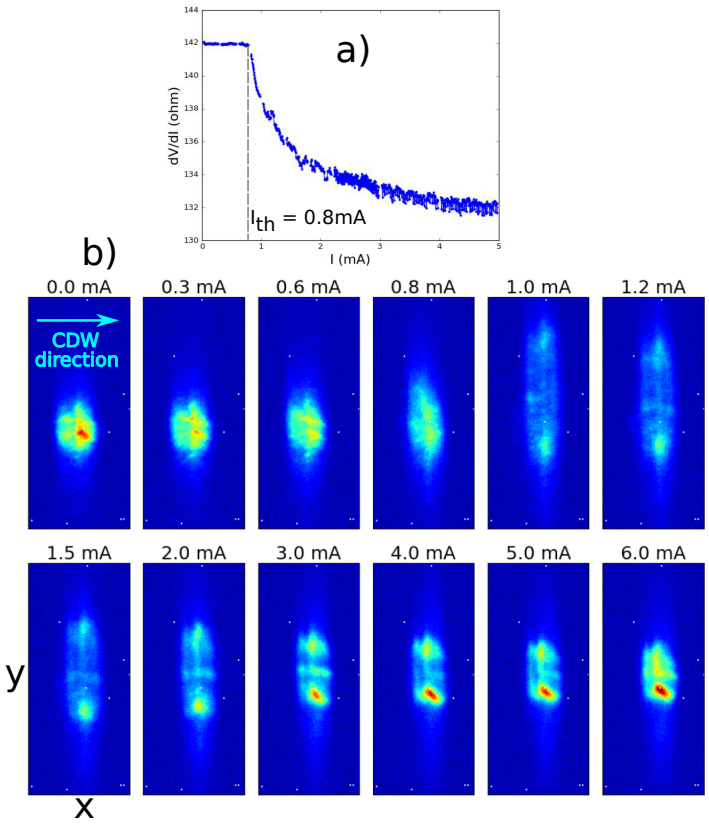

Figure 3.16: a) In-situ differential resistivity measurement performed during the experiment. The threshold at 0.8 mA is clearly visible. b) CDW satellite for several currents. For I close to I_{th}, the satellite width increases in the transverse direction and then decreases back for currents large compared to I_{th}. Note that the color scale is the same for each map.

deduced from Eq 2.9 where the diffracted X-ray intensity is $|A(Q)|^2$. We show in figure 3.17 the relative variation of Δ for each current in percent, formally $[\Delta(I) - \Delta(0\text{mA})]\,/\Delta(0\text{mA})$. This evolution is at most 5%, meaning that the CDW amplitude is almost constant when current is applied.

When current is applied to the sample, we observe an increase of the transverse width of the satellite as in [135]. However, this is not a simple broadening of the peak, which would mean a smooth variation of the CDW in the transverse direction. Speckle patterns can be observed due to interferences between several CDW domains, meaning the satellite is not simply a gaussian peak broadening under current but rather several peaks of irregular intensity as in figure 3.18 a). This pattern is an evidence of discontinuity of the CDW phase ϕ in the transverse direction. Since $NbSe_3$ is a crystal made of quasi-1D chain as in figure 1.9, this speckle indicates fast variation of ϕ from one chain to the other. One could say that the CDW is "broken" into several domains in the transverse direction for current close to I_{th}. Note that, using a X-ray beam with a low degree of coherence, one can't observe the speckle pattern but only a broadening of the peak.

In figure 3.18 b) we show the detector image from figure 3.16 b) summed along x (formally $\sum_x$ Intensity(x,y)) for each current. An abrupt evolution appear at

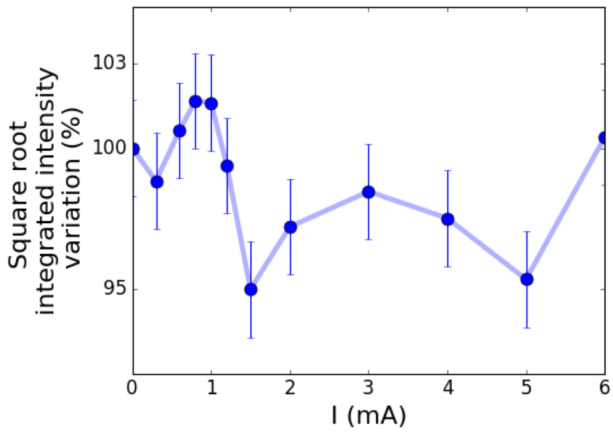

Figure 3.17: Relative variation of the square root integrated intensity of the CDW satellite reflection, proportional to the CDW amplitude Δ. The variation are at most 5%, meaning Δ is almost stable under current.

the threshold current I_{th} where the satellite widens and gets split in the transverse CDW direction. Then, when I increases above I_{th}, the CDW reflection relaxes back while still having a larger broadening than at zero current. One can observe, at high current, that the satellite is divided into 3 smaller peaks in transverse, which could already be observed in figure 3.16 b) at 3mA for example. One can interpret these as 3 CDW domains, maybe 3 steps on the sample surface, displaying a different shear value when current is applied.

In order to make a quantitative comparison of the loss of CDW coherence in the longitudinal and transverse directions, one can calculate the variation of the standard deviations as a function of current using the following formulas

$$\langle x \rangle = \sum_{x,y} x \times \text{Intensity}(x,y)$$
$$\sigma_x^2 = \sum_{x,y} (x - \langle x \rangle)^2 \times \text{Intensity}(x,y)$$

and similarly for σ_y. In this expressions, x and y correspond respectively to the vertical and horizontal pixel number shown in figure 3.16 b) while Intensity(x,y) is the X-ray diffracted intensity measured at pixel (x,y). σ_x and σ_y were expressed in $\mathring{A}^{-1}$ using the sample-detector distance $D = 7.5$m, the pixel size $p = 55\mu$m and the X-ray wavelength $\lambda = 1.31\mathring{A}$. σ_x and σ_y are associated to the CDW coherence in the longitudinal and in the transverse directions. As an example, for CDW satellite peak with a gaussian shape (the one at 0mA in figure 3.16 b)), σ_x and σ_y correspond to the Full Width at Half Maximum (FWHM) which is proportional to the inverse of the CDW longitudinal and transverse coherence lengths.

The transverse width σ_y shown in figure 3.19 a) presents a clear evolution as expected from figure 3.18 b). However, σ_y starts to increase before the threshold I_{th} which was not clear in figure 3.18 b). It then reaches a maximum at 1mA. When I is further increased, the transverse width σ_y starts to decrease, hence the

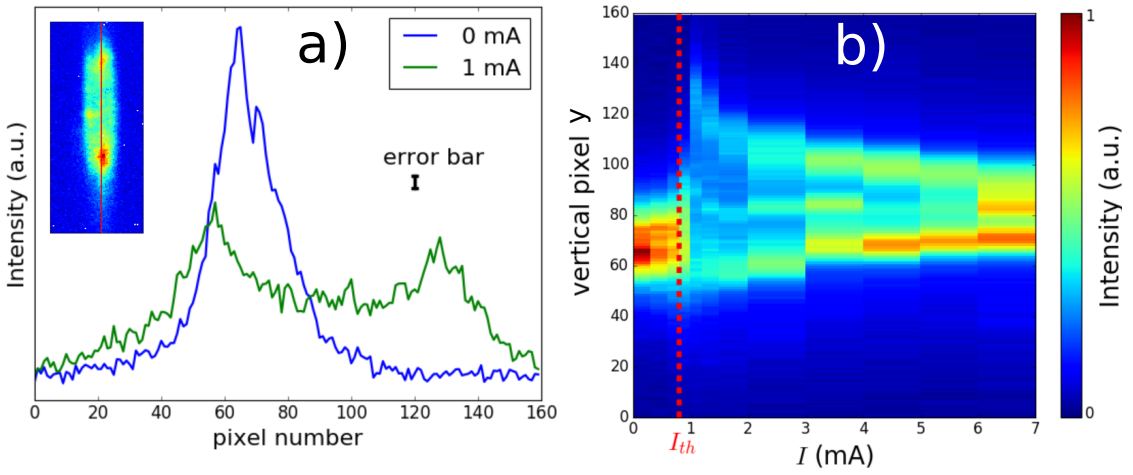

Figure 3.18: a)Transverse profile of the CDW satellite along the red line of the inset at 0 and 1 mA. Close to I_{th}, the peak is not gaussian anymore but presents sharp speckles, meaning a "breaking" of the phase coherence in the direction transverse to the CDW. b) Average of the detector images of figure 3.16 along x. An abrupt variation is observed at the threshold I_{th} which relaxes back at high current.

coherence between the 1D atomic chains of $NbSe_3$ is built back above I_{th}. Since having the solitons at the same longitudinal position on each atomic chains decreases the total energy, the sliding of these solitons helps the CDW to retrieve its transverse coherence at large currents. At high currents $I >> I_{th}$, σ_y reaches a plateau but is still larger than the one at zero current. On the other hand, the longitudinal width σ_x evolution is much smaller. Hence the coherence along the CDW longitudinal direction remains almost constant even close to the threshold current I_{th}. A small decrease of σ_x appears at the threshold (see figure 3.19 b)). The same behaviors of σ_x and σ_y was measured Danneau et al. [136]. However, the drop of σ_x at I_{th} could depends whether the measurement is performed close to the electrical contacts or not. In a paper by Requardt et al. [137], σ_x increases above the threshold for a measurement made 100μm from the contact. Since the CDW satellite shift above I_{th} is large near the contacts (see [137] figure 3) and almost zero at the center of the sample, we may expect σ_x to increase close to the contact and decrease in the center of the sample.

3.4.3 Longitudinal shift of the CDW satellite observed at LCLS

As a last result for this experiment, we observed a longitudinal shift of the CDW satellite reflection, similar to the one of figure 3.11. In figure 3.20 we show the average of the detector images of figure 3.16 integrated along y. A clear longitudinal shift of the peak is observed at the threshold I_{th}.

From this shift, one can calculate the CDW longitudinal component variation δq_x as function of the current. Calling the sample-detector distance D=7.5m, the pixel size p=55μm, the X-ray wavelength $\lambda = 1.31\mathring{A}$ and the Bragg's law angle at zero current θ=13.56°. We denote the variation of θ as $\delta\theta = \frac{p\delta x}{D}$ where δx is the

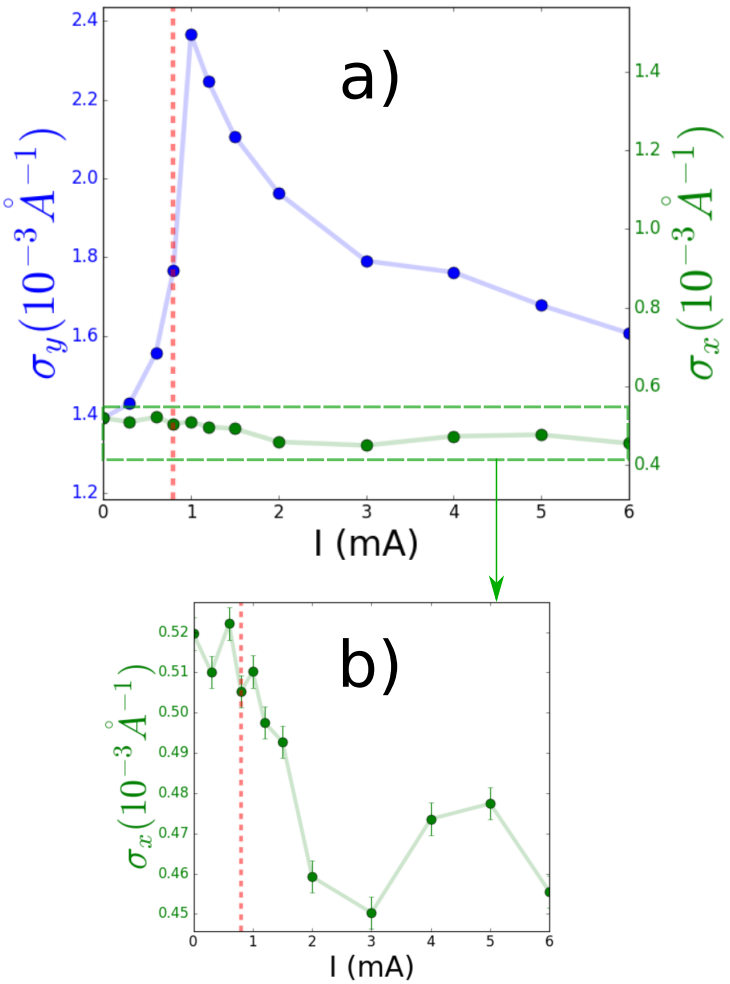

Figure 3.19: a)Standard deviation of the CDW satellite in the transverse (σ_y) and along the longitudinal CDW direction (σ_x). The scale is the same for both axes. A drastic increase of the transverse width σ_y is observed close to the threshold current followed by a continuous decrease for larger currents. In contrast, almost the evolution of the longitudinal width σ_x is much smaller. b) zoom on σ_x showing a decrease of the longitudinal width at I_{th}.

satellite shift on the detector in number of pixel. From Bragg's law $\frac{4\pi}{q}\sin(\theta) = \lambda$, and assuming the shift to be solely in the longitudinal direction, one gets

$$
\begin{aligned}
q + \delta q_x &= \frac{4\pi \sin(\theta + \delta\theta)}{\lambda} \\
q + \delta q_x &\approx \frac{4\pi \sin(\theta)}{\lambda} + \frac{4\pi \cos(\theta)}{\lambda}\delta\theta \\
\delta q_x(I) &= \frac{4\pi \cos(\theta) p}{\lambda D}\delta x(I)
\end{aligned}
$$

The result is shown in figure 3.21. Below the threshold current $I < I_{th}$, δq_x is almost constant. At $I = I_{th}$, a clear increase is observed which can be related to the presence of charged solitons inside the sample. Since each soliton correspond to a new CDW wavefront, the average CDW periods increases inducing this shift

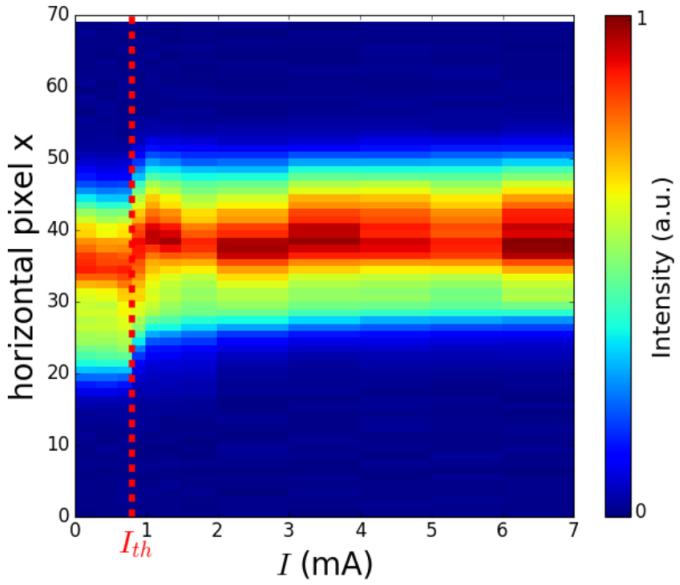

Figure 3.20: Average of the detector images of figure 3.16 along y, corresponding to the longitudinal CDW satellite direction. One can observe a shift at the threshold current I_{th}.

when $I \geq I_{th}$. At high current $I >> I_{th}$, the shift saturates to a constant value of $3.7{\times}10^{-4}\mathring{A}^{-1}$ in a similar way as the experiment from the literature displayed in figure 3.11 a). This shift is of the same order of magnitude as in [132].

To conclude, the coherent X-ray diffraction pattern of the CDW evolution under current shows that, close to the threshold current I_{th}, the CDW breaks in transverse. The soliton creation requires the CDW to be broken locally (meaning that the CDW amplitude drops to zero locally). Indeed, we observe in the bulk of the sample that applying current close to and larger to I_{th}, the elastic stress on the CDW system is too strong, inducing this "breaking" and a loss of transverse coherence measured by the speckle pattern which can only be observed using the highly coherent X-ray beam available at LCLS.

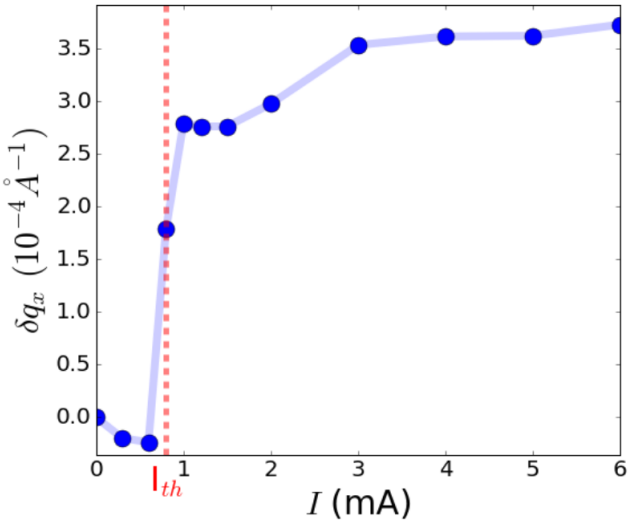

Figure 3.21: Variation of the longitudinal component δq_x of the CDW wavevector as a function of current. δq_x increases at the threshold from the presence of solitons in the sample. It then saturates at high currents to a constant value of the same order of magnitude as the one measured in [132]. Compare with figure 3.11 a).

Chapter 4

Micro-diffraction of $NbSe_3$ under currents: a strong surface pinning leading to a shear effect

This chapter presents the main experimental result of this thesis highlighting a CDW surface pinning by X-ray micro-Diffraction under applied current [138]. Surface pinning was already suspected from several resistivity measurements as a function of the sample cross section and distance between electrical contacts [139, 140, 141]. However, electrical measurements give a global response of the sample. Our micro-diffraction method is, in contrast, a local probe. Therefore, we were able to spatially resolve the transverse CDW shear and correlate this with a surface pinning effect.

The transverse pinning hypothesis was put forward by Feinberg and Friedel in their paper published in 1988 [113] in a phenomenological manner. In chapter 6, we will solve the CDW phase equation including surface pinning and show that the result is in agreement with several resistivity measurements.

In this chapter, we first present the experimental setup for micro-diffraction, then compare the CDW satellite (0,1,0)+$\vec{q}_{cdw}$ and Bragg (0,2,0) and show how one can calculate a local $\vec{q}_{cdw}$ as function of position on the sample, offering the opportunity to recover the CDW phase directly from the diffraction pattern, without the need of a coherent X-ray beam. We were expecting to see the longitudinal CDW deformation under current. Surprisingly, we observed that the evolution of the CDW is mainly dominated by shear deformations in the middle of the sample. Finally, we show how one can relate this to a surface pinning effect.

4.1 Experimental setup for micro-diffraction at the ID01 beamline of the ESRF

A specific preparation was made on the $NbSe_3$ sample used during this experiment. We wanted to compare a sliding CDW and a non-sliding one at the same time, from a single sample. Therefore, we used a special $NbSe_3$ sample, predesigned by a focused ion beam (FIB). A cut through the sample has been made before the experiment with an "L" shape. The sample is displayed in figure 4.1 a). Thus,

when applying current, only the sample's part above the FIB cut can contribute to the current. No current can cross the bottom part. Therefore, we can compare a static CDW from a CDW under current in the same sample. The lower part is not submitted to the current and the CDW should remain stable there. This is indeed what we have observed as will be shown in the following section. In contrast, the CDW in the upper part is strongly current dependent.

The sample preparation and the FIB cut has been done in Moscow by A.A. Sinchenko and A.P. Orlov ahead of the experiment. The sample size is 39μm $\times$ 3μm $\times$ 2.25mm, four gold contacts were evaporated as in figure 4.1 b) to perform in-situ 4 points current-voltage measurements and to observe the threshold current I_{th} during the diffraction experiment.

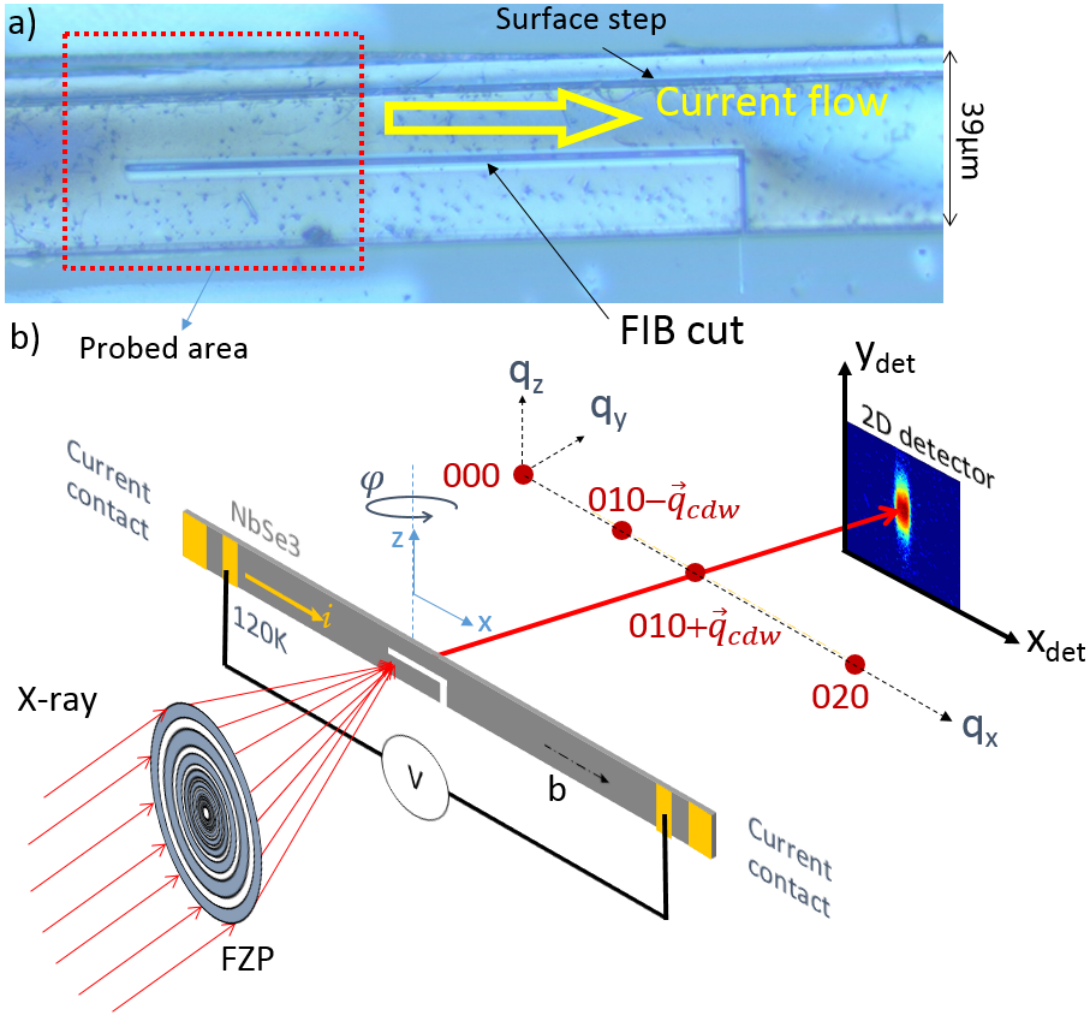

Figure 4.1: a) sample picture under optical microscope showing the FIB cut and the probed area in red. b) Sketch of the experimental setup (see the main text for more details).

In addition to this special sample preparation, we have used a new technique of diffraction that had just been put in place on the ID01 beamline of synchrotron ESRF. The main goal of this method is to be able to rapidly scan by diffraction, at wide angles, an area of about 100μm$\times$100μm by steps of 1μm with a 200$\times$300nm^2 focused X-ray beam. This technique was originally designed to map semiconductor

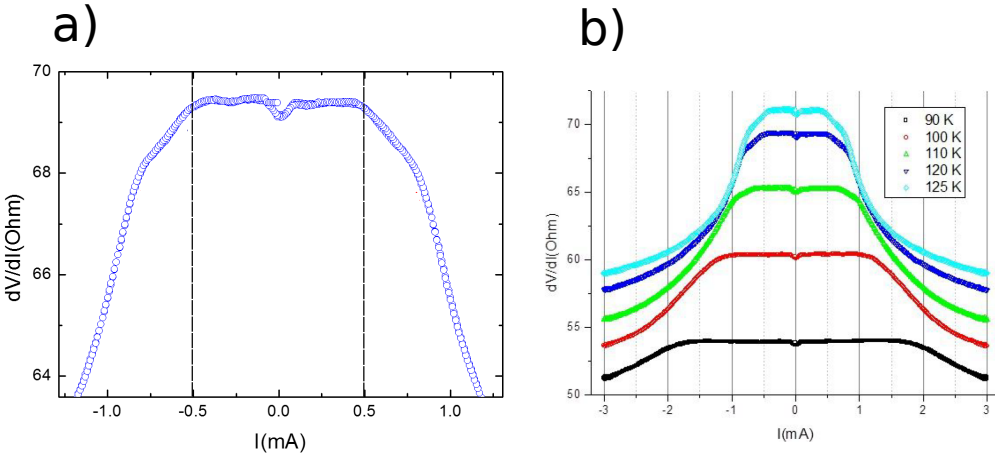

Figure 4.2: a) Differential resistivity as a function of current at 120K. One can see a drop at the threshold current I_{th} = 0.5 mA. b) Differential resistivity at several temperatures.

devices. We proposed to use it to study electronic crystals, in particular CDW systems.

To get high spatial resolution, a small X-ray beam is necessary. Here, we used a Fresnel Zone Plate (FZP) to focus it down to 200×300nm^2 at focal position. The FZP enables us to probe the CDW and the host crystal lattice locally since the beam spot is much smaller than the sample width.

The sample is placed in a cryostat and cooled down to 120K, below the 1^{st} CDW transition (see figure 1.10 c)). At this temperature, the CDW threshold current is I_{th} = 0.5 mA, see figure 4.2 a). The choice of the temperature is important. As we can see in figure 4.2 b), the resistivity curve is strongly temperature dependent. The threshold current doubles over 30K. We thus need to adjust the temperature to have a large enough threshold I_{th} in order to probe the CDW at I<I_{th} in the dV/dI plateau, but not too large to avoid sample heating by Joule effect.

A 8 keV X-ray beam is selected with a Si(111) monochromator and focused by the FZP on the sample, see figure 4.1 b). The diffracted beam is recorded using a fast-readout, photon-counting 2D pixel detector (Maxipix) made of a 516×516 array of 55μm square pixels, and placed at a distance of 70 cm from the sample. The FZP is mounted on a piezo-stage in order to map the sample surface accross the 90μm×50μm red area of figure 4.1 a) with a step size of 1μm. This mapping was done for several angles φ which defines the sample orientation regarding the X-ray beam, see figure 4.1 b).

The sample is placed on the setup with its b axis (corresponding to the CDW longitudinal direction) in the horizontal plane. Rocking curves are made for each position (11 points around the maximum of intensity by turning φ angle). We probe the $\vec{Q}_B$ = (0,2,0) Bragg reflection, associated to the atomic host lattice, and the CDW satellite $\vec{Q}_S$ = (0,1,0)+$\vec{q}_{cdw}$ where $\vec{q}_{cdw}$=(0,0.24,0) is directly associated to the CDW modulation (see figure 4.1 b)). We probe $\vec{Q}_S$ for different currents ranging from 0 to 1 mA and then inverting to -1 mA. The Bragg reflection $\vec{Q}_B$ was only measured for 0 and -1 mA to avoid going back and forth between Bragg and satellite and preventing a slight misalignment during the mechanical motion of the

diffractometer.

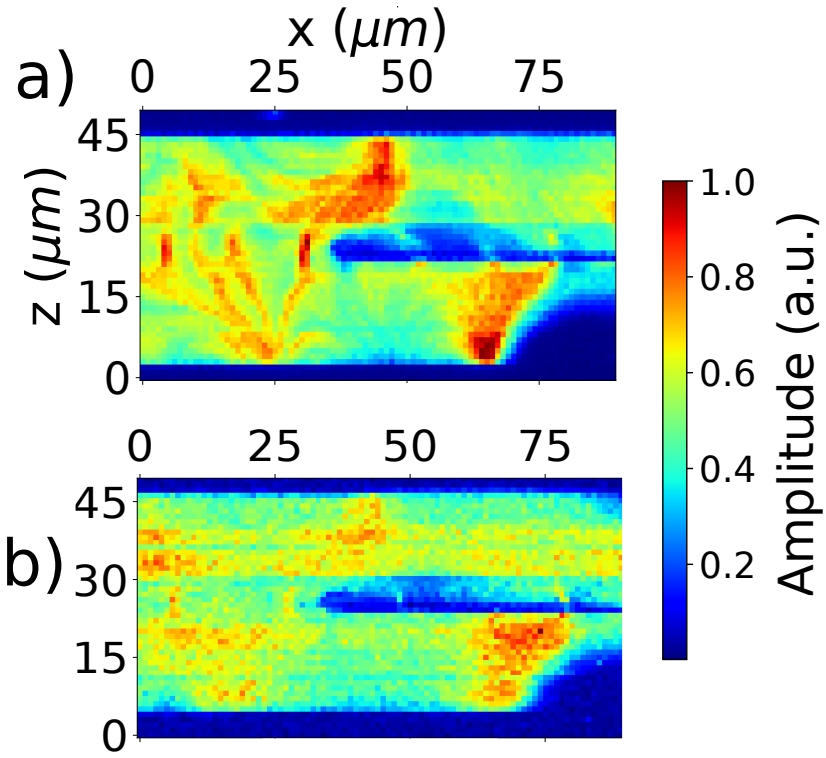

Figure 4.3: Integrated intensity of a) the (0,2,0) Bragg reflection and b) CDW satellite (0,1,0)+$\vec{q}_{cdw}$. The FIB cut and the sample's borders are clearly visible. The dark region in the lower right part is due to a main lattice deformation since it's visible on both the Bragg and satellite.

This specific measurement couples reciprocal and real spaces. We thus work in a 5D space, mixing the 3 coordinates of the Q wavevector and the 2D coordinates of the probed surface. Formally, what we measure is a 5D matrix of Intensity(φ, x, z, x_{det}, y_{det}) as function of :

- the sample orientation φ.
- the position (x,y) of the X-ray beam on the sample.
- the pixel position on the detector (x_{det}, y_{det}).

A lot of information can be obtained from this intensity matrix. The data set is very heavy and must be reduced somehow. This type of experiment was not feasible before because of a prohibitive step-by-step acquisition time. By using a continuous acquisition procedure and saving the images on a temporary buffer, considerable time has been saved, making it possible to have such maps (see [142] for more details). This technique has required us to implement a particular data analysis, much more complicated than in traditional diffraction experiments. These difficulties come, on the one hand, from the heaviness of the data storage (each map presented here is 100×100×20×3Mo = 0.6 Tera Bytes). On the other hand, the other difficulty is linked to the type of measurement itself. Indeed, these maps mixes the reciprocal space and the direct space and a considerable effort has to be made to extract from our set of data a relevant interpretation of the physical behavior of our system.

In the following, we present the relevant information that one can get from this type of local diffraction measurements. The first representation is the integrated intensity of each reflection (Bragg or satellite). It is obtained as function of position on the sample by summing over φ, x_{det} and y_{det} (see figure 4.3). This type of maps gives us information about the CDW amplitude as function of position (x,z) on the sample. With this picture, one can compare the Bragg in figure 4.3 a) and CDW satellite in b). The FIB line cut in the middle of the sample and the sample's borders are clearly visible, compare with red area in figure 4.1 a). A dark region in the lower right part of the sample can be seen as well. This region is on both the Bragg and satellite, therefore, it's a distortion from the main crystal lattice. We didn't go far enough in φ to obtain the full rocking curve in this region. Since, in the following, we will only consider the maximum of the rocking curve, this is not a problem.

As the CDW satellite intensity is related to the amplitude of the periodic distortion, seen from Eq2.9, which is itself related to the gap in the electronic dispersion, the map b) of figure 4.3 shows that the CDW is rather homogeneous in the sample.

4.2 Calculating the local wavevector in a transmission configuration

A much more interesting information can be extracted from our data set. One can have access to the local wavevector of the Bragg $\vec{Q}_B$(x,z) and CDW satellite $\vec{Q}_S$(x,y) as a function of position on the sample. Assuming small variations of the CDW under the beam spot area of $200\times300\text{nm}^2$, at each position, we measure a reflection at the given angles φ of the sample and δ, ν of the detector as in figure 4.4 a). δ and ν are the angles given by the detector center position plus a small variation given by the position (x_{det}, y_{det}) of the peak's centroid on the detector, knowing the sample-detector distance of 70cm.

The method used to obtain the angles (φ,δ,ν) of the peak maximum illustrated in figure 4.4 is the following. In b), for a given (x,z) position of the X-ray on the sample we measure the rocking curve depicted in c), which is the value of the sum of the intensity on a well-chosen region of interest of the detector for sample's orientation φ, formally $\sum_{x_{det},y_{det}}$Intensity(φ, x, z, x_{det}, y_{det}) for a given (x,z).

We choose the image taken at the nearest value of φ_{max} (the maximum of the rocking curve) and finally, for this specific φ, we calculate the centroid in (x_{det}, y_{det}) on the detector, thus giving the values of δ and ν for one position (x,z) on the sample.

Having the three angles and knowing the X-ray wavelength from the energy $\lambda = hc/E \approx 1.55\mathring{A}$, one can have the wavevector $\vec{Q}$ corresponding to the reflection. We know that $\vec{Q} = \vec{k}_f - \vec{k}_i$ where $\vec{k}_i$ and $\vec{k}_f$ are respectively the incident and scattered X-ray wavevector. These can be calculated in the sample frame from the angles (φ, δ, ν) using the sketch of figure 4.4 a)

$$\vec{k}_i = \frac{2\pi}{\lambda}\begin{pmatrix}-\sin(\varphi)\\ \cos(\varphi)\\ 0\end{pmatrix} ; \vec{k}_f = \frac{2\pi}{\lambda}\begin{pmatrix}\cos(\delta)\sin(\nu-\varphi)\\ \cos(\delta)\cos(\nu-\varphi)\\ \sin(\nu)\end{pmatrix} ; \vec{Q} = \vec{k}_f - \vec{k}_i \qquad (4.1)$$

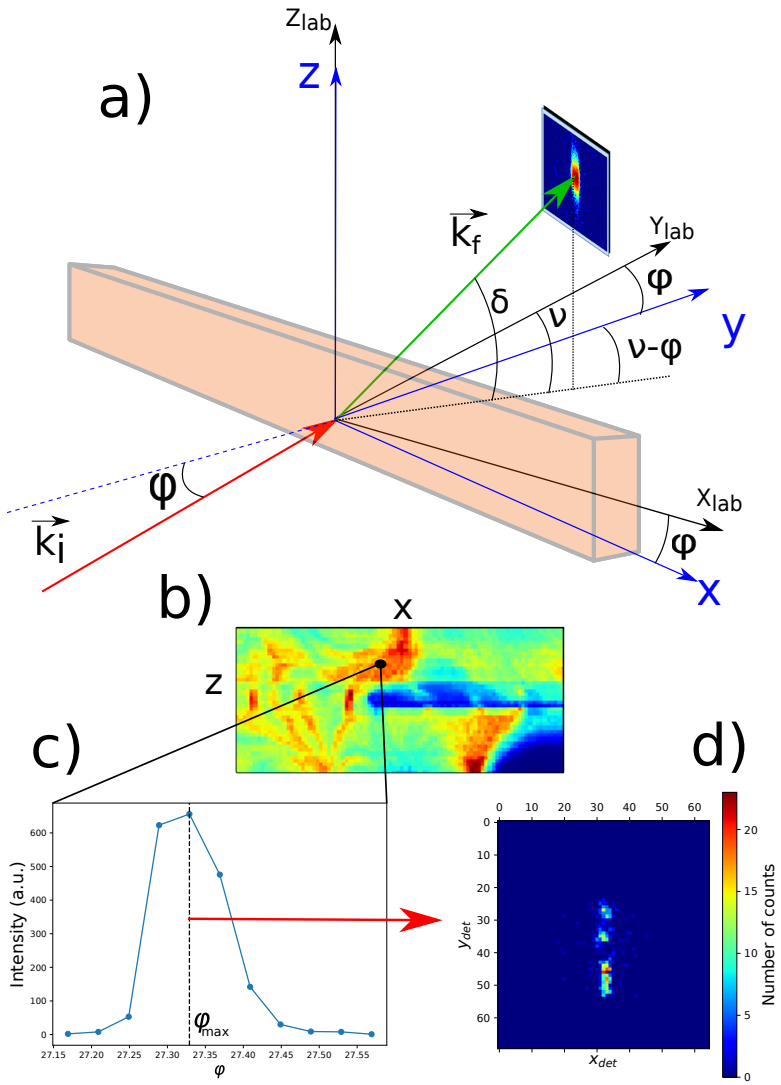

Figure 4.4: a) Sketch used to define the 3 following angles : φ of the sample and δ, ν of the detector. $\{x_{lab},y_{lab},z_{lab}\}$ and $\{x,y,z\}$ are respectively the laboratory and sample frames. b) At one pixel position (x,z) on the sample c) we choose the maximum of the rocking curve φ_{max}, and for this maximum d) we look at the centroid of the peak on the detector giving δ and ν.

Following this method, we got the dependence of wavevectors as a function of position (x,z) on the sample. We call these wavevectors respectively $\vec{Q}_B$ for the Bragg (0,2,0) and $\vec{Q}_S$ for the satellite (0,1,0)+$\vec{q}_{cdw}$ reflections. $\vec{Q}_B$ and $\vec{Q}_S$ are compared in figure 4.5 along with the corresponding integrated intensity similar to figure 4.3 but cut along z in order to have the map vertical boundaries to correspond to the sample's borders. The $\vec{Q}$ components are displayed along the (x,y,z) directions of figure 4.4 a), x corresponds to the sample b axis along which the CDW appears. This is visible in figure 4.5 where $Q_x >> Q_y$, Q_z as expected. In addition, we present in Appendix D a second method to obtain $\vec{Q}$ from the diffraction data and compare the results with the method used in this chapter, the difference is negligible, validating our data treatment.

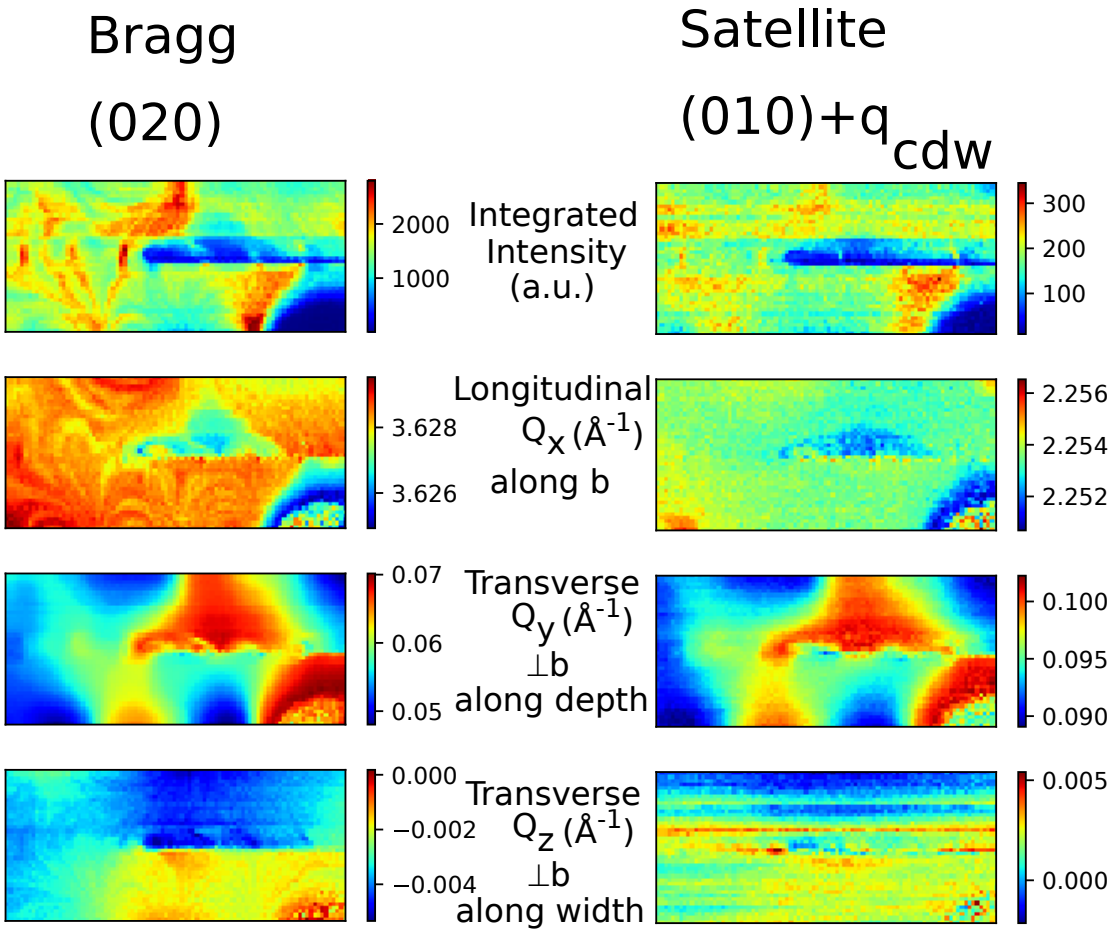

Figure 4.5: Comparison of the (0,2,0) Bragg and (0,1,0)+$\vec{q}_{cdw}$ CDW satellite integrated intensity and wavevector along the (x,y,z) directions of figure 4.4 at an applied current of -1mA. The CDW main direction is along x, corresponding to the b axis of $NbSe_3$.

The main difficulty is now to decorrelate crystal lattice distortions and CDW deformations under current. The Bragg wavevector $\vec{Q}_B$ can only vary with lattice distortions and won't be affected by a CDW modulation (only the reflection intensity could change). This feature can be seen from Eq2.9: for an incommensurate CDW, none of the terms in the Taylor expansion can move the Bragg position, up to any order.

On the other hand, the satellite wavevector $\vec{Q}_S$ is a sum of the Bragg (0,1,0) and the CDW wavevector $\vec{q}_{cdw}$. Hence, $\vec{Q}_S$ will vary with the CDW deformations but also with all crystal lattice distortions. Therefore, to check if an evolution of $\vec{Q}_S$ under applied current is only due to the CDW, one needs to check that the same feature is not visible on the Bragg $\vec{Q}_B$.

In order to remove the static crystal lattice distortion before applying current and visualize only the changes in the CDW wavevector, we subtract to each map the map of $\vec{Q}_S$ at 0.15mA. We couldn't do this with the map at 0mA since we did a small vertical shift in order to correct the sample position with respect to the X-ray beam for the next currents. This shift prevented us from correcting the other maps with the one at zero current. Since 0.15 mA is still below the threshold current I_{th} = 0.5mA, $\vec{Q}_S$(0.15mA) is very similar to $\vec{Q}_S$(0mA) hence the error made from this approximation is negligible and we can use these data for correction.

One can observe in figure 4.5 deformations of the host crystal lattice visible both on the Bragg (0,2,0) and on the satellite (0,1,0)+$\vec{q}_{cdw}$. These deformations are located near the sample borders and the FIB cut and are mainly along the Q_y axis (variations of the order of $\sim 10^{-2}\mathring{A}^{-1}$) while these variations are smaller along Q_x and Q_y ($\sim 10^{-3}\mathring{A}^{-1}$). The evolution of Q_y under current was dominated by these host lattice deformations but we could still observe a current dependence of Q_x and Q_z.

In the following, we mostly consider the variation of the CDW wavevector at a given applied current I defined by

$$\delta\vec{q}(I) \equiv \vec{Q}_S(I) - \vec{Q}_S(0.15\text{mA}) \tag{4.2}$$

4.3 Longitudinal CDW distortion under current

Now, we have to figure out what features are expected to be observed in this data set. First, the evolution of $\delta\vec{q}$ can be related to the CDW's phase ϕ by the following argument. The charge density in the CDW ground state, with no applied current, is given by $\rho(\vec{r}) = A\cos(2k_F x + \phi)$ where ϕ is a constant phase. When applying an external perturbation, both A and ϕ can become space dependent. This is the amplitudon and phason modes exposed in Appendix A. But the amplitudon mode costs more energy than the phason, hence we can assume A to be constant under current. This is confirmed by the fact that the intensity map of the satellite as in figure 4.3 did not change much with current. Therefore when applying current, the charge density is now considered to be $\rho(\vec{r}) = A\cos[2k_F x + \phi(\vec{r})]$.

Assume now that, for a given beam center position $\vec{r}_0 = (x_0,z_0)$ on the sample, the CDW phase varies much less than 2π inside the beam area of $200\times300\text{nm}^2$. One can Taylor expand this phase around $\vec{r}_0$ giving $\phi(\vec{r}$ around $\vec{r}_0) \approx \phi(\vec{r}_0) + (\vec{r}-\vec{r}_0).\vec{\nabla}\phi(\vec{r}_0)$. Inserting this into the charge density, we have

$$\rho(\vec{r} \text{ around } \vec{r}_0) \approx A\cos\left[\begin{pmatrix}2k_F+\phi_x(\vec{r}_0)\\ \phi_y(\vec{r}_0)\\ \phi_z(\vec{r}_0)\end{pmatrix}.\vec{r}+\phi(\vec{r}_0)-\vec{r}_0.\vec{\nabla}\phi(\vec{r}_0)\right] \tag{4.3}$$
$$= A\cos\left[2k_F x+\delta\vec{q}(\vec{r}_0).\vec{r}+\phi(\vec{r}_0)-\vec{r}_0.\delta\vec{q}(\vec{r}_0)\right]$$

recall that we are using the notation $\phi_x \equiv \frac{\partial\phi}{\partial x}$.

Going back to the derivation of Eq2.9, one can see that in a 3D case, the measured CDW wavevector $\vec{q}_{cdw}$ is directly what multiplies $\vec{r}$ in the charge density ρ. Reading directly from Eq4.3, the variation under current $\delta\vec{q}$ at a given pixel position (x_0,z_0) on the sample is directly (removing the subscripts 0 for clarity) [143, 142, 144]

$$\boxed{\delta\vec{q}(x,z) \equiv \begin{pmatrix}\delta q_x(x,z)\\ \delta q_y(x,z)\\ \delta q_z(x,z)\end{pmatrix} = \begin{pmatrix}\phi_x(x,z)\\ \phi_y(x,z)\\ \phi_z(x,z)\end{pmatrix}} \tag{4.4}$$

where the $2k_F$ disappeared since we subtracted the map at 0.15mA to get $\delta\vec{q}$, as said earlier.

Therefore, the wavevector variations observed as a function of current are directly related to the derivative of the CDW phase. But, since we know the CDW Lagrangian from the development described in Appendix A, we can predict the phase behavior in the presence of an electric field. Thus, in the following, we consider the free energy corresponding to the integral of the potential energy associated to ϕ in the Lagrangian density of EqA.11. Again, since the satellite intensity was stable under current, we can assume $\delta = 0$ in EqA.11. Lastly, we don't consider the impurity pinning term since it does not change qualitatively the phase behavior.

$$\mathcal{F}[\phi] \propto \int \left(\boxed{c_x^2\phi_x^2} + c_y^2\phi_y^2 + c_z^2\phi_z^2 + \boxed{\eta E x \phi_x}\right) d^3\vec{r} \tag{4.5}$$

Let's first consider the two terms in red and blue in Eq4.5. Under applied current, $E \neq 0$, a distortion of ϕ along x, $\phi_x \neq 0$, can lower the total energy according to the blue term. The sign of ϕ_x being related to the sign of the current. But the increase of ϕ_x has a limit since this costs energy through the red term. Therefore, by applying current, we expect to observe a finite value of ϕ_x which will minimize the total energy and this induces an evolution of δq_x with its sign reversing when one inverts the current.

As observed in figure 4.6 a), a crystal lattice distortion along x is visible on the Bragg (0,2,0). This impacts δq_x and the evolution we expect to see is partially lost in the noise when displaying the full map. Despite this, we can still extract an information from this map with the following method. We chose two regions where the Bragg was not too distorted. One above the line cut, the red rectangle in figure 4.6 a) and b), where the current is flowing. And one below the cut, the blue rectangle, where no current can flow, thus we expect no variation under current in this region. Then, we average the values of δq_x in these two regions for each current, and display the results in figure 4.6 c).

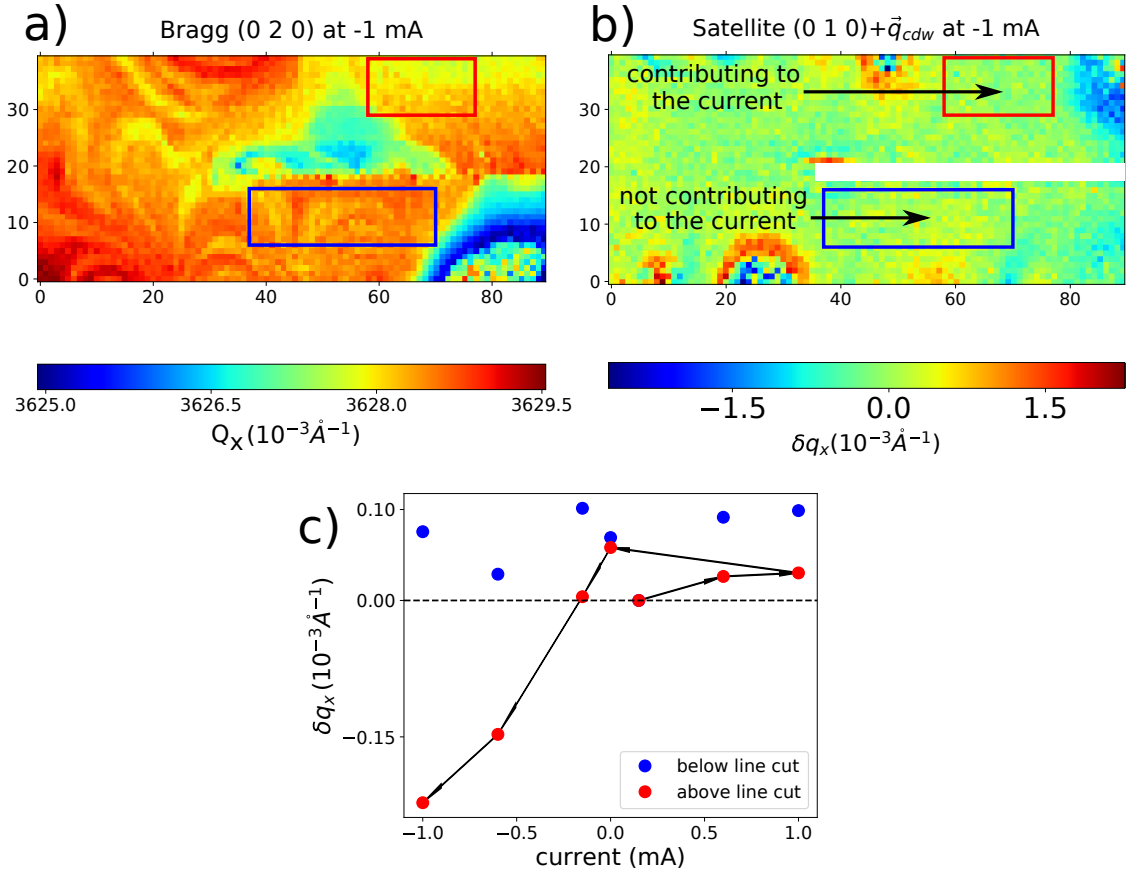

Figure 4.6: a) Map of the Q_x component of the (0,2,0) Bragg. b) Same for the CDW satellite after subtracting the map at 0.15mA. c) Average of b) in the red and blue rectangles, where the Bragg is not too distorted, as a function of current. The sign changes only in the region above the line cut where the current is flowing.

One can notice the change of the δq_x sign above the line cut when the current changes sign while δq_x doesn't display any specific feature under the line, as predicted. Hence, we can confirm a distortion of the phase in the CDW direction when applying a current, the order of magnitude ($10^{-4}\AA^{-1}$) being similar to the one observed in [132]. What's more, with the micro-diffration technique and the FIB cut, we are able to compare two CDW regions, one with current and one without it at the same time and on the same sample.

4.4 Transverse CDW deformation under current

The main and most interesting evolution observed when applying current is not the one of the longitudinal componentδq_x. In this section, we show the main result of this thesis which can only be observed in diffraction with a X-ray beam size smaller than the sample width, that wasn't the case in previous studies [132]. The relevant information is on the transverse component of the (0,1,0)+$\vec{q}_{cdw}$ satellite reflection $Q_{S,z}$, which corresponds to a shear deformation of the CDW. The results for four values of the current are displayed in figure 4.7 which are the z component of the

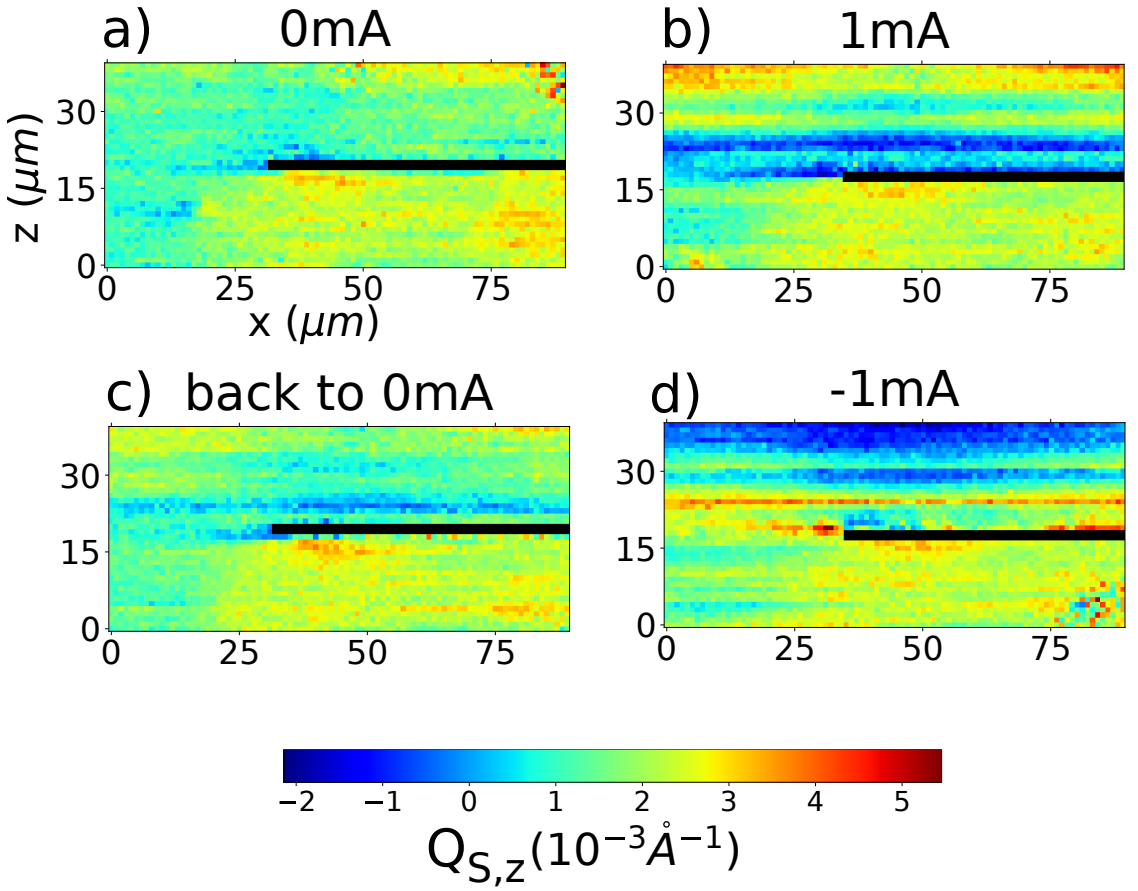

Figure 4.7: Map of the transverse z component of the CDW satellite $\vec{Q}_S$ at four different currents applied in the following order : 0 → 1 → back to 0 → -1 mA. See the main text for details.

satellite maps of figure 4.5 for different currents. We want to insist on the fact that we did not remove the map at 0.15mA yet in figure 4.7, this is not $\delta\vec{q}$ but directly the raw $\vec{Q}_S$, still, we observe a clear evolution with current.

We did the measurement at eight currents in the following order { 0; 0.15; 0.6; 1; back to 0; -0.15; -0.6; -1} in mA units. In figure 4.7, we show the maps at only four currents. The one at 0mA displays some deformations which are similar to what is observed on the Bragg shown in figure 4.5 on the Q_z row. The FIB cut induces a small deformation of the sample part below the cut with respect to the one above it.

The important feature is the evolution when current is applied. Comparing the maps at 0 and 1mA of figure 4.7 a) and b), we observe a strong evolution of the CDW above the line cut, where current flows. Going back to 0mA in c), the deformation is reduced but does not entirely disappear, maps a) and c) are a bit different. This hysteresis effect is well known in the literature, it was observed several times in resistivity measurements [131, 130, 129, 145, 146]. Finally, going to negative current at -1mA in d), the deformation is back but this time opposite to the one at +1mA in b). In contrast, no clear evolution is visible in the sample part below the FIB cut, where no current is flowing.

This evolution is not a thermal effect due to sample heating by the current since, if it was the case, the map at 1 and -1mA would be similar. On the contrary, these 2 maps are the inverse of one another in the part above the FIB cut. Furthermore, since we measured both the Bragg $\vec{Q}_B$ = (0,2,0) and the CDW satellite $\vec{Q}_S$ = (0,1,0)+$\vec{q}_{cdw}$ at -1mA, it is straightforward to extract the CDW wavevector for this current since $\vec{Q}_S - \frac{1}{2}\vec{Q}_B = \vec{q}_{cdw}$ as shown in figure 4.8.

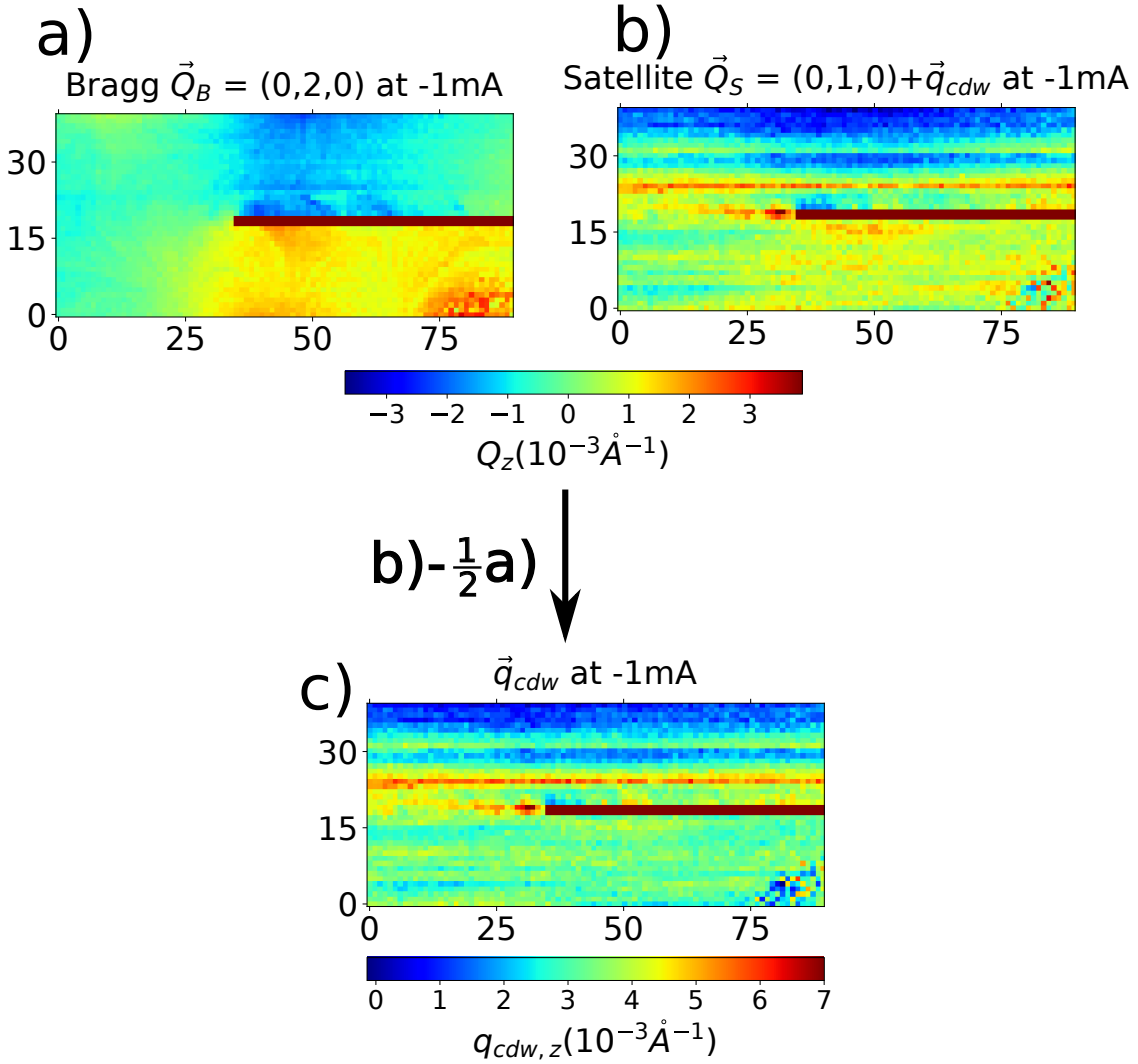

Figure 4.8: a) Bragg reflection $\vec{Q}_B$= (0,2,0) at -1mA. b) CDW satellite $\vec{Q}_S$ = (0,1,0)+$\vec{q}_{cdw}$ at -1mA. c) CDW wavevector calculated from a) and b) using $\vec{Q}_S - \frac{1}{2}\vec{Q}_B = \vec{q}_{cdw}$.

From this figure, one can see that the deformation of $\vec{Q}_S$ in b) is not visible on $\vec{Q}_B$ in a). Furthermore, calculating $\vec{q}_{cdw}$ in c), the difference in the map above and below the FIB cut is even more evident. All this shows that the observed transverse evolution is due to a CDW shear deformation under applied current, and can't be explained by Joule effect or a crystal lattice damaged by the X-ray beam.

4.5 CDW phase reconstruction and observation of surface pinning

Now the question is, why does the CDW displays this transverse distortion when one applies current. Remember from Eq4.4 that the CDW evolution along z is directly the phase derivative ϕ_z for which we can predict the behavior from the free energy expression. Coming back to Eq4.5, we had

$$\mathcal{F}[\phi] \propto \int \left(\boxed{c_x^2 \phi_x^2} + c_y^2 \phi_y^2 + \boxed{c_z^2 \phi_z^2} + \boxed{\eta E x \phi_x} \right) d^3\vec{r} \tag{4.6}$$

For the longitudinal distortion ϕ_x, the blue term favors a $\phi_x \neq 0$ while the red one favors a small $|\phi_x|$ hence the competition between these two terms will induces a finite ϕ_x when one applies currents.

But the only term including ϕ_z in Eq4.6 is the green one which favors a small $|\phi_z|$! Nothing else could induce a non zero ϕ_z since transverse deformation doesn't couple to the electric field. One can explain this by the following argument, at T = 0K, the total number of electrons condensed in the CDW is proportional to the wavevector modulus $|\vec{q}_{cdw}| = 2k_F$ at equilibrium. Under external perturbation, $\vec{q}_{cdw}$ modulus becomes

$$|\vec{q}_{cdw}| = \left| \begin{pmatrix} 2k_F + \phi_x \\ \phi_y \\ \phi_z \end{pmatrix} \right| = \sqrt{(2k_F + \phi_x)^2 + \phi_y^2 + \phi_z^2} \approx 2k_F + \phi_x + \mathcal{O}(\phi_x^2, \phi_y^2, \phi_z^2)$$

Thus, up to first order, a longitudinal deformation ($\phi_x \neq 0$) changes the total number of electrons condensated in the CDW while a shear distortion ($\phi_z \neq 0$) leaves this number constant. Hence, there is no term similar to the blue one of Eq4.6 for ϕ_z which could favor a shear deformation. But we **do** see a shear, thus our description is still missing an element to fully describe the CDW behavior under currents.

This additional element is still not obvious from the maps of figure4.7. Since the distortion is almost constant in the x direction above the FIB cut, we first average these maps along x see figure 4.9 a). The difference between below and above the FIB cut is even more drastic in this plot. Below the line $\langle \phi_z \rangle_x = \langle \delta q_z \rangle_x = \frac{1}{N_x} \sum_x \delta q_z$ (where N_x is the number of pixels along x) is almost current-independent and constant while above it, where current is flowing, the CDW transverse component is strongly deformed. What's more, the slope of $\langle \phi_z \rangle_x$ clearly depends on the sign of the applied electric field (compare red (+1mA) and blue (-1mA) curves in b)).

The curves are not smooth over the whole sample width but present sharp variations, specially near $z \sim 30\mu$m. This feature could be due to a step on the sample surface, visible from the optical microscope image of figure 4.1.

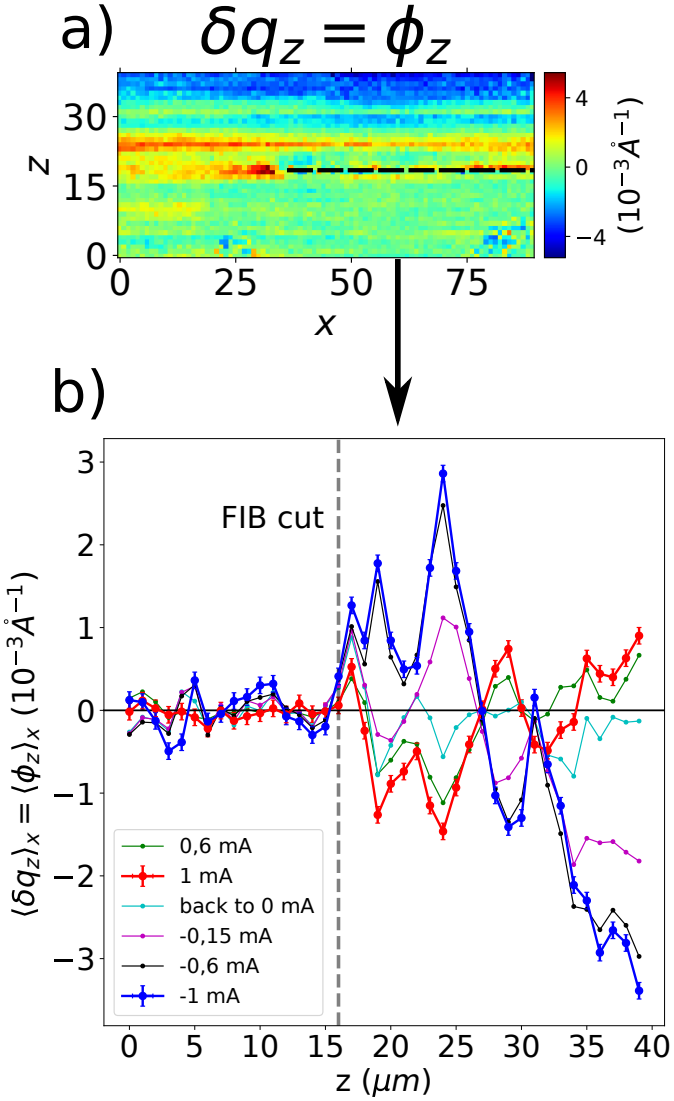

Figure 4.9: a) map of δq_z at -1 mA, the FIB cut is schematized by the dashed line. We average this map along x, and this at each current to produce the plot of $\langle \delta q_z \rangle_x = \frac{1}{N_x} \sum_x \delta q_z$ in b). Error bars are shown only for the blue and red curves at ± 1mA for clarity. The current sequence is in the same order as the legend from top to bottom.

Still, figure 4.9 doesn't give a clear answer to the question of why this transverse deformation occurs. Hence, we go even further in data treatment using an approximation. Comparing figure 4.6 c) and 4.9 b), one sees that $\delta q_x = \phi_x \sim 10^{-4}\mathring{A}^{-1}$ while $\delta q_z = \phi_z \sim 10^{-3}\mathring{A}^{-1}$. Hence, we simplify our problem by saying that $\phi(\vec{r}) \approx \phi(z)$.

With this in mind, we can have the CDW phase profile by integrating figure 4.9 along z in the following way :

$$\begin{cases} \langle \phi(z) \rangle_x = \sum_{z'<z} \langle \phi_z(z') \rangle_x dz' = \sum_{z'<z} \langle \delta q_z(z') \rangle_x dz' & (4.7) \\ \langle \phi(0) \rangle_x = 0 & (4.8) \\ \langle \phi(\text{upper border of the FIB cut}) \rangle_x = 0 & (4.9) \end{cases}$$

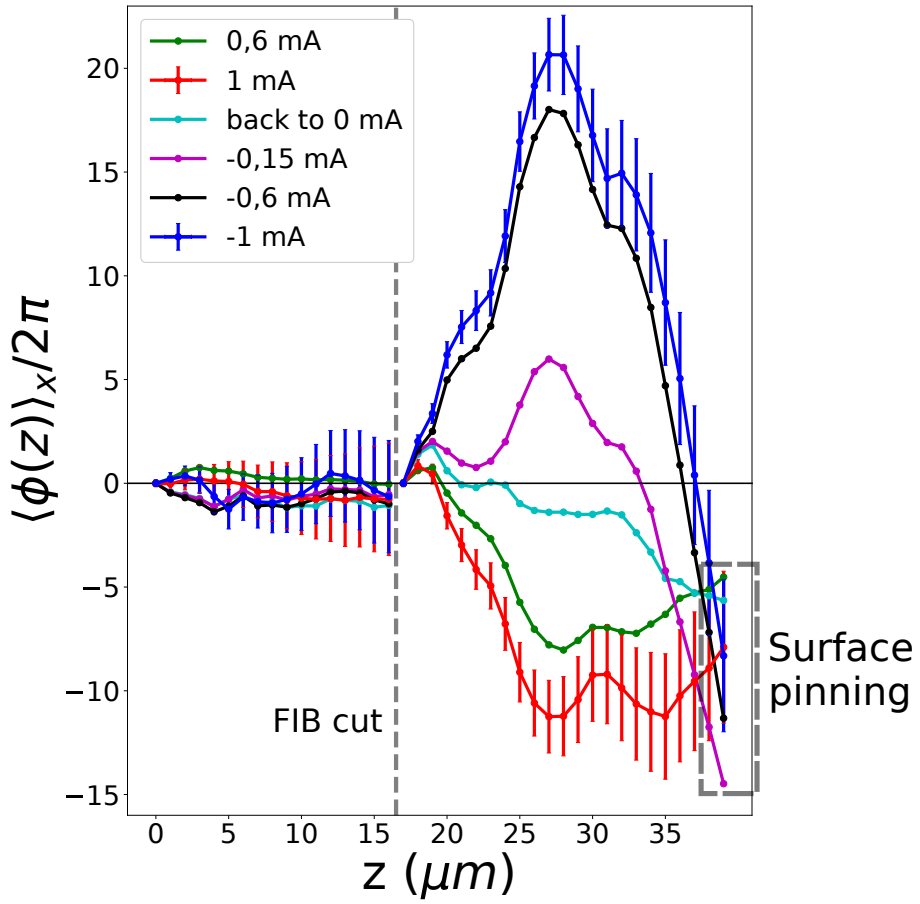

Figure 4.10: $\langle\phi(z)\rangle_x$ reconstruction from the $\langle\delta q_z\rangle_x = \langle\phi_z(z)\rangle_x$ data of figure 4.9. The phase is almost constant for all currents in the region below the FIB cut while it displays strong variations above the cut where current is flowing. We choose to pin the phase at the cut in Eq4.9 while no condition is imposed at the upper sample border z=39. Yet ϕ reaches the same value (-10±5)× 2π there for every current, indicating surface pinning. Error bars are shown only for the curves at ±1mA for clarity.

Eq4.7 is the discrete integral formula (since we have discrete data) with $dz' = 1\mu$m the vertical pixel size of map a) in figure 4.9. Eq4.8 and 4.9 are both boundaries conditions. As the FIB cut goes through the whole sample, there's no reason for continuity between the lower and upper border of the cut. We arbitrary choose the value 0 for both boundaries, but one can choose any other constant, and can even be different between Eq4.8 and 4.9, this doesn't affect the final interpretation.

The resulting ϕ is shown in figure 4.10 for each currents. Due to the integration, the curves are smoother than in figure 4.9. Again, we observe, as expected, a constant ϕ below the FIB cut since no current is flowing in this region.

For the error bars on the blue and red curves, since $\langle\phi(z)\rangle_x$ from Eq4.7 is a sum of several $\langle\phi_z\rangle_x$, the error bar on $\langle\phi\rangle_x$ is the sum of those on $\langle\phi_z\rangle_x$, formally $\text{error}[\langle\phi(z)\rangle_x] = \sum_{z'<z}\text{error}[\langle\phi_z(z')\rangle_x]$. Thus the error is growing as z increases as shown in figure 4.10 for $0 < z < 17$. But since there's no continuity at the FIB cut, the error is zero again at the upper border of the cut in $z = 18$ and starts growing again for $18 < z < 39$.

In the region above the cut, where the current is flowing, the phase presents a bell shaped curve with an orientation that depends on the sign of the current as one could already guess from figure 4.9. But the most interesting feature is located at the upper border of the sample $z = 39\mu$m. Remember from Eq4.9 that we arbitrary constraint pinning of the CDW phase at the FIB cut, which may or may not be true a priori. But we don't impose any constraint on the upper border of the sample at $z = 39\mu$m. Still, $\langle\phi(z)\rangle_x$ converges toward the same value of (-10±5)× 2π for every current. Hence, we can conclude that ϕ is pinned at the sample boundaries and this also validates our condition at the FIB cut Eq4.9.

CDW pinning at the sample surfaces was already suspected from several resistivity measurements showing finite size effects [139, 140, 141], see [34] for a complete review. But these are macroscopic probes. The X-ray micro-diffraction experiment presented here enables us to spatially resolve the CDW deformation and to conclude that, indeed, the CDW is pinned at the sample borders, this feature becoming apparent when one applies current to the system.

X-ray diffraction topography [147] and X-ray micro-diffraction [148] experiments performed on $NbSe_3$ showed a transverse deformation near surface steps. The authors of [148] did not conclude to a shear near the edges of the sample but they only looked at the maximum angle of the rocking curve corresponding to our φ angle of figure 4.4 c). Hence, the only observed one direction of $\vec{Q}_S$ in reciprocal space. Here, by seperating each component of the CDW satellite and comparing with the Bragg (0,2,0) we are able to definitely observe this shear effect near the edges.

4.6 CDW phase reconstruction in 2D as a function of current

In order to visualize this shear deformation as function of the 2D position (x,z) and understand what's happening near the end of the FIB cut, we made a reconstruction similar to Eq4.7, 4.8 and 4.9 but now starting from the upper border of the sample at z=39 :

$$\begin{cases} \phi(x, z = \text{upper border} = 39) = 0 & (4.10) \\ \phi(x, z) = -\sum_{z'>z} \phi_z(x, z')dz' & (4.11) \\ \phi(x \geq \text{end of the cut} = 36, z = \text{lower border of the cut} = 17) = 0 & (4.12) \end{cases}$$

Note the differences between Eq4.10, 4.11, 4.12 and Eq4.7, 4.8, 4.9. First, no average is performed along the longitudinal x direction in order to keep full 2D information. Then, we start the integration from the upper border of the sample since we are mostly interested in the sample part where current is flowing, above the FIB cut. We fix the phase at this border since we already saw that there is surface pinning. Then, since there's no reason for continuity between the regions above and below the cut, we fix ϕ at the lower part of this cut and we check that the condition 4.12 gives a continuous phase between parts $x \geq 36$ and $x < 36$ for most of the current values.

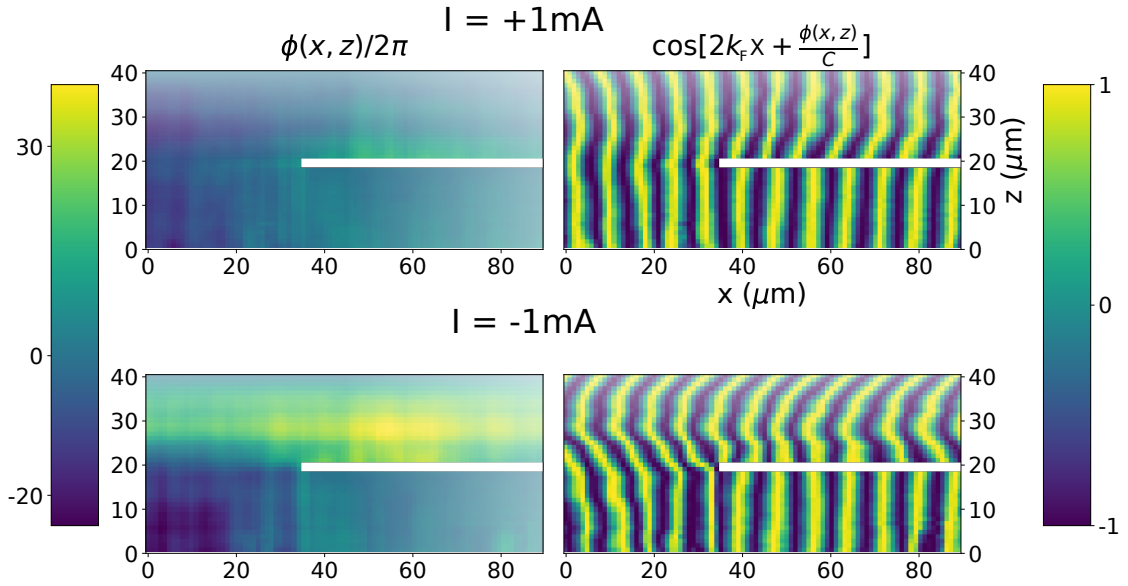

Figure 4.11: Left : Phase reconstruction using Eq4.10, 4.11 and 4.12. Right : schematic view of the CDW where the wavelength is considerably increased by manually adjusting the value of $2k_F$ in order to separate the wavefronts (in reality $\frac{2\pi}{2k_F} = 14\mathring{A}$). We divided the phase by an arbitrary constant $C = 210$ in order to properly visualize the wavefronts deformations under current.

This reconstruction is shown in the left part of figure 4.11 for the extremum current values ±1 mA along with a schematic reconstruction of the CDW $\rho(x, y) = \cos[2k_F x + \phi(x, z)]$ on the right part. One can clearly observe the wavefronts deformations in a direction depending on the sign of the applied electric field. The deformation is stronger in the map at -1mA. This could be due to the fact that the FIB cut is much closer to the left electrical contact (300 μm) than to the right one ($\sim$ 1mm), and since it has a 'L-shape' form (see figure 4.1), we don't expect a symmetric behavior between currents coming from the right or from the left electrical contact.

As already seen in figure 4.10, the CDW region below the FIB cut {x≥36, z≤17}, doesn't change much as a function of current since it is not flowing in this part of the sample. But the shear deformation above the cut is spreading toward the lower part of the sample after the end of the FIB line in the region {x<36, z≤17}.

The reconstruction of $\rho(x, y)$ for each current is displayed in figure 4.12. The shear effect is visible for every currents, not only at the extremum ±1mA. In addition, from the map at 'back to 0mA', one can see the hysteresis effect since the wavefronts are still deformed from the former positive current even though none is applied while measuring this particular map. The sharp variation of ρ near the end of the FIB cut ($x = 36$,z<17) highlighted by the red rectangle in figure 4.12 is only an artifact coming from our condition Eq4.12 which, for some currents, can lead to an artificial jump between $\phi(x = 35, z \leq 17)$ and $\phi(x = 36, z \leq 17)$. Again, in those maps, the CDW wavelength is increased to visualize the wavefronts (in reality $\lambda = \frac{2\pi}{2k_F} = 14\mathring{A}$) and ϕ is divided by a constant C=210, otherwise the distortion would be to big to be correctly visualized. Since the reference map was taken at

0.15mA, the corresponding map has straight wavefronts since $\phi = 0$ everywhere in it.

In conclusion, the micro-diffraction technique available at ID01 beamline of the ESRF synchrotron allowed us to spatially resolve the CDW deformation when current is applied. In addition, the 'L-shaped' FIB cut allowed us to compare directly on the same sample and at the same time a CDW region where current is flowing and one with no current, thus avoiding any experimental artifact coming from the comparison of 2 different samples at 2 different times.

The spatial resolution allowed us to observe a shear effect coming from a longitudinal distortion under electric field in figure 4.6 which was already observed in [132], and a surface pinning effect in figure 4.10 which was speculated from several resistivity measurements [139, 140, 141] but never actually observed and space resolved. This type of experiment could be performed in other CDW materials like o-TaS_3 showing a size dependent effect [139], or the typical blue bronze $K_{0.3}MoO_3$ to check if this phenomenon is specific to $NbSe_3$ or if it is something more general and common to several CDW systems. Finally, this measurement could be performed closer to the electrical contacts since the authors of [132] showed that the longitudinal distortion is stronger there, hence we would expect a stronger shear effect than the one observed here.

The shear was clearly visualized in our sample since its transverse size (39μm) is much smaller than its longitudinal one (2.25mm). This is a particular property of $NbSe_3$ which crystallizes faster along the b axis. This isn't the case in $K_{0.3}MoO_3$ for example, thus those samples would need a peculiar preparation to be able to observe the shear effect using X-ray micro-diffraction technique.

As a final remark, we must explain why the surface pinning effect was observed on δq_z but not on δq_y. This is due to the transmission configuration of our X-ray diffraction experiment. Since the X-ray beam go through the whole sample width along y, we can only measure $\delta\vec{q}$ averaged along y. This unavoidable averaging process prevents us from measuring any surface pinning effect along y. As can be observed on figure 4.9, a deformation from surface pinning is positive at one border and negative at the other (in figure 4.9 b) at -1mA δq_z is positive near the FIB cut $z = 17$ and negative at the upper sample border $z = 39$), hence the average is always zero for any current. Therefore, one can't observe surface pinning effects in the direction of the incident X-ray beam in a transmission configuration.

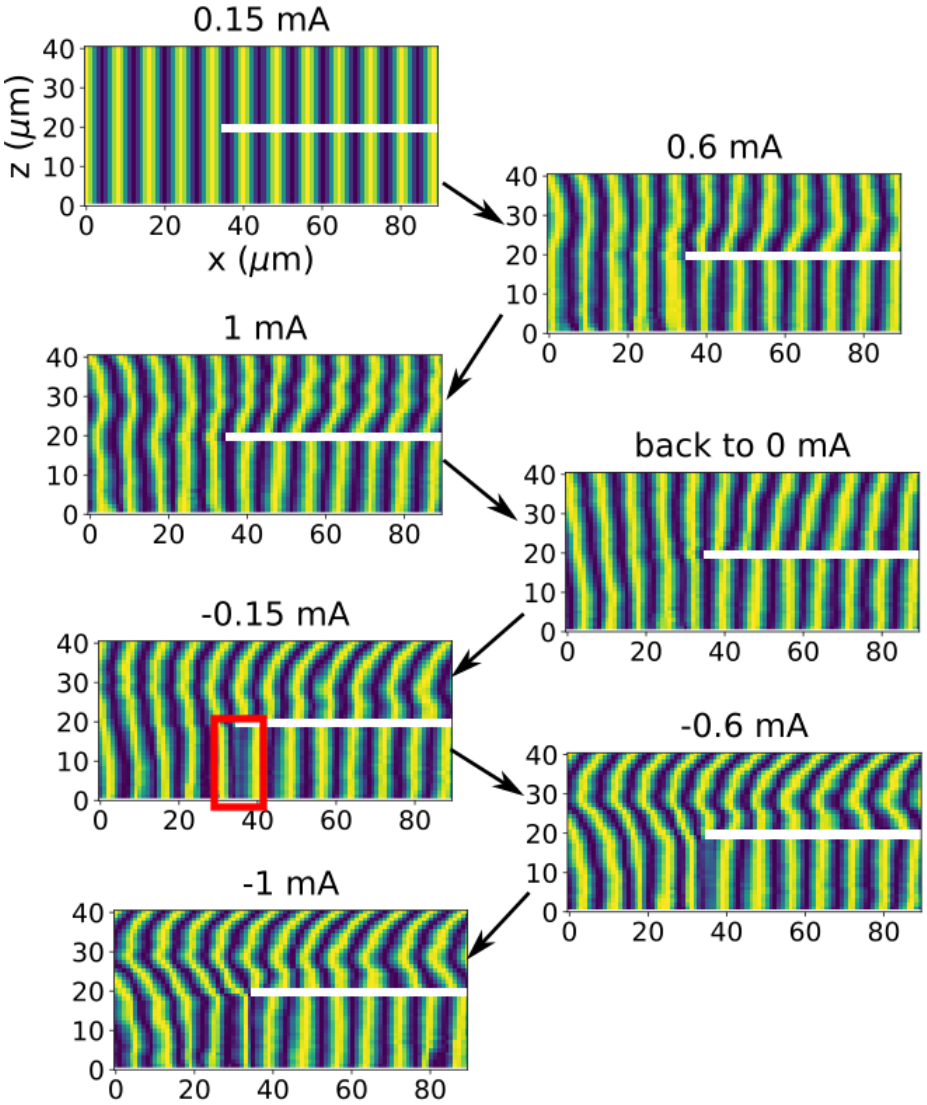

Figure 4.12: Reconstruction of the CDW charge density $\rho(x, z)$ for every applied current in the following order and in mA units { 0.15, 0.6, 1, back to 0, -0.15, -0.6, -1 } represented by the dark arrows. The red rectangle on the map at -0.15mA shows the position of the sharp ρ variation artifact coming from our condition Eq4.12

Chapter 5

Micro-diffraction of $TbTe_3$ under currents

In this chapter, we expose the results obtained on the TbTe3 system at the ID01 beamline of the ESRF synchrotron. The X-ray micro-diffraction method used here is similar to the one explained in chapter 4 for NbSe3. The aim of the experiment is to compare two sliding CDW systems which differ by their dimensionality. $TbTe_3$ is indeed a quasi-2D sample composed of several layers of Te atoms in which the CDW appears at 336K, which allowed us to work at room temperature, making this experiment easier than for $NbSe_3$. Furthermore, the $NbSe_3$ sample was thin enough (3μm) to perform diffraction in transmission geometry, as the X-ray beam goes through the sample thickness without being entirely absorbed (see figure 4.1 b)). In the case of $TbTe_3$, the sample has a larger thickness which prevented us from working in a transmission configuration. Therefore, the diffracted peaks were measured in reflection geometry as shown in figure 5.1.

The structure for this chapter is the following: first, since the setup configuration is different from the one of chapter 4, we explain how one can calculate the CDW wavevector from the diffracted CDW satellite. Then we present, some results on the CDW rotation under applied currents. Finally, we show that sample irradiation by the X-ray beam can create strong pinning centers for the CDW phase inducing a local compression-expansion.

5.1 Wavevector calculation in a reflection configuration

Since the setup is now in the reflection configuration, the calculation becomes more complicated, involving an additional angle. In chapter 4, the sample orientation was given by a single angle φ, while the CDW satellite $\vec{Q}_s = (1,15,0)+\vec{q}_{cdw}$ in $TbTe_3$ can only be reached by rotating the sample in two different directions, using two angles φ and η as shown in figure 5.1 where the sample is depicted as a dark-orange rectangular parallelepiped. The method is the following. Expressing the diffracted wavevector $\vec{Q} = \vec{k}_f - \vec{k}_i$ and the unit vectors $\vec{u}_a$, $\vec{u}_b$ and $\vec{u}_c$ along the crystal axis $\vec{a}$, $\vec{b}$ and $\vec{c}$ of $TbTe_3$ in the laboratory frame, one can get $\vec{Q}$ in the sample frame by

computing the scalar products of $\vec{Q}$ with $\vec{u}_a$, $\vec{u}_b$ and $\vec{u}_c$.

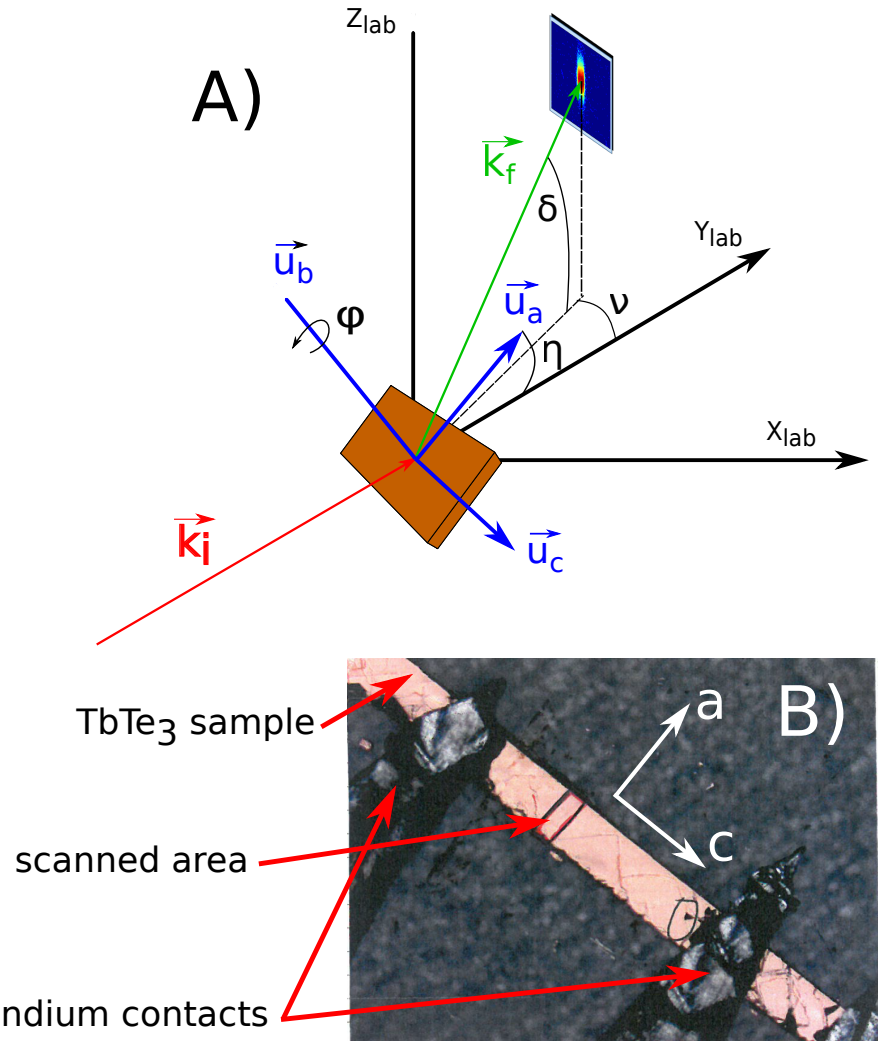

Figure 5.1: A) Sketch of the experimental setup with the notation used for the wavevector calculation described in the main text. $\vec{u}_a$, $\vec{u}_b$ and $\vec{u}_c$ are the unit vectors along the crystal axis $\vec{a}$, $\vec{b}$ and $\vec{c}$. $\vec{k}_i$ and $\vec{k}_f$ are respectively the incident and diffracted X-ray beams. The sample orientation is given by φ and η while the measured beam on the detector is given by ν and δ. B) Picture of the sample using an optical microscope. The 1^{st} scan was performed inside the area highlighted by the black rectangle.

In the lab frame $\{x_{lab}, y_{lab}, z_{lab}\}$, the diffracted wavevector is simply given by

$$\vec{Q} = \vec{k}_f - \vec{k}_i = \frac{2\pi}{\lambda_X} \begin{pmatrix} -\cos(\delta)\sin(\nu) \\ \cos(\delta)\cos(\nu) - 1 \\ \sin(\delta) \end{pmatrix}$$

where λ_X is the X-rays wavelength given by $\lambda_X = \frac{hc}{E}$ where E =7.4keV is the selected energy for this experiment. Now, we need the expression of the rotated sample frame expressed in the lab frame $\{\vec{u}_a(\eta,\varphi), \vec{u}_b(\eta,\varphi), \vec{u}_c(\eta,\varphi)\}$. For $\eta = \nu = 0$,

we have

$$\vec{u}_a(0,0) = \begin{pmatrix} 0 \\ 1 \\ 0 \end{pmatrix} \; ; \; \vec{u}_b(0,0) = \begin{pmatrix} 0 \\ 0 \\ 1 \end{pmatrix} \; ; \; \vec{u}_c(0,0) = \begin{pmatrix} 1 \\ 0 \\ 0 \end{pmatrix}$$

Next, η is a rotation around the x_{lab} axis while φ is a rotation around z_{lab} **only when η is null** since the motor of the φ rotation is fixed on the motor of the *eta* rotation. The corresponding rotation matrices are

$$R_\eta = \begin{pmatrix} 1 & 0 & 0 \\ 0 & \cos(\eta) & -\sin(\eta) \\ 0 & \sin(\eta) & \cos(\eta) \end{pmatrix} \; ; \; R_\varphi = \begin{pmatrix} \cos(\varphi) & \sin(\varphi) & 0 \\ -\sin(\varphi) & \cos(\varphi) & 0 \\ 0 & 0 & 1 \end{pmatrix}$$

and the sample frame vectors becomes $\vec{u}_j(\eta,\varphi) = R_\eta R_\varphi \vec{u}_j(0,0)$ where $j = a, b, c$. One has to be careful with the order of the two rotational matrix! The η rotation is always around the x_{lab} axis but the φ is only around z_{lab} for $\eta = 0$ as displayed in figure 5.1. Hence one needs to make the φ rotation first in the calculation $\vec{u}_j(\eta,\varphi)$. Finally the diffracted wavevector in the sample frame becomes

$$\vec{Q}_{\text{sample frame}} = \begin{pmatrix} \vec{Q}.\vec{u}_a(\eta,\varphi) \\ \vec{Q}.\vec{u}_b(\eta,\varphi) \\ \vec{Q}.\vec{u}_c(\eta,\varphi) \end{pmatrix}$$

Figure 5.2 displays $\vec{Q}_{\text{sample frame}}$ for the CDW satellite wavevector $\vec{Q}_s$ = (1,15,0) $+\vec{q}_{cdw}$ along the three crystal axis. Without current, we expect the CDW wavevector q_{cdw} to be along the c crystal axis [13]. We divided the components by a^*, b^* and c^* respectively to check the validity of our procedure, their value at room temperature were taken from [13]. As intended, since the CDW wavevector is along c at equilibrium, $\vec{Q}_{\text{sample frame}} \approx (1.01, 14.97, 0.22)$ is close to (1,15,0)$+\vec{q}_{cdw}$. The small discrepancy is probably due to a small and unavoidable error on the sample orientation when placed on the diffractometer. In figure 5.1, we assumed $\vec{u}_b$ to be perfectly vertical at $\eta, \varphi = 0$, but this is never exactly the case experimentally. One could add a shift in η, φ and χ where χ turns around the y_{lab} axis to correct this small error, but since we are mostly interested in the variations of the CDW wavevector, this little discrepancy isn't of importance for the following.

5.2 Rotation of the CDW under current observed from a shear effect

We perform a first micro-diffraction measurement of the CDW satellite $\vec{Q}_s$ = (1,15,0) + $\vec{q}_{cdw}$ in the middle of the sample, far from the electrical contacts. We measure, as in chapter 4, the 5D Intensity matrix $I(\eta, x, z, x_{det}, y_{det})$ as function of the sample orientation angle η, the position x, z of the X-ray micro-beam on the sample and the pixel coordinate on the detector x_{det}, y_{det}, the angles φ, δ and ν of figure 5.1 being held fixed.

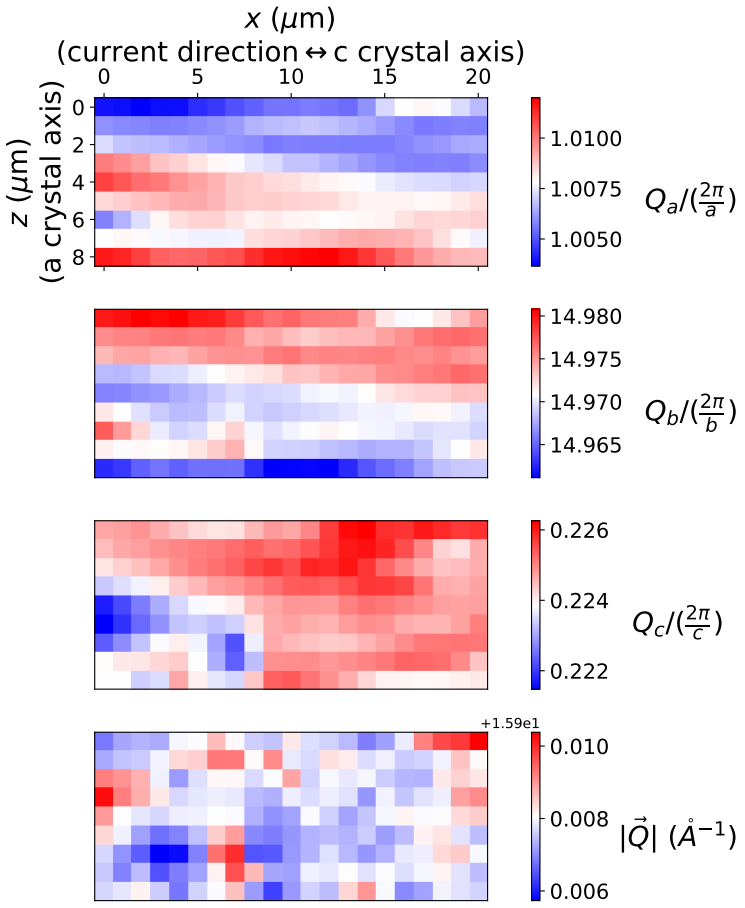

Figure 5.2: Example of maps of the 3 coordinates and module of the $\vec{Q}_s$ = (1,15,0)+$\vec{q}_{cdw}$ (where $\vec{q}_{cdw}$ is the CDW wavevector) satellite reflection associated to the CDW in TbTe3 obtained with our method. The 3 maps cover an 8μm×20μm area in the central part of the sample. q_{cdw} is along the c axis. The x and z directions correspond respectively to the c and a crystal axis, while b is perpendicular to the sample surface. The averaged wavevector is found to be equal to (1.01,14.97,0.22), very close to the expected (1,15,0)+q_{cdw}, validating our procedure.

In order to choose a homogeneous region on the sample, we present in figure 5.3 $\sum_{\eta,x_{det},y_{det}} I(\eta, x, z, x_{det}, y_{det})$ which correspond to the satellite integrated intensity as function of position on the sample.

In chapter 4, the $NbSe_3$ sample displayed a small width of 39μm, hence we were able to observe both edges in the maps of figure 4.3. In contrast, the $TbTe_3$ sample presented here has a much larger width (few mm), not allowing to scan both edges within the same map because the piezo motor range cannot exceed 100μm×100μm. What's more, one map takes half an hour to be measured, therefore we were also limited by a time constraint (only one week available to perform the experiment in synchrotron). We scan the middle of the sample (see figure 5.3), far from the edges and from the electrical contacts to measure the CDW evolution in the bulk of the sample. The white regions in the upper and lower parts of the map do not correspond to the sample borders but are areas where the satellite was out of the

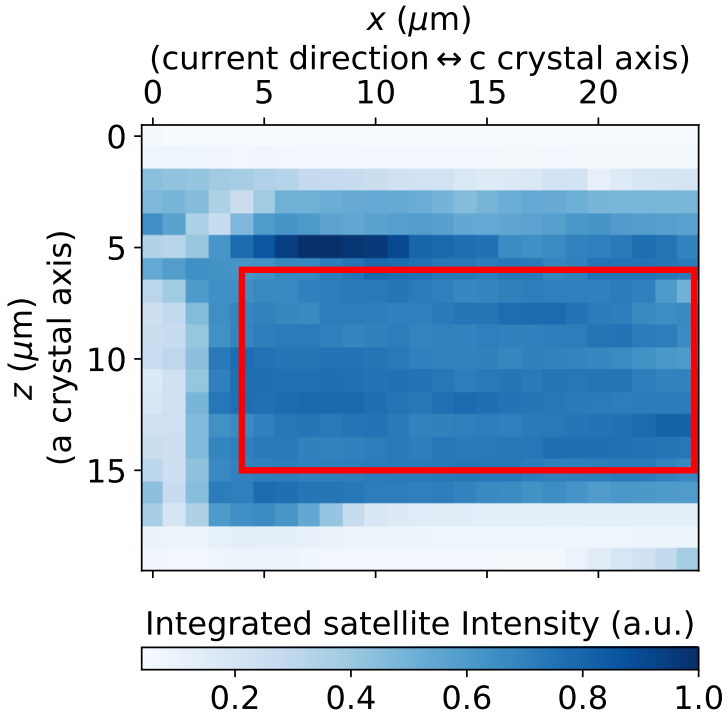

Figure 5.3: CDW satellite intensity as function of position on the sample. The white regions in the upper and lower parts are not the sample edges but regions where the satellite reflection was out of the detector and φ range. The red rectangle indicates the selected homogeneous region of 20μm×8μm.

detector and φ range. These perturbed areas have been discarded and only the homogeneous region included in the red rectangle in figure 5.3 has been treated. The satellite wavevector components at zero current are presented in figure 5.2. We performed the same maps with currents from 9mA to 50mA, then to -40mA and coming back to 0mA. A sharp threshold was observed at $I_{th} = 11mA$ in the differential resistivity $\frac{dV}{dI}$ curve shown in figure 5.5 a).

In the following, as with $NbSe_3$, we have compared the maps at a given current with the one without current in order to remove intrinsic deformations coming from the host crystal lattice. We subtract to each map the last one at 0 mA and study the vector $\delta\vec{q}(I) = \vec{Q}_s(I) - \vec{Q}_s(0\text{ mA})$. The resulting maps at the extremum currents ±40 mA are shown in figure 5.4 along the a,b and c crystal axis of $TbTe_3$.

The CDW wavevector $\vec{q}_{cdw}$ at equilibrium (when no current is applied) is along c [13]. As in $NbSe_3$ [132], one could expect a longitudinal distortion under applied electric field. But, as shown in figure 3.11 b), this longitudinal deformation is almost zero in the middle of the sample and is only strong near the contacts. Here, the experiment was probably done too far from the electrical contacts to be able to distinguish it. Therefore, the longitudinal strain is not visible in the maps δq_c in figure 5.4 e) and f).

On the other hand, δq_a and δq_b strongly evolve (figure 5.4 a), b), c) and d)). Moreover, this variation shows an inversion between positive and negative currents

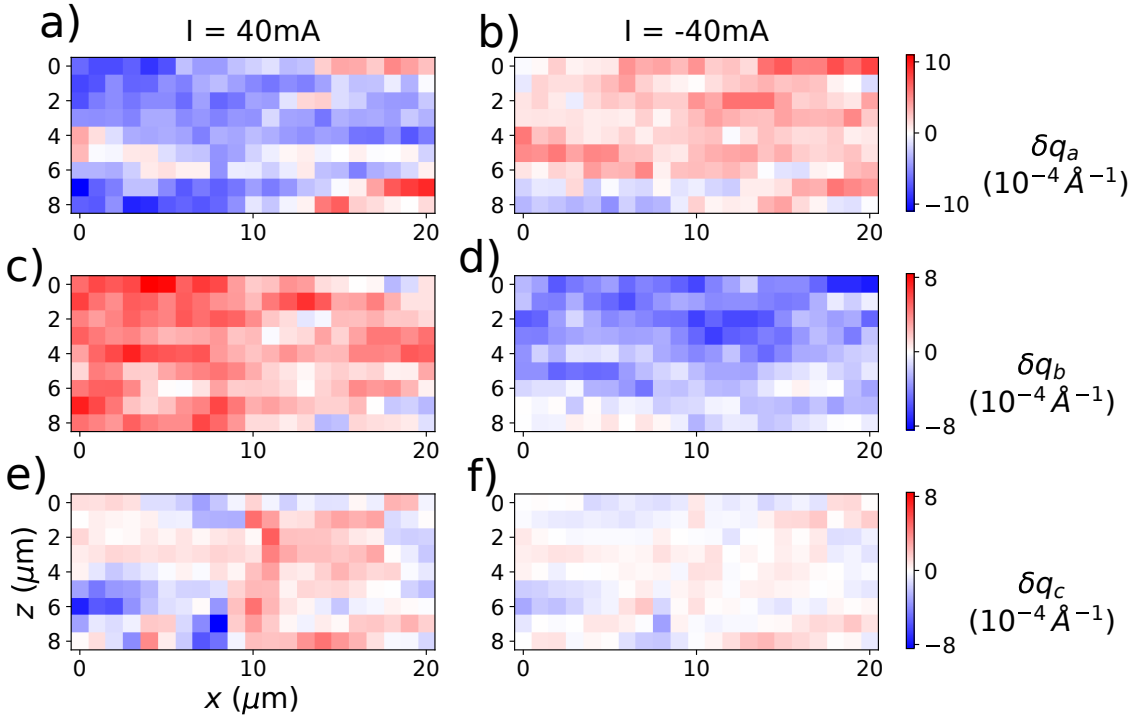

Figure 5.4: Maps of $\delta\vec{q}(I) = \vec{Q}_s(I) - \vec{Q}_s(0\ mA)$ along the a,b and c crystal axis of $TbTe_3$, corresponding to the CDW wavevector variations at the two strongest applied currents ± 40 mA.

illustrating a physical deformation of the CDW under currents. As for $NbSe_3$, sample heating by joule effect cannot be responsible for these variations, since positive and negative currents should, in that case, induce similar deformations. Furthermore, the evolution along the a axis in a) and b) is the inverse of the one along b in c) and d).

In order to have a better understanding of this evolution, we compute the averaged wavevector variation $\langle\delta\vec{q}\rangle = \frac{1}{N_x}\frac{1}{N_z}\sum_{x,z}\delta\vec{q}(x,z)$ where N_x and N_z are the numbers of pixels along x and z respectively. The result is presented in figure 5.5 along the a,b and c axis of $TbTe_3$. As anticipated from the maps of δq_c in figure 5.4 e) and f), no longitudinal strain is observed as a function of current on the average $\langle\delta q_c\rangle$ shown in green in figure 5.5.

On the other hand, an unambiguous evolution on $\langle\delta q_a\rangle$ and $\langle\delta q_b\rangle$ is observed, corresponding to a CDW shear effect, with a continuous variation depending on the sign of the current. Furthermore, the variations along the two transverse directions are inversed. At positive currents, δq_a decreases while δq_b increases. This indicates that the CDW is not compressed by the electric field but only rotates. This observation was pointed out in [149] from a fixed X-ray beam, with a 10μm$\times 10\mu$m spot size. Nevertheless, this is the first experiment observing this effect at the micrometer scale over a large area that shows that q_{cdw} rotates in the two transverse directions.

Regarding the hysteresis effect, while the macroscopic resistivity curve (figure 5.5 a)) shows a negligible hysteresis (only an asymmetry between positive and negative currents), a hysteresis is observed by diffraction. This is visible on $\langle\delta q_a\rangle$ and $\langle\delta q_b\rangle$ (figure 5.5 b)). The hysteresis effect observed in several CDW materials such as

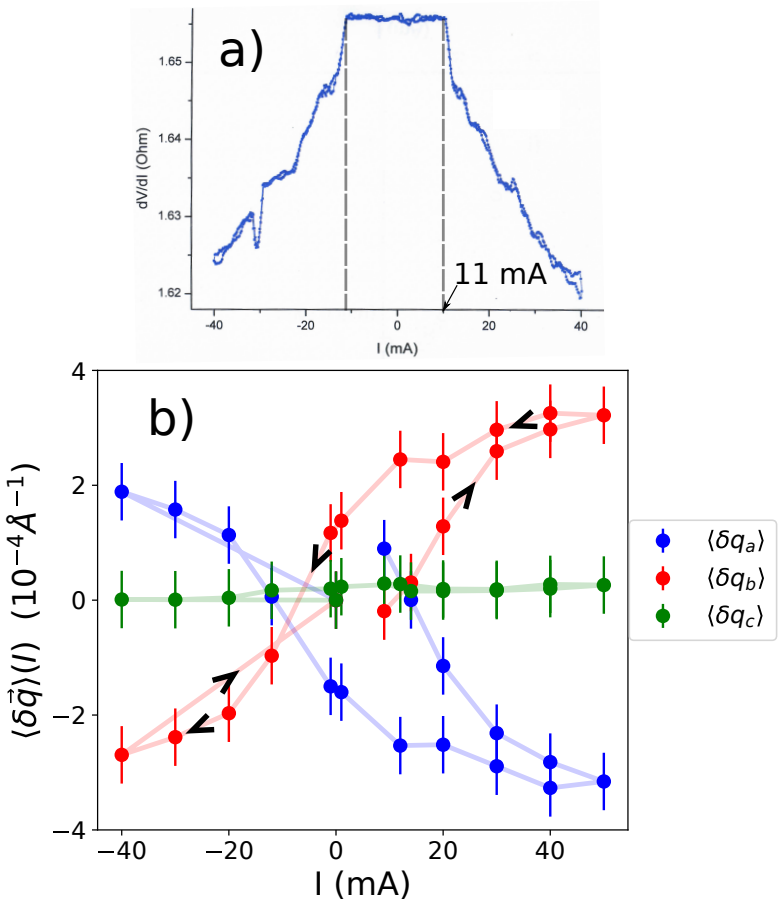

Figure 5.5: a) differential resistivity as a function of applied current showing a sharp threshold at I_{th} = 11 mA. b) Average of the $\delta\vec{q}$ components maps in obtained for each current corresponding to the variation of the CDW satellite wavevector along each $TbTe_3$ crystal axis. The longitudinal strain $\langle\delta q_c\rangle$ remains negligible. The observed variations of $\langle\delta q_a\rangle$ and $\langle\delta q_b\rangle$ correspond to a transverse deformation, the appearance of a CDW shear under current.

$NbSe_3$ (see chapter 4), $K_{0.3}MoO_3$ [129] or TaS_3 [130] is also relevant for the quasi-2D material $TbTe_3$.

Note that in figure 5.5 b), the hysteresis loops are not centered around zero, $\langle\delta q_b\rangle$ is slightly shifted toward positive values while $\langle\delta q_a\rangle$ is shifted toward negative ones. One can observe that the maximum value at high currents presents an asymmetry between positive and negative currents, for example $\langle\delta q_a\rangle(40mA) \approx -3 \neq -\langle\delta q_a\rangle(-40mA) \approx -2$. This feature probably comes from the fact that, prior to the experiment, we applied a negative current to the sample, hence "blocking" it in the lower (upper) part of the hysteresis loop of $\langle\delta q_b\rangle$ ($\langle\delta q_a\rangle$): a memory effect observed by diffraction.

5.2.1 Evolution of the CDW modulus under current

In order to confirm that the observed evolution is indeed a rotation and not a compression or expansion of the CDW, we compute the evolution of the CDW wavevec-

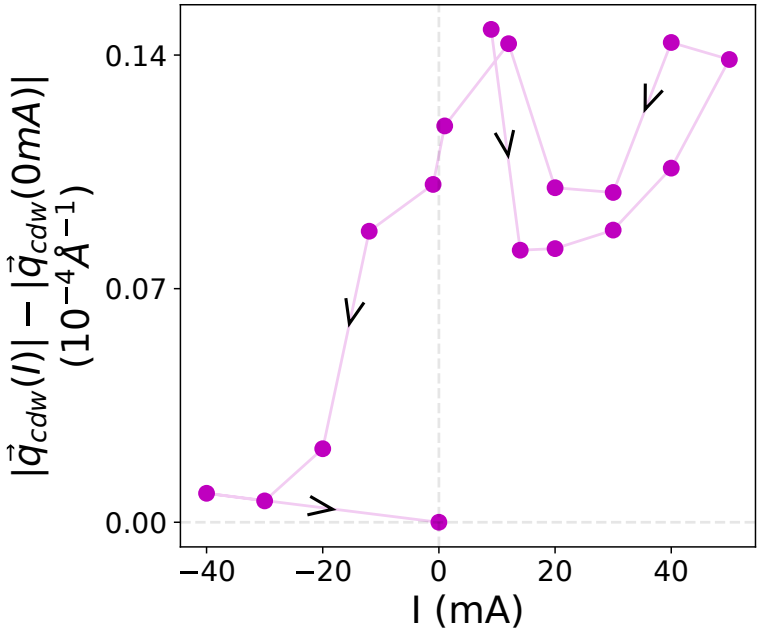

Figure 5.6: Variation of the CDW wavevector modulus as function of current. The maximum variation is one order of magnitude smaller than those of $\langle \delta q_b \rangle$ and $\langle \delta q_a \rangle$. Thus, the CDW deformation under current is essentially a rotation of the CDW wavefronts. Note that the error bars value (not shown here since they are too large) is $0.5 \times 10^{-4}\mathring{A}^{-1}$ (same as figure 5.5), hence they are larger than the modulus variations ($\sim 0.1 \times 10^{-4}\mathring{A}^{-1}$)

tor modulus $|\vec{q}_{cdw}|$ assuming that the Bragg (1 15 0) doesn't evolve under current. Since we don't measure directly $\vec{q}_{cdw}$ but the CDW satellite $\vec{Q}_s = (1\ 15{,}0) + \vec{q}_{cdw}$, we need to pay attention to the calculation. $\vec{q}_{cdw}$ at zero current is along the c axis in $TbTe_3$, and since we measure a satellite close to the (1,15,0) Bragg peak which has no component along c, we have $\vec{q}_{cdw}(0\text{ mA}) = \left[\vec{Q}_s(0\text{ mA}).\vec{u}_c\right]\vec{u}_c = Q_{s,0,c}\vec{u}_c$ where we defined $Q_{s,0,c} \equiv \vec{Q}_s(0\text{ mA}).\vec{u}_c$ to simplify the notation. When current is applied, the CDW wavevector becomes $\vec{q}_{cdw}(I) = \vec{q}_{cdw}(0\text{ mA}) + \delta\vec{q}$ with $\delta\vec{q} = \vec{Q}_s(I) - \vec{Q}_s(0\text{ mA})$ as previously defined. From these expressions one finds the variation of $|\vec{q}_{cdw}|$ to be

$$\begin{aligned}
\delta\,|\vec{q}_{cdw}(I)| &\equiv |\vec{q}_{cdw}(I)| - |\vec{q}_{cdw}(0\text{ mA})| \\
&= |\vec{q}_{cdw}(0\text{ mA}) + \delta\vec{q}| - |\vec{q}_{cdw}(0\text{ mA})| \\
&= |Q_{s,0,c}\vec{u}_c + \delta\vec{q}| - |Q_{s,0,c}\vec{u}_c| \\
&= \sqrt{Q_{s,0,c}^2 + |\delta\vec{q}|^2 + Q_{s,0,c} \times \underbrace{(\delta\vec{q}.\vec{u}_c)}_{\delta q_c}} - |Q_{s,0,c}|
\end{aligned}$$

This expression seems cumbersome but is easily computed, the result is shown in figure 5.6. No current dependence is observed on the modulus evolution. More importantly, the variations of the modulus in figure 5.6 are one order of magnitude smaller ($\sim 10^{-5}\mathring{A}^{-1}$) from those of $\langle \vec{q}_a \rangle$ and $\langle \vec{q}_b \rangle$ presented in figure 5.5 ($\sim 10^{-4}\mathring{A}^{-1}$). We can thus conclude that CDW deformation in the bulk of $TbTe_3$ under currents

is essentially a rotation of the CDW wavefronts without a measurable compression or expansion of the CDW lattice.

5.2.2 Not a strictly rigid CDW rotation

As a last point, looking at the maps of $\delta\vec{q}$ as a function of position in figure 5.4 we note that, at a given current, the components vary as a function of position by an order of magnitude of $\sim 10^{-4}\mathring{A}^{-1}$. For example, on the map of δq_c at 40mA (figure 5.4 e)), we observe variations between $\pm 8 \times 10^{-4}\mathring{A}^{-1}$. These same variations are visible in the lower parts of the rotational components δq_a and δq_b in figure 5.4 a) and b).

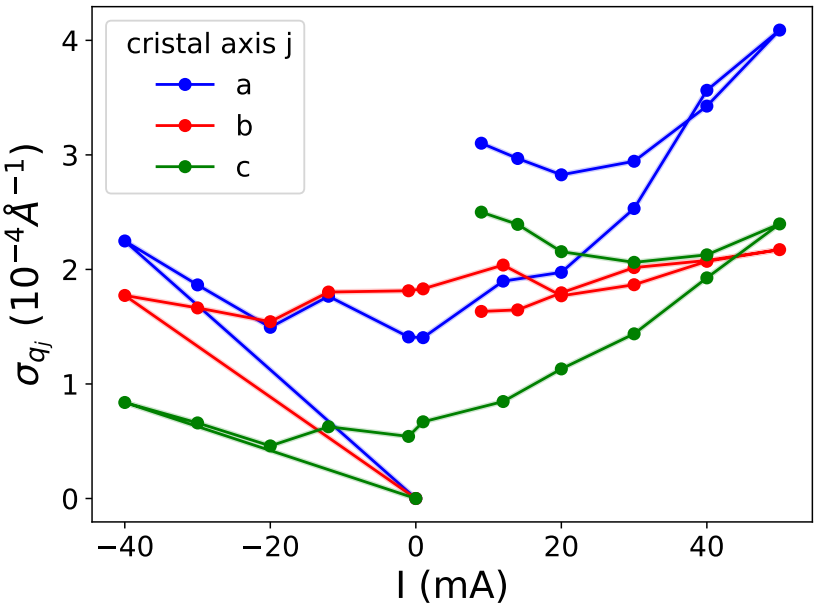

Figure 5.7: Standard deviation of each component of $\delta\vec{q}$ calculated from Eq5.1. The order of magnitude is the same as the average shown in figure 5.5, thus the CDW rotation is not perfectly rigid but displays local deviations as a function of position on the sample.

In order to make a quantitative comparison, we show in figure 5.7 the standard deviation calculated on the maps of figure 5.4 at each current. Formally, this standard deviation is

$$\sigma_{q_j} = \sqrt{\frac{1}{N_x N_z}\sum_{x,z}\left[\delta q_j(x,z) - \langle \delta q_j \rangle\right]^2} \text{ with } j = a, b, c \tag{5.1}$$

where N_x and N_z are the number of pixel along x and z respectively in the maps of figure 5.4. The results of figure 5.7 show that σ_{q_j} is of the same order of magnitude as the averaged variation $\langle \delta q_j \rangle$. This indicates that, while the CDW in $TbTe_3$ presents an averaged rotation under current, locally the CDW is distorted and the rotation is not strictly a rigid one.

5.2.3 Spatial dependence of the CDW rotation?

An issue still remains to be addressed here. Can one extract any space dependence of the CDW rotation in $TbTe_3$ from the maps in figure 5.4? In order to see if there is any difference between the left side of the map ($x \leq 10$) and the right side ($x > 10$) (since we expect a variation along the direction of the current), we perform an average of the δq_a and δq_b components (since $\langle \delta q_c \rangle$ was almost constant under currents) over these 2 regions.

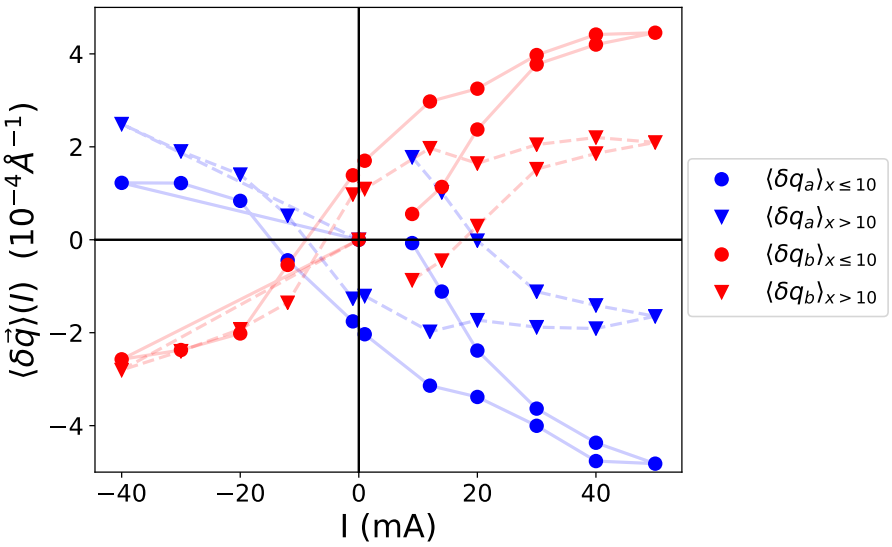

Figure 5.8: Average of the CDW satellite component variations $\delta\vec{q}$ similar to figure 5.5 but now calculated on the left region of the maps of figure 5.4 ($x \leq 10$ circles symbols) and on the right region ($x > 10$ triangles). For positive current, a clear difference is observed.

The results are shown in figure 5.8. As expected, they are similar to the ones of figure 5.5 in which the average was calculated over the whole map. A clear difference is observed between the left region (circles in figure 5.8) and the right one (triangles) for positive currents. The CDW rotation is stronger for $x \leq 10$ at large positive current. As for example $\langle \delta q_b \rangle_{x \leq 10} \approx 2 \times \langle \delta q_b \rangle_{x > 10}$ at 50mA. However, the same behavior is not observed for negative currents. This could be induced by the hysteresis effect. As said before, a negative current was applied in the sample prior to the synchrotron experiment, "freezing" the CDW wavevector components in the lower (upper) part in the hysteresis loop of $\langle \delta q_b \rangle$ ($\langle \delta q_a \rangle$).

Therefore, this result should be taken with a grain of salt. In order to have a clear and unambiguous answer for the spatial dependence of the CDW rotation in $TbTe_3$, one should make a X-ray diffraction experiment similar to the one of [132]. Using a beam spot of about ten micrometers, much bigger than the one used in this experiment, one could observe the variations on the CDW satellite reflection wavevector and intensity for several positions of the beam on the sample, scanning from the left to the right electrical contact. Then, applying current to the $TbTe_3$ sample, one can get the spatial dependence of the CDW rotation. In our experiment we had access only to a region of $20\mu m \times 9\mu m$, which is very small compared to the sample size of few mm^2.

In next section, we show that the X-ray beam can irradiates the $TbTe_3$ sample, inducing strong pinning centers for the CDW phase. This feature was also observed in the quasi-1D CDW material $NbSe_3$ by Rideau et al. in 2002 [150].

5.3 Strong CDW pinning centers from X-ray irradiation

5.3.1 First measured region

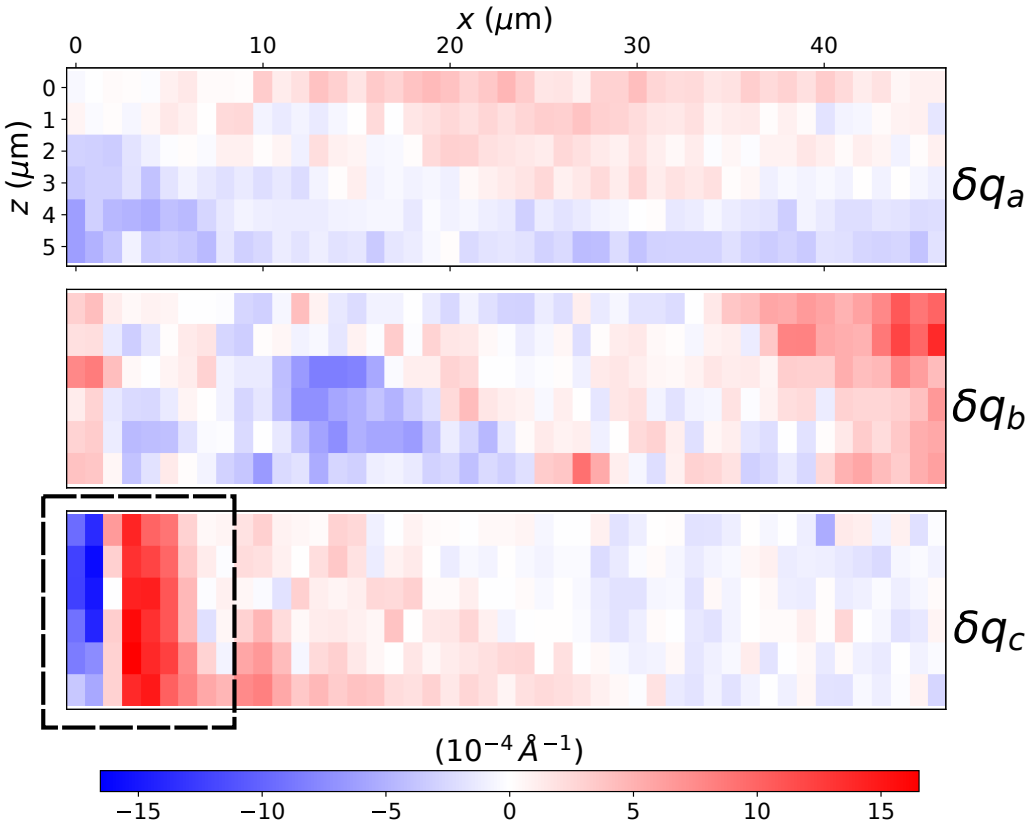

Figure 5.9: Variations of the tree coordinates $\delta\vec{q}_{cdw}$ in $TbTe_3$ in another area in the last measurement (n^o 8). Note that the scale is the same for each map. The dashed line dark rectangle highlights the irradiation zone.

We selected a different region from the one used in the previous section to perform our second kmap measurement. We measured again the wavevector components of $\vec{Q}_s = (1,15,0)+\vec{q}_{cdw}$ for 8 different currents in the same experimental conditions as before. The most interesting information from these maps is not the current dependence but the formation of a strong CDW deformation most probably induced by X-ray irradiation.

In order to observe the CDW evolution, we present in figure 5.9 the components of $\delta\vec{q}(m) = \vec{Q}_s(m) - \vec{Q}_s(1^{st}$ measurement) where m **is the measurement number and not the current value**, since we are interested in an irradiation over time and not on the current dependence here. Figure 5.9 corresponds to the last measurement

$\delta\vec{q}(8)$, the scale being the same for the three maps. One can see that the strongest deformation zone is a localized one, highlighted by the black rectangle, on the δq_c component, corresponding to the longitudinal CDW direction. On the other hand, no strong distortion occurs at this specific position in the two transverse direction δq_a and δq_b, meaning that these variations correspond to a CDW compression-expansion and not to a rotation.

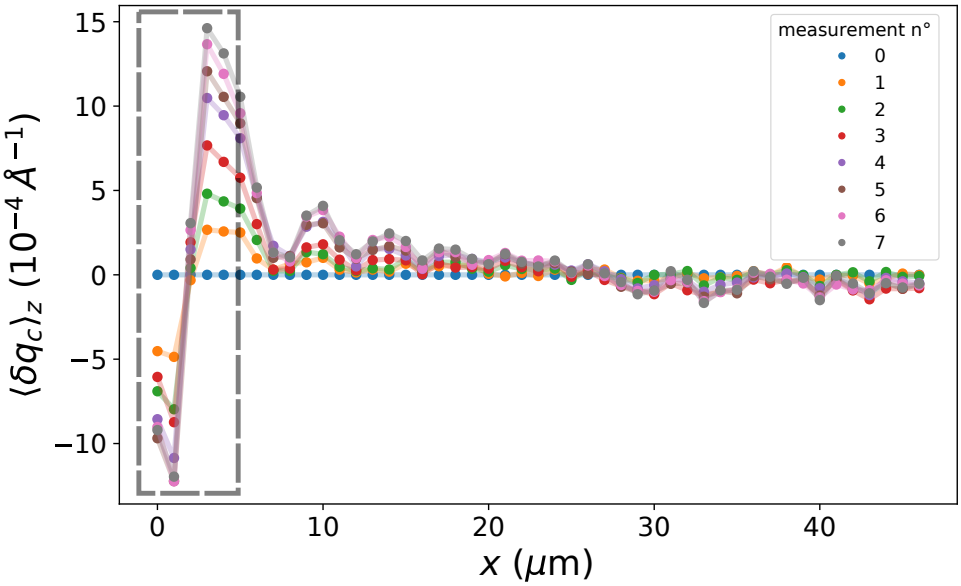

Figure 5.10: Average of δq_c map of figure 5.9 along z for several measurements, sorted in the order that they were performed. Each measurement lasted 30 minutes. We observe the formation of a strong pinning defect at the longitudinal position x=2, highlighted by the dashed line gray rectangle.

In order to visualize this defect creation over time, we make an average of the map of δq_c shown in figure 5.9 along z, formally $\langle \delta q_c(x) \rangle_z = \frac{1}{N_z} \sum_z \delta q_c(x, z)$. The results for several measurement numbers are shown in figure 5.10. The localized local distortion at $x \approx 2$ is clearly visible, the variation of the longitudinal strain δq_c being much stronger there than in the rest of the sample. The shape of this pinning center is similar to what the authors of [150] observed in $NbSe_3$ after a local irradiation (figure 4 in the article). One can identify some low amplitude oscillations of $\langle \delta q_c \rangle_z$ in the x direction (corresponding to the c axis of $TbTe_3$) which are still not properly understood by the author at the time of writing. One could make the hypothesis of a defect screening. Since a CDW compression or expansion induces a local charge density, these oscillations correspond to a spatially periodic charge and could be a way to screen the irradiation defect potential.

To make this pinning effect even clearer, we compute a simplified CDW phase from $\langle \delta q_c \rangle_z$ of figure 5.10. Remember from chapter 4 that the CDW satellite wavevector variations are related to the phase derivative by Eq4.4. Thus, $\delta q_c = \frac{\partial \phi}{\partial x}$ since the $TbTe_3$ c axis corresponds to the x direction of figure 5.10 (assuming that ϕ varies less than $2pi$ at the surface illuminated by the X-ray focused beam). Since the longitudinal deformation is stronger than the transverse ones (see figure 5.9),

we suppose that ϕ mainly depends on x. Therefore, we reconstruct ϕ, fixing a null phase at the defect position using

$$\begin{cases} \phi(x) = \sum_{x'<x} \langle \delta q_c(x') \rangle_z dx' \\ \phi(x = 2) = 0 \end{cases}$$

The result is shown in figure 5.11. We fixed ϕ to be zero at the position where $\langle \delta q_c \rangle_z$ varies the most (at $x = 2$) since this variation is most probably induced by CDW defect pinning. The variations are large near this defect as expected from figure 5.10 and ϕ is almost constant far from it.

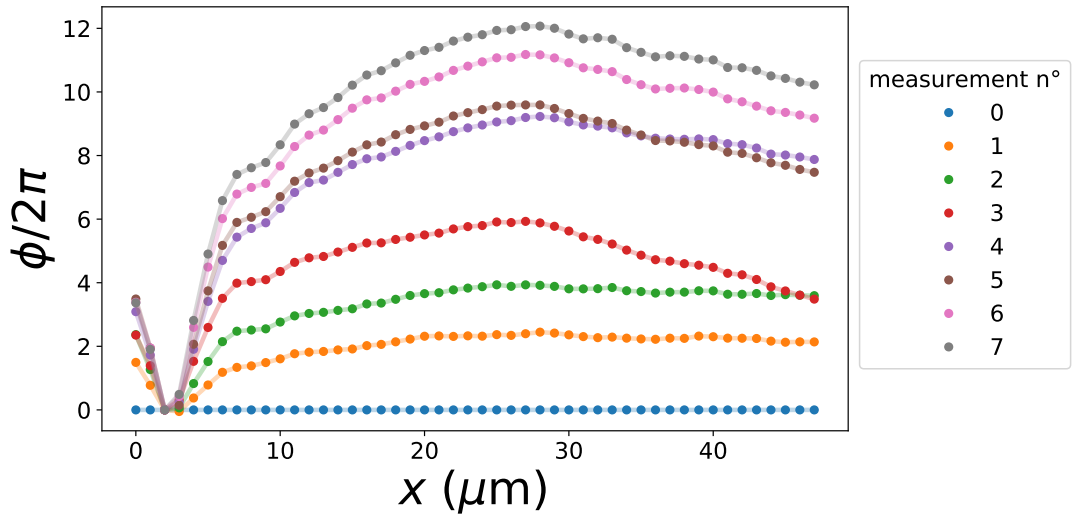

Figure 5.11: CDW phase ϕ reconstructed from its derivative given by δq_c in figure 5.10. We fixed $\phi(x = 2) = 0$ to stress that the fast variation there is most probably due to CDW pinning by an irradiation defect.

5.3.2 Second measured region and conclusion

We performed again the same measurement in another region of the sample and this time for 17 currents. In figure 5.12, we present the variation $\delta\vec{q}$ for the last measurement (the 17^{th} one). Again, we observe two irradiation defects which are only visible on the longitudinal CDW component δq_c. This confirms again what was observed in the first region in figure 5.9, meaning that these strong pinning defects induce a compression-expansion of the CDW but no rotation since no particular feature is observed on the transverse CDW components δq_a and δq_b in figure 5.12 at the defects positions $x \approx 16$ and $x \approx 60$.

Like for the first position, we show in figure 5.13 the map of δq_c averaged over the z direction for several measurements. Two defects are now clearly visible in $x \approx 16$ and $x \approx 60$ highlighted by the dashed line rectangles.

As a conclusion, using the X-ray micro-diffraction technique on the quasi-2D material $TbTe_3$, we were able to compare our results with the quasi-1D $NbSe_3$ of

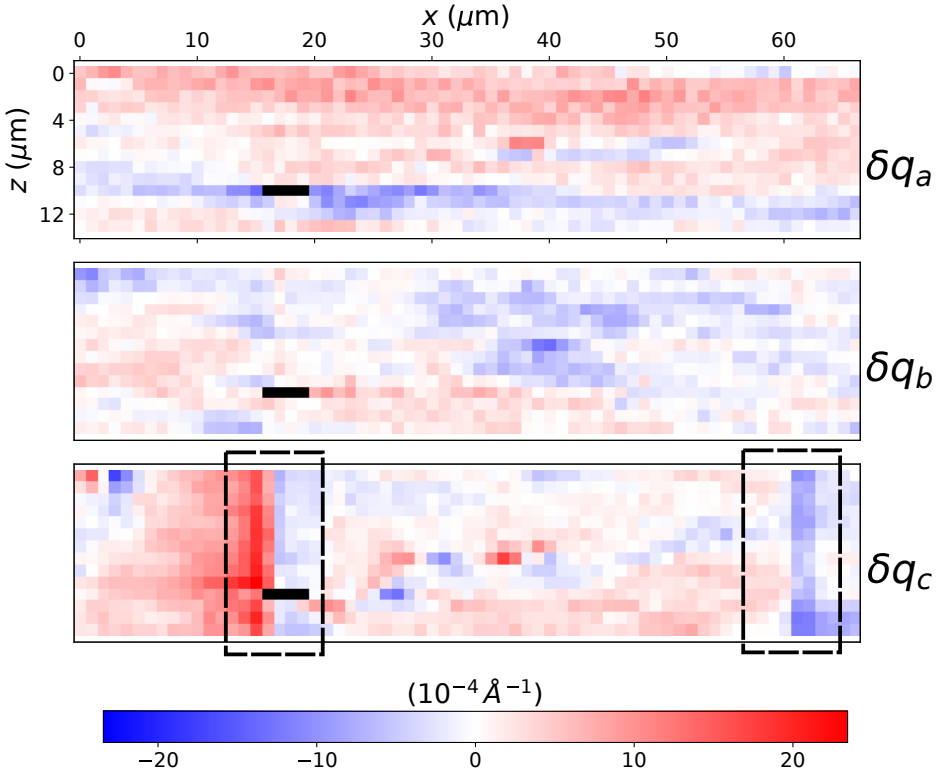

Figure 5.12: CDW wavevector variations for the last measurement (n° 17) in the second region. Dark pixels correspond to regions where we did not have the full rocking curve, hence $\delta\vec{q}$ wasn't calculated there. Two dark rectangles in the δq_c map highlight the presence of two irradiation defects.

chapter 4. We observed a significant CDW rotation under current displaying a clear hysteresis loop (figure 5.5) while no longitudinal strain was visible in the bulk of the sample. We checked that this is purely a rotation and not rotation+compression or expansion by computing the modulus as function of current (figure 5.6) which is small compared to the transverse δq_a and δq_b variations and shows no particular current dependence. Finally, we emphasize that this rotation is far from homogeneous in the measured region by calculating the standard deviation in figure 5.7.

In the second part, we made the observation that X-ray radiations can create pinning defects. Three irradiation defects were observed in two different regions. The interesting point is that they induce a CDW deformation in the longitudinal direction δq_c but show no particular feature in the transverse directions δq_a and δq_b and is almost constant in the transverse z direction. Therefore, the CDW reacts to the presence of these defects by a compression-expansion, but without any rotation.

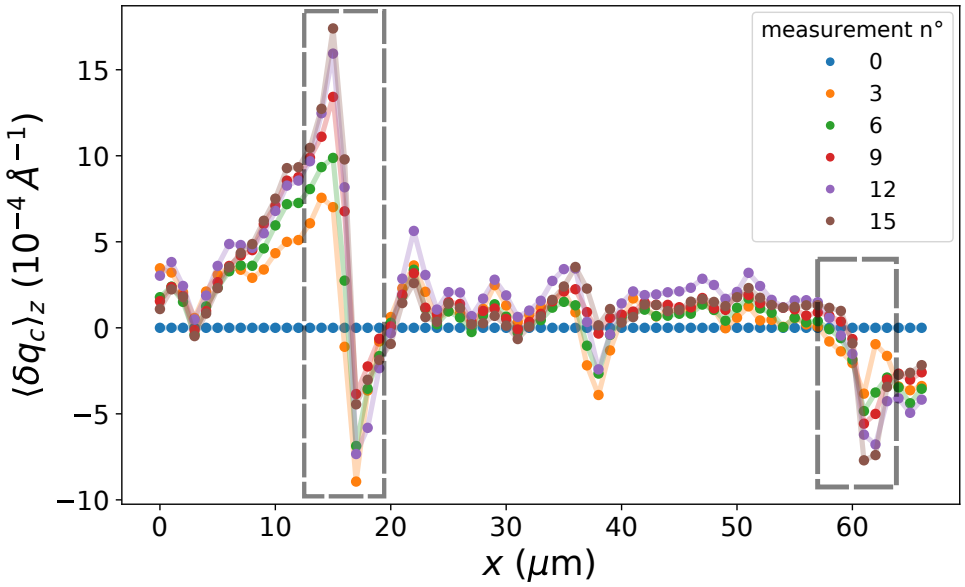

Figure 5.13: Average of the δq_c map shown in figure 5.12 along z for several measurements. Two defects are now visible in $x \approx 16$ and $x \approx 60$ evidenced by the two broken line rectangles.

Chapter 6

CDW phase calculation taking surface pinning into account

In chapter 3 we saw that above a certain threshold electric field E_{th} applied on a CDW system, the current-voltage relation becomes non-linear and the differential resistivity $\frac{dV}{dI}$ drops until it reaches a lower plateau for high currents (see figures 3.1 and 3.2). For an electric field higher than the threshold $E < E_{th}$, several theories presented in chapter 3 predict the periodic creation of charged solitons that travel through the whole sample from one contact to the other. This particular phenomenon induced an additional periodic current in the CDW state.

In chapter 3 and 4, when discussing about surface pinning, we made reference to several articles and reviews about finite size effects of CDW materials. In these papers, the authors present a dependence of the CDW threshold E_{th} on the sample dimensions, both in the longitudinal ($\parallel$ to $2\vec{k}_F$) and transverse ($\perp$ to $2\vec{k}_F$) directions, where $2\vec{k}_F$ is the CDW wavevector at equilibrium, when no current is applied to the sample.

The first of these effects is pinning of the CDW at the electrical contacts, also called "longitudinal" pinning. This was speculated from several resistivity measurments in $NbSe_3$ [151, 152, 141] and in TaS_3 [153]. This CDW longitudinal pinning at the electrical contacts, along $2\vec{k}_F$, leads to a compression at one side and a dilatation of the CDW wavelength at the other side. This effect has been observed by diffraction by two groups [132, 154], using respectively an X-ray beam width of 30μm and 0.8mm and probing $\vec{q}_{cdw}$ from one edge to the other.

The second effect is the dependence of E_{th} on of the sample cross section, observed again in $NbSe_3$ [140, 141] and in TaS_3 [139]. Gruner's review [27] and Zaitev-Zotov's review [34] list several experiments observing finite size effects in CDW materials.

The main result of this thesis is the observation of CDW surface pinning by X-ray micro-diffraction in chapter 4. We present here a theory that describes the CDW deformation under current, by taking into account fixed constraints of the CDW phase at the lateral surfaces. The behavior of E_{th} as a function of the sample dimensions is obtained and we fit the experimental data available in the several articles cited above.

Feinberg and Friedel [113] gave a phenomenological relation of E_{th} as a function

of the distance between the 2 electrical contacts considering bulk impurity pinning. On the other hand, they gave a microscopic interpretation of the surface pinning mechanism by surface steps in [113] and [33] p406-448. They mentioned several possible scenarios to explain this strong pinning effect from the sample surface such as the surface roughness, surface terraces acting as strong pinning centers.

I. Batistic et al. [155] calculated E_{th} considering the longitudinal pinning and found $E_{th} \propto L_x^{-\alpha}$ where L_x is the distance between the two contacts. They were using a 1D model ignoring the transverse pinning which certainly plays an important role. In this approach, the calculated threshold drops to zero for large L_x while experimentally, E_{th} converges to a finite value showing the necessity to consider CDW pinning from the transverse surfaces.

Finally Gruner [27] suggested a phenomenological formula for E_{th} and Borodin [139] proposed a threshold dependence on the sample cross-section (sample surface perpendicular to the CDW direction denoted A) in the form $E_{th} \propto A^{-1/2}$.

However, to my knowledge, nobody tried to solve this problem starting from the familiar 3D CDW Lagrangian given in EqA.11 of appendix A. Therefore, in this chapter, we use the phase part of EqA.11, fixing the phase in the tree directions: at the electrical contacts and on the 4 laterals surfaces. Then, with the phase slip process described in detail in appendix B, we compare the behavior of E_{th} measured in those papers with the one expected from our surface pinning interpretation.

6.1 CDW phase equation derivation and surface pinning conditions

In order to test our hypothesis of surface pinning effect with respect to the several resistivity measurements in the literature, we use part of the Lagrangian of EqA.11. In the previous chapter on X-ray micro-diffraction, when applying current, we observed a constant CDW satellite intensity. Since this diffracted intensity is related to the CDW amplitude by Eq2.9, we can consider this amplitude constant and fix $\delta = 0$ in EqA.11. In addition, we don't look at the CDW dynamics here, hence we work with the free energy $\mathcal{F}$ which is the potential energy part of the Lagrangian. Minimizing $\mathcal{F}$ gives the equilibrium state of the CDW

$$\mathcal{F}[\phi] \propto \int d^3\vec{r}\,\{c_x^2\phi_x^2 + c_y^2\phi_y^2 + c_z^2\phi_z^2 + \omega_0^2[1-\cos(\phi)] + \eta E x \phi_x\} \tag{6.1}$$

Recall the notation $\phi_j \equiv \frac{\partial\phi}{\partial j}$ with $j = x, y$ or z and the CDW direction at equilibrium is along x. In the following, we only need $\mathcal{F}$ up to a constant factor, hence it's not mandatory to find this overall factor to continue our calculation. As explained in appendix A, the first three elastic terms induce an energy cost if one deforms the CDW, the fourth term corresponds to bulk impurity pinning and the last one is the CDW interaction with the applied electric field E.

Using the Euler-Lagrange equation on $\mathcal{F}[\phi]$ to find its minimum

$$\sum_{j=x,y,z} \frac{\partial}{\partial j}\frac{\partial \mathcal{F}}{\partial \phi_j} - \frac{\partial \mathcal{F}}{\partial \phi} = 0$$
$$2c_x^2\phi_{xx} + 2c_y^2\phi_{yy} + 2c_z^2\phi_{zz} + \eta E - \omega_0^2 \sin(\phi) = 0$$
$$2\left(c_x^2\phi_{xx} + c_y^2\phi_{yy} + c_z^2\phi_{zz}\right) - \omega_0^2\phi \approx \eta E \tag{6.2}$$

where, in the last line, I assumed variation of ϕ to be small. We will show, when doing the comparison with the experimental data, that surface pinning has the same effect on the behavior of E_{th} as impurity pinning in resistivity measurements. Although more complicated, the general formula with $\omega_0 \neq 0$ is calculated. However, we will see that if ω_0 is set to zero, the obtained formula still correctly fits the experimental curves.

One must also include the following pinning conditions of the CDW phase at the lateral sample surface and at the electrical contacts

$$\phi\left(\pm\frac{L_x}{2}, y, z\right) = \phi\left(x, \pm\frac{L_y}{2}, z\right) = \phi\left(x, y, \pm\frac{L_z}{2}\right) = 0 \tag{6.3}$$

where we denoted L_x the distance between the electrical contacts, and L_y, L_z the sample size along y and z respectively. We fixed ϕ to be zero at the boundaries, which is an arbitrary choice. The choice of another initial value only increases the final result by a constant. To reproduce our experimental data in Fig 4.10, we should start with two different phases from one lateral surface to the other. Unfortunately, we couldn't choose a different value at each border due to a constraint from our calculation method. Still, Eq6.3 is sufficient enough to fit the resistivity data, no additional degree of freedom is needed.

We make a few change of variables in Eq6.2 to simplify the expression. On the other hand, we want the threshold field as function of sample dimension $E_{th}(L_x, L_y, L_z)$, hence, we leave the terms E on the right hand side. Furthermore, since we will take $\omega_0 \to 0$ at some point, we shouldn't divide by this parameter.

Having that in mind, we make the following variable change $j = c_j\sqrt{\frac{2}{\eta}}j'$ and $L_j = c_j\sqrt{\frac{2}{\eta}}L_j$ with $j = x, y$ and z, and $\omega^2 = \frac{\omega_0^2}{\eta}$. Our equation and boundary conditions becomes

$$\boxed{\left(\Delta' - \omega^2\right)\phi = E} \tag{6.4}$$

$$\boxed{\phi\left(\pm\frac{L'_x}{2}, y', z'\right) = \phi\left(x', \pm\frac{L'_y}{2}, z'\right) = \phi\left(x', y', \pm\frac{L'_z}{2}\right) = 0} \tag{6.5}$$

where $\Delta' = \frac{\partial^2}{\partial x'^2} + \frac{\partial^2}{\partial y'^2} + \frac{\partial^2}{\partial z'^2}$ is the laplacian operator. In the following sections, we drop the prime symbol for clarity but one must not forget to make the reverse variable change at the end of the calculation.

In next section, we present the Green function and image charge method, well known in electromagnetism, to solve the Eq6.4 with conditions Eq6.5.

6.2 An unusual name for an usual method

6.2.1 Green function solving the phase equation

The Green function method was first exposed by George Green in his book "An Essay on the Application of Mathematical Analysis to the Theories of Electricity and Magnetism" published in 1828 while working as a miller. This technique was widely used to solve electromagnetism problems and any physicist student have used it one way or another even if the name 'green function' was not explicitly written. In a nutshell, starting from a differential linear equation , this method provides a solution as an integral form. Let us start from the following 1D equation, the generalization in 3D being straightforward :

$$\hat{\mathcal{O}}_x \phi(x) = \rho(x) \tag{6.6}$$

where $\hat{\mathcal{O}}$ is a linear differential operator. By analogy the operator of Eq6.4 in 1D is $\hat{\mathcal{O}}_x = \frac{\partial^2}{\partial x^2} - \omega^2$, $\phi(x)$ is the function that we want to find and $\rho(x)$ is what we could call the "charge density". For example in Eq6.4 since the electric field is applied inside the sample, in 1D $\rho(x) = E$ for $x \in [-\frac{L_x}{2}, +\frac{L_x}{2}]$ and $\rho(x) = 0$ otherwise.

The green function $G(x, x')$ of the operator $\hat{\mathcal{O}}_x$ is defined as

$$\hat{\mathcal{O}}_x G(x, x') \equiv \delta(x - x') \tag{6.7}$$

One can show that the solution $\phi(x)$ is given by

$$\boxed{\phi(x) = \int G(x, x')\rho(x')\, dx'} \tag{6.8}$$

Acting with $\hat{\mathcal{O}}_x$ on this form of $\phi(x)$ one finds

$$\begin{aligned} \hat{\mathcal{O}}_x \phi(x) &= \int \hat{\mathcal{O}}_x G(x, x')\rho(x')\, dx' \\ &= \int \delta(x - x')\rho(x')\, dx' \\ &= \rho(x) \end{aligned}$$

which is indeed the Eq6.6. To summarize, after finding the green function which satisfies Eq6.7, one can have an integral form of the solution $\phi(x)$ with Eq6.8, and this for any value of $\rho(x)$ on the left hand side. Hence, having $G(x, x')$ allows to solve any type of problems of the form Eq6.6. With the Green function method, the integration in Eq6.8 can still be difficult to do in some cases. This will unfortunately be the case here.

As a simple example, let's take an electromagnetism case study in 3D. Say one wants to calculate the electric potential $U(\vec{r})$ given an electric charge density $\rho(\vec{r})$. $U(\vec{r})$ is given by the Poisson equation

$$-\Delta U(\vec{r}) = \rho(\vec{r})$$

Therefore, the corresponding operator is $\hat{\mathcal{O}}_{\vec{r}} = -\Delta_{\vec{r}}$, where we make explicit that $\Delta_{\vec{r}}$ acts only on the $\vec{r}$ variable. The corresponding green function is

$$-\Delta_{\vec{r}} G(\vec{r},\vec{r}') = \delta(\vec{r}-\vec{r}') \Longrightarrow G(\vec{r},\vec{r}') = \frac{1}{4\pi|\vec{r}-\vec{r}'|}$$

which simply is the Coulomb potential. Therefore, the potential created by a distribution of charges c_i located at position $\vec{r}_i$, $\rho(\vec{r}) = \sum_i c_i \delta(\vec{r}-\vec{r}_i)$ is given by the 3D version of Eq6.8, which is

$$\begin{aligned} U(\vec{r}) &= \int G(\vec{r},\vec{r}')\rho(\vec{r}')\, d^3\vec{r}' \\ &= \sum_i \frac{c_i}{4\pi|\vec{r}-\vec{r}_i|} \end{aligned}$$

A sledgehammer to crack a nut. Before calculating the green function for the operator of Eq6.4, we first have to introduce the image charge method to take into account boundary conditions.

6.2.2 Image charge to force surface pinning

The goal here is to find an electric potential given specific boundary conditions. Let's consider the problem displayed in figure 6.1 and let us calculate the potential $U(x,y)$ from a negative charge in $(x,y) = (d,0)$ with the boundary condition $U(0,y) = 0 \,\forall\, y$ (see figure 6.1 a)). The **uniqueness theorem** for Poisson equation makes this problem equivalent (if one wants to known the corresponding electric field) to the one of finding the electric potential of the 2 opposite charges in $(x,y) = (\pm d, 0)$ in figure 6.1 b). The positive red charge in b) is called the **image charge**.

We use this method to impose the conditions of Eq6.5, but first one has to make sure that Eq6.4 satisfies the uniqueness theorem. Let's consider $\phi_1(\vec{r})$ and $\phi_2(\vec{r})$ two **different** solutions of Eq6.4, both satisfying the boundary conditions Eq6.5. If we define $\psi \equiv \phi_1 - \phi_2$, we obtain

$$(\Delta - \omega^2)\psi = 0 \tag{6.9}$$

Using this property, we will show that $\psi = 0$, thus leading to ϕ_1 and ϕ_2 being in fact the same function. We need the following relation

$$\begin{aligned} \vec{\nabla}\left(\psi\vec{\nabla}\psi\right) &= \left(\vec{\nabla}\psi\right)^2 + \psi\Delta\psi \\ &= \left(\vec{\nabla}\psi\right)^2 + \omega^2\psi^2 \end{aligned}$$

where, in the second line, we used Eq6.9. Integrating this equation inside the CDW sample volume and using the divergence theorem we find

$$\begin{aligned} \int_V \vec{\nabla}\left(\psi\vec{\nabla}\psi\right) &= \int_V \left[\left(\vec{\nabla}\psi\right)^2 + \omega^2\psi^2\right] d^3\vec{r} \\ \int_S \psi\vec{\nabla}\psi &= \int_V \left[\left(\vec{\nabla}\psi\right)^2 + \omega^2\psi^2\right] d^3\vec{r} \end{aligned}$$

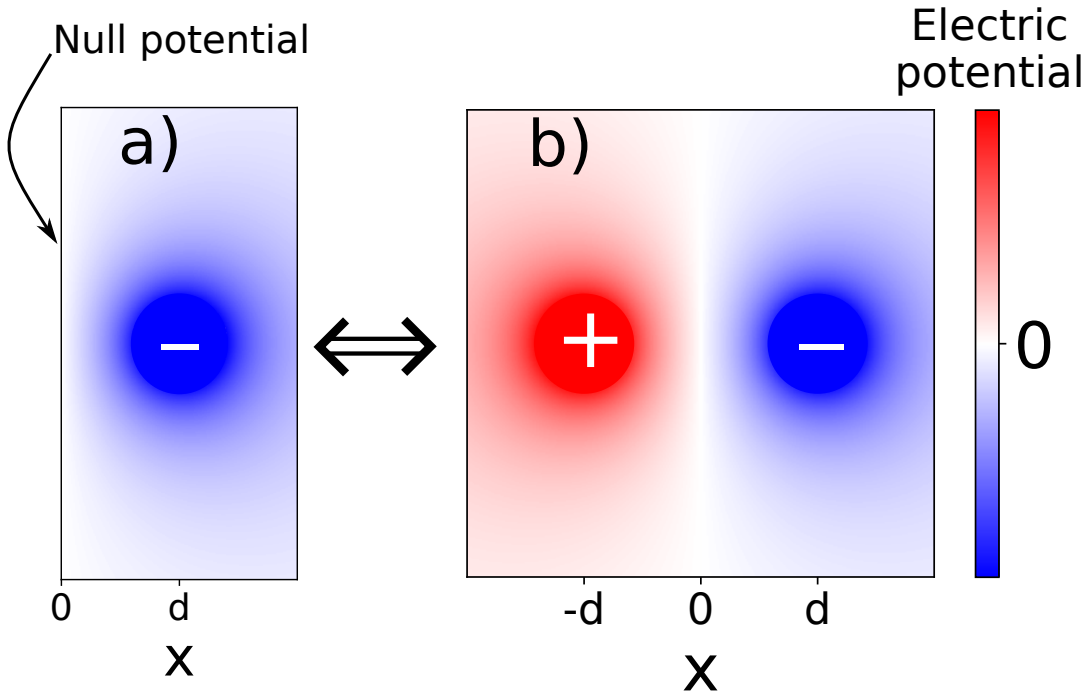

Figure 6.1: Solving the problem of an electric potential $U(x, y)$ with 1 negative charge positioned at $(x, y) = (d, 0)$ with the conditions $U(0, y) = 0$ in a) is equivalent to computing the potential given by 2 opposite charges in $(x, y) = (\pm d, 0)$ in b).

The left hand side is null, since $\phi_1 = \phi_2 \rightarrow \psi = 0$ at the boundaries from Eq6.5. Moreover, on the right hand side, we have the sum of two squares, hence for the integral to vanish, both of these term have to be null resulting in $\psi(\vec{r}) = 0$ inside the sample, thus $\phi_1 = \phi_2$ in the material, cqfd.

In conclusion Eq6.4 and 6.5 uniquely define the solution inside the sample and one can use the image charge method to solve our problem.

6.3 Calculation and comparison with the analytic solution in 1D.

In this section, we present the step by step calculation in 1D for pedagogical purpose, the steps are similar in higher dimensions. Additionally, in 1D, an analytic solution exists and can be used for comparison. Eq6.4 and 6.5 become in 1D

$$\phi''(x) - \omega^2\phi(x) = E \text{ for } x \in \left[-\frac{L}{2}, +\frac{L}{2}\right] \tag{6.10}$$

$$\phi\left(\pm\frac{L}{2}\right) = 0 \tag{6.11}$$

which is solved analytically by

$$\phi_{ana}(x) = \frac{E}{\omega}\left[\frac{\cosh\left(x\sqrt{\omega}\right)}{\cosh\left(\frac{L\sqrt{\omega}}{2}\right)} - 1\right] \tag{6.12}$$

In future plots, we will compare at $\omega = 0$, and use the solution

$$\lim_{\omega \to 0} \phi_{ana}(x) = -\frac{E}{2}\left(x - \frac{L}{2}\right)\left(x + \frac{L}{2}\right) \tag{6.13}$$

For our method, we first need the 1D green function given by

$$\left(\frac{\partial^2}{\partial x^2} - \omega^2\right) G(x, x') = \delta(x - x')$$

Since our operator $\left(\frac{\partial^2}{\partial x^2} - \omega^2\right)$ has a translation invariance symmetry, the green function becomes $G(x, x') = G(x - x')$ and the equation can easily be solved in Fourier space

$$(-q^2 - \omega^2)G(q) = 1 \Longrightarrow G(q) = \frac{-1}{q^2 + \omega^2} \tag{6.14}$$

The second step is to construct the images charges in order to satisfy the condition $\phi\left(\pm\frac{L}{2}\right) = 0$. A step by step construction of the "charge density" $\rho(x)$ of equation 6.8 is shown in figure 6.2.

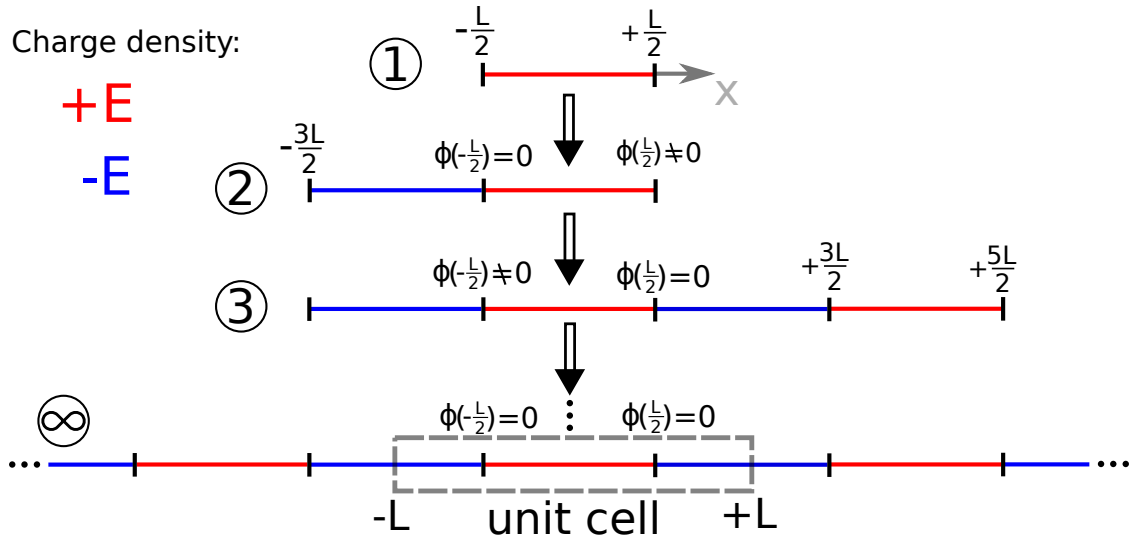

Figure 6.2: Step by step construction of the image charge density $\rho(x)$ of equation Eq6.8. Details are given in the main text.

Step ①, starting from our equation 6.10, a uniform charge density $+E$ is displayed in red in the first step of figure 6.2. The corresponding density is formally $\rho_1(x) = \left(E \text{ for } x \in \left[-\frac{L}{2}, +\frac{L}{2}\right]\right) = E \times \Pi\left(\frac{x}{L}\right)$ where Π is the gate function defined by $\Pi\left(|x| < \frac{1}{2}\right) = 1$ and $\Pi\left(|x| > \frac{1}{2}\right) = 0$.

Step ②, to have $\phi\left(-\frac{L}{2}\right) = 0$, we add a negative image charge $-E$ for $x \in \left[-\frac{3L}{2}, -\frac{L}{2}\right]$ in blue, treating the sample border in $-\frac{L}{2}$ as one could call an "anti-mirror". Formally, the density is changed to $\rho_2(x) = \rho_1(x) - E \times \Pi\left(\frac{x+L}{L}\right)$.

Step ③, for the second condition $\phi\left(+\frac{L}{2}\right) = 0$, we treat again the sample border in $+\frac{L}{2}$ as a "anti-mirror", adding an uniform charge $-E$ for $x \in \left[\frac{L}{2}, \frac{3L}{2}\right]$ in blue and

a uniform $+E$ for $x \in \left[\frac{3L}{2}, \frac{5L}{2}\right]$ in red. The density becomes $\rho_3 = \rho_2 - E \times \Pi\left(\frac{x-L}{L}\right) + E \times \Pi\left(\frac{x-2L}{L}\right)$.

Step (4) to (∞), But by the end of step (3), the phase at the left border is no longer at zero anymore, $\phi\left(-\frac{L}{2}\right) \neq 0$. Hence, one need to treat again the left boundary as an "anti-mirror" and add images charges to the left side until $\phi\left(-\frac{L}{2}\right) = 0$ again. However, the same problem occurs on the right sample border, $\phi\left(+\frac{L}{2}\right) \neq 0$. Hence in order to have a null phase on both sample boundaries, one needs to go back and forth between the left and right sides, adding images charges until having an infinite lattice of alternating positive and negative charges E.

Considering step (∞) in figure 6.2, the charge density has a periodicity of $2L$:

$$\rho(x) = \sum_{p=-\infty}^{+\infty} \rho_{unit}(x - p \times 2L)$$

where ρ_{unit} is the charge density of the unit cell of this periodic lattice shown in figure 6.2. It can be written in real space as a sum of several gate functions, formally:

$$\rho_{unit}(x) = E\left[-\Pi\left(\frac{2\left(x + \frac{3L}{4}\right)}{L}\right) + \Pi\left(\frac{x}{L}\right) - \Pi\left(\frac{2\left(x - \frac{3L}{4}\right)}{L}\right)\right]$$

Working with those expression in real space would be almost impossible. However, since $G(x, x') = G(x - x')$ in our case, Eq6.8 becomes a convolution and thus a simple product in Fourier space.

$$\phi(x) = \int G(x - x')\rho(x')\, dx' \Longrightarrow \phi(q) = G(q)\rho(q) \tag{6.15}$$

Finally, the problem is more easily solvable in the Fourier space where $\rho(q)$, the FT of an infinite periodic lattice of charges, is a sum of Dirac peaks.

Before we obtain the expression of $\rho(q)$, we need to find $\rho_{unit}(q)$. Since the Fourier transform of a gate function is a simple cardinal sine function and using some trigonometric identities, we obtain:

$$\rho_{unit}(q) = E\frac{8\sin^2\left(\frac{qL}{4}\right)\sin\left(\frac{qL}{2}\right)}{q} \tag{6.16}$$

and the Fourier transform of the full charge density reads:

$$\begin{aligned}
\rho(q) &= \int_{-\infty}^{+\infty} dx\, e^{-iqx} \sum_{p=-\infty}^{+\infty} \rho_{unit}(x - p2L) \\
&= \int_{-\infty}^{+\infty} du\, e^{-iqu} \rho_{unit}(u) \sum_{p=-\infty}^{+\infty} e^{-iqp2L} \\
&= \rho_{unit}(q)\frac{\pi}{L} \sum_{h=-\infty}^{+\infty} \delta\left(q - n\frac{\pi}{L}\right)
\end{aligned} \tag{6.17}$$

which is equivalent to the diffraction problem of an infinite crystal with an unit cell pattern given by ρ_{unit}.

Finally, starting from the integral form of the phase Eq6.8, difficult to handle numerically, we deal with an infinite sum expression, by computing the inverse Fourier transform of Eq6.15 using Eq6.14 and Eq6.17, one obtains:

$$\begin{aligned}\phi(x) &= \int G(q)\rho(q)e^{iqx}\,\frac{dq}{2\pi} \\ &= -\frac{1}{2L}\sum_{h=-\infty}^{+\infty}\frac{\rho_{unit}\left(h\frac{\pi}{L}\right)}{\left(h\frac{\pi}{L}\right)^2+\omega^2}e^{-ih\frac{\pi}{L}x}\end{aligned}$$

This expression can be simplified using the facts that $\rho_{unit}(-h\frac{\pi}{L}) = \rho_{unit}(h\frac{\pi}{L})$ and $\rho_{unit}(0) = 0$.

$$\phi(x) = -\frac{1}{L}\sum_{h=1}^{+\infty}\frac{\rho_{unit}\left(h\frac{\pi}{L}\right)}{\left(h\frac{\pi}{L}\right)^2+\omega^2}\cos\left(h\frac{\pi}{L}x\right)$$

Finally, we can remove the even terms in the sum since

$$\begin{cases} h = 2n \text{ even } \rightarrow \rho\left(2n\dfrac{\pi}{L}\right) = 0 \\ h = 2n+1 \text{ odd } \rightarrow \rho\left((2n+1)\dfrac{\pi}{L}\right) = \dfrac{4EL(-1)^n}{\pi(2n+1)} \end{cases}$$

ending with the expression

$$\boxed{\phi(x) = -\frac{4E}{\pi}\sum_{n=0}^{+\infty}\frac{(-1)^n}{(2n+1)\left\{\left[(2n+1)\frac{\pi}{L}\right]^2+\omega^2\right\}}\cos\left[(2n+1)\frac{\pi}{L}x\right]} \tag{6.18}$$

The number of terms taken into account in the numerical resolution influence the precision of the solution. Writing $\phi_N(x) \equiv -\frac{4E}{\pi}\sum_{n=0}^{N}\cdots$, the comparison between the 1D analytical formula ϕ_{ana} of Eq6.13 and ϕ_N for $\omega = 0$, $L = 1$ and $E = 1$, is shown in figure 6.3 for a sum taking into account 1 (N=0), 2 (N=1) and 101 (N=100) terms.

Inside the sample, for $x \in \left[-\frac{L}{2}, \frac{L}{2}\right]$, the numerical sum ϕ_N is close to ϕ_{ana}. On the other hand, outside the sample, for $|x| > \frac{L}{2}$, the formula given by the green function and image charge method deviates from the analytic form. This is expected since the uniqueness theorem stipulates that the solution is only uniquely defined **inside** the sample boundaries, without any assumption on its behavior outside the boundaries.

ϕ_N rapidly converges toward the analytic solution with N. The 1^{st} term $N = 0$ in figure 6.3 is already close to ϕ_{ana}. Note that the series in Eq6.18 is convergent since, for large n, it converges as $\sim \sum \frac{1}{n^3}$. Since the series is a sum of terms of alternating sign, one can expect a convergence even faster than $\frac{1}{n^3}$.

Since the relevant quantity is the phase derivative at the electric contact in $\frac{L}{2}$ (see appendix B), the analytic derivative $\phi'_{ana} = x$ and the derivative of ϕ_N are shown

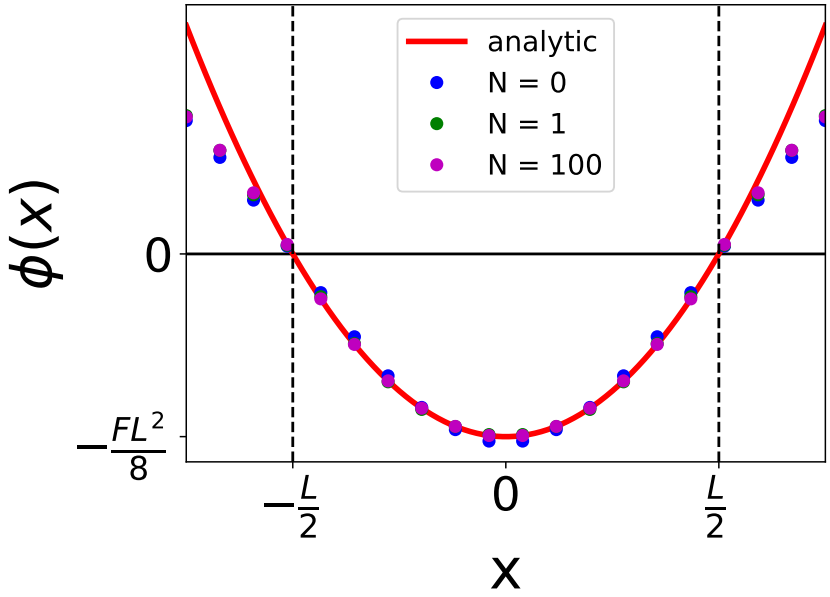

Figure 6.3: Comparison of the 1D analytical solution ϕ_{ana} and the one given by green function and image charge method up to a finite term ϕ_N. The 2 solutions are close to one another only inside the sample for $|x| \leq \frac{L}{2}$ as expected. Surprisingly, the convergence is very fast. Even the 1^{st} term of the sum ($N=0$) is close the ϕ_{ana}.

in figure 6.4 for $\omega = 0$, $L = 1$ and $E = 1$. We can notice that the convergence of ϕ' is slower than for the phase ϕ and that the largest error is at the sample borders. Since, to compare our calculation with experimental data, we will need the phase derivative at the boundary, we will have to control the convergence rate in $x = \frac{L}{2}$.

6.4 2D and 3D CDW phase solutions.

6.4.1 2D CDW phase solution

For the 2D case the equation and conditions Eq6.10 becomes

$$\left(\frac{\partial^2}{\partial x^2} + \frac{\partial^2}{\partial y^2} - \omega^2\right)\phi(x,y) = E$$
$$\phi\left(\pm\frac{L_x}{2}, y\right) = \phi\left(x, \pm\frac{L_y}{2}\right) = 0$$

The green function is now

$$G(\vec{q}) = \frac{-1}{|\vec{q}|^2 + \omega^2} \tag{6.19}$$

The image charge density construction becomes more involved but, following the same procedure as for the 1D case, now in two dimension, one finds the image charge density of figure 6.5. This is again a periodic lattice of gate functions, alternating between $\pm E$. The unit cell for this periodic lattice is highlighted by the dashed

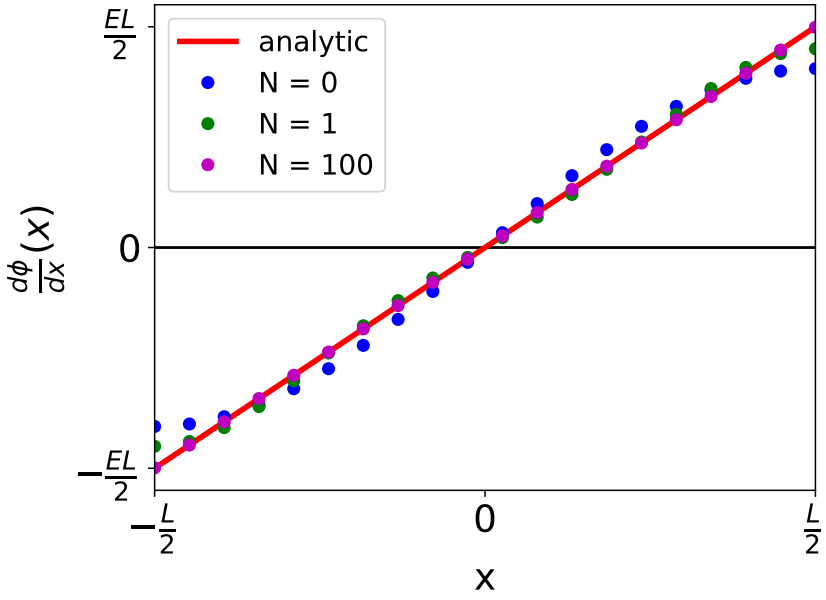

Figure 6.4: Derivative of ϕ inside the sample given by the analytic formula and the sum form from green function and image charge method.

line dark rectangle at the center of the figure. The real space expression of the unit cell charge density $\rho_{unit}(x, y)$ is a product of gate functions, a quite cumbersome formula, but its Fourier transform simply reads:

$$\rho_{unit}(\vec{q}) = E\frac{64\sin\left(\frac{q_x L_x}{2}\right)\sin^2\left(\frac{q_x L_x}{4}\right)\sin\left(\frac{q_y L_y}{2}\right)\sin^2\left(\frac{q_y L_y}{4}\right)}{q_x q_y} \tag{6.20}$$

where we denoted $\vec{q} = (q_x, q_y)$. Comparing this 2D expression with Eq6.16, one could readily guess the 3D version of $\rho_{unit}(\vec{q})$.

Following the same steps as in the 1D case to find $\phi(x, y)$, using the symmetry between positive and negative terms in the sum and removing null terms, one finds the 2D solution

$$\begin{aligned}\phi(x,y) = -\frac{16E}{\pi^2}\sum_{n_x=0}^{+\infty}\sum_{n_y=0}^{+\infty}&\frac{(-1)^{n_x+n_y}}{(2n_x+1)(2n_y+1)}\times \\ &\frac{1}{\left[(2n_x+1)\frac{\pi}{L_x}\right]^2+\left[(2n_y+1)\frac{\pi}{L_y}\right]^2+\omega^2}\times \\ &\cos\left[(2n_x+1)\frac{\pi}{L_x}x\right]\cos\left[(2n_y+1)\frac{\pi}{L_y}y\right]\end{aligned} \tag{6.21}$$

Note the similarities between Eq6.21 in 2D and 6.18 in 1D. This function is displayed in figure 6.6 a) for $\omega = 0$, $E = 1$, $L_x = 3$, $L_y = 1$ summing terms with n_x and n_y going from 0 to 100. The function drops to zero on the sample borders due to the cosine terms in Eq6.21 as required.

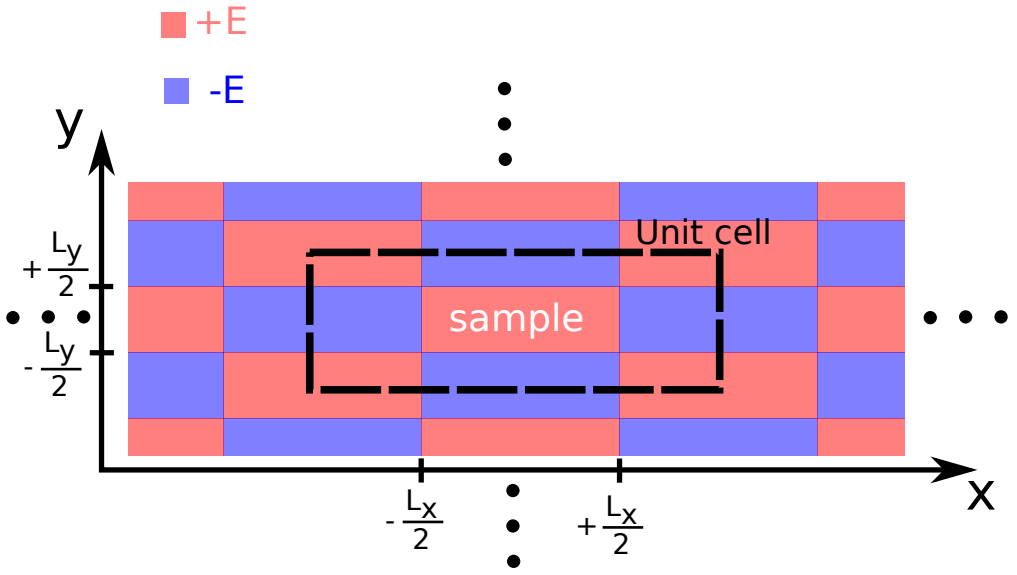

Figure 6.5: Image charge construction for the 2D case. The sample is the red rectangle in the middle for which $|x| \leq \frac{L_x}{2}$ and $|y| \leq \frac{L_y}{2}$. Following the same steps as in figure 6.2, we end up with an infinite 2D lattice of gate functions of alternating sign.

The soliton creation processus (phase-slip) [156, 157, 158, 99, 159] is induced by the longitudinal deformation of the CDW given by $\partial\phi/\partial x$ since only this term couples with the electric field, see Eq6.1. As described in appendix B, above a certain threshold $\partial\phi/\partial x > \phi'_c$, a vortex ring spontaneously appear at the contact and increases in size until annihilating at the sample transverse borders, leaving behind him a soliton. Thus, the important quantity for a comparison with experiments is the phase longitudinal derivative as a function of the electric field. In addition, since the vortex ring size that one needs to take into account to describe the phase-slip process is small compared to the CDW dimension, one needs only the maximum value of $\partial\phi/\partial x$, the process taking place in a small region near this maximum position.

Differentiating the 2D expression 6.21 to find $\partial\phi/\partial x$, one gets the function displayed in figure 6.6 b). As expected, the derivative is stronger near the contacts at $x = \pm\frac{L_x}{2}$. More precisely, the longitudinal strain $\partial\phi/\partial x$ is larger at $(x, y) = (\frac{L_x}{2}, 0)$ as far away from the lateral surfaces as possible. Hence, one needs only to take into account the strain value at this particular position to compare with experimental data.

6.4.2 3D CDW phase solution

We don't go into the detail of the 3D computation since the procedure is similar to the 1D and 2D cases. The equation and conditions are given in Eq6.4 and 6.5. The green function has the same expression as in 2D Eq6.19. We directly give the expression of $\rho_{unit}(\vec{q})$ that one could guess comparing the expressions in 1D and 2D

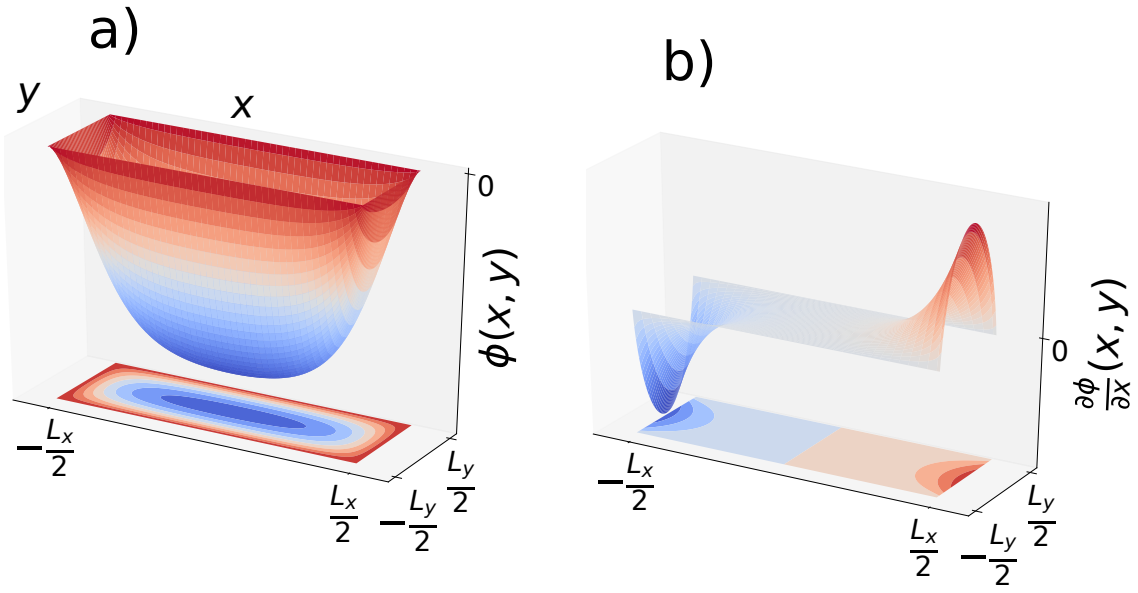

Figure 6.6: a) ϕ solution in 2D Eq6.21 for $\omega = 0$, $E = 1$, $L_x = 3$, $L_y = 1$ considering the terms with $n_x, n_y \leq 100$ in the sum Eq6.21. b) derivative of ϕ along x in 2D. The longitudinal strain induced by the applied electric field is larger near the electrical contacts in $\pm\frac{L_x}{2}$

$$\rho_{unit}(\vec{q}) = E\frac{512\sin\left(\frac{q_xL_x}{2}\right)\sin^2\left(\frac{q_xL_x}{4}\right)\sin\left(\frac{q_yL_y}{2}\right)\sin^2\left(\frac{q_yL_y}{4}\right)\sin\left(\frac{q_zL_z}{2}\right)\sin^2\left(\frac{q_zL_z}{4}\right)}{q_xq_yq_z} \tag{6.22}$$

And finally the phase expression is now

$$\begin{aligned}\phi(\vec{r}) = -\frac{64E}{\pi^3}\sum_{n_x=0}^{+\infty}\sum_{n_y=0}^{+\infty}\sum_{n_z=0}^{+\infty}\frac{(-1)^{n_x+n_y+n_z}}{(2n_x+1)(2n_y+1)(2n_z+1)}\times \\ \frac{1}{\left[(2n_x+1)\frac{\pi}{L_x}\right]^2+\left[(2n_y+1)\frac{\pi}{L_y}\right]^2+\left[(2n_z+1)\frac{\pi}{L_z}\right]^2+\omega^2}\times \\ \cos\left[(2n_x+1)\frac{\pi}{L_x}x\right]\cos\left[(2n_y+1)\frac{\pi}{L_y}y\right]\cos\left[(2n_z+1)\frac{\pi}{L_z}z\right]\end{aligned} \tag{6.23}$$

which, again, directly derives from its 1D and 2D forms (Eq6.18 and 6.21). In appendix E, we check that this is indeed the solution of Eq6.4. One could guess the shape of the 3D ϕ function from the one in 2D presented in figure 6.6. To represent this 3D function $\phi(x, y, z)$, several slices are shown in figure 6.7 a) where the phase amplitude is represented by color scales. In this figure, we choose $\omega = 0$, $E = 1$, $L_x = 3$, $L_y = L_z = 1$ and sum terms with $n_x, n_y, n_z \leq 100$ in Eq6.23. As in 1D and 2D, $|\phi|$ is larger at the center of the sample and drops to zero at each borders.

The longitudinal strain $\propto \partial\phi/\partial x$ is shown in figure 6.7 b). As for the 1D and 2D cases in figure 6.4 and 6.6 b), the strain is stronger at the sample border at $x = \pm\frac{L_x}{2}$.

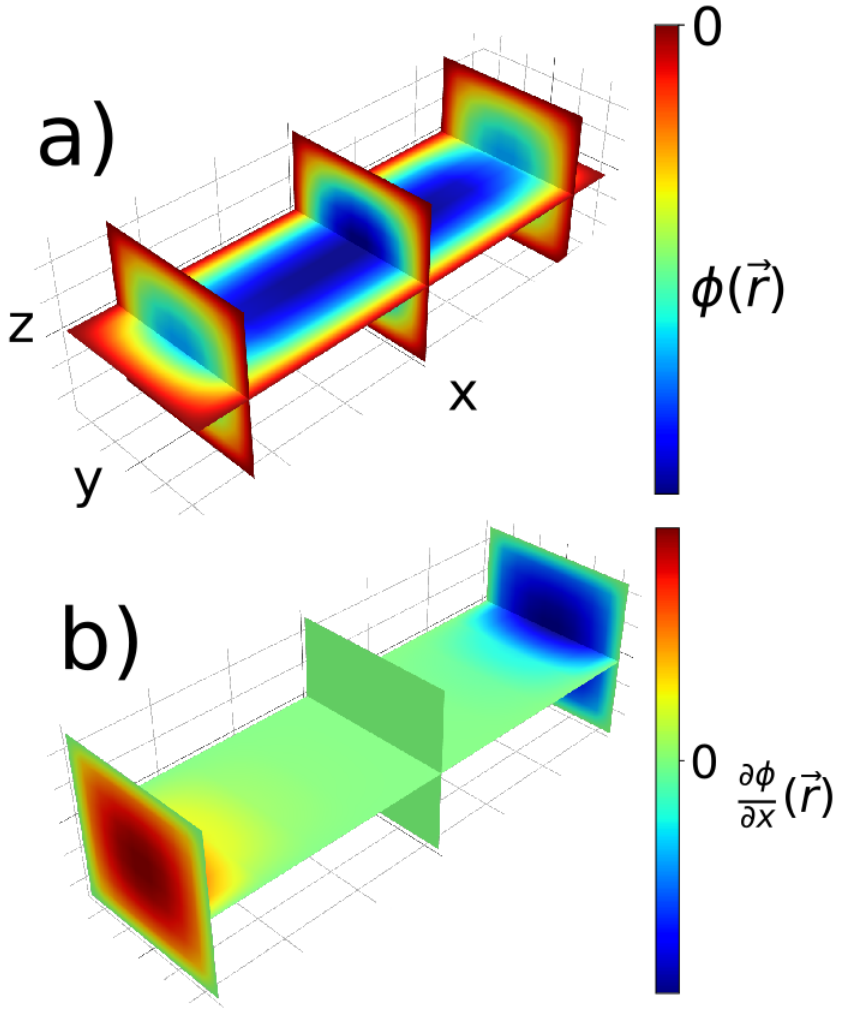

Figure 6.7: a) CDW phase given by Eq6.23. b) Longitudinal derivative $\frac{\partial\phi}{\partial x}$. To illustrate these two functions in a 3D space (x,y,z), we show cutting planes with the value of ϕ represented in a color scale.

Furthermore, this strain decreases to zero as one approach the transverse borders at $y = \pm\frac{L_y}{2}$ and $z = \pm\frac{L_z}{2}$. Since, during the phase-slip process, the relevant vortex ring size is of the order of the CDW coherence length ξ as explained in appendix B, which is small compared to sample dimensions, one can merely consider the maximum of this derivative which is localized at $(x, y, z) = (L_x/2, 0, 0)$

$$\frac{\partial\phi}{\partial x}\left(\frac{L_x}{2}, 0, 0\right) = \frac{64E}{\pi^2 L_x}\sum_{n_x=0}^{+\infty}\sum_{n_y=0}^{+\infty}\sum_{n_z=0}^{+\infty}\frac{(-1)^{n_y+n_z}}{(2n_y+1)(2n_z+1)}\times \frac{1}{\left[(2n_x+1)\frac{\pi}{L_x}\right]^2+\left[(2n_y+1)\frac{\pi}{L_y}\right]^2+\left[(2n_z+1)\frac{\pi}{L_z}\right]^2+\omega^2} \tag{6.24}$$

Hopefully, one can perform the sum over n_x using the following relation

$$\sum_{n=0}^{\infty} \frac{1}{(2n+1)^2+a^2} = \frac{\pi}{4a}\tanh\left(\frac{\pi a}{2}\right)$$

from which it follows that

$$\frac{\partial\phi}{\partial x}\left(\frac{L_x}{2},0,0\right) = \frac{16EL_x}{\pi^3}\sum_{n_y,n_z=0}^{+\infty}\frac{(-1)^{n_y+n_z}}{(2n_y+1)(2n_z+1)a_{n_y,n_z}}\tanh\left(\frac{\pi a_{n_y,n_z}}{2}\right) \quad (6.25)$$

$$\text{where } a^2_{ny,n_z} = \left[(2n_y+1)\frac{L_x}{L_y}\right]^2 + \left[(2n_z+1)\frac{L_x}{L_z}\right]^2 + \left(\frac{\omega L_x}{\pi}\right)^2$$

Changing our variable back to the original ones, we have

$$\boxed{\begin{array}{l}\dfrac{\partial\phi}{\partial x}\left(\dfrac{L_x}{2},0,0\right) = \dfrac{8\eta EL_x}{\pi^3 c_x^2}\displaystyle\sum_{n_y,n_z=0}^{+\infty}\frac{(-1)^{n_y+n_z}}{(2n_y+1)(2n_z+1)a_{n_y,n_z}}\tanh\left(\frac{\pi a_{n_y,n_z}}{2}\right) \\ \text{where } a^2_{ny,n_z} = \left[(2n_y+1)\dfrac{c_y}{L_y}\dfrac{L_x}{c_x}\right]^2 + \left[(2n_z+1)\dfrac{c_z}{L_z}\dfrac{L_x}{c_x}\right]^2 + \dfrac{1}{2}\left(\dfrac{\omega_0 L_x}{\pi c_x}\right)^2\end{array}}$$

(6.26)

As explained in details in appendix B, a soliton appears by the phase slip process whenever the applied electric field induces $\frac{\partial\phi}{\partial x}\left(\frac{L_x}{2},0,0\right) \geq \phi'_c$ where $\phi'_c \approx 1.1/\xi$. Hence, the threshold electric field when surface pinning are taken into account is given by the equation

$$E_{th} = \frac{\phi'_c\pi^3 c_x^2}{8\eta L_x \sum\limits_{n_y,n_z=0}^{+\infty}\frac{(-1)^{n_y+n_z}}{(2n_y+1)(2n_z+1)a_{n_y,n_z}}\tanh\left(\frac{\pi a_{n_y,n_z}}{2}\right)} \quad (6.27)$$

We need to control the convergence of the sum in Eq6.26. So as not to break the continuity of the manuscript, this point will be discussed in the final section. However, the conclusion is that numerically if terms $n_y, n_z \leq 100$ are taken into account, the relative error on $\frac{\partial\phi}{\partial x}(\frac{L_x}{2},0,0)$ is smaller than 1%.

6.5 Comparison between theory and experiments

6.5.1 Threshold field E_{th} dependence on the distance between electrical contacts L_x

Several resistivity experiments on $NbSe_3$ and TaS_3 samples showed a clear dependence of E_{th} on the distance between electrical contacts L_x in small samples. For

a large sample length, the threshold becomes independent of L_x. We show in the following that indeed Eq6.27 agree with this behavior.

Since we didn't find the elastic constants c_y and c_z in the literature, we use the following four parameters fitting function

$$E_{th,fit}\left(L_x, \{p_1, p_2, p_3, p_4\}\right) = \frac{p_1}{L_x \sum_{n_y,n_z=0}^{+\infty} \frac{(-1)^{n_y+n_z}}{(2n_y+1)(2n_z+1)a_{n_y,n_z}} \tanh\left(\frac{\pi a_{n_y,n_z}}{2}\right)} \tag{6.28}$$

$$\text{with } a^2_{ny,n_z} = \left[(2n_y+1)p_2 L_x\right]^2 + \left[(2n_z+1)p_3 L_x\right]^2 + \left(p_4 L_x\right)^2$$

where $\{p_1, p_2, p_3, p_4\}$ is the set of four fit parameters.

As a first study, we use this function to fit an experiment by Prester performed in 1985 [151] in which the author measured E_{th} for several distance between the contacts L_x in a $NbSe_3$ sample. The experimental data are displayed in figure 6.8 as black dots.

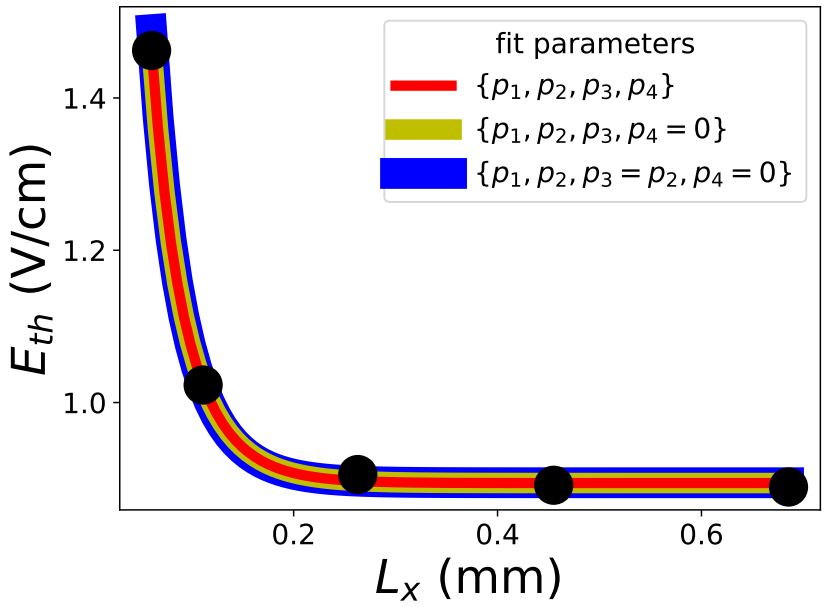

Figure 6.8: dark dots : experimental data from [151]. red curve : fit using Eq6.28 leaving all parameters $\{p_1, p_2, p_3, p_4\}$ frees. yellow curve: fit after fixing $p_4 = 0$. blue curve: fit after fixing $p_4 = 0$ and $p_3 = p_2$.

First, we perform the fit with all four parameters $\{p_1, p_2, p_3, p_4\}$ free. The result is shown as the red curve in figure 6.8 and coincide nicely with the experimental data. The corresponding set of parameters is $\{p_1, p_2, p_3, p_4\} = \{0.08,\ 8.0,\ 0.86\,,\ 0.\}$. But the related standard deviation are $\{\sigma_{p_1}, \sigma_{p_2}, \sigma_{p_3}, \sigma_{p_4}\} = \{0.02,\ 0.9,\ 1230,\ 0.\}$, therefore, something is clearly wrong with our fit since $\sigma_{p_3} \gg p_3$. What's more, the covariance matrix has large non diagonal elements, meaning that the fitting parameters are not independent, and one could find a good fit with different sets of $\{p_1, p_2, p_3, p_4\}$.

Since our function has too many parameters, we remove bulk impurity pinning $\omega_0 \to 0$ meaning we now fit with $E_{th,fit}(L_x, \{p_1, p_2, p_3, p_4 = 0\})$. The result is displayed in figure 6.8 as a yellow curve. Again, the fit is close to experimental data. Hence, our first result, *surface pinning and bulk impurity pinning can induce similar features in resistivity experiments*. The resistivity experiment shown here gives the response of the full sample, said another way, we measure an average of the whole sample reaction to the external current. Thus, one can't make the difference between bulk pinning and surface pinning with those data only. Since our diffraction measurement in chapter 4 clearly shows a strong surface pinning effect, we can conclude that one doesn't necessarily need to include CDW interaction with bulk impurities to describe its dynamics.

But still, the covariance matrix displays large non-diagonal elements. Meaning that several sets of parameters can fit the data. To visualize this, in figure 6.9, we show the residual variance at $p_4 = 0$ and for several fixed values of p_2 and p_3, hence fitting with only p_1 as free. A symmetry appear bewteen p_2 and p_3 which is expected since $p_2 \sim$ pinning on surface along y, and $p_3 \sim$ pinning on surface along z. Therefore, we constrain the fit even more by fixing $p_3 = p_2$ meaning that we constrain p_2 and p_3 to be on the diagonal of figure 6.9. Doing so, we expect the non-diagonal elements of the covariance matrix to be smaller.

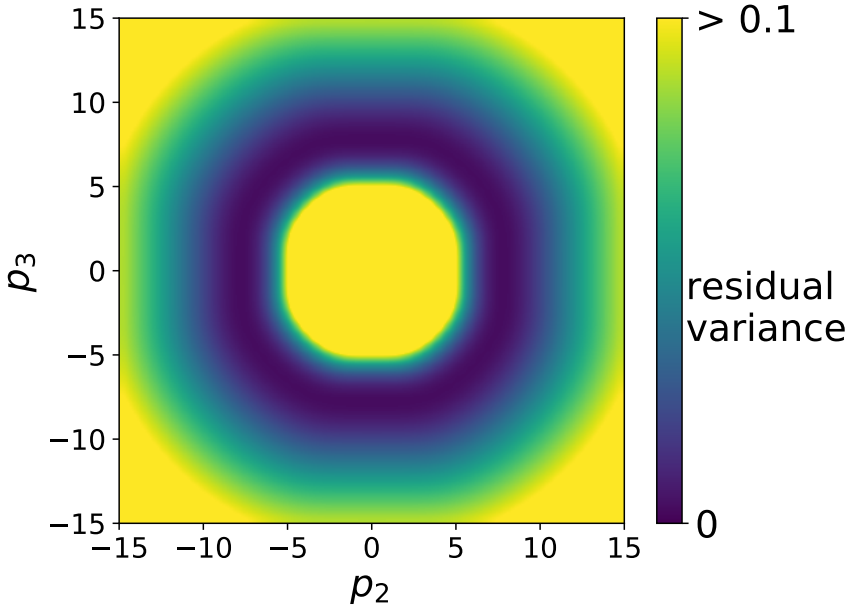

Figure 6.9: residual variance from the fit of Prester data of figure 6.8 fixing $p_4 = 0$ and for several fixed values of p_2 and p_3, thus only p_1 is left free in Eq6.28. This plot shows that several set values $\{p_2, p_3\}$ gives the lowest residual variance in dark blue.

Finally, the last fit using $E_{th,fit}(L_x, \{p_1, p_2, p_3 = p_2, p_4 = 0\})$ is shown as the blue curve of figure 6.8. The corresponding set of parameters are $\{p_1, p_2, p_3, p_4\}$ are $\{0.084 \pm 0.002,\ 6.0 \pm 0.2,\ p_3 = p_2,\ p_4 = 0\}$ and the non-diagonal element of the covariance matrix are smaller than for the two previous fits.

Figure 6.10 presents several experimental data from Prester on $NbSe_3$ [151] and one experiment by Mihaly on TaS_3 [153] along with the fit using the expression of

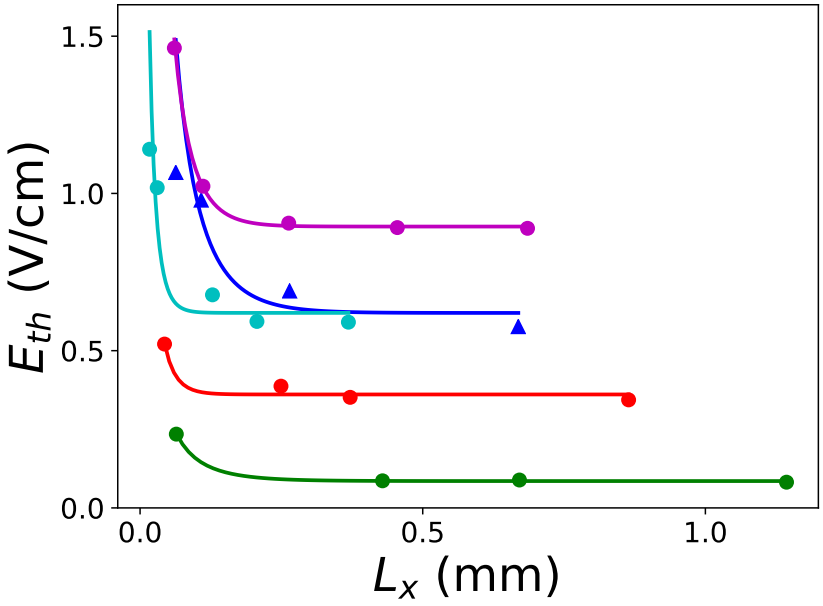

Figure 6.10: Fit using $E_{th,fit}(L_x, \{p_1, p_2, p_3 = p_2, p_4 = 0\})$ from Eq6.28. Dots correspond to several samples measured by Prester on $NbSe_3$ [151] while blue triangles correspond to an experiment of Mihaly on TaS_3 samples [153].

$E_{th,fit}(L_x, \{p_1, p_2, p_3 = p_2, p_4 = 0\})$, meaning only p_1 and p_2 are not fixed. Unfortunately, the samples transverse dimensions L_y and L_z are not given in [151], hence one can't do a comparison of the transverse elastic components c_y and c_z from the fits. A more systematic study is needed before one can conclude that the evolution of E_{th} as function of the distance between contacts follows undeniably from CDW surface pinning.

Figure 6.11 shows a measure of the threshold voltage $V_{th} = L_x \times E_{th}$ as a function of the distance between contacts performed by Zettl and Gruner in 1984 on a $NbSe_3$ sample [152]. We used formula Eq6.28 times L_x along with the reduced parameters set $\{p_1, p_2, p_3 = p_2, p_4 = 0\}$. Again, the transverse sample dimensions are not given, hence one can't get the values c_x/c_y and c_x/c_z from the fit.

6.5.2 Threshold field E_{th} dependence on the sample cross-section

One of the most important experiment for us here was performed by Borodin et al. in 1986 on small TaS_3 samples [139]. They showed a dependence of E_{th} on the sample cross-section (the section perpendicular to the CDW wavevector) indicating an influence of the transverse surfaces on the CDW conduction. The experimental data are presented in figure 6.12 as blue dots, each dot corresponding to one sample. Unfortunately, longitudinal length L_x changes between each samples. But we can still fit these data using Eq6.27 considering L_x equal for each samples using two arguments presented below.

Three groups of samples were used 1) cross-section S=10-100μm^2, L_x=1mm 2)

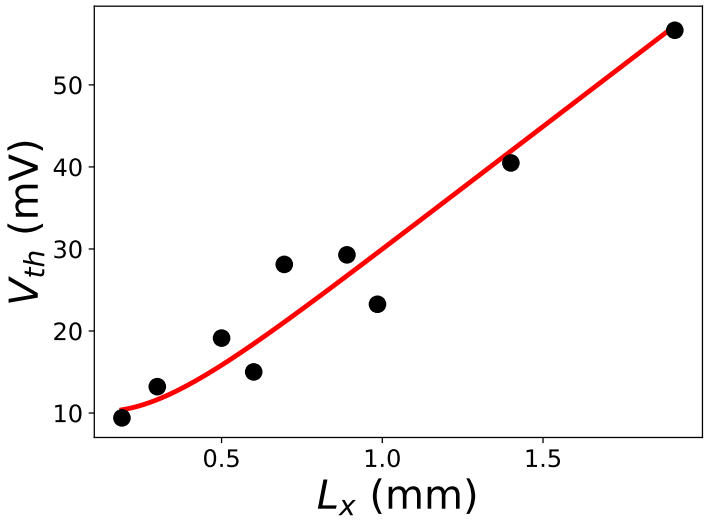

Figure 6.11: black dots : experimental data from Zettl and Gruner [152] of the threshold voltage as function of the distance between electrical contacts in $NbSe_3$. red curve: fit using $V_{th} = L_x \times E_{th}$ of Eq6.28 with the reduced parameters set $\{p_1, p_2, p_3 = p_2, p_4 = 0\}$

S=0.1-1μm^2, L_x = 10-100μm 3) S $\sim 10^{-2}\mu$m^2, L_x = 10-100μm. Those 3 groups are distinguishable in figure 6.12 where dots forms three clusters numbered 1), 2) and 3). Our 1^{st} argument is that E_{th} in TaS_3 increases up to 10mV/cm when the cross-section is changed while it only reached 1mV/cm when changing L_x from the blue triangular markers in figure 6.10. Hence, one can conclude that the influence of the variation of L_x on E_{th}, in this experiment, are much smaller than the one from varying the cross-section. Our 2^{nd} argument is even more convincing. Sample from group 2) and 3) each have L_x varying between 10 and 100 μm. Still E_{th} of group 3) is much higher than in group 2) (figure 6.12 is in $\log_{10}$ scale), meaning that this increase is mainly due to the variation of the cross-section. Therefore, one can indeed make the approximation of a constant L_x for the fit since the strongest effect is induced by the cross-section variation.

Again, the fit parameter space was to large and using the full function, we had a covariance matrix with strong non-diagonal elements. Hence we constraint again the fit function and use the following

$$E_{th,fit}(A, \{p_1, p_2\}) = \frac{p_1}{\sum_{n_y,n_z=0}^{+\infty} \frac{(-1)^{n_y+n_z}}{(2n_y+1)(2n_z+1)a_{n_y,n_z}} \tanh\left(\frac{\pi a_{n_y,n_z}}{2}\right)} \tag{6.29}$$

$$\text{with } a_{ny,n_z} = p_2\sqrt{\frac{(2n_y+1)^2 + (2n_z+1)^2}{A}}$$

where A is the sample cross-section. The result is presented as the red curve in figure 6.12 and coincide nicely with experimental data.

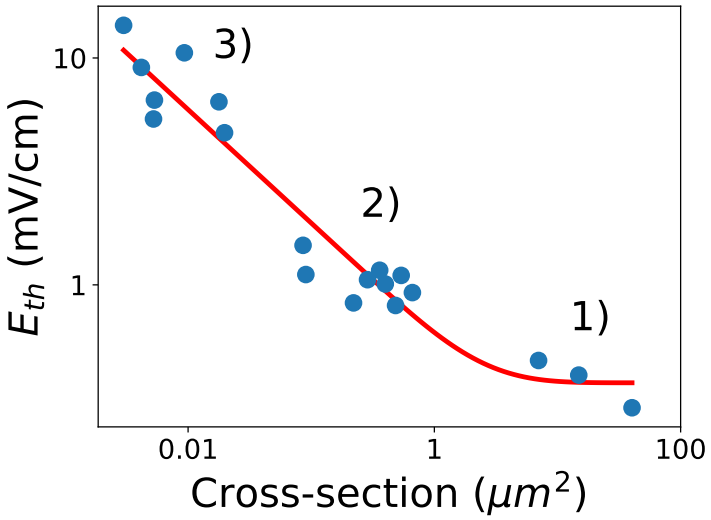

Figure 6.12: blue dots : threshold E_{th} dependence on the sample cross-section from [139]. red curve : fit using Eq6.29. 1), 2) and 3) correspond to the three different sample groups used by Borodin.

6.5.3 Threshold field E_{th} dependence on the sample dimensions L_x, L_y and L_z

Finally, Yetman and Gill [141] measured the threshold electric field E_{th} in several $NbSe_3$ samples of different dimensions (meaning with different L_x, L_y and L_z). Thus, we can directly fit these data using the following function

$$E_{th,fit}(L_x, L_y, L_z, \{p_1, p_2, p_3\}) = \frac{p_1}{L_x \sum_{n_y,n_z=0}^{+\infty} \frac{(-1)^{n_y+n_z}}{(2n_y+1)(2n_z+1)a_{n_y,n_z}} \tanh\left(\frac{\pi a_{n_y,n_z}}{2}\right)} \quad (6.30)$$

$$\text{with } a^2_{ny,n_z} = \left[(2n_y+1)p_2\frac{L_x}{L_y}\right]^2 + \left[(2n_z+1)p_3\frac{L_x}{L_z}\right]^2$$

We removed the specimens displaying a high resistivity at room temperature, which could be either due to a bad crystal or to the electrical contacts resistance. The result is presented in figure 6.13 a). Blue dots correspond to experimental data and red ones to the fit. Most of the fitting points are close to experiment but some of them display a large discrepancy, especially for the first 3 data points. Those three points correspond to specimens coming from the same crystal. Their deviation could come from a poor original crystal. Since they affect the fit, we removed them in figure 6.13 b) and run the fit again. The fit is much better and almost all the points are in agreement with the fitting function. From this fit, we have $\{p_1, p_2, p_3\} = \{24 \pm 2, 2.3 \pm 0.4, 1.0 \pm 0.2\}$.

But, again, one needs to stress an important point. As for the previous fits, several sets $\{p_1, p_2, p_3\}$ could coincide with these experimental data. In addition, we did not include impurity pinning in Eq6.30 since surface pinning acts all the same on the measurement of E_{th}. Therefore, we can't, from this fit, say whether one has

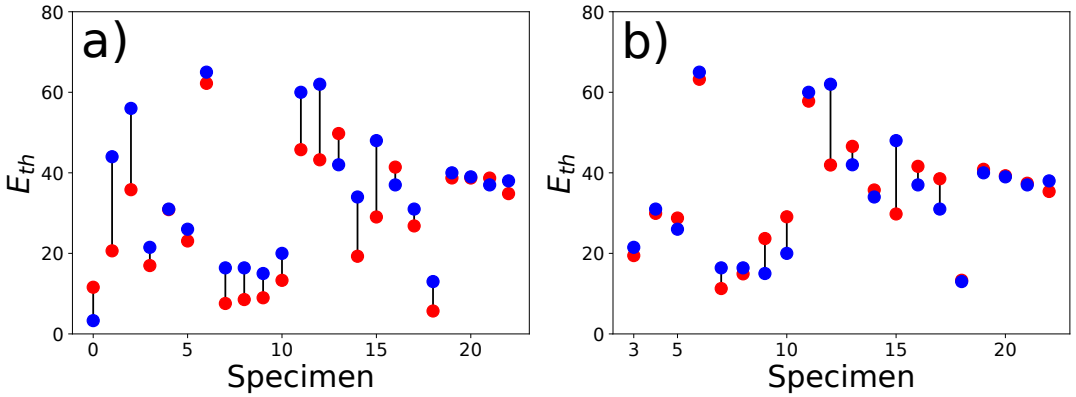

Figure 6.13: blue dots : Threshold electric field E_{th} measured by Yetman and Gill in $NbSe_3$ specimens of different size [141]. red dots : fit using Eq6.30. in b) we perform a fit after removing the 3 first data points coming from the same crystal which was affecting the overall fit.

to take bulk pinning into account or not to have an agreement with experiments.

To obtain a final conclusion on the effect of surface pinning on E_{th}, one needs the value of the transverse CDW elastic constants c_y and c_z. Having these two values, one could fix $p_2 = \frac{c_y}{c_z}$ and $p_3 = \frac{c_z}{c_x}$ in Eq6.30 and observe if bulk pinning is needed or not.

6.6 Hypotheses on the origin of surface pinning

6.6.1 Frontal pinning of the CDW wavefronts by rough surfaces

Before concluding this chapter, we should present several hypotheses on the origin of CDW surface pinning. First, we present a proposition by Feinberg, then we describe a suggestion made by Gill of a commensurate CDW at the surface of the material. We must say right away that no experience at the time of writing can give a clear and indisputable answer on the reason for surface pinning.

Surface pinning was proposed by Gill in 1984 in [160] (p377-386) from current-voltage measurements. Later in 1986, Borodin et al. observed the threshold electric field E_{th} dependence on the sample cross-section [139] (see figure 6.12), finally, in 1987, Yetman and Gill measured E_{th} on several samples with different sizes [141] (see figure 6.13) and concluded again to surface pinning effects.

Feinberg and Friedel proposed an origin of surface pinning from steps on the surface [113, 33]. In figure 6.14 a), they present a CDW with surface perfectly flat and perpendicular to the CDW wavefronts. In this idealized case, the CDW is free to distort longitudinally under applied electric field. In the more realistic case b), the surface are rough, presenting small steps on a microscopic scale displayed in c). These steps induce a frontal pinning of the CDW wavefronts, thus involving a tranverse CDW deformation under current and also limiting the longitudinal strain, hence one would still observe a finite value of E_{th} for large separation between

electrical contacts as seen in figure 6.10 and 6.11. The last case is presented in figure 6.14 d) where the edges are smooth as in a) but are not perpendicular to the CDW wavefronts. Therefore, when the wavefronts are moving from left to right their length has to increases, thus electrons must condense into the CDW near the surface. This process can pin the CDW at the surface as explained in [33] p407-448.

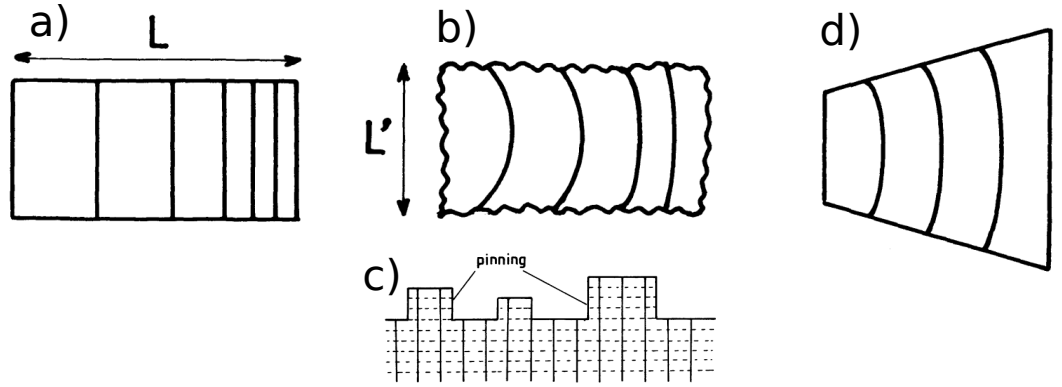

Figure 6.14: a) For a sample with surfaces perfectly perpendicular to CDW wavefronts, the CDW is free to move longitudinally. b) and c) In a real sample, the surface are rough on a microcospic scale. This induces a frontal pinning of the CDW wavefronts. d) In the case of edges making an angle with the wavefronts, while the CDW is moving, electrons condense near the surface, this mechanism can possibly pin the CDW at the surface. a),b) and d) from [33]. c) from [113]

6.6.2 Observation of the CDW at the surface using STM and grazing incidence X-ray diffraction from the literature

Several experimental techniques can be used to probe the surface of a sample. The most common one being Scanning Tunneling Microscopy (STM). This technique probes the first atomic layer, hence it removes most of the contributions coming from the bulk of the sample. A second experimental technique to probe the surface is grazing-incident X-ray diffraction. In the grazing incident configuration, the angle between the X-ray beam and the sample surface is smaller than the critical angle. Therefore, only an evanescent wave enters the sample. Since this wave is exponentially damped, it only penetrates on a small distance of the order of few nanometers inside the sample. Thus, this second technique probes the first atomic layers and is mainly surface sensitive. Since the atomic configuration is slightly different at the surface compared to the bulk, one could fear that the CDW disappear there. In fact, this is not the case for a large variety of CDW materials.

Carpenelli et al. observed in STM a CDW at the lead-coated surface of a germanium crystal [161] with a critical temperature of $T_c \approx -20°\text{C}$. Some experiments reported in the literature show that several members of the blue bronze family present a CDW at the sample surfaces. Brun et al. showed, using STM, a CDW at the surface in $Rb_{0.3}MoO_3$ [162]. Mallet et al. observe, again in STM, a surface CDW in $K_{0.9}Mo_6O_{17}$ [163]. Zhu et al., on the other hand, used grazing-incident

X-ray diffraction to probe the surface of $K_{0.3}MoO_3$ and observed a surface CDW similar to the one of the bulk.

More interesting for us is the presence of a CDW in the quasi-2D material $TbTe_3$, on which we performed the kmap experiment of chapter 5. In 2007 Fang et al. observed with a STM and at a temperature of ∼6K a surface CDW phase in $TbTe_3$ [164]. This feature was later observed in 2016 by Fu et al. but now on a temperature range of 298-355K [165]. But, and this is more interesting, a novel feature occurs at the surface. Remember from figure 1.11 that the CDW in $TbTe_3$ appears in the Te plane. Those planes are almost squares, but the small discrepancy between the length of the lattice parameters a and c makes the 1^{st} CDW appear at high temperature along c. From figure 1.12, we see that a second CDW appears at lower temperature in some members of the Rare-earth tritellurides family along a. But this doesn't happen in $TbTe_3$. At least, this is true in the bulk of the sample since figure 1.12 is obtained from bulk X-ray diffraction. On the other hand, the second CDW along a was observed at the surface at low [164] and high [165] temperature in $TbTe_3$ using STM. What's more Fu et al. noticed separated regions with a CDW along c or one along a but also regions where these two perpendicular CDW states coexist[165].

Finally, the surface CDW was observed in STM by Gammie et al. in TaS_3 [166], by Burk et al. in 1T-TaS_2 [167], by Brun et al. in $NbSe_3$ [29, 168, 169]. Murphy et al. used grazing incident X-ray diffraction and observed a CDW at the surface of a $NbSe_2$ sample [170]. Thus, one can see that it's quite common for the CDW phase to appear even at the sample borders.

6.6.3 Hypothesis of a commensurate surface CDW

We propose here an interpretation on the origin of surface pinning different from the one of Feinberg (rough surfaces). The author found that Yetman and Gill made the same guess in their article in 1987 [141]. Citing these authors "It seems not unlikely, for example, that a layer of CDW adjacent to the surface experiences increased pinning associated with an increase in amplitude or, perhaps, **with a slight change in a wavevector to a value commensurate with the lattice periodicity**".

Indeed, for some materials, the surface CDW is different from the one in the bulk. In the case of $NbSe_2$ [170], the bulk transition temperature is $T_{c,B,NbSe_2}$ = 33.5±0.2K while at the surface $T_{c,S,NbSe_2} = 34.9 \pm 0.4\text{K} = T_{c,B} + 1.4 \pm 0.6\text{K}$, thus the CDW should have a higher amplitude at the surface. Even more apparent, in $NbSe_3$ [29], the second CDW has a bulk transition temperature $T_{c,B,NbSe_3}$ = 59K while at the surface $T_{c,S,NbSe_3}$ = 70-75K, thus almost 15K above the bulk. Therefore, as suspected by Yetman and Gill, the CDW at the surface can indeed be very different compared to the one in the bulk.

Some experiments reported in the literature show a lock-in of the CDW wavevector to a commensurate value in the bulk of the sample. Moncton et al. observed this behavior in 2H-$TaSe_2$ by neutron diffraction [171], and Pouget used X-ray diffraction to observe this commensurate transition in $K_{0.3}MoO_3$ [11]. McMillan proposed a Landau-type theory to follow this transition [172] but the given free energy is not

directly related to a microscopic description. In the following, starting from the microscopic Hamiltonian, we show that, even for an electronic band filling (a given number of electrons N_{el}) which should induce a incommensurate CDW, the system will choose to lock itself in a commensurate CDW state.

Example of a commensurability 2 CDW

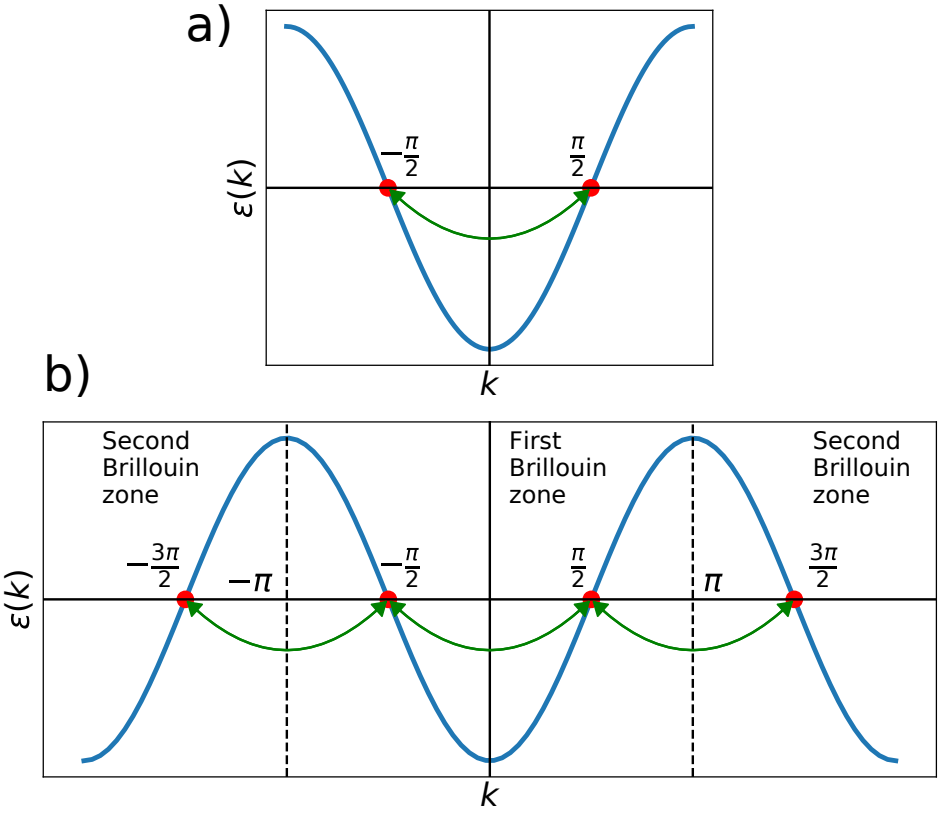

Figure 6.15: a) Electronic band at half filling. In the incommensurate case, we only take into account electron-hole coupling in the first brilouin zone. b) For the commensurate case, one needs to add coupling in the other Brillouin zones.

In chapter 1, we slightly lied when introducing the CDW transition for pedagogical purpose. we hope to fix it here. Remember that the CDW wavevector is directly given by the number of electrons N_{el} by $\lambda_{cdw} = \frac{2\pi}{q_{cdw}} = \frac{2\pi}{2k_F}$ where k_F is proportional to N_{el}. Therefore, changing N_{el}, one could make the CDW become incommensurate (ICDW) or commensurate (CCDW). By incommensurate, we mean that the CDW wavelength can't be written as a fraction times the lattice parameter, $\lambda \neq \text{fraction} \times a$.

In figure 1.2, we choose a commensurate half filling $\lambda = 2 \times a \equiv 2$ (we fix $a = 1$ for simplicity in the following) and said that the CDW phase comes from a coupling between electrons and holes close to the fermi surface at $\pm\frac{\pi}{2}$ (see figure 6.15 a)). This coupling opens a gap in the electronic band at low temperature and the energy band becomes the one of figure 1.5 that we give again here : $E(k) = \pm\sqrt{\epsilon(k)^2 + |\Delta|^2}$. But we forgot to take also into account that the CDW is commensurate, meaning

one has to take into account coupling in the second Brillouin zone as shown in figure 6.15 b). The effective Hamiltonian of Eq1.8 now becomes

$$H_{eff} = \sum_k \begin{pmatrix} c_k^\dagger & c_{k+2k_F}^\dagger \end{pmatrix} \begin{pmatrix} \epsilon_k & |\Delta| \left(e^{i\phi} + e^{-i\phi}\right) \\ |\Delta| \left(e^{-i\phi} + e^{i\phi}\right) & -\epsilon_k \end{pmatrix} \begin{pmatrix} c_k \\ c_{k+2k_F} \end{pmatrix}$$

where ϕ correspond to the CDW phase. After diagonalization of the central matrix, we find the commensurability 2 CCDW energy band

$$E_{\text{com},2}(k) = \pm\sqrt{\epsilon(k)^2 + 4|\Delta|^2 \cos^2(\phi)}$$

First, the CCDW electronic spectrum now depends on the phase ϕ, which is not the case for the ICDW, meaning that the total electronic energy also depends on ϕ, thus the CDW is pinned to the host lattice. Then, the gap can becomes larger than the one of an ICDW since for $\phi = 0$, we have a gap of $4|\Delta|$ while it is only of $2|\Delta|$ in the ICDW (see figure 6.16). What's more, the lower band for which $E(k) < 0$ is lower in energy for a CCDW. This is the starting point of our surface CCDW hypothesis. Since in the commensurate case, the valence band is lowered regarding the ICDW case, the CDW could lower its electronic energy by lock-in into a CCDW even if $\frac{2\pi}{2k_F}$ is incommensurate.

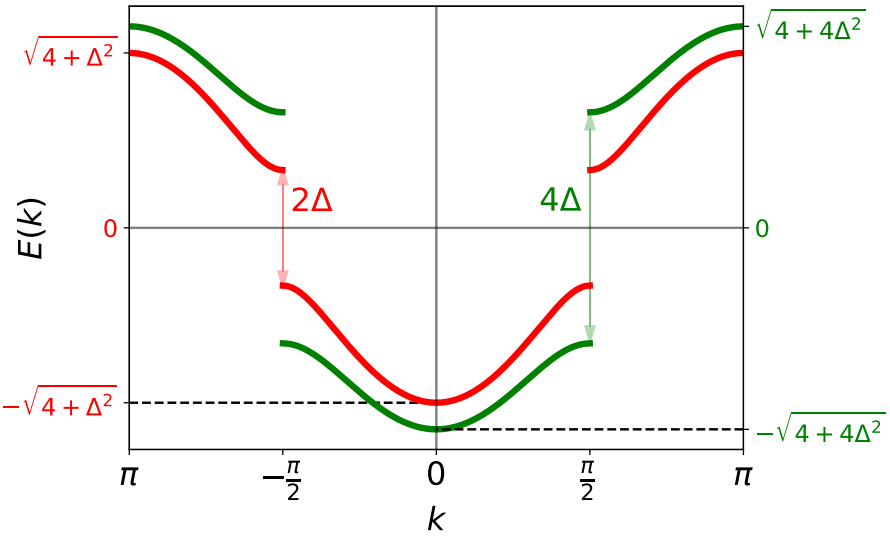

Figure 6.16: Red : electronic energy band in the CDW state. Without taking commensurability effects into account $E(k) = \sqrt{\epsilon(k)^2 + \Delta^2}$. Green : With the commensurability effects of figure 6.15 b), the energy now becomes $E(k) = \sqrt{\epsilon(k)^2 + 4\Delta^2 \cos^2(\phi)}$. We choose $\phi = 0$ for this plot.

CDW commensurability lock-in at null temperature

However, the case $\lambda = 2$ is an easy one. Therefore, in the following we perform exact diagonalization (up to numerical precision) of the CDW Hamiltonian written in real space as in appendix C (writing $|\Delta|$ as Δ for simplicity of notation)

$$\mathcal{H} = \sum_{n=1}^{N_{site}} \left[\Delta \cos \left[\frac{2\pi}{\lambda} n + \phi(n) \right] c_n^\dagger c_n - \left(c_{n+1}^\dagger c_n + c_n^\dagger c_{n+1} \right) \right] \equiv \vec{\psi}^\dagger h(\lambda, \phi) \vec{\psi}$$

where λ is the CDW wavelength, N is the number of atomic site (900 in our numerical calculations) and

$$\vec{\psi} = \begin{pmatrix} c_1 \\ c_2 \\ \vdots \\ c_{N_{site}} \end{pmatrix} ; \vec{\psi}^\dagger = \begin{pmatrix} c_1^\dagger & c_2^\dagger & \dots & c_{N_{site}}^\dagger \end{pmatrix}$$

$$h(\lambda, \phi) = \begin{pmatrix} \Delta \cos\left(\frac{2\pi}{\lambda} + \phi\right) & -1 & 0 & ... & 0 & 0 \\ -1 & \Delta \cos\left(\frac{2\pi}{\lambda} 2 + \phi\right) & -1 & ... & 0 & 0 \\ \vdots & \vdots & \vdots & \vdots & \vdots & \vdots \\ 0 & 0 & 0 & ... & -1 & \Delta \cos\left(\frac{2\pi}{\lambda} N_{site} + \phi\right) \end{pmatrix}$$

The electronic band in the CDW state is directly given by the eigenvalues of h, which are computed using python.

For a given filling, not taking into account the spin of the electron, we compute the total energy at fixed ϕ in the following way. Calling again the number of electron N_{el} and knowing that the step size in k space is $dk = \frac{2\pi}{N_{site}}$, the fermi wavevector is $k_F = dk \times \frac{N_{el}}{2}$ and finally the CDW wavelength is $\lambda = \frac{2\pi}{2k_F} = \frac{N_{site}}{N_{el}}$. Therefore, in our numerical treatment, λ is always commensurate since it's a fraction (remember that the crystal lattice parameter is equal to 1 here). But far from a simple commensuration (like $\lambda = 2, 3, 4...$ etc), the CDW can be seen as "almost incommensurate".

At a fixed electron filling N_{el}, the total electronic energy, which is a function of the CDW phase ϕ, becomes

$$E_{tot}(\phi) = \text{Sum of the } N_{el} \text{ lowest eigenvalues of } h\left(\lambda = \frac{N_{site}}{N_{el}}, \phi\right)$$

$E_{tot}(\phi)$ for a filling resulting in λ close to 2 and 3 are shown in figure 6.17 a) and b) respectively. As expected, when λ departure from a simple commensurability value (2 in a) and 3) in b)), it becomes almost independent of ϕ. The small ϕ dependence in b) for $\lambda = 2.98$ and 2.99 is probably due to the finite size of our numerical system (N=900). What's more, one can observe that the ϕ dependence is stronger for the simplest commensurability, for example $E_{tot}(\phi)$ displays larger variations in the case $\lambda = 2$ than for $\lambda = 3$.

Moving on to the CDW lock-in phenomenon, we first need to clarify our question. Say we have a fixed number of electrons N_{el}. The theory of Peierls transition tells us that the system at T=0K is a CDW with wavelength $\lambda = \frac{N_{site}}{N_{el}}$ which we choose to be "almost incommensurate" ($\lambda \neq 2,3,4,...$etc), therefore in the ICDW state. The ground state corresponds to a filled valence band and an empty conduction band as

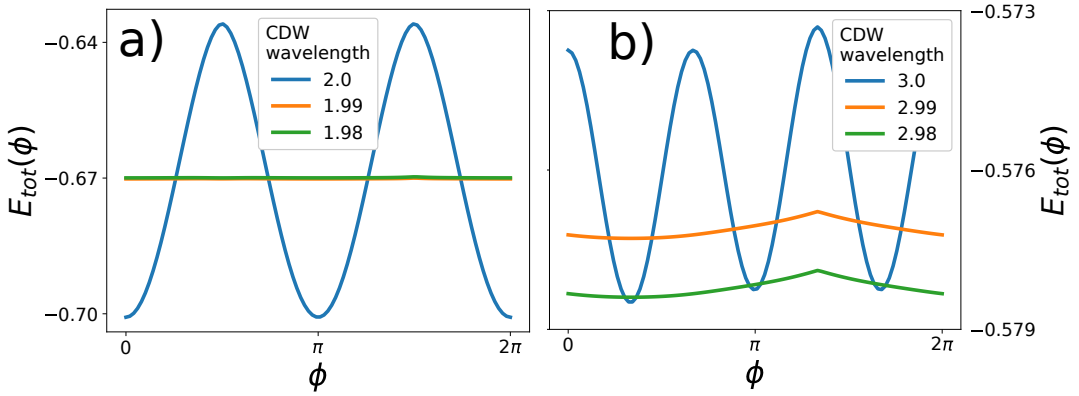

Figure 6.17: Dependence of the total electronic energy $E_{tot}(\phi)$ on the CDW phase ϕ given by Eq6.31.

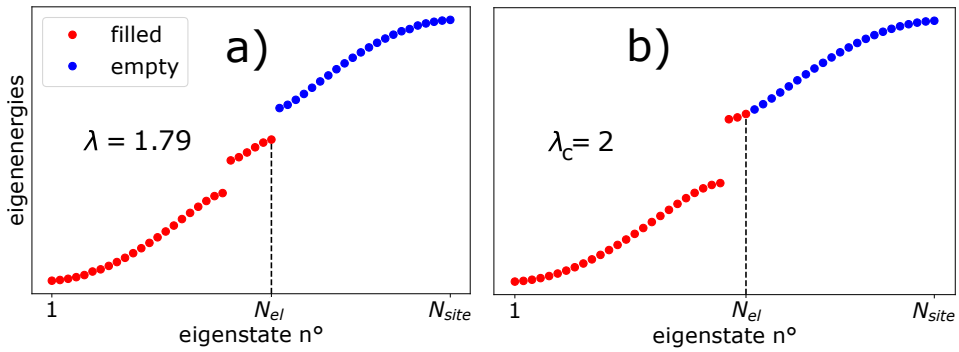

Figure 6.18: At fixed number of electrons N_{el}, Peierls theory tells us that the ground state is a CDW of wavelength $\lambda = \frac{N_{site}}{N_{el}}$ as in a). b) forcing the CDW to be commensurate instead with wavelength λ_c, the gap is larger and this could lower the total energy. But some electrons need to be in the conduction band which cost a certain amount of energy, making the CCDW state unfavorable if λ is far from λ_c.

in a) of figure 6.18. Now say λ is higher but close to a simple commensurate value $\lambda > \lambda_c = 2, 3, 4, ...$ etc. If the atomic lattice is **forced** into the CCDW state, meaning we forced the CDW periodicity to be λ_c and not $\lambda = \frac{N_{site}}{N_{el}}$, in this CCDW phase the valence band is filled but since it only contains $\lambda_c \times N_{site}$ states ($< \lambda \times N_{site} = N_{el}$), the remaining electrons will have to go in the conduction band as in b) of figure 6.18. As a first guess, since the valence band is lower in energy in the CCDW state than in the ICDW one (compare green and red bands of figure 6.16), taking only into account the valence band, one would say that the CCDW state is favored. But one must not forget about the remaining electrons in the conduction band of the CCDW, which cost energy. If λ is too far from λ_c, there will be too many electrons in the conduction band and the CCDW is not favored anymore. Therefore, we expect the CDW to lock-in into a CCDW state for an electronic filling N_{el} inducing a $\lambda = \frac{N_{site}}{N_{el}}$ close to a commensurate value λ_c, but when λ is far from λ_c, the CDW has a lower total electronic energy in the ICDW state.

To obtain figure 6.19, we compared the electronic energy for a ICDW and the closest CCDW given by (choosing the value ϕ which minimize the CCDW from

figure 6.17)

$$E_{tot,ICDW} = \text{Sum of the } N_{el} \text{ lowest eigenvalues of } h\left(\lambda = \frac{N_{site}}{N_{el}}, \phi\right)$$
$$E_{tot,CCDW} = \text{Sum of the } N_{el} \text{ lowest eigenvalues of } h\left(\lambda_c, \phi\right)$$

where λ_c is the closest simple commensurate value. By comparison of $E_{tot,ICDW}$ and $E_{tot,CCDW}$ we know at T=0K if the CDW is in a commensurate or in an incommensurate state.

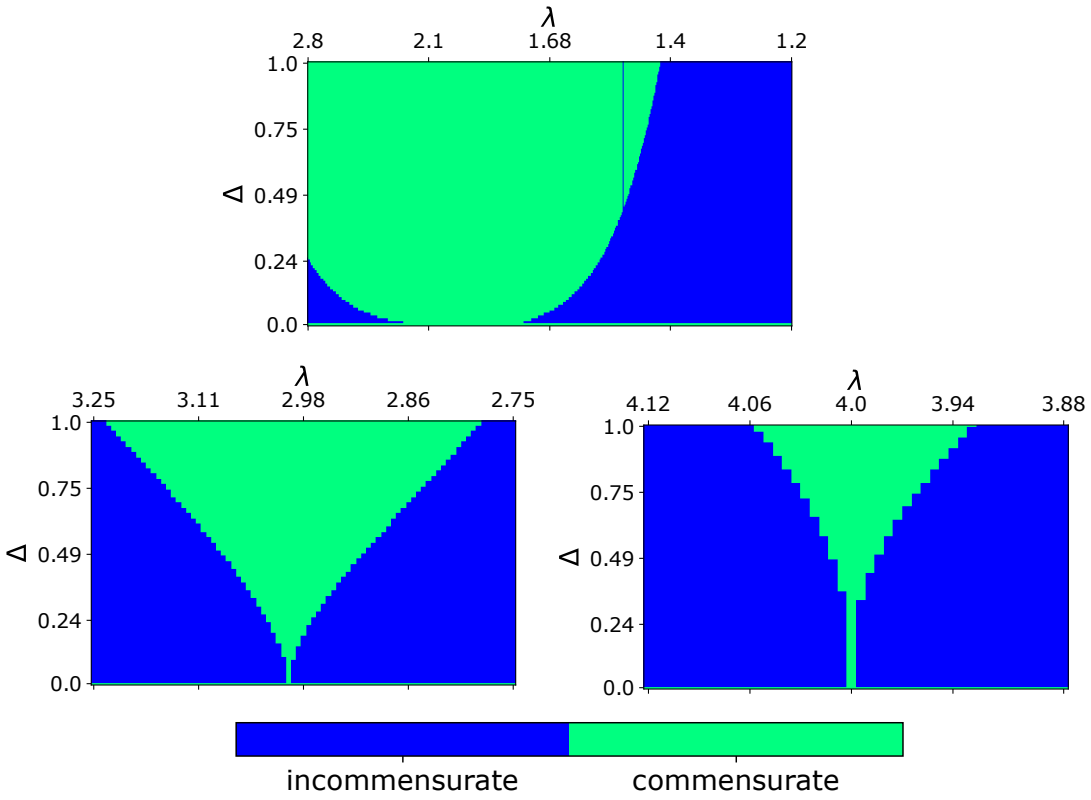

Figure 6.19: Comparing the total electronic energy of the ICDW and of the CCDW (respectively a) and b) in 6.18), we observe that for some electronic filling N_{el} (equivalently the incommensurate wavelength $\lambda = N_{site}/N_{el}$) and at some CDW amplitude Δ, the CCDW state is lower in energy than the ICDW, inducing a lock-in of the CDW to a commensurate state at 0K.

The results for λ_c= 2,3 and 4 are shown in figure 6.19 for several N_{el} (meaning several λ) and for $0 < \Delta < 1$. One can observe that, for λ close to the commensurate value λ_c, the CDW will lock into the CCDW state, this is even more true for large value of the gap Δ. We need to emphasize that this result is valid at T=0K. When temperature is higher, the CCDW state is less favorable since more and more electrons are promoted to the conduction band, which is higher in energy for the CCDW than for the ICDW (see figure 6.16).

As a last word, we saw in Appendix C that a local jump in ϕ, called soliton, can lower one electronic state of the conduction band as in figure C.1. It was

proposed (see [18, 172]) that the CDW ground state for a filling inducing a λ close to a commensurate value would be a CCDW state with local jumps in the phase called discommensurations (for example, the soliton presented in appendix A can be seen as a discommensuration with a jump of $+2\pi$). Adding these effects into our Hamiltonian, we could expect the green region of figure 6.19 to increases in size.

Again, this commensurate CDW still has the status of an hypothesis. STM spatial resolution is still not enough to make the difference between a surface CCDW and an ICDW with a wavelength close to a commensurate value. To access a better resolution of q_{cdw} and measure the surface, one needs to use grazing incident X-ray diffraction. Problem is, if the CDW is composed of CCDW regions periodically separated by discommensurations (localized phase jumps), the measured CDW mean wavevector won't be $\frac{2\pi}{\lambda_c}$, where λ_c is a commensurate wavelength, but instead one will measure $q_{cdw} = \frac{2\pi}{\lambda_c} + \frac{J}{l}$ where J is the phase jump of one discommensuration (2π for a soliton) and l the distance bewteen the periodic discommensurations. Therefore, the measured wavelength would seem incommensurate. To avoid this misinterpretation, one need to use a coherent X-ray beam with a coherence length at least of the order of l. If discommensurations are present at the surface, one will observe speckles as the supersatellites of figure 3.9, thus being able to make the difference between a strictly incommensurate CDW and CCDW regions separated by discommensurations.

6.7 Checking the numerical error convergence for the fits

The fit function 6.28, 6.29 and 6.30 are given by an infinite sum. But, numerically, one can only sum a finite number of terms. Therefore, one needs to evaluate the relative error that we make when cutting this sum in order to trust the numerous fits shown in the preceding sections. Since this is a tedious but necessary discussion about mathematics, we kept it for the last section of this chapter.

Looking at Eq6.26 and since we didn't consider bulk impurity pinning ($\omega_0 \to 0$), we need to control the convergence of the following sum

$$S(k_1, k_2) = \sum_{n_1=0}^{\infty} \sum_{n_2=0}^{\infty} \frac{(-1)^{n_1+n_2}}{(2n_1+1)(2n_2+1)a_{n_1,n_2}} \tanh\left(\frac{\pi}{2} a_{n_1,n_2}\right)$$
$$\text{where } a^2_{n_y,n_z} = \left[(2n_1+1)k_1\right]^2 + \left[(2n_2+1)k_2\right]^2 \tag{6.31}$$

This double series convergence at large n_1, n_2, for which the hyperbolic tangent term tends to one, goes as an "alternating sign inverse square" $\sim \frac{(-1)^n}{(2n+1)^2}$. But if $k_1, k_2 \ll 1$, one can taylor expand the tanh term and find a convergence as

$$\frac{(-1)^{n_1+n_2}}{(2n_1+1)(2n_2+1)a_{n_1,n_2}} \tanh\left(\frac{\pi}{2} a_{n_1,n_2}\right) \approx \frac{\pi}{2} \frac{(-1)^{n_1+n_2}}{(2n_1+1)(2n_2+1)}$$

Which goes as an "alternating sign inverse linear" convergence. Therefore, the lowest convergence rate is for this specific case $k_1, k_2 \ll 1$ and once this case is

understood, we expect all other series $S(k_1, k_2)$ for another set of parameters k_1, k_2 to converge faster. Defining this limit case sum for which $k_1, k_2 = 0$

$$S_{\text{limit},N_1,N_2} = \sum_{n_1=0}^{N_1} \sum_{n_2=0}^{N_2} \frac{(-1)^{n_1+n_2}}{(2n_1+1)(2n_2+1)} \tag{6.32}$$

where we made explicit that the sum is calculated up to a finite terms N_1 and N_2. The relative error made in this limit case $k_1, k_2 = 0$ is

$$\begin{aligned} E_{\text{limit},N_1,N_2} &\equiv \left| \frac{S_{\text{limit},\infty,\infty} - S_{\text{limit},N_1,N_2}}{S_{\text{limit},\infty,\infty}} \right| \\ &= \left| 1 - \left[1 + \frac{2}{\pi}(-1)^{N_1} \Phi\left(-1, 1, \frac{3}{2} + N_1\right) \right] \left[1 + \frac{2}{\pi}(-1)^{N_2} \Phi\left(-1, 1, \frac{3}{2} + N_2\right) \right] \right| \end{aligned} \tag{6.33}$$

where we used Mathematica to obtain the formula on the right hand side in which $\Phi(z, s, a)$ is the Lerch transcendent function. This relative error when both $N_1, N_2 = N$ is displayed in figure 6.20

We want to have a relative error less than 1% when performing the fit in order to avoid any numerical artifact. From figure 6.20, we observe that one need to sum up to the 63^{th} term to reach an error smaller than 1%.

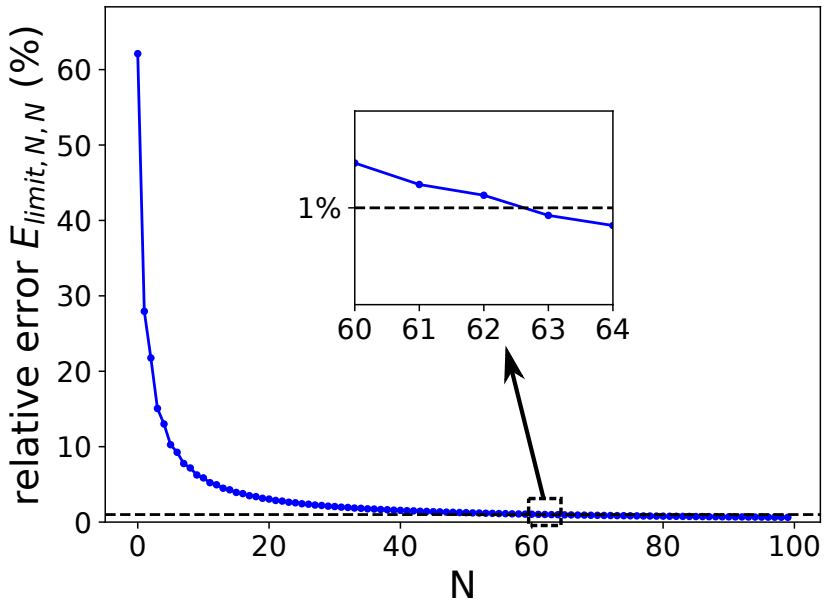

Figure 6.20: Relative error in the limit $k_1, k_2 = 0$ given by Eq6.33 with $N_1, N_2 = N$. Since we want an error smaller than 1% for the fits, we need to go up to the 63^{th} term in the sum as shown in the zoom.

To confirm that both N_1 and N_2 need to be greater than 63, we calculate E_{limit,N_1,N_2} for $N_1 \neq N_2$ and look where this error is smaller than 1%. The result is shown in figure 6.21 where the green color correspond to a set $\{N_1, N_2\}$ for

which $E > 1\%$ while in the blue regions $E < 1\%$. Since S is a series of terms with an alternating sign (from the $(-1)^{n_1+n_2}$ factor), we observe oscillations for low values of N_1 and N_2, but to be certain to have $E < 1\%$, one needs to reach the "non-oscillatory" region in the lower right corner, thus having at least $N_1, N_2 > 63$ as expected.

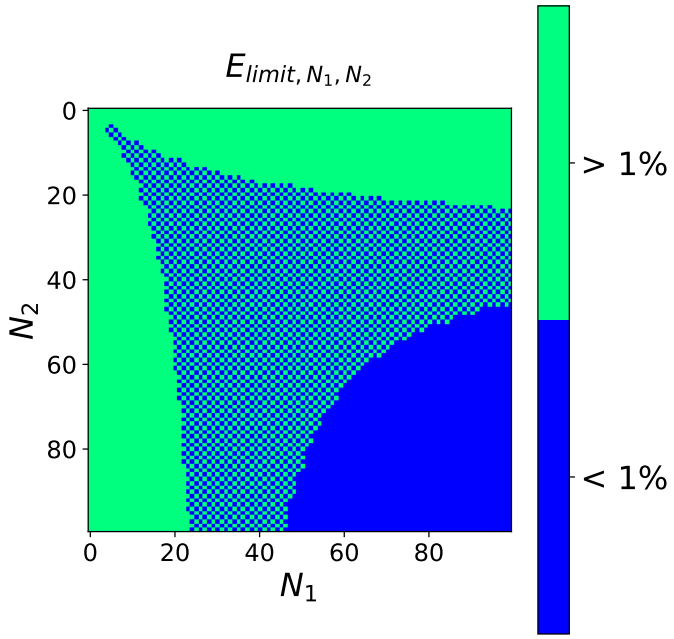

Figure 6.21: Relative error from Eq6.33 as function of N_1 and N_2. In green regions $E_{limit} > 1\%$ while in the blue ones $E_{limit} < 1\%$.

Therefore, in the general case $k_1, k_2 \neq 0$, for the sum $S(k_1, k_2)$ of Eq6.31 to reach a convergence of 1%, one simply need to calculate the terms for which $N_1, N_2 \leq 63$. In order to quantitatively confirm this, we calculate for several set $\{k_1, k_2\}$ the relative error given by the formula similar to Eq6.33

$$
\begin{aligned}
S_{N_1,N_2}(k_1,k_2) &= \sum_{n_1=0}^{N_1}\sum_{n_2=0}^{N_2} \frac{(-1)^{n_1+n_2}}{(2n_1+1)(2n_2+1)a_{n_1,n_2}} \tanh\left(\frac{\pi}{2}a_{n_1,n_2}\right) \\
E_{N_1,N_2}(k_1,k_2) &\equiv \left|\frac{S_{2000,2000}(k_1,k_2) - S_{N_1,N_2}(k_1,k_2)}{S_{2000,2000}(k_1,k_2)}\right|
\end{aligned}
\tag{6.34}
$$

where, since no closed form formula of $S_{\infty,\infty}(k_1, k_2)$ is available, we approximated it with $S_{2000,2000}(k_1, k_2)$.

The results are shown in figure 6.22 for several sets $\{k_1, k_2\}$. As expected from the discussion above, the worst case scenario is for $k_1, k_2 \ll 1$ where the convergence goes as E_{limit,N_1,N_2} presented in figure 6.21. In conclusion, to make a relative error smaller than 1% in calculating the sum Eq6.31, one needs to go up to the terms $N_1, N_2 \geq 63$. While running the several fits presented in this chapter, we choose to go up to $N_1, N_2 \geq 100$ for safety.

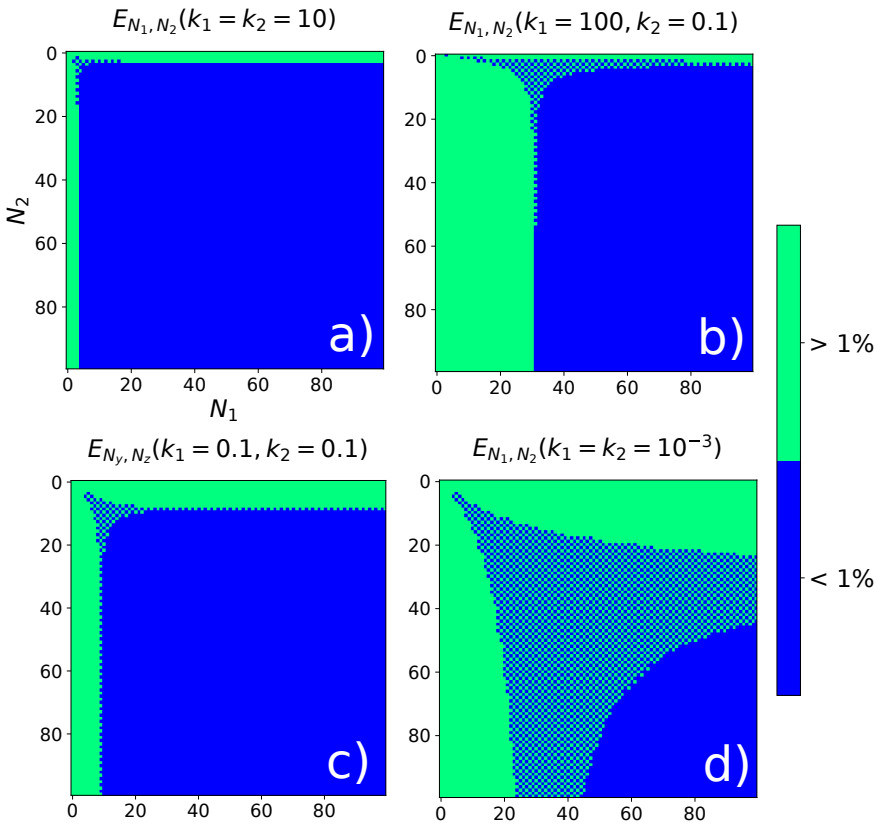

Figure 6.22: Relative error from Eq6.34 for several sets $\{k_1, k_2\}$. One can observe that the worst convergence behavior is obtain in the case $k_1, k_2 \ll 1$ displayed in d).

Conclusion and an open problem

Despite the fact that the first CDW theory was issued 65 years ago and the 1^{st} experimental evidence in TTF-TCNQ [3] was made 46 years from now, the CDW transition still provides many open topics as we have shown at the end of chapter 1. New CDW materials were discovered in this 21^{st} century like the Rare-earth tritellurides family to which $TbTe_3$ belongs (the sample studied in chapter 5). Furthermore, the discovery of CDW in cuprate superconductors led to new questions on the competition between CDW and superconductivity. Finally, experimental techniques evolve fast, for example the Free electron laser used during this PhD work achieved first lasing in April 2009. These new techniques open new topics, even about well-known CDW materials. This is the case in this thesis, in chapter 4, we study $NbSe_3$, for which the resistivity anomaly induced by the CDW was observed in 1976. Still, using the recently developed X-ray micro-diffraction setup at ID01 beamline of the ESRF, we were able to observe a new characteristic of this material, the CDW surface pinning in a space resolved manner.

We performed many experiments at instruments in large scale facilities during my thesis, we didn't mention all of them in this manuscript. Regarding X-ray diffraction from synchrotron, we went to SOLEIL (Orsay, France) on beamlines Crystal and Diffabs, ESRF (Grenoble, France) on beamline ID01 to perform the kmap experiments of chapter 4 and 5, MAXIV (Lund, Sweden) on beamline Nanomax for yet another X-ray micro-diffraction experiment on TbTe3. Finally, we had the opportunity to perform time-resolved X-ray diffraction at the Free electron laser LCLS (Stanford,USA) on beamline XCS. Since this experiment was performed in the last year of this PhD, we could only show preliminary results presented at the end of chapter 3.

The main result of this thesis is the observation of CDW surface pinning using the X-ray micro-diffraction technique on $NbSe_3$ described in chapter 4. This feature was supposed from resistivity experiments but with micro-diffraction we have a spatial micrometric resolution of the transverse CDW deformation under current. Many X-ray diffraction experiments were performed on $NbSe_3$ but they were done with a beamspot larger than the sample width, hence averaging the shear effect, making it invisible. What's more, we made sure that this feature wasn't observed on the Bragg, thus showing that this is an evolution of the CDW and not of the host crystal lattice.

Having observed this pinning, we wanted to check if this effect could fit several resistivity experiments from the literature in chapter 6. The author only found phenomenological formulas in the literature used to fit these data. The charge transport by soliton presented in chapter 3 and the phase slip process of appendix

B are well known from the literature. But surface pinning was never taken into account. From the CDW Lagrangian (or equivalently the free energy), the author calculated ϕ including surface pinning. The full expression is cumbersome but after controlling the numerical error, we were able to fit several experimental data. One question remains, we observed that for this types of resistivity measurements, bulk impurity pinning (ω_0 term) and surface pinning had the same effects. Therefore, further studies are needed to know whether it is relevant to make a theory with bulk impurity pinning or not, the ω_0 term being used frequently in the literature.

Then, we used the X-ray micro-diffraction technique to study the bulk of $TbTe_3$ in chapter 5. We observed a transverse deformation under current showing a hysteretic behavior which correspond to a CDW rotation (no compression-expansion). Since we were far from the sample borders, we can't conclude whether this shear is due to surface pinning in $TbTe_3$ or not. What's more, the author didn't find resistivity experiments showing size effects for this material as those performed on $NbSe_3$ and TaS_3 shown in chapter 6. Therefore, the question remains open on the origin of this CDW rotation under current. Finally, we observed the formation of strong pinning centers created by X-ray irradiation where the CDW presents a compression-expansion but no rotation.

We presented two small experimental results in chapter 3. The CDW solitons were observed with the use of coherent X-ray diffraction in $K_{0.3}MoO_3$. We went to ID01 beamline of ESRF to try and observe them in $NbSe_3$. Since the soliton diffraction pattern didn't appear, we have a lower boundary value of the distance between solitons in $NbSe_3$ in the middle of the sample $l_{NbSe_3} > 1.33\mu$m. Lastly, we shown preliminary results of the LCLS experiment showing a transverse "breaking" of the CDW in $NbSe_3$ under currents which (since the X-ray beam was coherent) creates a speckle pattern in the direction perpendicular to the CDW wavevector.

Using a coherent X-ray beam available at the free electron lasers but also in many synchrotron beamlines (including beamline ID01 of the ESRF), one could observe the hysteresis effect of the CDW under current. This hysteresis is visible in several results of this thesis. For example in chapter 4 on $NbSe_3$, in the reconstruction "back to 0 mA" in figure 4.12 the wavefront are still distorted. Even more obvious, a clear hysteresis loop is visible in figure 5.5 on $TbTe_3$. In the literature, this hysteresis effect was observed on several CDW materials in electrical conductivity experiments.

If this effect comes from CDW solitons being "blocked" inside the material from damping when current is stopped, one could observe these CDW phase jumps using a coherent X-ray beam. One should observe a speckle pattern on the CDW satellite peak. Scanning the sample from one electrical contact to the other, one can measure where the solitons are blocked, close to the contacts or in the middle of the sample.

The X-ray micro-diffraction tool used in chapter 4 and 5 is a very power technique that gives access to the local deformation of the CDW and could be used for many experiments. We give some ideas in the following list:

- We couldn't tell if the CDW rotation in $TbTe_3$ under current measured in chapter 5 was due to a surface pinning effect since we only scanned in the middle of the sample, far from the border. To solve this open problem, one can make the same micro-diffraction experiment under current near the sample upper and lower border. If the deformation is positive near one border and negative at the other (as

in $NbSe_3$, see figures 4.7 and 4.9) then one can confirm that the rotation is indeed due to surface pinning.

- In $NbSe_3$, in chapter 4, we used the micro-diffraction technique to scan in the middle of the sample, far from the electrical contacts. The question remains open of how the shear deformation varies from one contact to the other. Is this effect stronger near the electrical contacts or in the middle of the sample? How does this shear affect the solitons creations at the contacts? One could answer these questions making a map similar to the ones of chapter 4 close to the right and left contacts.

- $K_{0.3}MoO_3$ is a typical CDW material with a real metal-to-insulator transition. What's more, to this day, it's the only CDW material in which the soliton super satellites were observed with coherent X-ray diffraction (figure 3.9 of chapter 3). Furthermore, the longitudinal deformation and surface pinning effect were only measured by diffraction on $NbSe_3$ (surface pinning can be deduced in TaS_3 from the threshold measurements presented in chapter 6). Making a micro-diffraction experiment on $K_{0.3}MoO_3$ near the borders and close to the electrical contacts would show if whether or not the longitudinal deformation and surface pinning are phenomenons common to several CDW material or not.

- Several papers from the literature show a reaction of the CDW to a current applied in the transverse direction [173, 174, 175, 176, 177] (in this thesis we only applied current in the longitudinal direction). Making a micro-diffraction scan near the current injection, one could observe the local CDW evolution under this transverse electric field and see if it fit the theoretical prediction [173].

As a last word, we end this manuscript with an open problem.

6.8 Soliton antisoliton annihilation at the center of the sample?

In chapter 3, we showed how the creation of solitons ($+2\pi$ CDW phase jump) near the electrical contact can explain the non-linear I-V behavior in the CDW state. We presented two diffraction experiments consistent with this theory. The creation process (phase-slip) was explained in the following way. Under an applied electric field, the CDW undergoes an expansion at the left electrical contact (see figure 3.6). The system can release some elastic energy by creating a soliton near the contact. Under the electric field, the soliton starts to slide in the sample toward the right contact. After a transient acceleration, it reaches a stationary speed v as was shown by Fogel et al. [112].

But we forgot to talk about what happens at the right contact of figure 3.6. If the current injection is symmetric, we expect antisoliton (-2π phase jump) to be created there. Under the electric field, they will travel toward the left contact and the situation becomes the one presented in figure 6.23 in which soliton and antisoliton travel toward each other.

The question is, what happens when the solitons and antisolitons meet? Two cases may occur. First, the soliton equation always present a damping term as in Eq3.1 from its coupling with lattice vibrational modes (corresponding to phonons slightly modified by the presence of the solitons). It was shown that during a soliton-

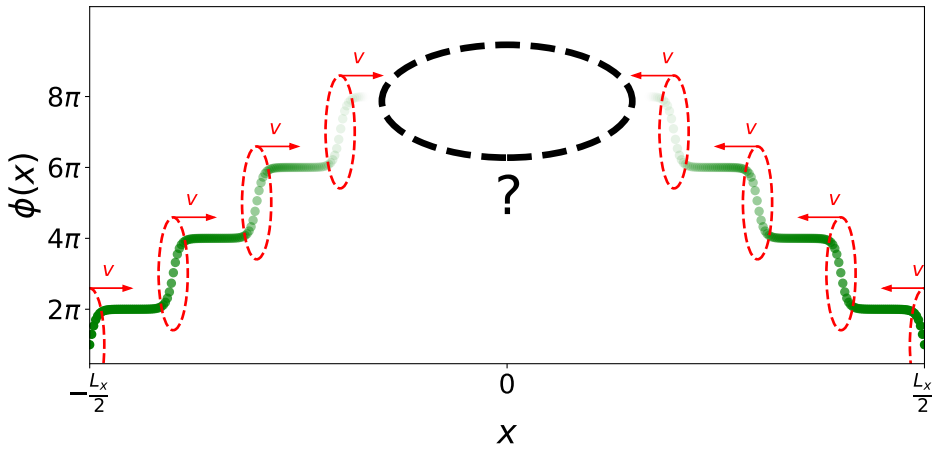

Figure 6.23: If the current injection is symmetric, we expect soliton (+2π phase jump) to be created at the left contact and antisoliton (-2π) at the right contact with the same speed v but traveling in opposite directions. If this is the case, what happens when they collide in the middle of the sample?

antisoliton collision, if their relative speed is small enough (or if damping is strong enough), they can form a bound state called "breather" and gradually disappear by damping [178, 111]. But if their relative speed is large enough (or damping small enough), they can pass through each other having only a small dephasing from their interaction [111].

Therefore, the two cases are quite different. Since one can increase the solitons speed by increasing the applied field, one could observe the transition between the first and second case. The questions whether this transition could be studied and is the field value necessary to observe this transition accessible experimentally are still open at the time of writing.

Appendix A

Constructing the Lagrangian from experimental observations

A.1 CDW order parameter and standard type of Lagrangian

In this appendix, we show how to construct the Lagrangian of a 1D CDW and how to connect its parameters with some experimental observations. Then, we give a generalized 3D expression.

The usual order parameter for a CDW is its gap Δ. Adding the possibility of spatial and time fluctuation, the gap can be written as [18]

$$\Delta(x,t) = [\Delta_0 + \delta(x,t)]\, e^{i\phi(x,t)}$$

where Δ_0 is the equilibrium (real) value of the gap without external perturbation, ϕ refers to phase fluctuation (equivalent to the phase in the CDW charge density $\rho(x,t) = A\cos[2k_F x + \phi(x,t)]$) and finally δ is the deviation of the gap modulus from equilibrium.

A standard Lagrangian density expression with the allowed symmetries of the system is

$$\mathcal{L}_0 = \alpha\left[|\Delta_t|^2 - c^2|\Delta_x|^2 - \omega_A^2\delta^2\right]$$

where α is an overall constant of no interest (which disappears in the Euler-Lagrange equation) here since we only consider a CDW phase and I will fix $\alpha \equiv 1$. c and ω_A are constants whose relation to experiments will be explained in the next sections. We used the notation $\Delta_i \equiv \frac{\partial\Delta}{\partial i}$, where $i = x, t$. Developing this expression, one finds

$$\boxed{\begin{aligned}\mathcal{L}_0 =& \delta_t^2 - c^2\delta_x^2 - \omega_A^2\delta^2 \\ &+(\Delta_0+\delta)^2\left(\phi_t^2 - c^2\phi_x^2\right)\end{aligned}} \tag{A.1}$$

A.2 CDW phase collective mode : the phason

Assuming a constant amplitude δ, the Euler Lagrange equation of EqA.1 for the phase ϕ is

$$\phi_{tt} - c^2\phi_{xx} = 0 \tag{A.2}$$

A wave-like solution of the form $\phi(x,t) = \phi_0 e^{i(\omega_\phi t - qx)}$ gives the following dispersion relation

$$\begin{aligned} -\omega_\phi^2 + c^2q^2 &= 0 \\ \omega_\phi &= cq \end{aligned} \tag{A.3}$$

This is called the phason mode of the CDW. It was observed in a neutron scattering experiment by Pouget et al. in 1991 [179] leading to an experimental value of the phason velocity $c = 3.3 \pm 0.5 \times 10^5$ cm/sec in $K_{0.3}MoO_3$ at 175K. This parameter depends on the temperature as reported by Hennion et al. in 1992, by neutron scattering [180].

A.3 CDW amplitude collective mode : the amplitudon

This time, taking ϕ as a constant and deriving the Euler-Lagrange equation for δ we get

$$\delta_{tt} - c^2\delta_{xx} - b\delta = 0$$

The wave-solution $\delta(x,t) = \delta_0 e^{i(\omega_\delta t - qx)}$ leads to the following dispersion

$$\begin{aligned} -\omega_\delta^2 + c^2q^2 - \omega_A^2 &= 0 \\ \omega_\delta &= \sqrt{c^2q^2 + \omega_A^2} \end{aligned} \tag{A.4}$$

Therefore, ω_A correspond the frequency of the amplitude mode at $q = 0$, called gap of the amplitude mode. This was measured in $K_{0.3}MoO_3$ using neutrons by Pouget et al. [179] and in Raman spectroscopy by Travaglini and Wachter [181]. Again, b is temperature dependent as was measured in [179].

A.4 Incorporating impurity pinning to avoid an infinite conductivity

The Lagrangian constructed above does not depend on the absolute value of the CDW phase ϕ. Therefore, it still has translation invariance, leading to an infinite conductivity. As said in chapter 3, this is not the case experimentally and one needs to include a pinning term, coming from either interactions with impurities or surface pinning.

What's more, since ϕ is a phase, adding or removing a multiple of 2π does not change anything to the physical description. Hence, an effective impurity pinning term is

$$\boxed{\mathcal{L}_{pin} = -(\Delta_0 + \delta)^2 \omega_0^2 \left[1 - \cos(\phi)\right]} \tag{A.5}$$

which fixes ϕ to be a multiple of 2π in the ground state.

Including this term, the equation giving the phason dispersion EqA.2 becomes

$$\boxed{\phi_{tt} - c^2 \phi_{xx} + \omega_0^2 \sin(\phi) = 0} \tag{A.6}$$

Assuming a small wave amplitude $\phi(x,t) = \phi_0 e^{i(\omega_\phi t - qx)}$ with $\phi_0 \ll 2\pi$, the equation becomes

$$\begin{aligned} &\phi_{tt} - c^2 \phi_{xx} + \omega_0^2 \phi \approx 0 \\ &\omega_\phi = \sqrt{c^2 q^2 + \omega_0^2} \end{aligned} \tag{A.7}$$

As seen from this new dispersion relation, pinning introduces a gap in the phason mode $\omega(q = 0) = \omega_0$ which was measured in [179] in $K_{0.3}MoO_3$ leading to $\frac{\omega_0^2}{2\pi} = 0.2 \pm 0.1$ THz for a temperature between 130 and 170 K.

A.5 Soliton from the non-linear pinning term

Of even more interest for us is the equation A.6. This is known as the Sine-Gordon equation which involves non-linearity and a topologically protected solution, the "soliton" [111]

$$\begin{aligned} \phi_{sol}(x,t) &= 4\text{atan}\left[\exp\left(\pm\frac{x - x_0 - vt}{l_s}\right)\right] \\ l_s &= \frac{c}{\omega_0}\sqrt{1 - \left(\frac{v}{c}\right)^2} \end{aligned} \tag{A.8}$$

where the + sign correspond to a soliton and − to an antisoliton, x_0 is the soliton's position at $t = 0$, v its speed and l_s its width. The solution is depicted at a fixed time t in figure A.1. ϕ_s is a $+2\pi$ (-2π for an antisoliton) jump of the phase localized on a typical distance l_s and moving at a constant speed v.

From the expression of l_s, we see that the maximum soliton speed is the phason velocity c. Furthermore, as the speed increases, l_s decreases and the soliton becomes thinner. One can see this phenomenon as a relativistic Lorentz contraction where the speed of light is replaced with the phason velocity c. Compare the Lorentz factor $\gamma = 1/\sqrt{1 - \left(\frac{v}{c_{\text{light}}}\right)^2}$ with the expression of l_s.

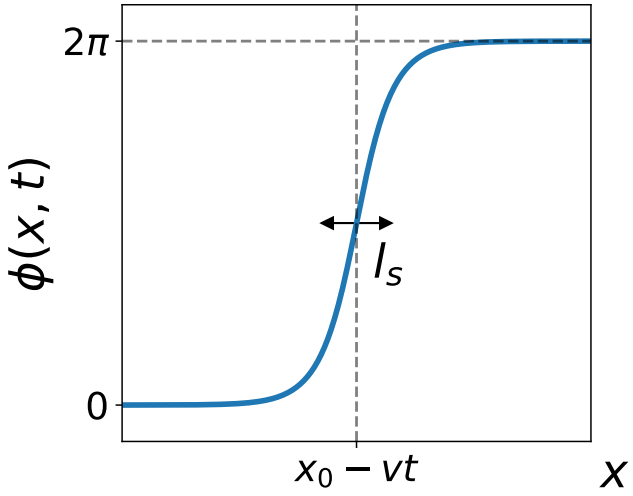

Figure A.1: Topological soliton solution of EqA.6 corresponding to a localized $+2\pi$ jump of the phase.

A.6 Interaction of the CDW with an electric field

Since the CDW is a periodic electric charge density, one expects a distortion to occur when an electric field E is applied to the sample. Hence, we must add a term to the Lagrangian EqA.1 in order to include E. One could construct this term from a microscopic theory [103] but this needs quite the mathematical artillery including the chiral anomaly inherent to the theoretical description, due to an approximation of the energy band as a linear one [182] (instead of a cosine form). Instead, we will use a quantitative argument.

First, one can show that there are 2 electrons per wavelength by the following argument :

- Take a 1D crystal with lattice parameter a. In k space, the distance between each discrete state is $dk = \frac{2\pi}{L}$.

- The number of electrons N_{el} (taking into account the spin) is two times the number of states between $-k_F$ and $+k_F$, where k_F is the Fermi wavevector. Hence $N_{el} = 2\frac{2k_F}{dk} = \frac{2k_F L}{\pi}$

- The number of CDW periods of the whole system is $N_\lambda = \frac{L}{\lambda_{cdw}}$, where λ_{cdw} is the CDW wavelength. Since $\lambda_{cdw} = \frac{2\pi}{2k_F}$, one gets $\boxed{N_\lambda = \frac{k_F L}{\pi} = 2N_{el}}$ cqfd.

This quantitative argument is only true at $T = 0$ K.

Thus, one can add 2 electrons to the CDW system by changing the fermi wavevector $k_F \rightarrow k_F + dk$. This additional charge can be described as well with the CDW's phase derivative ϕ since the new charge density $\rho = A\cos[(2k_F + dk)x] \Longleftrightarrow A\cos[2k_F x + \phi(x)]$ where $\phi(x) = dk \times x$. One can generalize this to a local expression of an additional charge density (see [18] p110) given by $\rho_{ad}(x) \equiv -(\Delta_0 + \delta)^2 \eta \frac{\partial \phi}{\partial x}$ where $(\Delta_0 + \delta)^2 \eta = \frac{2e}{dk}$ at $T = 0$ K.

In conclusion, a deformation of the CDW along x leads to a local charge which interacts with the local electric potential. Since, in this thesis, we are only interested

in the case of a constant E, with a corresponding potential Ex, then the electric field term in the Lagrangian density is

$$\boxed{\mathcal{L}_{el} = -(\Delta_0 + \delta)^2 \eta E x \phi_x} \tag{A.9}$$

Using EqA.1, A.5 and A.9, one finds the following Euler-Lagrange equation in 1D

$$\boxed{\phi_{tt} - c^2 \phi_{xx} + \omega_0^2 \sin(\phi) = \eta E} \tag{A.10}$$

A.7 3D form of the Lagrangian for surface pinning problem

To take into account surface pinning, we need the 3D version of the Lagrangian which is given here

$$\boxed{\begin{aligned} \mathcal{L}_{3D}[\delta, \phi] =& \delta_t^2 - c_x^2 \delta_x^2 - c_y^2 \delta_y - c_z^2 \delta_z - \omega_A^2 \delta^2 \\ &+ (\Delta_0 + \delta)^2 \{ \phi_t^2 - c_x^2 \phi_x^2 - c_y^2 \phi_y^2 - c_z^2 \phi_z^2 \\ &- \omega_0^2 \left[1 - \cos(\phi) \right] \\ &- \eta E x \phi_x \} \end{aligned}} \tag{A.11}$$

We will use parts of this Lagrangian in the main text, depending on the specific feature we want to shed light on.

Appendix B

Vortex ring energy in the presence of an electric field

B.1 Energy of a vortex-ring without electric field

As explained in details in appendix A, under external perturbation (an electric field in our case), one can describe the CDW using the gap Δ in the electronic spectrum as an order parameter, allowing for spatial and temporal fluctuations $\Delta(\vec{r},t) = [\Delta_0 + \delta(\vec{r},t)]\, e^{i\phi(\vec{r},t)}$ where ϕ is the CDW phase. The periodic electronic density in the CDW phase is $\rho(\vec{r},t) = A(\vec{r},t)\cos[2k_F x + \phi(\vec{r},t)]$, with A related to $|\Delta|$.

A vortex (antivortex) in a CDW system is a configuration where the phase $\phi(\vec{r})$ varies by 2π (-2π) as one moves around the center (following the green arrow in figure B.1 b)). A modulation of the phase costs an elastic energy as shown in appendix A, and since the phase gradient becomes infinite at the vortex's center the amplitude $|\Delta(\vec{r})|$ must drop to zero near the vortex center position, otherwise the elastic energy would diverge (black dot in Fig. B.1).

In order to visualize the relation between the phase vortices and the soliton, a vortex-antivortex configuration is depicted in Figure B.2. As seen in this figure, a soliton is located in between the 2 vortices centers. Hence a soliton can be created in a CDW system by the creation of a vortex-antivortex configuration and increasing the distance between the 2 centers until the 2 vortices annihilate at the sample boundaries. This is the so-called "phase-slip" process. This phenomenon cost a finite amount of energy, therefore it only occurs if the applied electric field is large enough. In order to have an expression of this threshold field, a derivation of the vortex-antivortex pair energy is given here.

As seen in Fig B.2, there are 2 lines starting at the vortices centers where ϕ jumps from 0 to 2π. Since ϕ is a phase $\phi = 2\pi$ is equivalent to $\phi = 0$ and the phase is in fact continuous on these lines. But one can use the fact that ϕ is non analytic there to perform the calculation. First, we perform a rotation of the vortices in order to have this non-analytic line between the 2 centers as if Fig B.3. Now the soliton located in the middle of the pair seems different but since ϕ is a phase, $\phi - 2\pi \Leftrightarrow \phi$, hence the configurations of Fig B.3 b) and Fig B.2 b) are strictly equivalent.

In the following calculation, we forget about the amplitude part in the energy and

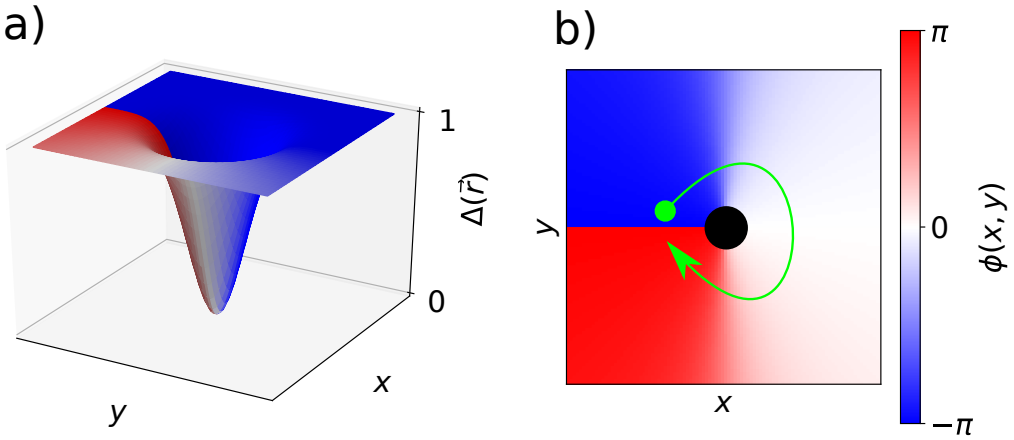

Figure B.1: a) Amplitude of the CDW close to the vortex 's center b) Phase $\phi(x,y)$ in the presence of a vortex. The phase change by $+2\pi$ as one follows the green arrow. Since the phase's gradient becomes infinite at the vortex's center, the amplitude drops to zero there, symbolized by the black dot.

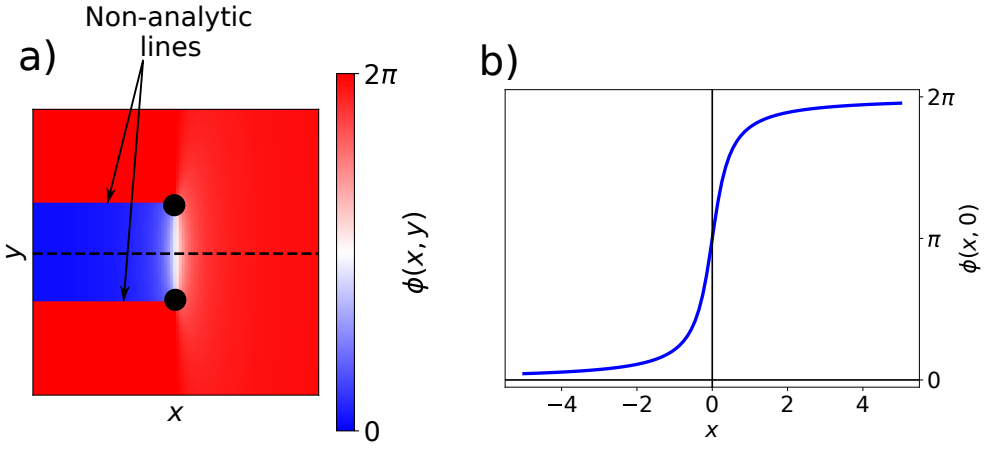

Figure B.2: a) Vortex-antivortex configuration. The black dots correspond to the center of the vortex and antivortex respectively. b) Phase value along the black dashed line of a). A soliton is located in between the 2 centers.

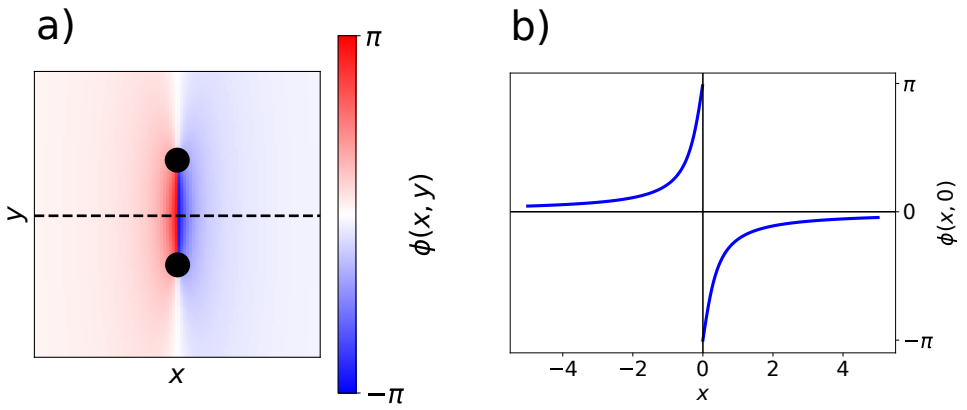

Figure B.3: a) vortex-antivortex configuration after a rotation. The "non-analytical" line is now between the vortices'centers. b) The soliton in between the centers. Since ϕ is a phase, $\phi - 2\pi \Leftrightarrow \phi$ and the soliton configuration presented here is equivalent to the one of Fig B.2 b).

only consider the phase elastic energy in order to have a closed form expression. We assume that the amplitude drops abruptly to 0 at a distance ξ from the vortex center where ξ is the CDW coherence length. Using a Runge-kutta numerical method, we could show that Δ drops exponentially to 0 near the center on a length scale of the order of ξ, hence our approximation is justified.

The 2D elastic energy expression is (see appendix A)

$$\begin{aligned} E_{pair} &= \iint \left(\vec{\nabla}\phi\right)^2 d^2\vec{r} \\ &= \iint \left[\vec{\nabla}.\left(\phi\vec{\nabla}\phi\right) - \phi\Delta\phi\right] d^2\vec{r} \end{aligned} \tag{B.1}$$

For a vortex at the origin, the gradient and laplacian read

$$\begin{aligned} \vec{\nabla}\phi_v &= \frac{1}{r}\vec{u_\theta} \\ \vec{\nabla}(\vec{\nabla}\phi_v) = \Delta\phi &= \frac{1}{r}\frac{\partial}{\partial\theta}(\frac{1}{r}) = 0 \,\forall r \neq 0 \end{aligned}$$

Since at the vortex's center the amplitude goes to 0, the laplacian term in (B.1) can be dropped and the energy expression becomes

$$\begin{aligned} E_{pair} &= \iint \vec{\nabla}.(\phi\vec{\nabla}\phi)d^2\vec{r} \\ &= \oint_\Sigma \phi\vec{\nabla}\phi.d\vec{l} \end{aligned} \tag{B.2}$$

where Σ correspond to the boundary of the function's domain. Remembering that the function as a non-analitycal line (see Fig B.3), one needs to include it as a boundary. Σ is depicted in red in Fig B.4 for a vortex-antivortex configuration.

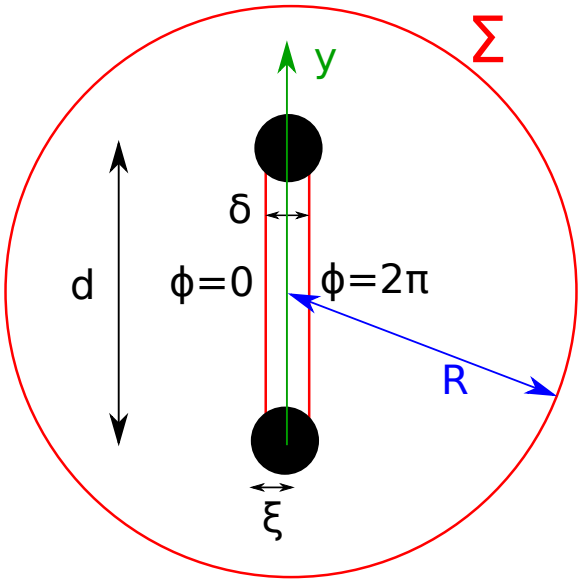

Figure B.4: The contour corresponding to Σ in (B.2) correspond to the red one when $\delta \to 0$ and $R \to \infty$. The 2 black circle of radius ξ are the vortex and antivortex centers of figure B.3, where the CDW amplitude drops to zero $|\Delta| = 0$.

Since $\vec{\nabla}\phi \propto 1/|\vec{r} - \vec{r}_{cen}|$ where $\vec{r}_{cen}$ is the vortex center position, the energy term coming from the red circle in Fig B.4 tends to 0 as $R \to \infty$.Then, for $\delta \to 0$, only the red line on the right where $\phi = 2\pi$ will contribute to (B.2). Using $\vec{\nabla}\phi = \pm\frac{1}{r}\vec{u_\theta}$ where the $+$ sign is for the vortex and $-$ sign for the antivortex, (B.2) becomes

$$\begin{aligned} E_{pair} &= 2\pi \int_{\xi}^{d-\xi} (\frac{1}{y} - \frac{1}{y-d})\, dy \\ &= 2\pi[\ln(\frac{d-\xi}{\xi}) - \ln(\frac{d-\xi-d}{\xi-d})] \\ &= 2\pi \ln(\frac{(d-\xi)^2}{\xi^2}) \\ &= 4\pi \ln(\frac{d-\xi}{\xi}) \end{aligned} \tag{B.3}$$

This was for the creation of a soliton in 2D by a vortex-antivortex pair. But since the CDW appears in 3D material, one needs a way to create the soliton in 3D. This is done by a vortex ring, see Figure B.5, which is a combination of vortex-antivortex pairs along a circle, whence the name "vortex-ring". The soliton is located inside the ring similarly to figure B.2 a).

Since the vortex ring is a combination of vortex-antivortex pairs in a rotational symmetry, the energy of the ring is equal to the one of 1 pair times half the ring perimeter (the "half" is here to avoid counting each pair twice).

$$E_{vr} = E_{pair} \times \frac{2\pi d}{2} = 4\pi^2 d \ln(\frac{d-\xi}{\xi}) \tag{B.4}$$

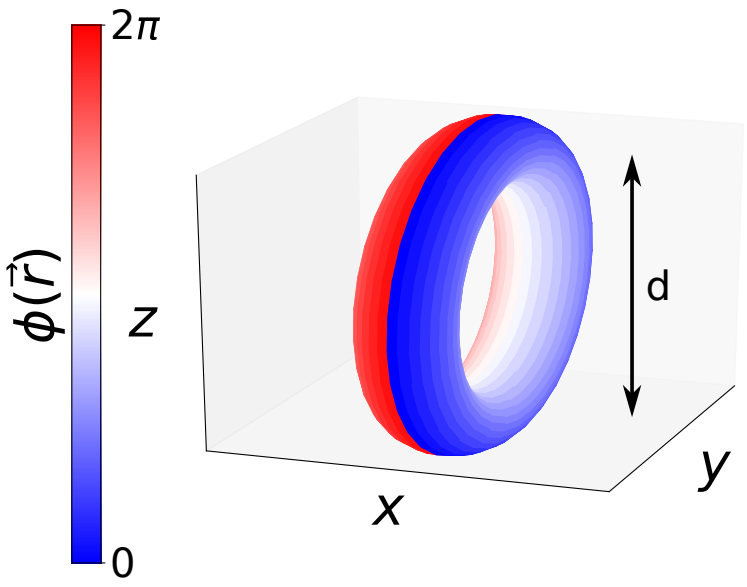

Figure B.5: Phase ϕ in the presence of a vortex ring. Only a surface at a given distance of the ring is depicted. ϕ increases by 2π as one goes around the ring.

B.2 Relaxation of the CDW elastic energy by the soliton inside the vortex-ring

But, since (B.4) is always positive, why would a vortex ring appear in the CDW? The answer comes from the lowering of the elastic energy caused by the soliton. In the presence of an external electric field (an applied current), the CDW distorts. The presence of a soliton partially relaxes the strain near the electrical contacts, hence the soliton at the center of the vortex ring lowers the total energy. But since it cost some energy to create the ring, this process doesn't happen if the electric field is not strong enough. Above a threshold field, the ring is spontaneously created and a soliton appears in the CDW near one of the contacts. This is called the "phase-slip" process.

In the presence of an electric field and a vortex ring, the phase is $\phi(\vec{r}) \equiv \phi_0(\vec{r}) + \phi_{vr}(\vec{r})$ where ϕ_0 is the distortion due to the electric field and ϕ_{vr} the one due to the vortex ring. The energy expression is

$$\begin{aligned} E &= \iiint (\vec{\nabla}\phi)^2 d^3\vec{r} \\ E &= \iiint [(\vec{\nabla}\phi_0)^2 + 2\vec{\nabla}\phi_0\vec{\nabla}\phi_{vr} + (\vec{\nabla}\phi_{vr})^2] d^3\vec{r} \end{aligned} \tag{B.5}$$

The first term correspond to the elastic energy without vortex ring which is not important for us here since it's present whether the ring exists or not. The last one is the energy of the ring without electric field which is already given in (B.4). Only the second term is of importance here.

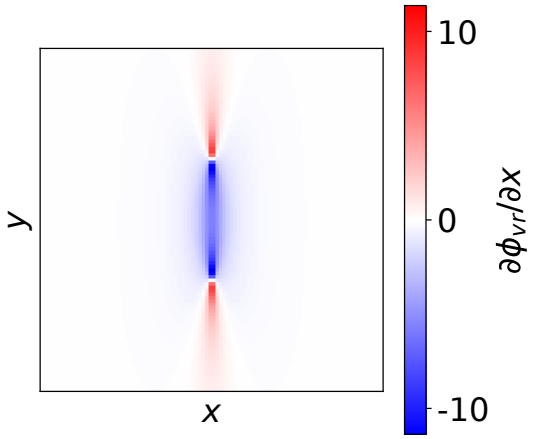

Figure B.6: Derivative along x of the phase of Figure B.2. The derivative is non-null only near the center of the vortex ring.

As said in chapter 6, the ring starts growing in $(x, y, z) = (L_x/2, 0, 0)$, far from the sample transverse borders in $y = \pm L_y/2$ and $z = \pm L_z/2$. From Eq6.23, one can find that $\frac{\partial \phi_0}{\partial y}(\frac{L_x}{2}, 0, 0) = \frac{\partial \phi_0}{\partial z}(\frac{L_x}{2}, 0, 0) = 0$. As seen in figure B.6, $\frac{\partial \phi_{vr}}{\partial x} \neq 0$ only near the ring center. Furthermore, assuming that $\frac{\partial \phi_0}{\partial x}$ varies slowly regarding the vortex ring size, one can make the approximation $\frac{\partial \phi_0}{\partial x}(\frac{L_x}{2}, y, z) \approx \frac{\partial \phi_0}{\partial x}(\frac{L_x}{2}, 0, 0)$ and take this constant term out of the integral.

Performing the calculation first for a vortex-antivortex pair, the relaxation energy reads

$$E_{relax\,pair} = \frac{\partial \phi_0}{\partial x} \iint \frac{\partial \phi_{vr}}{\partial x}\, dxdy$$

where we now write $\partial\phi_0/\partial x(L_x/2, 0, 0)$ as $\partial\phi_0/\partial x$ for simplicity of notation. Using Mathematica to perform the integral, we found

$$E_{relax\,pair} = -d\pi \frac{\partial \phi_0}{\partial x}$$

This is the value for one vortex-antivortex pair. Taking into account all the perimeter for a vortex ring (divided by 2 to avoid double counting as before), one finds

$$E_{relax} = -\pi^2 d^2 \frac{\partial \phi_0}{\partial x} \tag{B.6}$$

The total energy of the ring in the presence of an external electric field is the sum of B.4 and B.6

$$E_{tot} = 4\pi^2 d \ln(\frac{d - \xi}{\xi}) - \pi^2 d^2 \frac{\partial \phi_0}{\partial x} \tag{B.7}$$

This energy is depicted as a function of the ring diameter d in Figure B.7.

For a zero electric field $\frac{\partial \phi_0}{\partial x} = 0$ and the vortex ring costs a positive amount of energy (blue curve of Figure B.7) hence the phase slip process won't occur. As the electric field increases, $\frac{\partial \phi_0}{\partial x}$ increases and the competition between the positive d term

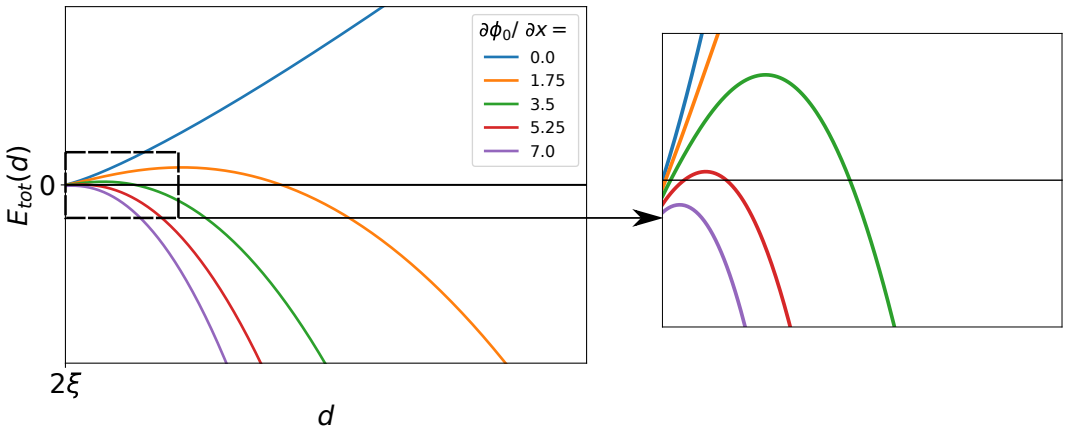

Figure B.7: Energy EqB.7 as a function of the vortex ring diameter d for different value of the strain term $\partial\phi_0/\partial x$. For a non zero strain, an energy barrier forbid the vortex ring to appear (blue,orange,green and red curve). For a large enough strain (purple curve), $E_{tot}(d)$ is always negative and the ring can spontaneously appear.

and negative d^2 in (B.7) induces a negative energy for the ring at large diameter d. Hence the ring configuration becomes favorable. But a positive energy barrier forbid the ring to appear at zero temperature (orange,green and red curve of Figure B.7). As the electric field increases, this barrier height decreases progressively. Once this barrier attains 0, the ring's energy is always negative (purple curve of Fig B.7) hence the ring spontaneously appears and a soliton is created at the contact. Defining ϕ_c' the critical value of $\frac{\partial\phi_0}{\partial x}$ where $E_{tot} \leq 0 \,\forall\, d$, an expression for this critical strain can be obtained by the following arguments. As seen in Fig. B.7, the equation $E_{tot}(d_0) = 0$ has 2 solutions for $\frac{\partial\phi_0}{\partial x} < \phi_c'$, 1 solution for $\frac{\partial\phi_0}{\partial x} = \phi_c'$ and none for $\frac{\partial\phi_0}{\partial x} > \phi_c'$. Hence, finding the value d_0 which satisfy the equation and then, the value $\frac{\partial\phi_0}{\partial x}$ for which d_0 becomes undefined gives directly ϕ_c'.

$$E_{tot}(d_0) = 0 \rightarrow d_0 = \frac{\frac{\partial\phi_0}{\partial x}\xi - 4\mathrm{W}(-\frac{1}{4}\frac{\partial\phi_0}{\partial x}\xi e^{\frac{1}{4}\frac{\partial\phi_0}{\partial x}\xi})}{\frac{\partial\phi_0}{\partial x}}$$

Where $\mathrm{W}(x)$ is the Lambert W function, inverse of the function $f(x) = xe^x$. Since this function is defined only for $x \geq -1/e$, the critical strain is given by

$$\begin{aligned} -\frac{1}{4}\phi_c'\xi e^{\frac{1}{4}\phi_c'\xi} &= -\frac{1}{e} \\ \frac{1}{4}\phi_c'\xi &= \mathrm{W}(e^{-1}) \\ \phi_c' &= \frac{4\mathrm{W}(e^{-1})}{\xi} \approx \frac{1.1}{\xi} \end{aligned} \tag{B.8}$$

The corresponding ring size at the critical strain ϕ_c' is

$$d_0 = \left[1 + \frac{1}{\mathrm{W}(e^{-1})}\right]\xi \approx 4.6 \times \xi$$

which is small compared to the sample dimensions, thus justifying the approximation $\vec{\nabla}\phi_0(\frac{L_x}{2}, y, z) \approx \vec{\nabla}\phi_0(\frac{L_x}{2}, 0, 0)$ that we used in the integral of EqB.5.

Appendix C

Does a CDW soliton contains an electron?

C.1 Expression of the electronic density in the presence of a CDW soliton

A qualitative argument for the presence of an electron in a CDW soliton is that there is one electron per wavelength in the CDW. Since the soliton (2π phase jump) adds exactly one wavelength, an electron should be localized there. In order to verify this qualitative argument, we used a numerical exact diagonalization on the CDW Hamiltonian (in which a units change is made to simplify the notation)

$$\mathcal{H} = \sum_{n=-N_{site}/2}^{N_{site}/2} \left[\Delta \cos\left[qn + \phi(n)\right] c_n^\dagger c_n - \left(c_{n+1}^\dagger c_n + c_n^\dagger c_{n+1}\right)\right]$$

where N_{site} is the number of site (we choose 600 sites), Δ is the CDW's amplitude, q the CDW's wavevector ($\frac{2\pi}{6}$ in our case), c and $c^\dagger$ are electron annihilation and creation operators and finally $\phi(n)$ is the CDW phase for which we use the expression of a soliton localized in the middle of the atomic chain

$$\phi(n) = 4 \times \text{atan}[\exp(\frac{n}{l_s})] \tag{C.1}$$

where l_s is the soliton width.

To perform exact diagonalization, we need to write the Hamiltonian as $\mathcal{H} = \vec{\psi}^\dagger h \vec{\psi}$ with

$$\vec{\psi} = \begin{pmatrix} c_{-N_{site}/2} \\ c_{-N_{site}/2+1} \\ \vdots \\ c_{N_{site}/2} \end{pmatrix} ; \vec{\psi}^\dagger = \begin{pmatrix} c_{-N_{site}/2}^\dagger & c_{-N_{site}/2+1}^\dagger & \cdots & c_{N_{site}/2}^\dagger \end{pmatrix}$$

$$h = \begin{pmatrix} f\left(-\frac{N_{site}}{2}\right) & -1 & 0 & 0 & ... & 0 & 0 \\ -1 & f\left(-\frac{N_{site}}{2}+1\right) & -1 & 0 & ... & 0 & 0 \\ 0 & -1 & f\left(-\frac{N_{site}}{2}+2\right) & -1 & ... & 0 & 0 \\ & & & \vdots & & & \\ 0 & 0 & 0 & 0 & ... & -1 & f\left(\frac{N_{site}}{2}\right) \end{pmatrix}$$

where we make use of the shorthand notation $f(n) = \Delta \cos[nq + \phi(n)]$.

Writing $D = U^T h U$ where D is a diagonal matrix and U is an orthogonal matrix (since h is real), one can write the Hamiltonian as $\mathcal{H} = \vec{\psi}^\dagger U D U^T \vec{\psi} \equiv \vec{\phi}^\dagger D \vec{\phi}$ where

$$\vec{\phi} = \begin{pmatrix} e_{-N_{site}/2} \\ e_{-N_{site}/2+1} \\ \vdots \\ e_{N_{site}/2} \end{pmatrix}$$

e_n being the creation operator for the n^{th} eigenstate. The relation between the operators c and e is given by

$$\begin{aligned} U^T \vec{\psi} &= \vec{\phi} \\ \vec{\psi} &= U \vec{\phi} \\ c_n &= \sum_j U_{nj} e_j \Longrightarrow c_n^\dagger = \sum_j U_{nj} e_j^\dagger \end{aligned}$$

leading to the expression of the operator of the electronic density on site n

$$\rho_n = c_n^\dagger c_n = \sum_{lj} U_{nj} U_{nl} e_j^\dagger e_l$$

Therefore, for a state $|S\rangle$ with a given band's filling, the electronic density is

$$\begin{aligned} \rho(n) &= \langle S|\rho_n|S\rangle \\ &= \sum_{jl} U_{nj} U_{nl} \langle S|e_j^\dagger e_l|S\rangle \\ &= \sum_{jl} U_{nj} U_{nl} \delta_{jl} [1 - \theta(j - N_{el})] \\ \rho(n) &= \sum_{j<N_{el}} U_{nj}^2 \end{aligned} \tag{C.2}$$

where $N_{el} = \frac{N_{site}}{\lambda}$ is the number of electrons in the CDW system and λ is the CDW wavelength.

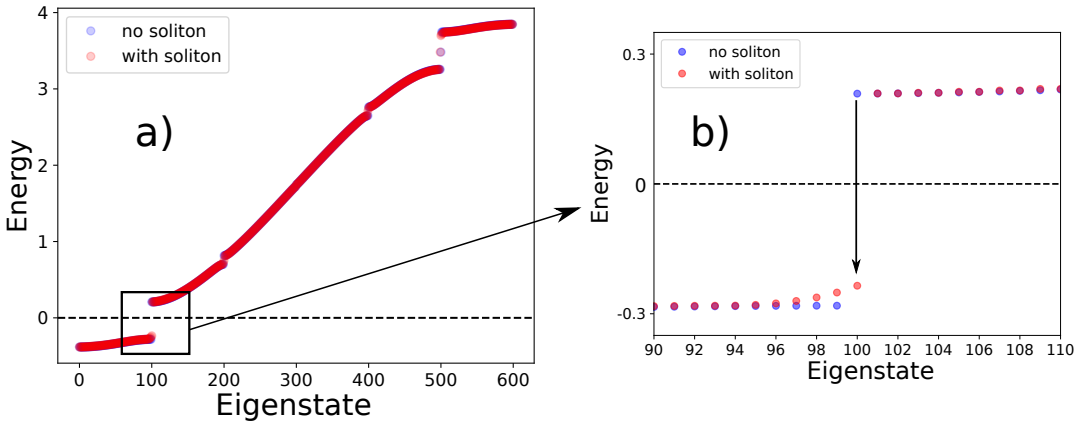

Figure C.1: a) Energy band for a CDW of wavelength $\lambda = 6$ with and without soliton. The 2 bands overlap for most eigenstates except near the gap. b) zoom on the eigenstates near the gap. The presence of the soliton induces a reduction of the 1^{st} exited state's energy schematized by the black arrow.

C.2 Numerical results and confirmation of the presence of an electron inside the soliton

As said earlier, we perform a numerical exact diagonalization for a CDW with wavelength $\lambda = 6$ and a chain of 600 sites (a multiple of λ). Furthermore, we add a chemical potential $h \to h + \mu \mathbb{1}$ where $\mathbb{1}$ is the identity matrix and $\mu = 2\cos(\pi/6)$ in order to have a null fermi energy. The result for the energy band with and without soliton is shown in Figure C.1.

The 2 bands overlap for most of the eigenstates, but, looking closely to the states near the gap (Fig. C.1(b)), one can observe that the 1^{st} excited state above the Fermi level lowers in energy due to the presence of the soliton. Therefore, a solitonic distortion of the CDW costs an elastic energy but also leads to the reduction of the energy cost of adding an electron.

One question still remains unanswered. Is the additional electron localized near the soliton or does it spreads over the whole atomic chain? In order to get the answer, we show a plot of the difference between the electronic density as a function of position of the CDW ground state where $N_{el} = \frac{N_{site}}{\lambda}$ eigenstates are filled $\rho_{GS}(n)$ and for a state with filling $N_{el} + 1$ in the presence of a soliton $\rho_{\text{sol}\,GS+1}(n)$

This difference as a function of position $\delta\rho(n) = \rho_{\text{sol}\,GS+1}(n) - \rho_{GS}(n)$ is depicted in Fig.C.2. As expected, $|\delta\rho(n)|$ is larger near the soliton (centered on site $n = 0$). Therefore, one could conclude that the additional electron is located in the vicinity of the soliton. Unfortunately, $\delta\rho$ varies between positive and negative values, hence with this illustration, we are still unable to say with certainty where is the additional electron.

In order to get a final answer, we plot the integrated density of the additional

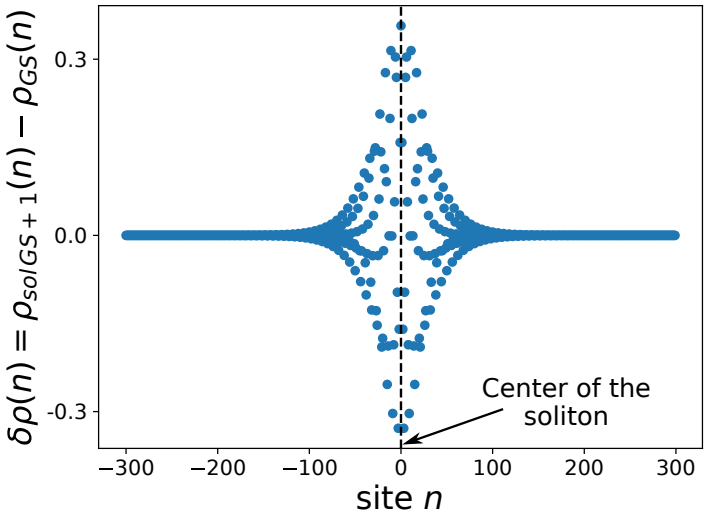

Figure C.2: Difference of the electronic densities as a function of position n between a CDW with $N_{el} = \frac{N_{site}}{\lambda}$ lowest eigenstates filled (corresponding to the CDW groundstate) and a CDW with the soliton and filling $N_{el} + 1$. The soliton is centered in the middle of the chain on site $n = 0$ indicated by the dotted line. The difference is stronger at the soliton position.

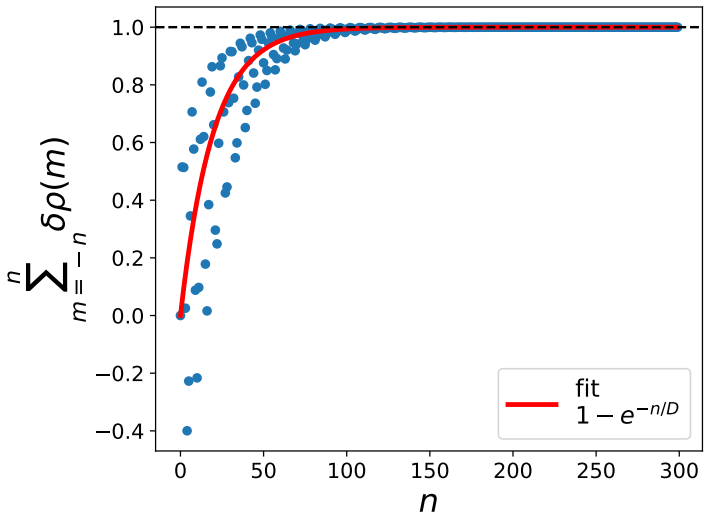

Figure C.3: Probability $P(e^- \in [-n; n])$ to find the additional electron between the soliton center and n sites further. The electron is exponentially localized near the soliton. An exponential fit is added (red curve).

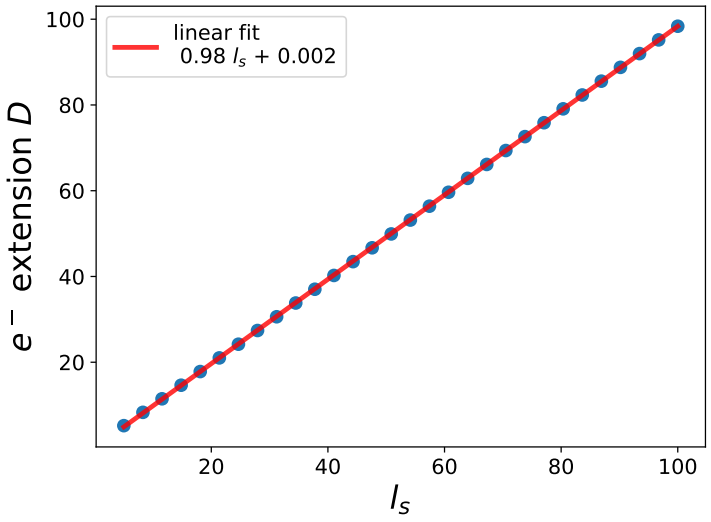

Figure C.4: Additional electron extension D given by the fit of Fig.C.3 as a function of the soliton width l_s (see Eq.C.1). The linear fit in red shows that $D \approx l_s$.

electron $\delta\rho(n)$ starting around the soliton center.

$$P\left(\text{additional electron} \in [-n; n]\right) = \sum_{m=-n}^{n} \delta\rho(m)$$

Which corresponds to the probability to find the additional electron between the soliton center and n sites further. This probability is sketched in Fig.C.3. The electron is exponentially localized near the center of the soliton as expected. A fit is performed using the function $1 - e^{-n/D}$ in order to extract this probability extension parameter D.

Finally, this prodcedure is performed several time for different value of the soliton width l_s (see Eq.C.1) in order to get $D(l_s)$, see Fig.C.4. As seen in this last figure, the electron extension is linear as a function of the soliton width l_s. We can even approximate $D \approx l_s$.

Therefore, we can conclude that, indeed the soliton presence reduces the cost in energy needed to add an electron in the CDW and this additional electron is confined inside the soliton on a typical length scale l_s.

Appendix D

Second method for the kmap wavevector calculation

In this appendix, we present a second method used for the wavevector calculation in order to check the validity of the data treatment presented in chapter 4. Remember from figure 4.4 that in the micro-diffraction experiment, we measured a 5D matrix : Intensity(φ, x, z, x_{det}, y_{det}) where φ is the rotation angle of the $NbSe_3$ sample with respect to the X-ray beam, (x, z) is the position of the beam spot on the sample and finally (x_{det}, y_{det}) is the pixel position on the detector.

Each set of 3 values $(\varphi, x_{det}, y_{det})$ corresponds to a wavevector $\vec{Q}$ in reciprocal space that can be calculated from Eq4.1, where δ and ν are related to x_{det} and y_{det}. Using the first method in chapter 4, for each position on the sample (x, y), we took the value of φ_{max} corresponding to the maximum of the rocking curve and for this φ_{max}, we calculated the centroid on the detector to find the averaged (x_{det}, y_{det}). On the other hand, for our second method presented here, we compute an average at the end directly on $\vec{Q}$. First, we calculate the 3D matrices $Q_{matrix,i}(\varphi, x_{det}, y_{det})$ (where i=x, y or z) giving for *each* values of $(\varphi, x_{det}, y_{det})$ (not only for the centroid) the corresponding wavevector components using again Eq4.1. Then, the averaged wavevector $\vec{Q}$ at each position (x, z) on the sample is computed via the formula

$$Q_i(x,z) = \frac{\sum\limits_{\varphi, x_{det}, y_{det}} Q_{matrix,i}(\varphi, x_{det}, y_{det}) \times \text{Intensity}(\varphi, x, z, x_{det}, y_{det})}{\sum\limits_{\varphi, x_{det}, y_{det}} \text{Intensity}(\varphi, x, z, x_{det}, y_{det})} \qquad \text{(D.1)}$$

where $i = x, y, z$

where the denominator is a normalization factor. A comparison between the first method used in chapter 4 and the second method presented here is shown in figure D.1 for the CDW satellite reflection (0,1,0)+$\vec{q}_{cdw}$ at -1mA. One can see that the maps are almost identical for both methods.

In addition here, we reproduce figures 4.9 and 4.10 of chapter 4 in order to confirm the CDW surface pinning interpretation. In figure D.2, we compare the results of figure 4.9 using the first method (circular symbols) and the second (triangle symbols). The difference between the two is small and one needs to zoom on the data to see a difference.

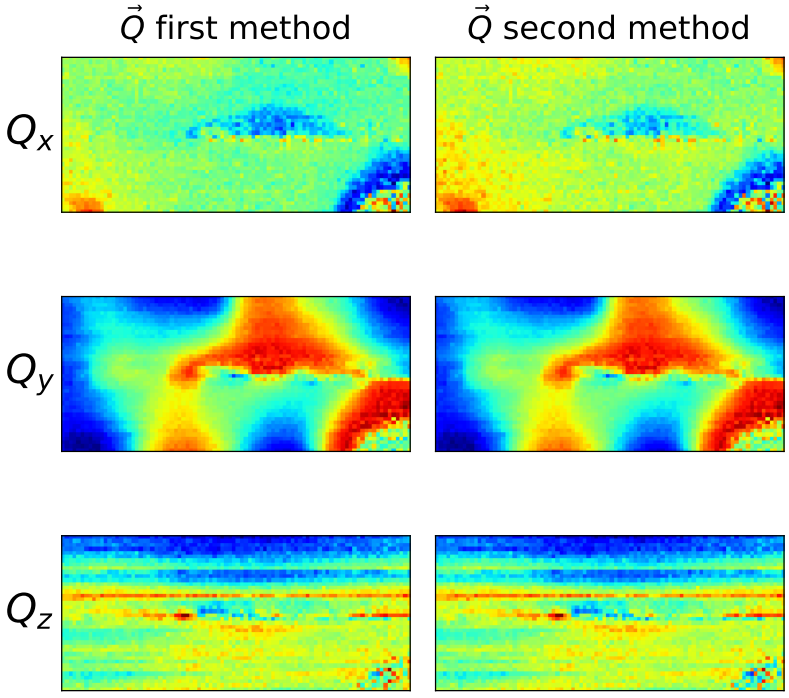

Figure D.1: Calculated wavevector components for the CDW satellite reflection (0,1,0)+$\vec{q}_{cdw}$ using the first method presented in chapter 4 on the left and those using the second method EqD.1 on the right.

Finally, the phase calculated by our two methods is shown in figure D.3 a), again with circular symbol for the first method and triangles for the second. The difference being too small to be observed, we show in b) the phase difference between the 2 methods. In comparison to the variation of ϕ ($\sim 20 \times 2\pi$) in a), the difference is negligible ($\sim 0.4 \times 2\pi$) in b). Therefore, we can conclude that the observed surface pinning effect is not dependent on the method used to find the average diffracted wavevector $\vec{Q}$.

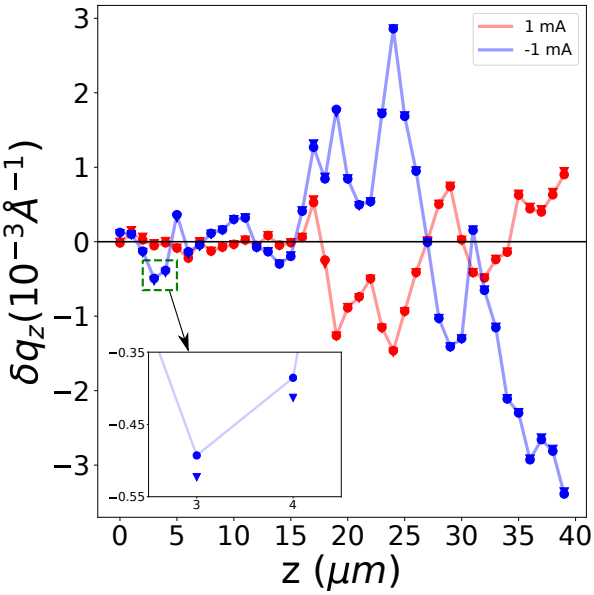

Figure D.2: Comparison of the results of figure 4.9 presented in chapter 4 at $\pm 1mA$ using the first method (circular symbols) and the second (triangles). The two methods gives similar result. The small difference can only be observed by zoom in as shown in the inset.

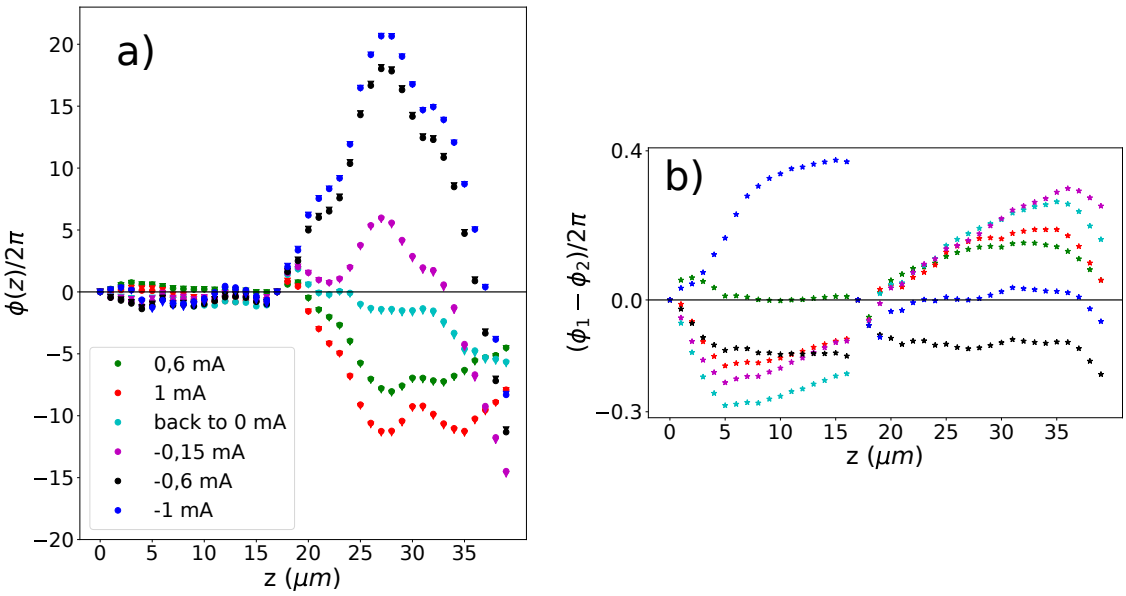

Figure D.3: a) CDW phase ϕ calculated with our two methods. The circular symbols correspond to the first method ($\equiv \phi_1$) while the triangles to the second ($\equiv \phi_2$). b) Phase difference between the 2 methods $(\phi_1 - \phi_2)/2\pi$. The difference is negligible compared to the variations of ϕ.

Appendix E

Verification of the 3D pinned phase solution

In this small appendix, we check that the pinned CDW phase solution Eq6.23 indeed satisfies the original equation 6.4 and the condition 6.5. The equation and conditions are given again here

$$(\Delta - \omega^2)\phi = E \tag{E.1}$$

$$\phi(\pm\frac{L_x}{2}, y, z) = \phi(x, \pm\frac{L_y}{2}, z) = \phi(x, y, \pm\frac{L_z}{2}) = 0 \tag{E.2}$$

where $\Delta = \frac{\partial^2}{\partial x^2} + \frac{\partial^2}{\partial y^2} + \frac{\partial^2}{\partial z^2}$. The corresponding solution from the green function and image charges method

$$\begin{aligned}\phi(\vec{r}) = -\frac{64E}{\pi^3} \sum_{n_x=0}^{+\infty} \sum_{n_y=0}^{+\infty} \sum_{n_z=0}^{+\infty} \frac{(-1)^{n_x+n_y+n_z}}{(2n_x+1)(2n_y+1)(2n_z+1)} \times \\ \frac{1}{\left[(2n_x+1)\frac{\pi}{L_x}\right]^2 + \left[(2n_y+1)\frac{\pi}{L_y}\right]^2 + \left[(2n_z+1)\frac{\pi}{L_z}\right]^2 + \omega^2} \times \\ \cos\left[(2n_x+1)\frac{\pi}{L_x}x\right] \cos\left[(2n_y+1)\frac{\pi}{L_y}y\right] \cos\left[(2n_z+1)\frac{\pi}{L_z}z\right]\end{aligned} \tag{E.3}$$

Obviously this function satisfies the boundaries conditions E.2 from the three cosines terms. Verifying that this function satisfies E.1 is a harder issue. Putting this solution into the left hand side of E.1, one finds

$$\begin{aligned}(\Delta - \omega^2)\phi = +\frac{64E}{\pi^3} \sum_{n_x=0}^{+\infty} \sum_{n_y=0}^{+\infty} \sum_{n_z=0}^{+\infty} \frac{(-1)^{n_x+n_y+n_z}}{(2n_x+1)(2n_y+1)(2n_z+1)} \times \\ \cos\left[(2n_x+1)\frac{\pi}{L_x}x\right] \cos\left[(2n_y+1)\frac{\pi}{L_y}y\right] \cos\left[(2n_z+1)\frac{\pi}{L_z}z\right]\end{aligned} \tag{E.4}$$

which should be equal to the constant E of the right hand side of E.1. At first sight, this formula still depends on x, y, z from the cosine terms, meaning that all we've done in chapter 6 would be wrong...

Fortunately, this is not the case and we are saved by a formula derived from the taylor development of the atan function and the expression of the cosine as a sum of complex exponential

$$\begin{aligned} K(a) &= \sum_{n=0}^{\infty} \frac{(-1)^n}{2n+1} \cos\left[(2n+1)a\right] \\ &= \frac{1}{2} \sum_{n=0}^{\infty} \frac{(-1)^n}{2n+1} \left[\left(e^{ia}\right)^{2n+1} + \left(e^{-ia}\right)^{2n+1} \right] \\ &= \frac{1}{2} \left[\operatorname{atan}\left(e^{ia}\right) + \operatorname{atan}\left(e^{-ia}\right) \right] \end{aligned}$$

where, for our purpose, a will be set equal to $\frac{\pi}{L_j} j$ where $j = x, y, z$ to link this sum to EqE.4. The goal is to prove that $K(a)$ is actually independent of a. To move forward, we first need to understand what the meaning of an inverse tangent of a complex number. Defining the complex number b as

$$b \equiv \operatorname{atan}(z) \tag{E.5}$$

where z is also complex. We want an expression of b as function of z without going through an inverse tangent. Defining

$$c \equiv e^{ib} \tag{E.6}$$

we first find the expression of c as a function of z, using

$$\tan(b) = \frac{\sin(b)}{\cos(b)} = -i \frac{e^{ib} - e^{-ib}}{e^{ib} + e^{ib}} = -i \frac{c - c^{-1}}{c + c^{-1}}$$

and since, from E.5, $\tan(b) = z$, we have

$$\begin{aligned} -i \frac{c - c^{-1}}{c + c^{-1}} &= z \\ c^2 &= \frac{i - z}{i + z} \\ e^{2ib} &= \frac{i - z}{i + z} \\ b = \operatorname{atan}(z) &= \frac{1}{2i} \ln\left(\frac{i - z}{i + z}\right) \end{aligned}$$

where, in the second line, we used EqE.6. In the last line, we choose the first branch of the complex logarithm function which is of importance for the end of the calculation. Applying our result to the atan terms in $K(a)$, we find

$$\begin{aligned} K(a) &= \frac{1}{4i} \ln \left[\frac{(i - e^{ia})\,(i - e^{-ia})}{(i + e^{ia})\,(i + e^{-ia})} \right] \\ &= \frac{1}{4i} \ln(-1) = \frac{1}{4i} \ln \left(e^{i\pi} \right) \\ &= \frac{\pi}{4} \end{aligned}$$

where, going to the last line, we remembered that our complex logarithm was defined on the first branch. As was anticipated, $K(a)$ is actually independent of a, hence the formula E.4 does'nt depend on either x, y or z. Using our final expression of $K(a)$ to calculate EqE.4 we find

$$(\Delta - \omega^2)\phi = \frac{64E}{\pi^3} \times \left(\frac{\pi}{4} \right)^3 = E$$

which is indeed the right hand side of E.1, everything is fine.

References

[1] P. Monçeau, N. P. Ong, A. M. Portis, A. Meerschaut, and J. Rouxel. Electric field breakdown of charge-density-wave—induced anomalies in nbse$_3$. *Phys. Rev. Lett.*, 37:602–606, Sep 1976.

[2] A. Rojo-Bravo, V. L. R. Jacques, and D. Le Bolloc'h. Collective transport of charges in charge density wave systems based on traveling soliton lattices. *Phys. Rev. B*, 94:201120, Nov 2016.

[3] M.Saitoh P.W.Anderson, P.A.Lee. Remarks on giant conductivity in TTF-TCNQ. *Solid State Communications*, 13:595–598, September 1973.

[4] H. Frohlich. On the theory of superconductivity: The one-dimensional case. *Proc. R. Soc. Lond.*, 223:296–305, May 1954.

[5] J. Bardeen, L. N. Cooper, and J. R. Schrieffer. Theory of superconductivity. *Phys. Rev.*, 108:1175–1204, Dec 1957.

[6] Rudolf Peierls. *Quantum theory of solids*. Oxford university press, 1955.

[7] Rudolf Peierls. *More surprises in Theoretical Physics*. Princeton university press, 1991.

[8] N. D. Mermin and H. Wagner. Absence of ferromagnetism or antiferromagnetism in one- or two-dimensional isotropic heisenberg models. *Phys. Rev. Lett.*, 17:1133–1136, Nov 1966.

[9] P. C. Hohenberg. Existence of long-range order in one and two dimensions. *Phys. Rev.*, 158:383–386, Jun 1967.

[10] J. Chaussy et al. Phase transitions in NbSe3. *Solid State Communications*, 20:759–763, November 1976.

[11] A.H. Moudden et R. Moret J.P. Pouget, C. Noguera. Structural study of the charge-density-wave phase transition of the blue bronze : K0.3MoO3. *J. Phys. France*, 46:1731–1742, October 1985.

[12] C. F. Eagen, S. A. Werner, and R. B. Saillant. Amplitude and nature of the charge-density-wave displacements in $K_2Pt(CN)_4Br_{0.3}.3.2D_2O$ (KCP) at low temperatures. *Phys. Rev. B*, 12:2036–2041, Sep 1975.

[13] Nancy Ru. *Charge density wave formation in Rare-Earth Tritellurides*. PhD thesis, Stanford University, 2008.

[14] Eric Fawcett. Spin-density-wave antiferromagnetism in chromium. *Rev. Mod. Phys.*, 60:209–283, Jan 1988.

[15] V. L. R. Jacques, C. Laulhé, N. Moisan, S. Ravy, and D. Le Bolloc'h. Laser-induced charge-density-wave transient depinning in chromium. *Phys. Rev. Lett.*, 117:156401, Oct 2016.

[16] Pierre Monceau. Electronic crystals: an experimental overview. *Advances in Physics*, 61(4):325–581, 2012.

[17] Alexander Altland and Ben Simons. *Condensed Matter Field Theory (second edition)*. Cambridge university press, 2010.

[18] George Gruner. *Density waves in solids*. Perseus Publishing, 1994.

[19] H. W. Myron, J. Rath, and A. J. Freeman. Generalized electronic susceptibility and charge-density waves in $1T-TaS_2$ and $1T-TaSe_2$. *Phys. Rev. B*, 15:885–889, Jan 1977.

[20] W. Kohn. Image of the fermi surface in the vibration spectrum of a metal. *Phys. Rev. Lett.*, 2:393–394, May 1959.

[21] H. Frohlich. Interaction of electrons with lattice vibrations. *Proc. R. Soc. A*, 215, December 1952.

[22] H. A. Mook and Charles R. Watson. Neutron inelastic scattering study of tetrathiafulvalene tetracyanoquinodimethane (TTF-TCNQ). *Phys. Rev. Lett.*, 36:801–803, Apr 1976.

[23] F. Schmitt, P. S. Kirchmann, U. Bovensiepen, R. G. Moore, L. Rettig, M. Krenz, J.-H. Chu, N. Ru, L. Perfetti, D. H. Lu, M. Wolf, I. R. Fisher, and Z.-X. Shen. Transient electronic structure and melting of a charge density wave in TbTe3. *Science*, 321(5896):1649–1652, 2008.

[24] M.Greenblatt K.V.Ramanujachary, B.T.Collins and J.V.Waszczak. Charge-density-wave instability in $TlMo_6O_{17}$, a new quasi-two-dimensional purple bronze. *Solid State Communications*, 59:647–652, September 1986.

[25] C. W. Chu, J. M. E. Harper, T. H. Geballe, and R. L. Greene. Pressure dependence of the metal-insulator transition in tetrathiofulvalinium tetracyanoquinodimethane (TTF-TCNQ). *Phys. Rev. Lett.*, 31:1491–1494, Dec 1973.

[26] Piers Coleman. *Introduction to Many-Body Physics*. Cambridge university press, 2015.

[27] G. Grüner. The dynamics of charge-density waves. *Rev. Mod. Phys.*, 60:1129–1181, Oct 1988.

[28] R. S. Kwok, G. Gruner, and S. E. Brown. Fluctuations and thermodynamics of the charge-density-wave phase transition. *Phys. Rev. Lett.*, 65:365–368, Jul 1990.

[29] Christophe Brun, Zhao-Zhong Wang, Pierre Monceau, and Serguei Brazovskii. Surface charge density wave phase transition in $NbSe_3$. *Phys. Rev. Lett.*, 104:256403, Jun 2010.

[30] Joseph H. Ross, Zhiyue Wang, and Charles P. Slichter. Nmr study of the structure and motion of charge density waves in $nbse_3$. *Phys. Rev. Lett.*, 56:663–666, Feb 1986.

[31] D. C. Johnston. Thermodynamics of charge-density waves in quasi one-dimensional conductors. *Phys. Rev. Lett.*, 52:2049–2052, Jun 1984.

[32] L.P. Gor'kov G. Grüner. *Charge Density Waves in Solids*. Elsevier Science Publishers, 1989.

[33] Claire Schlenker. *Low-dimensional electronic properties of molybdenum bronzes and oxides*. Kluwer Academic Publishers, 1989.

[34] Sergei V Zaitsev-Zotov. Finite-size effects in quasi-one-dimensional conductors with a charge-density wave. *Physics-Uspekhi*, 47(6):533–554, jun 2004.

[35] B. Keimer et al. From quantum matter to high-temperature superconductivity in copper oxides. *Nature*, 518:179–186, February 2015.

[36] V.Ya. Pokrovskii S.G. Zybtsev and S.V. Zaitsev-Zotov. 'quantized' states of the charge-density wave in microcrystals of k0.3moo3. *Nature Communications*, 1, October 2010.

[37] Mariya A. Lizunova, Florian Schreck, Cristiane Morais Smith, and Jasper van Wezel. Visualizing the connection between edge states and the mobility edge in adiabatic and nonadiabatic topological charge transport. *Phys. Rev. B*, 99:115114, Mar 2019.

[38] Tao Wu, Hadrien Mayaffre, Steffen Krämer, Mladen Horvatic, Claude Berthier, W. N. Hardy, Ruixing Liang, D. A. Bonn, and Marc-Henri Julien. Magnetic-field-induced charge-stripe order in the high-temperature superconductor yba2cu3oy. *Nature*, 477(7363):191–194, 2011.

[39] X. M. Chen et al. Charge density wave memory in a cuprate superconductor. *Nature Communications*, 10, 2019.

[40] W. D. et al. Wise. Charge-density-wave origin of cuprate checkerboard visualized by scanning tunnelling microscopy. *Nature Physics*, 4:696 EP –, Jul 2008.

[41] Eduardo H. da Silva Neto, Pegor Aynajian, Alex Frano, Riccardo Comin, Enrico Schierle, Eugen Weschke, András Gyenis, Jinsheng Wen, John Schneeloch, Zhijun Xu, Shimpei Ono, Genda Gu, Mathieu Le Tacon, and Ali Yazdani.

Ubiquitous interplay between charge ordering and high-temperature superconductivity in cuprates. *Science*, 343(6169):393–396, 2014.

[42] J. E. Hoffman, E. W. Hudson, K. M. Lang, V. Madhavan, H. Eisaki, S. Uchida, and J. C. Davis. A four unit cell periodic pattern of quasi-particle states surrounding vortex cores in bi2sr2cacu2o8+δ. *Science*, 295(5554):466–469, 2002.

[43] X. Montiel, T. Kloss, and C. Pépin. Local particle-hole pair excitations by su(2) symmetry fluctuations. *Scientific Reports*, 7(1):3477, 2017.

[44] X. Montiel, T. Kloss, and C. Pépin. Effective su(2) theory for the pseudogap state. *Phys. Rev. B*, 95:104510, Mar 2017.

[45] C Morice, D Chakraborty, X Montiel, and C Pépin. Pseudo-spin skyrmions in the phase diagram of cuprate superconductors. *Journal of Physics: Condensed Matter*, 30(29):295601, jun 2018.

[46] Y Okajima, H Kawamoto, M Shiobara, K Matsuda, S Tanda, and K Yamaya. Charge-density-wave sliding in ring-shaped crystals of nbse3. *Physica B: Condensed Matter*, 284-288:1659 – 1660, 2000.

[47] M. Tsubota, K. Inagaki, T. Matsuura, and S. Tanda. Aharonov-bohm effect in charge-density wave loops with inherent temporal current switching. *EPL (Europhysics Letters)*, 97(5):57011, mar 2012.

[48] M. Tsubota, K. Inagaki, and S. Tanda. Quantum interference of charge-density waves: Evidence for topological crystals of tas3. *Physica B: Condensed Matter*, 404(3):416 – 418, 2009.

[49] Toru Matsuura, Taku Tsuneta, Katsuhiko Inagaki, and Satoshi Tanda. Topological effects of charge density waves in ring-shaped crystals of $Nbse_3$. *Phys. Rev. B*, 73:165118, Apr 2006.

[50] Taku Tsuneta, Satoshi Tanda, Katushiko Inagaki, Yoshitoshi Okajima, and Kazuhiko Yamaya. New crystal topologies and the charge-density-wave in nbse3. *Physica B: Condensed Matter*, 329-333:1544 – 1545, 2003. Proceedings of the 23rd International Conference on Low Temperature Physics.

[51] Toru Matsuura, Katsuhiko Inagaki, and Satoshi Tanda. Evidence of circulating charge density wave current: Shapiro interference in $nbse_3$ topological crystals. *Phys. Rev. B*, 79:014304, Jan 2009.

[52] K. Nakatsugawa, T. Fujii, and S. Tanda. Quantum time crystal by decoherence: Proposal with an incommensurate charge density wave ring. *Phys. Rev. B*, 96:094308, Sep 2017.

[53] Alfred Shapere and Frank Wilczek. Classical time crystals. *Phys. Rev. Lett.*, 109:160402, Oct 2012.

[54] Frank Wilczek. Quantum time crystals. *Phys. Rev. Lett.*, 109:160401, Oct 2012.

[55] C. Laulhé, T. Huber, G. Lantz, A. Ferrer, S. O. Mariager, S. Grübel, J. Rittmann, J. A. Johnson, V. Esposito, A. Lübcke, L. Huber, M. Kubli, M. Savoini, V. L. R. Jacques, L. Cario, B. Corraze, E. Janod, G. Ingold, P. Beaud, S. L. Johnson, and S. Ravy. Ultrafast formation of a charge density wave state in $1t-tas_2$: Observation at nanometer scales using time-resolved x-ray diffraction. *Phys. Rev. Lett.*, 118:247401, Jun 2017.

[56] T. Huber, S. O. Mariager, A. Ferrer, H. Schäfer, J. A. Johnson, S. Grübel, A. Lübcke, L. Huber, T. Kubacka, C. Dornes, C. Laulhe, S. Ravy, G. Ingold, P. Beaud, J. Demsar, and S. L. Johnson. Coherent structural dynamics of a prototypical charge-density-wave-to-metal transition. *Phys. Rev. Lett.*, 113:026401, Jul 2014.

[57] Anshul Kogar, Alfred Zong, Pavel E. Dolgirev, Xiaozhe Shen, Joshua Straquadine, Ya-Qing Bie, Xirui Wang, Timm Rohwer, I-Cheng Tung, and Yafang Yang. Light-Induced Charge Density Wave in $LaTe_3$. *arXiv e-prints*, page arXiv:1904.07472, Apr 2019.

[58] Alfred et al. Zong. Evidence for topological defects in a photoinduced phase transition. *Nature Physics*, 15(1):27–31, 2019.

[59] Alfred Zong, Xiaozhe Shen, Anshul Kogar, Linda Ye, Carolyn Marks, Debanjan Chowdhury, Timm Rohwer, Byron Freelon, Stephen Weathersby, Renkai Li, Jie Yang, Joseph Checkelsky, Xijie Wang, and Nuh Gedik. Ultrafast manipulation of mirror domain walls in a charge density wave. *Science Advances*, 4(10), 2018.

[60] I. et al. Vaskivskyi. Fast electronic resistance switching involving hidden charge density wave states. *Nature Communications*, 7:11442 EP –, May 2016. Article.

[61] Yaroslav A. et al. Gerasimenko. Intertwined chiral charge orders and topological stabilization of the light-induced state of a prototypical transition metal dichalcogenide. *npj Quantum Materials*, 4(1):32, 2019.

[62] J. Demsar, K. Biljaković, and D. Mihailovic. Single particle and collective excitations in the one-dimensional charge density wave solid $k_{0.3}moo_3$ probed in real time by femtosecond spectroscopy. *Phys. Rev. Lett.*, 83:800–803, Jul 1999.

[63] F. Flicker and Jasper van Wezel. Quasiperiodicity and 2d topology in 1d charge-ordered materials. *EPL (Europhysics Letters)*, 111(3):37008, aug 2015.

[64] G. Li, W. Z. Hu, D. Qian, D. Hsieh, M. Z. Hasan, E. Morosan, R. J. Cava, and N. L. Wang. Semimetal-to-semimetal charge density wave transition in $1t-tise_2$. *Phys. Rev. Lett.*, 99:027404, Jul 2007.

[65] Anshul Kogar, Melinda S. Rak, Sean Vig, Ali A. Husain, Felix Flicker, Young Il Joe, Luc Venema, Greg J. MacDougall, Tai C. Chiang, Eduardo Fradkin, Jasper van Wezel, and Peter Abbamonte. Signatures of exciton condensation in a transition metal dichalcogenide. *Science*, 358(6368):1314–1317, 2017.

[66] F. Weber, S. Rosenkranz, J.-P. Castellan, R. Osborn, R. Hott, R. Heid, K.-P. Bohnen, T. Egami, A. H. Said, and D. Reznik. Extended phonon collapse and the origin of the charge-density wave in $2h-\mathrm{nbse}_2$. *Phys. Rev. Lett.*, 107:107403, Sep 2011.

[67] P. Quémerais. Theory of charge density wave depinning by electromechanical effect. *EPL (Europhysics Letters)*, 117(5):57004, mar 2017.

[68] C. M. Varma and A. L. Simons. Strong-coupling theory of charge-density-wave transitions. *Phys. Rev. Lett.*, 51:138–141, Jul 1983.

[69] N. P. Ong and J. W. Brill. Conductivity anisotropy and transverse magnetoresistance of nbse_3. *Phys. Rev. B*, 18:5265–5271, Nov 1978.

[70] J. Schäfer, M. Sing, R. Claessen, Eli Rotenberg, X. J. Zhou, R. E. Thorne, and S. D. Kevan. Unusual spectral behavior of charge-density waves with imperfect nesting in a quasi-one-dimensional metal. *Phys. Rev. Lett.*, 91:066401, Aug 2003.

[71] J. Chaussy, P. Haen, J.C. Lasjaunias, P. Monceau, G. Waysand, A. Waintal, A. Meerschaut, P. Molinié, and J. Rouxel. Phase transitions in nbse3. *Solid State Communications*, 20(8):759 – 763, 1976.

[72] Vladimir E. Fedorov, Sofya B. Artemkina, Ekaterina D. Grayfer, Nikolay G. Naumov, Yuri V. Mironov, Alexander I. Bulavchenko, Vladimir I. Zaikovskii, Irina V. Antonova, Alexander I. Komonov, and Maxim V. Medvedev. Colloidal solutions of niobium trisulfide and niobium triselenide. *J. Mater. Chem. C*, 2:5479–5486, 2014.

[73] Christos Malliakas, Simon J. L. Billinge, Hyun Jeong Kim, and Mercouri G. Kanatzidis. Square nets of tellurium : Rare-earth dependent variation in the charge-density we of rete3 (re = rare-earth element). *Journal of the American Chemical Society*, 127(18):6510–6511, 2005.

[74] H. J. Kim, C. D. Malliakas, A. T. Tomić, S. H. Tessmer, M. G. Kanatzidis, and S. J. L. Billinge. Local atomic structure and discommensurations in the charge density wave of cete_3. *Phys. Rev. Lett.*, 96:226401, Jun 2006.

[75] V. Brouet, W. L. Yang, X. J. Zhou, Z. Hussain, R. G. Moore, R. He, D. H. Lu, Z. X. Shen, J. Laverock, S. B. Dugdale, N. Ru, and I. R. Fisher. Angle-resolved photoemission study of the evolution of band structure and charge density wave properties in $r\mathrm{te}_3$ (r = Y, la, ce, sm, gd, tb, and dy). *Phys. Rev. B*, 77:235104, Jun 2008.

[76] Hong Yao, John A. Robertson, Eun-Ah Kim, and Steven A. Kivelson. Theory of stripes in quasi-two-dimensional rare-earth tellurides. *Phys. Rev. B*, 74:245126, Dec 2006.

[77] V. Brouet, W. L. Yang, X. J. Zhou, Z. Hussain, N. Ru, K. Y. Shin, I. R. Fisher, and Z. X. Shen. Fermi surface reconstruction in the cdw state of $cete_3$ observed by photoemission. *Phys. Rev. Lett.*, 93:126405, Sep 2004.

[78] A. A. Sinchenko, P. D. Grigoriev, P. Lejay, and P. Monceau. Spontaneous breaking of isotropy observed in the electronic transport of rare-earth tritellurides. *Phys. Rev. Lett.*, 112:036601, Jan 2014.

[79] J. J. Hamlin, D. A. Zocco, T. A. Sayles, M. B. Maple, J. H. Chu, and I. R. Fisher. Pressure-induced superconducting phase in the charge-density-wave compound terbium tritelluride. *Phys. Rev. Lett.*, 102:177002, Apr 2009.

[80] A. Sacchetti, E. Arcangeletti, A. Perucchi, L. Baldassarre, P. Postorino, S. Lupi, N. Ru, I. R. Fisher, and L. Degiorgi. Pressure dependence of the charge-density-wave gap in rare-earth tritellurides. *Phys. Rev. Lett.*, 98:026401, Jan 2007.

[81] W. L. Bragg. *Proceedings of the Cambridge Philosophical Society, Volume XVII.* Cambridge University Press, October 1912 - May 1914.

[82] Jens Als-Nielsen and Des McMorrow. *Elements of Moder X-Ray Physics.* John Wiley and Sons, Ltd Publisher, 2011.

[83] Franck Laloë Claude Cohen-Tannoudji, Bernard Diu. *Mécanique quantique I.* Hermann, 1977.

[84] J. N. Clark, X. Huang, R. Harder, and I. K. Robinson. High-resolution three-dimensional partially coherent diffraction imaging. *Nature Communications*, 3:993 EP –, Aug 2012. Article.

[85] K. D. Finkelstein, Qun Shen, and S. Shastri. Resonant x-ray diffraction near the iron k edge in hematite (α-fe_2o_3). *Phys. Rev. Lett.*, 69:1612–1615, Sep 1992.

[86] L.C. Bourne and A. Zettl. Elastic anomalies in the charge density wave conductor k0.3moo3. *Solid State Communications*, 60(10):789 – 792, 1986.

[87] A. A. Sinchenko, P. Lejay, and P. Monceau. Sliding charge-density wave in two-dimensional rare-earth tellurides. *Phys. Rev. B*, 85:241104, Jun 2012.

[88] A.A. Sinchenko, P. Lejay, O. Leynaud, and P. Monceau. Unidirectional charge-density-wave sliding in two-dimensional rare-earth tritellurides. *Solid State Communications*, 188:67 – 70, 2014.

[89] A. A. Sinchenko, P. Lejay, O. Leynaud, and P. Monceau. Dynamical properties of bidirectional charge-density waves in $erte_3$. *Phys. Rev. B*, 93:235141, Jun 2016.

[90] A. Sinchenko, P.D. Grigoriev, P. Lejay, O. Leynaud, and P. Monceau. Anisotropy of conductivity in rare-earth tritellurides in the static and sliding states of the cdw. *Physica B: Condensed Matter*, 460:21 – 25, 2015. Special Issue on Electronic Crystals (ECRYS-2014).

[91] A. Zettl, G. Grüner, and A. H. Thompson. Charge-density-wave transport in orthorhombic tas_3. i. nonlinear conductivity. *Phys. Rev. B*, 26:5760–5772, Nov 1982.

[92] R. M. Fleming, D. E. Moncton, and D. B. McWhan. X-ray scattering and electric field studies of the sliding mode conductor $nbse_3$. *Phys. Rev. B*, 18:5560–5563, Nov 1978.

[93] P. Segransan at al. Nmr evidence of the frohlich mode in rb0.30moo3. In Shoji Tanaka and Kunimitsu Uchinokura, editors, *Proceedings of the Yamada Conference XV on Physics and Chemistry of Quasi One-Dimensional Conductors*, pages 120 – 122. Elsevier, 1986.

[94] R. E. Thorne, W. G. Lyons, J. W. Lyding, J. R. Tucker, and John Bardeen. Charge-density-wave transport in quasi-one-dimensional conductors. i. current oscillations. *Phys. Rev. B*, 35:6348–6359, Apr 1987.

[95] Kazushige Nomura and Kôichi Ichimura. Stm observation of sliding motion of cdw in k0.3moo3. *Solid State Communications*, 71(2):149 – 152, 1989.

[96] P. Beauchene, J. Dumas, A. Janossy, J. Marcus, and C. Schlenker. Cdw transport in a0.30moo3: Crystal quality, inhomogeneous conductivity and contact geometry. *Physica B+C*, 143(1):126 – 128, 1986.

[97] Kazumi Maki. Creation of soliton pairs by electric fields in charge-density—wave condensates. *Phys. Rev. Lett.*, 39:46–48, Jul 1977.

[98] Kazumi Maki. Soliton pair creation and low-temperature electrical conductivity of charge-density-wave condensates. *Phys. Rev. B*, 18:1641–1646, Aug 1978.

[99] S. Brazovskii and S. Matveenko. On the current conversion problem in charge density wave crystals. i. solitons. *J. Phys. I France*, 1(2):269–280, 1991.

[100] Yu. I. Latyshev, P. Monceau, S. Brazovskii, A. P. Orlov, and T. Fournier. Observation of charge density wave solitons in overlapping tunnel junctions. *Phys. Rev. Lett.*, 95:266402, Dec 2005.

[101] D. Le Bolloc'h, V. L. R. Jacques, N. Kirova, J. Dumas, S. Ravy, J. Marcus, and F. Livet. Observation of correlations up to the micrometer scale in sliding charge-density waves. *Phys. Rev. Lett.*, 100:096403, Mar 2008.

[102] U. Eckern and A. Geier. Microscopic theory of charge-density wave systems. *Zeitschrift für Physik B Condensed Matter*, 65(1):15–27, Mar 1986.

[103] Hideo Yoshioka Masahiko Hayashi. On the ginzburg-landau free energy of charge density waves with a three-dimensional order. *Arxiv*, October 2000.

[104] S. A. Brazovskiĭ, S. A. Gordyunin, and N. N. Kirova. An exact solution of the Peierls model with an arbitrary number of electrons in the unit cell. *Soviet Journal of Experimental and Theoretical Physics Letters*, 31:456, April 1980.

[105] S. A. Brazovskiĭ. *Self-localized excitations in the Peierls-Fröhlich state*, pages 173–184. World Scientific, 1996.

[106] H. Fukuyama and P. A. Lee. Dynamics of the charge-density wave. i. impurity pinning in a single chain. *Phys. Rev. B*, 17:535–541, Jan 1978.

[107] Hidetoshi Fukuyama. Pinning in peierls-fröhlich state and conductivity. *Journal of the Physical Society of Japan*, 41(2):513–520, 1976.

[108] Nobukazu Teranishi and Ryogo Kubo. On impurity pinning of one-dimensional charge density waves. *Journal of the Physical Society of Japan*, 47(3):720–728, 1979.

[109] P. A. Lee and T. M. Rice. Electric field depinning of charge density waves. *Phys. Rev. B*, 19:3970–3980, Apr 1979.

[110] P.A. Lee, T.M. Rice, and P.W. Anderson. Conductivity from charge or spin density waves. *Solid State Communications*, 14(8):703 – 709, 1974.

[111] Michel Peyrard and Thierry Dauxois. *Physique des solitons*. EDP Sciences, 2004.

[112] M. B. Fogel, S. E. Trullinger, A. R. Bishop, and J. A. Krumhansl. Dynamics of sine-gordon solitons in the presence of perturbations. *Phys. Rev. B*, 15:1578–1592, Feb 1977.

[113] Feinberg, D. and Friedel, J. Elastic and plastic deformations of charge density waves. *J. Phys. France*, 49(3):485–496, 1988.

[114] Satish Ramakrishna, Michael P. Maher, Vinay Ambegaokar, and Ulrich Eckern. Phase slip in charge-density-wave systems. *Phys. Rev. Lett.*, 68:2066–2069, Mar 1992.

[115] Ji-Min Duan. Homogeneous quantum phase slippage in bulk charge-density-wave systems. *Phys. Rev. B*, 48:4860–4863, Aug 1993.

[116] Kazumi Maki. Quantum phase slip in charge and spin density waves. *Physics Letters A*, 202(4):313 – 316, 1995.

[117] Noriyuki Hatakenaka, Masato Shiobara, Ken-ichi Matsuda, and Satoshi Tanda. Dimensional crossover of quantum nucleation processes in charge-density-wave phase slips. *Phys. Rev. B*, 57:R2003–R2005, Jan 1998.

[118] John Bardeen. Theory of non-ohmic conduction from charge-density waves in $nbse_3$. *Phys. Rev. Lett.*, 42:1498–1500, May 1979.

[119] John Bardeen. Tunneling theory of charge-density-wave depinning. *Phys. Rev. Lett.*, 45:1978–1980, Dec 1980.

[120] J. R. Tucker, J. H. Miller, K. Seeger, and John Bardeen. Tunneling theory of ac-induced dc conductivity for charge-density waves in $nbse_3$. *Phys. Rev. B*, 25:2979–2982, Feb 1982.

[121] John Bardeen. Macroscopic quantum tunneling in quasi one-dimensional metals. ii. theory. *Phys. Rev. Lett.*, 55:1010–1013, Aug 1985.

[122] John Bardeen. *Depinning of Charge-Density-Waves by Quantum Tunneling*, pages 136–143. Springer, Boston, MA, 2001.

[123] S. G. Lemay, M. C. de Lind van Wijngaarden, T. L. Adelman, and R. E. Thorne. Spatial distribution of charge-density-wave phase slip in $nbse_3$. *Phys. Rev. B*, 57:12781–12791, May 1998.

[124] V. L. R. Jacques, D. Le Bolloc'h, S. Ravy, J. Dumas, C. V. Colin, and C. Mazzoli. Evolution of a large-periodicity soliton lattice in a current-driven electronic crystal. *Phys. Rev. B*, 85:035113, Jan 2012.

[125] G Mihály, P Beauchêne, and J Marcus. Charge-density wave conduction with extremely low differential resistance in k0. 3moo3: Current oscillations. *Solid state communications*, 66(2):149–152, 1988.

[126] Kazushige Nomura, Katsushi Fukuda, Ryuta Kohsaka, and Takashi Sambongi. Electric response of sliding cdw in blue bronzes. *Japanese Journal of Applied Physics*, 26(S3-1):609, 1987.

[127] Kazushige Nomura and Kôichi Ichimura. Stm observation of sliding motion of cdw in k0. 3moo3. *Solid state communications*, 71(2):149–152, 1989.

[128] K. Nakajima, Y. Sawada, and Y. Onodera. Nonequilibrium stationary coupling of solitons. *Journal of Applied Physics*, 46(12):5272–5279, 1975.

[129] L. Mihaly and G. X. Tessema. Dielectric hysteresis and relaxation in the charge-density-wave compound $k_{0.3}moo_3$. *Phys. Rev. B*, 33:5858–5861, Apr 1986.

[130] L. Mihály and G. Grüner. The onset of current carrying charge density wave state in tas3: Switching, hysteresis, and oscillation phenomena. *Solid State Communications*, 50(9):807 – 811, 1984.

[131] A. Zettl and G. Grüner. Onset of charge-density-wave conduction: Switching and hysteresis in $nbse_3$. *Phys. Rev. B*, 26:2298–2301, Aug 1982.

[132] S. Brazovskii, N. Kirova, H. Requardt, F. Ya. Nad, P. Monceau, R. Currat, J. E. Lorenzo, G. Grübel, and Ch. Vettier. Plastic sliding of charge density waves: X-ray space resolved-studies versus theory of current conversion. *Phys. Rev. B*, 61:10640–10650, Apr 2000.

[133] V. L. R. Jacques, D. Le Bolloc'h, E. Pinsolle, F.-E. Picca, and S. Ravy. Estimation of coherence properties of an undulator-generated x-ray beam from near-field and far-field slit diffraction visibilities. *Phys. Rev. B*, 86:144117, Oct 2012.

[134] S Reiche. Transverse coherence properties of the lcls x-ray beam. Technical report, 2006.

[135] E. Pinsolle, N. Kirova, V. L. R. Jacques, A. A. Sinchenko, and D. Le Bolloc'h. Creep, flow, and phase slippage regimes: An extensive view of the sliding charge-density wave revealed by coherent x-ray diffraction. *Phys. Rev. Lett.*, 109:256402, Dec 2012.

[136] R. Danneau, A. Ayari, D. Rideau, H. Requardt, J. E. Lorenzo, L. Ortega, P. Monceau, R. Currat, and G. Grübel. Motional ordering of a charge-density wave in the sliding state. *Phys. Rev. Lett.*, 89:106404, Aug 2002.

[137] H. Requardt, F. Ya. Nad, P. Monceau, R. Currat, J. E. Lorenzo, S. Brazovskii, N. Kirova, G. Grübel, and Ch. Vettier. Direct observation of charge density wave current conversion by spatially resolved synchrotron x-ray studies in $nbse_3$. *Phys. Rev. Lett.*, 80:5631–5634, Jun 1998.

[138] E. Bellec, I. Gonzalez-Vallejo, V. L. R. Jacques, A. A. Sinchenko, A. P. Orlov, P. Monceau, S. J. Leake, and D. Le Bolloc'h. Evidence of Charge Density Wave transverse pinning by x-ray micro-diffraction. *arXiv e-prints*, page arXiv:1905.03499, May 2019.

[139] D.V. Borodin, F.Ya. Nad', Ya.S. Savitskaya, and S.V. Zaitsev-Zotov. Nonlinear effects in small o-tas3 samples. *Physica B+C*, 143(1):73 – 75, 1986.

[140] J. McCarten, D. A. DiCarlo, M. P. Maher, T. L. Adelman, and R. E. Thorne. Charge-density-wave pinning and finite-size effects in $nbse_3$. *Phys. Rev. B*, 46:4456–4482, Aug 1992.

[141] P.J. Yetman and J.C. Gill. Size-dependent threshold fields for fröhlich conduction in niobium triselenide: Possible evidence for pinning by the crystal surface. *Solid State Communications*, 62(3):201 – 206, 1987.

[142] Steven J. Leake et al. The Nanodiffraction beamline ID01/ESRF: a microscope for imaging strain and structure. *Journal of Synchrotron Radiation*, 26(2):571–584, Mar 2019.

[143] P. Godard, M. Allain, and V. Chamard. Imaging of highly inhomogeneous strain field in nanocrystals using x-ray bragg ptychography: A numerical study. *Phys. Rev. B*, 84:144109, Oct 2011.

[144] Gilbert André Chahine et al. Imaging of strain and lattice orientation by quick scanning X-ray microscopy combined with three-dimensional reciprocal space mapping. *Journal of Applied Crystallography*, 47(2):762–769, Apr 2014.

[145] R. P. Hall, M. F. Hundley, and A. Zettl. Switching and phase-slip centers in charge-density-wave conductors. *Phys. Rev. Lett.*, 56:2399–2402, Jun 1986.

[146] R. P. Hall, M. F. Hundley, and A. Zettl. Switching and charge-density-wave transport in $nbse_3$. i. dc characteristics. *Phys. Rev. B*, 38:13002–13018, Dec 1988.

[147] Y. Li, S. G. Lemay, J. H. Price, K. Cicak, K. O'Neill, K. Ringland, K. D. Finkelstein, J. D. Brock, and R. E. Thorne. Imaging shear in sliding charge-density waves by x-ray diffraction topography. *Phys. Rev. Lett.*, 83:3514–3517, Oct 1999.

[148] A. F. Isakovic, P. G. Evans, J. Kmetko, K. Cicak, Z. Cai, B. Lai, and R. E. Thorne. Shear modulus and plasticity of a driven charge density wave. *Phys. Rev. Lett.*, 96:046401, Jan 2006.

[149] D. Le Bolloc'h, A. A. Sinchenko, V. L. R. Jacques, L. Ortega, J. E. Lorenzo, G. A. Chahine, P. Lejay, and P. Monceau. Effect of dimensionality on sliding charge density waves: The quasi-two-dimensional $tbte_3$ system probed by coherent x-ray diffraction. *Phys. Rev. B*, 93:165124, Apr 2016.

[150] Denis Rideau, Pierre Monceau, R Currat, H Requardt, F Nad, Emilio Lorenzo, S Brazovskii, Carsten Detlefs, and Gerhard Grübel. X-ray scattering evidence for macroscopic strong pinning centers in the sliding cdw state of nbse3. *Europhysics Letters, v.56, 289-295 (2001)*, 57, 02 2002.

[151] M. Prester. Size effect in $nbse_3$: Length dependence of the threshold field. *Phys. Rev. B*, 32:2621–2624, Aug 1985.

[152] A. Zettl and G. Grüner. Phase coherence in the current-carrying charge-density-wave state: ac-dc coupling experiments in $nbse_3$. *Phys. Rev. B*, 29:755–767, Jan 1984.

[153] G. Mihály, Gy. Hutiray, and L. Mihály. Local distortion of pinned charge density waves in orthorombic tas3. *Solid State Communications*, 48(3):203 – 205, 1983.

[154] D. DiCarlo, E. Sweetland, M. Sutton, J. D. Brock, and R. E. Thorne. Field-induced charge-density-wave deformations and phase slip in $nbse_3$. *Phys. Rev. Lett.*, 70:845–848, Feb 1993.

[155] Batisti´c, I., Bjelis, A., and Gor'kov, L.P. Generation of the coherent pulses by the cdw-motion. solutions of the microscopic model equations. *J. Phys. France*, 45(6):1049–1059, 1984.

[156] S. A. Brazovskiĭ. *Self-localized excitations in the Peierls-Fröhlich state*, pages 173–184. World Scientific Series in 20th Century Physics, 1996.

[157] Serguei Brazovskii and Thomas Nattermann †. Pinning and sliding of driven elastic systems: from domain walls to charge density waves. *Advances in Physics*, 53(2):177–252, 2004.

[158] S. Brazovskii and S. Matveenko. *Solitons in Charge Density Wave Crystals*, pages 125–135. Springer US, Boston, MA, 1991.

[159] S. Brazovskii and S. Matveenko. On the current conversion problem in charge density wave crystals. ii. dislocations. *J. Phys. I France*, 1(8):1173–1185, 1991.

[160] Jeno Solyom Gyula Hutiray. *Charge density waves in solids*. Springer, 1984.

[161] Joseph M. Carpinelli, Hanno H. Weitering, E. Ward Plummer, and Roland Stumpf. Direct observation of a surface charge density wave. *Nature*, 381(6581):398–400, 1996.

[162] C. Brun, J. C. Girard, Z. Z. Wang, J. Marcus, J. Dumas, and C. Schlenker. Charge-density waves in rubidium blue bronze $rb_{0.3}Moo_3$ observed by scanning tunneling microscopy. *Phys. Rev. B*, 72:235119, Dec 2005.

[163] P. Mallet, K. M. Zimmermann, Ph. Chevalier, J. Marcus, J. Y. Veuillen, and J. M. Gomez Rodriguez. Contrast reversal of the charge density wave stm image in purple potassium molybdenum bronze $k_{0.9}mo_6o_{17}$. *Phys. Rev. B*, 60:2122–2126, Jul 1999.

[164] A. Fang, N. Ru, I. R. Fisher, and A. Kapitulnik. Stm studies of $tbte_3$: Evidence for a fully incommensurate charge density wave. *Phys. Rev. Lett.*, 99:046401, Jul 2007.

[165] Ling Fu, Aaron M. Kraft, Bishnu Sharma, Manoj Singh, Philip Walmsley, Ian R. Fisher, and Michael C. Boyer. Multiple charge density wave states at the surface of $TbTe_3$. *Phys. Rev. B*, 94:205101, Nov 2016.

[166] G. Gammie, J. S. Hubacek, S. L. Skala, R. T. Brockenbrough, J. R. Tucker, and J. W. Lyding. Scanning tunneling microscopy of the charge-density wave in orthorhombic tas_3. *Phys. Rev. B*, 40:11965–11968, Dec 1989.

[167] B. Burk, R. E. Thomson, A. Zettl, and John Clarke. Charge-density-wave domains in 1t-tas_2 observed by satellite structure in scanning-tunneling-microscopy images. *Phys. Rev. Lett.*, 66:3040–3043, Jun 1991.

[168] Serguei Brazovskii, Christophe Brun, Zhao-Zhong Wang, and Pierre Monceau. Scanning-tunneling microscope imaging of single-electron solitons in a material with incommensurate charge-density waves. *Phys. Rev. Lett.*, 108:096801, Feb 2012.

[169] Christophe Brun, Zhao-Zhong Wang, and Pierre Monceau. Scanning tunneling microscopy at the $nbse_3$ surface: Evidence for interaction between $\mathbf{q_1}$ and $\mathbf{q_2}$ charge density waves in the pinned regime. *Phys. Rev. B*, 80:045423, Jul 2009.

[170] B.M Murphy, J Stettner, M Traving, M Sprung, I Grotkopp, M Müller, C.S Oglesby, M Tolan, and W Press. Surface behaviour at the charge density wave transition in nbse2. *Physica B: Condensed Matter*, 336(1):103 – 108, 2003. Proceedings of the Seventh International Conference on Surface X-ray and Neutron Scattering.

[171] D. E. Moncton, J. D. Axe, and F. J. DiSalvo. Study of superlattice formation in $2h$-$nbse_2$ and $2h$-$tase_2$ by neutron scattering. *Phys. Rev. Lett.*, 34:734–737, Mar 1975.

[172] W. L. McMillan. Theory of discommensurations and the commensurate-incommensurate charge-density-wave phase transition. *Phys. Rev. B*, 14:1496–1502, Aug 1976.

[173] Gilles Montambaux. Density waves in a transverse electric field. *Phys. Rev. B*, 54:R17273–R17275, Dec 1996.

[174] A. Ayari and P. Monceau. Transverse injection inhomogeneity in charge-density waves and reduction of the threshold field. *Phys. Rev. B*, 66:235119, Dec 2002.

[175] A. A. Sinchenko, P. Monceau, and T. Crozes. Transverse voltage in a quasi-one-dimensional nbse3 conductor with a charge density wave in zero magnetic field. *JETP Letters*, 93(2):56, Mar 2011.

[176] Song Yue, Mingliang Tian, and Yuheng Zhang. Modulation of the transverse current effect of charge density waves in $k_{0.3}moo_3$. *Phys. Rev. B*, 64:113102, Aug 2001.

[177] Yi Zheng, Zhu-An Xu, Jing-Qin Shen, and Xuan-Jia Zhang. Asymmetric modulation of the transverse current effect of charge-density wave in the blue bronze k0.3moo3. *Physics Letters A*, 305(6):433 – 436, 2002.

[178] N. F. Pedersen, M. R. Samuelsen, and D. Welner. Soliton annihilation in the perturbed sine-gordon system. *Phys. Rev. B*, 30:4057–4059, Oct 1984.

[179] J. P. Pouget, B. Hennion, C. Escribe-Filippini, and M. Sato. Neutron-scattering investigations of the kohn anomaly and of the phase and amplitude charge-density-wave excitations of the blue bronze $k_{0.3}moo_3$. *Phys. Rev. B*, 43:8421–8430, Apr 1991.

[180] B. Hennion, J. P. Pouget, and M. Sato. Charge-density-wave phase elasticity of the blue bronze. *Phys. Rev. Lett.*, 68:2374–2377, Apr 1992.

[181] G. Travaglini and P. Wachter. Charge-density-wave-phase—mode evidence in one-dimensional $k_{0.3}moo_3$. *Phys. Rev. B*, 30:1971–1978, Aug 1984.

[182] Zhao-bin Su and B. Sakita. Chiral symmetry and chiral anomaly in an incommensurate charge-density-wave system. *Phys. Rev. Lett.*, 56:780–783, Feb 1986.

Introduction

Une onde de densité de charge (ODC) est une phase de la matière à basse température proposée par Herbert Fröhlich en 1954 et indépendamment par Peierls en 1955. Cette transition se produit dans les systèmes métalliques dans lesquels un « nesting » de la surface de Fermi induit un fort pic de susceptibilité électronique au vecteur d'onde 2kf, où kf est le vecteur d'onde de Fermi. Cette caractéristique conduit à un amollissement du phonon à 2kf lorsque la température diminue, appelé anomalie de Kohn. Lorsque que l'on atteint la température critique Tc, la fréquence de ce phonon tombe à zéro et le réseau atomique "gèle", ce qui induit une nouvelle modulation périodique au vecteur d'ondes 2kf dans le réseau atomique appelée ODC. Cette modulation ouvre un gap dans la bande d'énergie électronique, c'est donc une transition de type métal-isolant. Comme l'ODC induit une nouvelle périodicité dans le réseau atomique, elle peut être mesurée par diffraction de rayons X. À la transition, des pics de diffraction, communément appelés satellites ODC, apparaissent à ±2kf des pics de Bragg. En étudiant l'évolution d'un satellite sous l'effet d'une perturbation externe (champ électrique, pression, etc...) on peut mesurer la déformation de l'ODC (compression, rotation, etc...).

Nous avons étudié deux types de matériaux ODC durant cette thèse. Tout d'abord, le cristal quasi-1D $NbSe_3$ composé de chaînes atomiques 1D faiblement couplées entre elles. Ce cristal présente 2 transitions CDW, une première à 144K le long de ces chaînes et une seconde à 59K. Nous avons seulement mesurée la première CDW les expériences étant faites à 120K, au-dessus de la deuxième transition. Le second matériau est le quasi-2D $TbTe_3$, un membre de la famille des tritellures de terres rares, constitué de plusieurs plans presque carrés d'atomes de Te dans lesquels une CDW apparaît à 336K donc au-dessus de la température ambiante, ce qui facilite son étude.

Sous courant, la phase ODC présente une caractéristique intéressante. Lorsqu'on mesure la courbe courant-tension (I-V) dans la phase CDW, à faible I le matériau suit une simple loi d'Ohm linéaire mais au-dessus d'un seuil de courant Ith, la courbe s'écarte de cette loi d'Ohm et un courant supplémentaire est mesuré, celui-ci n'apparaissant pas dans la phase métallique haute température. De plus, par une analyse spectrale, on peut remarquer que ce courant additionnel est périodique dans le temps avec une fréquence de l'ordre de dizaines de kHz. Plus surprenant encore, une expérience de diffraction de rayons X cohérent sur le matériau ODC $K0.3MoO3$ a montré que 2 pics de diffraction, que l'on appelle supersatellites, apparaissent de chaque côté du satellite CDW au-dessus du courant seuil I>Ith. Ces pics supplémentaires correspondent à une nouvelle périodicité dans le réseau atomique avec une longueur d'onde de 0,5µm, donc bien plus grande que la longueur d'onde CDW qui est de quelques Å. Ceci a été interprété comme un réseau périodique de solitons de l'ODC, créés à la cathode et annihilés à l'anode et chacun transportant deux électrons.

Ce "processus de glissement de phase" était couramment utilisé dans la littérature pour comprendre certaines expériences de résistivité sur plusieurs matériaux CDW. Lorsqu'un champ

électrique (courant) est appliqué sur l'échantillon, la CDW se déforme près du contact électrique. D'un côté, la longueur d'onde du CDW diminue (compression) et de l'autre côté, elle augmente (expansion). Au-dessus d'un champ de seuil, la déformation de l'ODC est suffisamment forte pour qu'un soliton (saut de phase +2pi) apparaisse au niveau du contact afin de diminuer l'énergie élastique due à la déformation. Ce soliton est ensuite accélérée par le champ électrique et se déplace d'un contact à l'autre. Un soliton étant un objet topologique, il est très robuste contre les perturbations. Fogel et al. ont montré que lorsque le soliton passe par un potentiel d'interaction localisé due à une impureté ou un défaut dans le materiau, il n'est que temporairement ralenti, sa formes est aussi légèrement changée mais l'impureté ne peut pas annihiler le soliton, sauf dans le cas d'un très fort potentiel d'interaction.

À la recherche d'un réseau de solitons dans NbSe3

Étant donné que les pics des supersatellites du réseau de solitons n'ont été observés que dans le matériau ODC K0.3MoO3, nous avons voulu retrouver ce réseau dans NbSe3 sous la première transition CDW à 120K. Nous effectuons la diffraction des rayons X sur la ligne de lumière ID01 du synchrotron ESRF de Grenoble. Les contacts en or ont été évaporés avant l'expérience dans une configuration à 4 points. L'échantillon est ensuite inséré dans un cryostat et la mesure courant-tension est effectuée in-situ. Le cryostat est ensuite placé sur un diffractomètre Huber 3+2 cercles. Nous mesurons ensuite le pic du satellite CDW (0,1+2kf,0) et augmentons le courant espérant observer les supersatellites induit par les solitons.

Sachant que ce type de mesure a déjà été effectué auparavant et qu'aucun supersatellite n'a encore été observé (seule une petite asymétrie du satellite CDW au-dessus de Ith), nous avions besoin d'une meilleure résolution dans l'espace réciproque. ID01 possède, pour des expériences de diffraction à haute résolution, un long tube sous vide avec en extrémité un détecteur de rayons X Andor 2D, permettant ainsi d'avoir une distance détecteur-échantillon de 6,5m. De plus, nous avons utilisé un couple de fentes placées avant l'échantillon pour avoir un faisceau de rayons X cohérent.

Malheureusement, nous n'avons pas observé de supersatellites même lorsqu'un courant beaucoup plus élevé que le seuil I=3.5Ith fut appliqué à l'échantillon. Néanmoins, on peut obtenir une limite inférieure pour la périodicité l du réseau de solitons dans NbSe3 à 120K: si ce réseau existe alors l>1,33µm.

Diffraction X de NbSe3 avec un faisceau cohérent à LCLS

La seconde expérience porte sur la diffraction de rayons X par NbSe3 sous courant faite au laser à électrons libres LCLS (FEL) à Stanford. Au lieu d'utilisé un anneau de stockage circulaire, un FEL est constitué d'un long tube sous vide (3,2 km pour LCLS) dans lequel les électrons sont accélérés d'une manière linéaire. À l'extrémité de l'accélérateur, un onduleur agit sur les électrons pour générer un faisceau de rayons X dans une large gamme d'énergie allant de 280eV à 11,2 kev. De plus, le faisceau de rayons X a un fort degré de cohérence, ce qui signifie que ce faisceau de rayons

X peut être presque considéré comme une onde plane. Par conséquent, nous pouvons observer des interférences entre des régions de l'échantillon séparées par plusieurs micromètres. Ce qui n'est généralement pas le cas sur la plupart des lignes de lumière en synchrotron.

Tout d'abord, nous vérifions la cohérence du faisceau en mesurant la diffraction du faisceau direct par un système de fentes fermées sur 10µm×10µm mesurée sur un détecteur CSPAD-2.3M placé à 7,5m des fentes. Nous observons une figure de diffraction en forme de sinus cardinal comme prévue par la théorie. Ceci indique que notre faisceau X a une longueur de cohérence supérieure à 10µm (nous avons calculé qu'elle est de 90µm). Ensuite, nous mesurons le satellite CDW (0,1,0)+qcdw (qcdw est le vecteur d'onde CDW) en appliquant le courant inférieur puis supérieur au courant seuil Ith. Nous avons observé une brutale augmentation de la largeur transversale du pic lorsque I est proche du seuil. Mais l'intensité intégrée de ce satellite ODC est constante sous courant, ce qui signifie que la CDW ne disparaît pas. De plus, du « speckle » est visible en transverse près d'Ith, c'est à dire que le satellite "se brise" en plusieurs morceaux. On peut interpréter ceci comme une perte de cohérence transverse entre les chaines d'atomes du cristal NbSe3 près du courant seuil. Lorsque le courant augmente davantage au-dessus du seuil th, la largeur transverse diminue, ce qui signifie que la cohérence entre les chaînes est se reforme lorsque le courant additionnel de l'ODC apparaît. En revanche, la largeur longitudinale est constante en fonction de I, donc la cohérence le long des chaînes 1D n'est pas affectée par le courant.

Pour finir, nous mesurons un déplacement longitudinal du pic satellite CDW au seuil qui est interprété comme l'apparition de solitons dans notre échantillon au-dessus de Ith. Puisque chaque soliton rajoute un front d'onde ODC, on observe en moyenne une compression de celle-ci, d'où ce déplacement longitudinal du pic. À courant plus élevé, ce décalage se stabilise à une valeur constante d'environ 3,5×10-4Å-1.

Micro-diffraction du matériau quas-1D NbSe3 sous courant et blocage de surface

Le résultat principal de cette thèse fut obtenu lors d'une expérience de diffraction de rayons X réalisée sur la ligne de lumière ID01 de l'ESRF. Nous avons utilisé le setup de micro-diffraction disponible à ID01 appelé kmap. En utilisant une lentille de Fresnel, nous sommes capables de focaliser les rayons X et d'atteindre une taille de faisceau sur notre échantillon de 100µm×100µm. Par conséquent, nous pouvons mesurer le pic de diffraction correspondant au satellite CDW en fonction de la position du faisceau X sur notre échantillon. A partir de ces données, nous pouvons calculer l'évolution spatiale de l'ODC sous courant (rotation, compression, dilatation...). Afin de faire la différence entre une distorsion du réseau atomique hôte et une distorsion de l'ODC, nous avons mesuré le satellite CDW (0,1,0)+qcdw ainsi que le pic de Bragg (0,2,0). Une déformation de l'ODC sous l'effet du courant devrait être visible sur le satellite mais n'induirait rien sur le pic de Bragg.

De plus, avant de commencer l'expérience au synchrotron, nous avons fait un trou en forme de "L" dans l'échantillon à l'aide d'un faisceau d'ions focalisés (FIB). Grâce à cela, nous avons pu séparer l'échantillon en 2 régions. Lorsque l'on applique le courant, seule la partie supérieure de l'échantillon, celle au-dessus du trou, peut contribuer au courant tandis qu'aucun courant ne peut circuler dans la partie inférieure. De cette façon, on peut comparer directement une région de NbSe3 où le courant circule par rapport à une autre sans courant en même temps, ce qui nous assure que les variations observées sont effectivement dues au transport de charge.

Formellement, nous mesurons une matrice 5D de l'intensité du satellite CDW en fonction de 5 paramètres : φ l'angle entre le faisceau incident de rayons X et l'échantillon NbSe3, (x,z) la position du faisceau X focalisé sur notre échantillon et finalement (xdet,ydet) la position du pixel sur le détecteur 2D. Nous pouvons extraire plusieurs informations de cette matrice. Tout d'abord, en intégrant sur φ, xdet et ydet on obtient l'amplitude de l'ODC en fonction de la position (x,z) sur l'échantillon. Cette amplitude n'ayant pas évolué en fonction du courant nous concluons que l'ODC ne disparaît pas lorsque le courant est appliqué comme nous avons déjà pu l'observer à LCLS.

Une seconde information, plus intéressante, peut être obtenue à partir de notre matrice 5D. En calculant le barycentre en φ, xdet et ydet, nous pouvons obtenir les composantes moyennes du vecteur d'onde Qi(x,z) (avec i=x,y,z) en fonction de la position (x,z) sur l'échantillon, où x est la direction longitudinale de l'ODC et y,z les deux directions transverses. Les variations de ce vecteur d'onde sous courant obtenues pour le satellite CDW, appelé δq, correspondent directement à l'évolution du vecteur d'onde CDW (après s'être assuré que ces variations ne sont pas également observées sur le pic de Bragg).

Tout d'abord, sur la composante longitudinale δqx, nous avons mesuré à nouveau une compression (dilatation) de l'ODC sous courant positif (négatif) dans la région au-dessus du trou fait par le FIB (où le courant circule) tandis que δqx est constant dans la région inférieure (où il n'y a pas de courant). Cependant, l'information la plus intéressante et la plus inattendue est celle observée sur la composante transversale δqz, correspondant à un cisaillement des fronts d'onde ODC. Nous avons mesuré ce cisaillement uniquement dans la région supérieure avec une évolution qui s'inverse lorsque l'on passe d'un courant positif à négatif. Nous pouvons donc être sûrs qu'il s'agit bien d'un effet du courant. Si cet effet avait été induit par un échauffement par effet Joule, l'évolution devrait être similaire pour un courant positif et négatif.

On peut décrire l'ODC par une densité de charge $\rho(x,y,z)=A\cos(2kfx+\phi(x,y,z))$ où A est l'amplitude de l'ODC, 2kf le vecteur d'onde CDW à courant nul et ϕ(x,y,z) la phase CDW avec laquelle on peut décrire une compression, dilatation ou rotation de l'ODC. On peut montrer que δq est directement la dérivée spatiale de ϕ, on peut donc calculer ϕ en intégrant δqz pour y voir plus clair sur l'origine du cisaillement observé sous courant. Ce faisant, nous trouvons un ϕ avec une forme parabolique et, plus important encore, la valeur de ϕ varie essentiellement dans le volume de l'échantillon, mais est presque constante aux limites de l'échantillon, sur la surface. Ceci indique que l'ODC est coincé sur les surfaces de l'échantillon. Lorsque le courant est appliqués à

NbSe3, l'ODC a tendance à se comprimer, mais comme elle ne peut pas se déplacer en surface, les front d'onde de l'ODC se déforment et prennent une forme parabolique, la direction de cette déformation étant fixée par le signe du courant. Cet effet d'épinglage de l'ODC sur la surface a été proposé dans la littérature pour expliquer les résultats de différentes mesures de résistivité effectuées sur des échantillons ayant des sections transversales différentes. Cependant, c'est la première fois que cet effet est observé et spatialement résolu.

Micro-diffraction du matériau quasi-2D TbTe3 sous courant: rotation de l'ODC et effet d'irradiation

Pour notre dernier résultat expérimental, nous utilisons la même technique de micro-diffraction décrite dans la section précédente sur la ligne de lumière ID01 au synchrotron ESRF, mais cette fois-ci sur le matériau quasi-2D TbTe3. L'ODC dans TbTe3 apparaît au-dessus de la température ambiante, ce qui rend l'expérience bien plus facile que pour NbSe3 car aucun système de refroidissement n'est nécessaire. Une mesure courant-tension à 4 points est utilisée pour observer le courant de seuil Ith. Le faisceau de rayons X focalisé par la FZP est ensuite utilisé pour scanner le milieu de l'échantillon, mesurant le pic de diffraction satellite ODC (1,15,0)+qcdw en fonction de la position sur l'échantillon. À l'aide d'une procédure similaire à celle utilisée dans le cas de NbSe3, nous pouvons calculer l'évolution du vecteur d'onde CDW δq(x,z) localement en fonction du courant, où (x,z) est la position du faisceau X sur l'échantillon TbTe3. Comme indiqué précédemment, TbTe3 est un cristal orthorhombique (nous appelons ses 3 axes cristallographiques a, b et c) composé de plans d'atome Te parallèles au plan (a,c) dans lequel l'ODC apparaît le long de l'axe c. Par décomposition de δq le long de a, b et c on peut distinguer entre une compression-dilatation de l'ODC induisant un changement de δqc tandis qu'une rotation correspond à des variations de δqa et δqb.

Dans une première région, nous avons mesuré une évolution claire de δqa et δqb sous courant I tandis que δqc reste constant, ce qui signifie que les fronts d'ondes CDW tournent sous courant tout en gardant la même périodicité. La rotation s'inverse lorsque le signe du courant passe de positif à négatif, ce qui confirme qu'il s'agit effectivement d'un effet physique. De plus, en affichant les valeurs δqa et δqb en fonction de I, on peut observer un cycle d'hystérésis. Cette hystérèse de l'ODC sous courant a été observée dans la littérature pour plusieurs matériaux ODC tel que TaS3, K0.3MoO3 et nous l'avons aussi vu dans NbSe3 pendant l'expérience de micro-diffraction. Afin de vérifier que l'évolution de l'ODC est strictement une rotation sans compression, nous calculons l'évolution du module du vecteur d'onde CDW. Aucune dépendance en courant n'est visible, ce qui confirme une rotation pure de l'ODC sous courant dans TbTe3, sans compression ni dilatation. Enfin, nous avons calculé l'écart-type spatial de δq qui démontre que la rotation n'est pas strictement rigide mais qu'elle varie fortement en fonction de la position sur l'échantillon.

Dans une deuxième ainsi qu'une troisième région, nous avons observé la création d'un défaut localisé qui fixe l'ODC induit très probablement par l'irradiation de notre échantillon par les

rayons X. Proche de ce défaut, seul δqc évolue alors que δqa et δqb restent constants, ce qui signifie que ce défaut induit une compression-dilatation de l'ODC mais aucune rotation. Une oscillation spatiale de δqc est visible, et qui n'est pas encore comprise au moment de la rédaction du présent rapport. Étant donné qu'une compression de l'ODC entraîne une densité de charge locale, ces oscillations pourraient être une forme d'écrantage du défaut par l'ODC.

Calcul de la phase de l'ODC avec un blocage de surface et comparaison avec des expériences de résistivité

Sachant que nous avons observé un blocage de l'ODC sur la surface dans NbSe3 par micro-diffraction, nous voulons confirmer que cet effet permet d'expliquer plusieurs mesures d'Ith en fonction des dimensions de l'échantillon (longueur, largeur, épaisseur) faites sur NbSe3 et TaS3 dans la littérature. Nous utilisons la théorie communément admise d'une conduction électrique de l'ODC par créations périodique de solitons chargés. Sous champ électrique, l'ODC se dilate (compresse) près du contact électrique gauche (droit). Ceci est décrit par une phase ODC dépendant de l'espace $\phi(x,y,z)$. Si la dérivée longitudinale de cette phase $\partial\phi/\partial x$ atteint un seuil $\phi c'$, l'ODC se "fracture" au niveau contact et se reforme avec l'addition d'un soliton. Typiquement, ϕ est considérée comme dépendant uniquement de la direction longitudinale x avec comme condition aux bords un blocage de l'ODC au niveau des contacts. Cependant, cette simplification ne permet pas d'expliquer la dépendance observée expérimentalement d'Ith en fonction des dimensions transverses de l'échantillon (largeur et épaisseur).

Pour résoudre ce problème, nous calculons l'évolution de ϕ lors de l'application d'un champ électrique en tenant compte du blocage de l'ODC au niveau des contacts ainsi qu'à la surface de l'échantillon. Nous avons utilisé la méthode des fonctions de Green et des charges images pour obtenir une expression de ϕ sous la forme d'une somme triple infinie. En 1D, cette solution se simplifie en une forme analytique. Sachant que l'expression 3D ne peut pas être réduite, nous contrôlons tout d'abord la convergence de cette somme infinie afin d'avoir une maitrise sur l'erreur commise lors du fit des données expérimentales. Grâce à cette solution, nous effectuons un fit de plusieurs ensembles de données provenant de Mihaly et al, Prester et al, Zettl et Gruner, Borodin, Yetman et Gill.

Enfin, nous décrivons les hypothèses microscopiques sur l'origine du blocage de l'ODC en surface données par Feinberg et Friedel. Nous avons choisi de poursuivre l'idée de Yetman et Gill d'une ODC commensurables au niveau des surfaces de l'échantillon. À l'aide d'un calcul numérique, nous démontrons que, même dans le cas d'un remplissage de bande électronique qui devrait mener à une ODC incommensurable, la phase ODC commensurable est plus basse en énergie et, par conséquent, le système se bloque dans cette phase. Plusieurs expériences STM ont montré que l'ODC en surface était différente de celle mesurée dans le volume. Par exemple, la deuxième transition CDW dans NbSe3 dans le volume apparaît à 59K tandis qu'en surface, elle a été mesurée à 70-75K, soit presque 15K au-dessus.

Conclusion

Les travaux présentés dans ce manuscrit ont pour fil conducteur l'utilisation de grands instruments (synchrotron et laser à électrons libres) pour l'étude de la diffraction des rayons X par les matériaux à ondes de densité de charge. En utilisant l'installation récente de micro-diffraction sur la ligne de lumière ID01 de l'ESRF sur un échantillon de NbSe3, nous avons pu observer, avec une résolution spatiale, le blocage de l'ODC sur la surface de l'échantillon, confirmant ainsi cette hypothèse utilisée dans la littérature pour expliquer des mesures du courant seuil Ith en fonction des dimensions des échantillons. Nous avons ensuite fait une étude théorique de la validité de cet effet de blocage comme cause de la dépendance d'Ith en fonction de la section transverse de l'échantillon. En utilisant de nouveau la micro-diffraction sur TbTe3, nous avons observé la rotation des fronts d'onde de l'ODC sous courant et mesuré une compression au niveau d'un défaut d'irradiation. Enfin, grâce au fort degré de cohérence du faisceau de rayons X à LCLS, nous avons mesuré la "rupture" de l'ODC en transverse au courant seuil ainsi qu'une compression longitudinale. Tous ces résultats démontre la pertinence d'utiliser les nouvelles techniques expérimentales disponibles dans ces grands instruments sur des matériaux connus pour mettre en lumière des effets collectifs encore non observés.

université PARIS-SACLAY
ÉCOLE DOCTORALE
Physique en Île-de-France (EDPIF)

Titre : Étude de matériaux onde de densité de charge sous courant par diffraction de rayons X

Mots clés : Onde de densité de charge, incommensurable, diffraction, rayons X, micro-diffraction, soliton

Résumé : Ce manuscrit a pour sujet principal la diffraction par rayons X des matériaux ondes de densité de charges (ODC). Nous avons étudié le cristal quasi-1D NbSe3 ainsi que le quasi-2D TbTe3. Plusieurs grands instruments ont été utilisés pour cette étude, le synchrotron ESRF de Grenoble sur la ligne ID01 ainsi que le laser à électron libre LCLS à Stanford. Premièrement, grâce à la cohérence du faisceau X à LCLS, nous avons pu observer une perte de cohérence transverse dans NbSe3 lors de l'application d'un courant électrique au-dessus d'un certain seuil ainsi qu'une compression longitudinale de l'ODC. Ensuite, à l'ESRF, nous avons utilisé un faisceau X focalisé au micromètre par une Fresnel zone plate pour scanner l'ODC localement par diffraction sur NbSe3 puis ensuite sur TbTe3. Lorsqu'un courant est appliqué sur l'échantillon, nous avons observé une déformation transverse indiquant que l'ODC est bloquée au niveau de la surface de l'échantillon dans NbSe3. Dans le cas de TbTe3, l'ODC tourne sous courant présentant un cycle d'hystérésis lorsque le courant passe continument de positif à négatif. Nous avons aussi pu constater dans plusieurs régions, toujours pour TbTe3, la création de défauts d'irradiation localisés induisant une compression-dilatation de l'ODC. Dans une dernière partie théorique, nous montrons comment la théorie du transport électrique de l'ODC par un train de solitons portants chacun une charge ainsi que la prise en compte du blocage de l'ODC sur la surface de l'échantillon que nous avons vu expérimentalement permet de comprendre plusieurs mesures de résistivité en fonction des dimensions de l'échantillon trouvées dans la littérature. Nous présentons ensuite plusieurs idées pour expliquer du blocage de l'ODC sur les surfaces au niveau microscopique et proposons l'hypothèse d'une ODC commensurable en surface (et incommensurable dans le volume).

Title : Study of charge density wave materials under current by X-ray diffraction

Keywords : Charge density wave, incommensurate, diffraction, X-ray, micro-diffraction, soliton

Abstract : The main subject of this manuscript is the X-ray diffraction of charge density wave (CDW) materials. We studied the quasi-1D NbSe3 crystal and the quasi-2D TbTe3. Several large instruments facilities were used for this study, the ESRF synchrotron in Grenoble on the ID01 line and the LCLS free electron laser in Stanford. First, thanks to the coherence of the X-beam at LCLS, we were able to observe a loss of transverse coherence in NbSe3 when applying an electrical current above a certain threshold as well as a longitudinal compression of the CDW. Then, at the ESRF, we used an X-ray beam focused on the micrometer scale by a Fresnel zone plate to scan the CDW locally by diffraction on NbSe3 and on TbTe3. When a current is applied to the sample, we observed a transverse deformation indicating that the CDW is pinned on the sample surface in NbSe3. In the case of TbTe3, the CDW rotates under current showing a hysteresis cycle when one is continuously changing from positive to negative current. We have also observed in several regions, in TbTe3, the creation of localized irradiation defects inducing a compression-dilation of the CDW. In a last theoretical part, we show how the theory of electric transport in the CDW state by a train of charged solitons, as well as taking into account the CDW pinning on the surface of the sample that we have seen experimentally, allows us to understand several resistivity measurements, found in the literature, made on samples with different dimensions. Finally, we present several ideas for an explanation of the CDW pinning at the surfaces on a microscopic level and propose the hypothesis of a commensurate CDW on the surface (and incommensurate in volume).

Université Paris-Saclay
Espace Technologique / Immeuble Discovery
Route de l'Orme aux Merisiers RD 128 / 91190 Saint-Aubin, France